Charles University

Faculty of Science

Study programme: Analytical chemistry

Mgr. Romana Jarošová, Ph.D.

CARBON-BASED ELECTRODES: FROM DETECTION OF BIOLOGICALLY SIGNIFICANT COMPOUNDS TO APPLICATION IN NEURODEGENERATIVE DISEASES

UHLÍKOVÉ ELEKTRODY: OD DETEKCE BIOLOGICKY VÝZNAMNÝCH LÁTEK PO APLIKACI V NEURODEGENERATIVNÍCH CHOROBÁCH

Doctoral Thesis

Supervisor: Prof. RNDr. Jiří Zima, CSc.

Consultants: Prof. RNDr. Jiří Barek, CSc.

RNDr. Hana Dejmková, Ph.D.

Prague, 2023

I declare that all the results used and published in this doctoral Thesis have been obtained by my own experimental work and that all the ideas taken from work of others are properly referred to in the text and the literature survey. I am aware that the prospective use of the results, published in this Thesis, outside the Charles University is possible only with a written agreement of the university.

I also declare that neither this Thesis nor its significant part has been submitted in any form for another degree or diploma at any university or other institution of tertiary education.

Lawrence, Kansas, USA — Mgr. Romana Jarošová, Ph.D.

February 28th, 2023

This dissertation is based on experiments carried out in the period from 2014 till 2022 at Charles University, Faculty of Science, Department of Analytical Chemistry, UNESCO Laboratory of Environmental Electrochemistry. The research fellowship in the laboratory of Prof. Greg M. Swain at the University of Michigan, Faculty of Natural Science, Department of Chemistry, East Lansing, Michigan, USA, was a significant part of the thesis. Finally, some experiments were carried out under the mentorship of Prof. Michael Johnson, at the University of Kansas, Lawrence, Kansas.

ACKNOWLEDGEMENTS

Where would I be, and what would I be without you?

I remember sitting in a library during my second year as a graduate student, and stumbling upon a quotation from an old dissertation thesis: "*Where would I be, and what would I be without you?*" At the time, I found it slightly pathetic, as the thesis was dedicated to the author's wife. Little did I know that several years later, I would be writing my own acknowledgments and using the same "pathetic" sentence, thinking about where I would be and what I would do without YOU.

YOU - Professor Jiří Zima. You have been my academic advisor, my mentor, the person I could email at 2 a.m., telling you all about my concerns, self-doubts, or just having random questions. You would always respond at 6 a.m., providing academic advice, and adding a joke or a couple of warming words when you saw that I needed them. Without you, I would have probably given up on this PhD journey. Looking back at my time in your lab, I may not have done anything extraordinary, but I always felt an unspoken support from you, and I knew that you were there, ready to be my rock. This thesis would never exist without you, Professor Zima, so thank you for all the bigger or smaller things you have ever done for me.

YOU, Professor Jiří Barek. Although you have never been my direct mentor, you have dramatically changed my life. Thank you, Professor Barek, for the biggest opportunity of my life. I would not be where I am today without the chance you gave me.

I do not have to go far from Lab No. 112 when thinking about all those people who have directed me through my graduate school life. Dr. Hana Dejmková is certainly one of the most important people. Of course, there are many great mentors, but Hanka has also become my dear friend, and I will always be thankful for her academic pieces of advice, as well as our friendship.

There are so many people in the Chemistry building who deserve to be acknowledged here! Veronika Skalická, Vašek Skalický, Viktor and Marie Datková - you all have helped me more than you can even think, shared my happy moments, or listened to my problems, and I will always remember those days with you all.

Lastly, I would like to thank my mom, dad, sister, husband, and all the people who have helped me reach this point.

Thank you.

I would like to express my gratitude for the generous financial support provided by the Ministry of Education, Youth and Sports of the Czech Republic, Specific University Research, and Grant Agency of the Czech Republic (project P206/12/G151).

ABSTRACT

CARBON BASED ELECTRODES: FROM DETECTION OF BIOLOGICALLY SIGNIFICANT COMPOUNDS TO APPLICATION IN NEURODEGENERATIVE DISEASES

By

Romana Jarošová

Carbon is a truly remarkable element that is essential to life on Earth, and its unique properties have made it an indispensable component in an astonishingly diverse array of applications. Whether serving as a fuel source or as a key component in electronic devices, carbon's ability to exist in different forms, each with their distinct physical and chemical properties, contributes to its widespread and continued use. Electrode production is one of the areas where carbon found its significant use.

This thesis represents a unique combination of fundamental and applied electrochemistry using carbon-based electrodes. It explores a wide range of topics, from evaluating electrode microstructure as a critical factor affecting its electroanalytical behavior, to the use of carbon-based electrodes in Alzheimer's disease (AD) research.

The first part of this Thesis focuses on the electrochemical performance of carbon-based electrodes with distinct microstructures. Specifically, this section discusses two novel electrode materials: boron-doped diamond and nitrogen-incorporated tetrahedral amorphous carbon. The microstructure of each electrode was investigated, and the role of electrode microstructure in determining biologically significant compounds was explored, with a particular focus on tyrosine, tryptophan, pyocyanin, and isatin. This section of the Thesis provides valuable insights into the electrochemical behavior of carbon-based electrodes, and highlights the importance of electrode microstructure in the detection of biologically relevant molecules.

In contrast, the second part of this Thesis delves into the application of carbon-based electrodes in neuroscience research. Carbon electrodes have been essential in advancing our understanding of the central nervous system, with carbon-fiber microelectrodes (CFME) becoming the gold standard for single-unit recording in neuroscience research. This section

identifies several critical challenges related to the detection of neurochemically significant compounds, which were addressed using fast scan cyclic voltammetry at CFME. This resulted in the development of two novel methods for the detection and quantification of neurologically relevant compounds, namely oxytocin and glutamate. Furthermore, the CFME was used in a study investigating the potential role of dopamine in AD, where a possible link between cognitive decline and alterations in dopamine levels in an AD zebrafish animal model was described. This section of the Thesis provides valuable insights into the practical application of carbon-based electrodes in neuroscience research, showcasing their potential in identifying and quantifying neurochemically important compounds.

ABSTRAKT

UHLÍKOVÉ ELEKTRODY: OD DETEKCE BIOLOGICKY VÝZNAMNÝCH LÁTEK PO APLIKACI V NEURODEGENERATIVNÍCH CHOROBÁCH

Romana Jarošová

Uhlík je pozoruhodný prvek, který je nezbytný pro život na Zemi, a jeho jedinečné vlastnosti ho činí nezbytnou součástí ohromně rozmanitého spektra aplikací. Bez ohledu na to, zda slouží jako zdroj paliva nebo jako klíčová součást elektronických zařízení, schopnost uhlíku existovat v různých formách, každá s vlastními fyzikálními a chemickými vlastnostmi, přispívá k jeho rozsáhlému využití. Jednou z významných oblastí, kde uhlík nachází své uplatnění, je výroba elektrod.

V této disertační práci byly propojeny světy základní a aplikované elektrochemie, kde uhlíkové elektrody hrají základní roli. Práce pokrývá širší spektrum; od zhodnocení mikrostruktury uhlíkových elektrod, jež je kritickým faktorem ovlivňující elektroanalytické chování elektrod, až po využití uhlíkových elektrod pro výzkum spojený s Alzheimerovou chorobou.

První část této disertační práce se zaměřuje na porovnání rozdílných strukturálních a elektroanalytických vlastností uhlíkových elektrod, s akcentem na borem dopovaný diamant a dusíkem modifikovaný amorfní tetraedrický uhlík. Zmíněné elektrodové materiály byly použity pro detekci biologicky významných látek, konkrétně tyrosinu, tryptofanu, pyocyaninu a isatinu. Tato část práce poskytuje cenné poznatky o elektroanalytickém chování uhlíkových elektrod, přičemž zdůrazňuje důležitost mikrostruktury elektrod při volbě vhodného elektrodového materiálu k detekci konkrétních molekul.

Ve druhé části byly uhlíkové elektrody použity pro výzkum v oblasti neurovědy. Uhlíkové elektrody jsou klíčovým prvkem při studiu centrálního nervového systému s využitím elektrochemie, přičemž uhlíkové vláknové mikroelektrody se staly zlatým standardem v této oblasti. V této disertační práci byly identifikovány specifické problémy související s detekcí neurochemicky významných sloučenin, které byly následně řešeny s využitím uhlíkových vláknových mikroelektrod. Výsledkem tohoto úsilí byl vývoj dvou nových metod pro stanovení

a kvantifikaci oxytocinu a glutamátu v mozku Dánia pruhovaného. Konečně, uhlíkové vláknové mikroelektrody byly použity pro studium zkoumající potenciální roli dopaminu v Alzheimerově chorobě, načež byl popsán možný vztah mezi kognitivním úpadkem a změnami hladin dopaminu v mozku. Tato část disertační práce poskytuje cenné poznatky o praktickém využití uhlíkových elektrod v neurovědcích výzkumech, ukazuje jejich potenciál při identifikaci a kvantifikaci neurochemicky důležitých sloučenin.

TABLE OF CONTENTS

ACKNOWLEDGEMENTS……4

ABSTRACT……6

ABSTRAKT……8

KEYWORDS……12

KLÍČOVÁ SLOVA……...12

LIST OF SYMBOLS AND ABBREVIATIONS……..13

CHAPTER 1. INTRODUCTION……..14

CHAPTER 2. CARBON ELECTRODES……16

2.1. Glassy Carbon……17

2.2. Boron-Doped Diamond……...18

2.3. Nitrogen-Incorporated Tetrahedral Amorphous Carbon……19

CHAPTER 3. UTILIZATION OF CARBON-BASED ELECTRODES IN NEUROSCIENCE..22

3.1. Molecules of Interests: Unravelling the Challenges……23

3.1.1. Oxytocin……...23

3.1.2. Glutamate..... 24

3.1.3. Dopamine..... 24

3.2. Fast-scan Cyclic Voltammetry for Rapid Electrochemical Detection……26

3.2.2. Color Plots 28

3.3. Carbon-Fiber Microelectrodes……29

3.4. Animal Models in Neuroscience……30

3.4.1. Zebrafish…….. 31

3.4.1.1. Zebrafish as an Animal Model for Alzheimer's Disease..... 32

CHAPTER 4. RESULTS AND DISCUSSION……33

4.1. Boron Doped Diamond and Nitrogen Incorporated Tetrahedral Amorphous Carbon Electrodes: A Critical Comparison of the Electrode's Electroanalytical Performance (Appendix I-III)……..33

4.4. Optimized Sawhorse Waveform for the Measurement of Oxytocin Release in Zebrafish (Appendix IV)……41
4.5. In situ Electrochemical Monitoring of Caged Compound Photochemistry: An Internal Actinometer for Substrate Release (Appendix V)……..48
4.6. Impaired Dopamine Release and Latent Learning in Alzheimer's Disease Model Zebrafish (Appendix VI)……53
CHAPTER 5. CONCLUSION……...57
CHAPTER 6. REFERENCES……59
APPENDIX I (Publication 1)……75
APPENDIX II (Publication 2)……... 87
APPENDIX III (Publication 3)…….. 96
APPENDIX IV (Publication 4)……107
APPENDIX V (Publication 5)……. 116
APPENDIX VI (Publication 6)……137
APPENDIX VII - CONFIRMATION OF PARTICIPATION…….146
APPENDIX VIII - LIST OF PUBLICATIONS, PRESENTATIONS, ACHIEVEMENTS, AND GRANTS……....147

KEYWORDS

Boron-doped diamond
Carbon electrodes
Carbon microstructure
Electrochemistry
Neurotransmitter
Nitrogen-incorporated tetrahedral amorphous carbon
Voltammetry
Zebrafish

KLÍČOVÁ SLOVA

Borem dopovaný diamant
Uhlíkové elektrody
Mikrostruktura uhlíku
Elektrochemie
Neurotransmiter
Dusíkem dopovaný čtyřboký amorfní uhlík
Voltametrie
Dánio pruhované

LIST OF SYMBOLS AND ABBREVIATIONS

4HPAA	4-hydroxyphenylacetic acid
aCSF	artificial cerebrospinal fluid
AD	Alzheimer's disease
BDD	boron-doped diamond
CFME	carbon-fiber microelectrode
CV	cyclic voltammetry
DA	dopamine
FIA	flow injection analysis
FSCV	fast-scan cyclic voltammetry
GC	glassy carbon electrode
HPLC-UV	high performance liquid chromatography with ultraviolet spectrophotometric detection
OKA	okadaic acid
OXT	oxytocin
*p*HP	*p*-hydroxyphenacyl
RSD	relative standard deviation
SEM	scanning electron microscopy
t*a*-C	tetrahedral amorphous carbon
t*a*-C:N	nitrogen-doped tetrahedral amorphous carbon

CHAPTER 1. INTRODUCTION

The presented Thesis is based on the following six first author manuscripts which are attached as Appendix part I – VII.

1. **Jarošová, R.**; Rutherford, J.; Swain, G. M. Evaluation of a Nitrogen-Incorporated Tetrahedral Amorphous Carbon Thin Film for the Detection of Tryptophan and Tyrosine Using Flow Injection Analysis with Amperometric Detection. *Analyst* **2016**, *141* (21), 6031–6041.

2. **Jarošová, R**.; Sanchez, S.; Haubold, L.; Swain, G. M. Isatin Analysis Using Flow Injection Analysis with Amperometric Detection – Comparison of Tetrahedral Amorphous Carbon and Diamond Electrode Performance. *Electroanalysis* **2017**, *29* (9), 2147–2154.

3. **Jarosova, R.**; Irikura, K.; Rocha-Filho, R.; Swain, G. Detection of Pyocyanin with a Boron-Doped Diamond Electrode Using Flow Injection Analysis with Amperometric Detection and Square Wave Voltammetry. *Electroanalysis* **2021**, *34*, 1–12.

4. **Jarosova, R**.; Douglass, A. D.; Johnson, M. A. Optimized Sawhorse Waveform for the Measurement of Oxytocin Release in Zebrafish. *Anal. Chem.* **2022**, *94* (6), 2942-2949.

5. **Jarosova, R**.; Kaplan, S. V.; Field, T. M.; Givens, R. S.; Senadheera, S. N.; Johnson, M. A. In Situ Electrochemical Monitoring of Caged Compound Photochemistry: An Internal Actinometer for Substrate Release. *Anal. Chem.* **2021**, *93* (5), 2776-2784.

6. **Jarosova, R.**;***** Niyangoda, S. S.; Hettiarachchi, P.; Johnson, M. A. Impaired Dopamine Release and Latent Learning in Alzheimer's Disease Model Zebrafish. *ACS Chem. Neurosci.* **2022**, *13* (19), 2924–2931.

Carbon-based electrodes have emerged as a versatile and promising platform for a wide range of applications, including electroanalysis, electrosynthesis, electrochemical storage and conversion. Carbon electrodes have gained wide popularity, owing to their low cost, chemical inertness, high mechanical strength, rich surface chemistry, and a compatibility with a wide variety of solvents and electrolytes. In order to achieve optimal utilization of carbon electrodes, a full understanding and precise control of various parameters that govern their electrochemical behavior is necessary. These parameters include the kinetics of heterogeneous electron transfer processes, the capacitance of the electrodes, and the adsorption processes that occur on their surfaces.

The first part of this Thesis is focused on comparing two superior electrode materials: boron-doped diamond (BDD) electrode, and nitrogen-incorporated tetrahedral amorphous carbon

(t*a*-C:N) electrode. BDD electrode is a well-known material with excellent attributes, such as low background current, wide working potential window, weak molecular adsorption, and excellent microstructural stability. t*a*-C:N, often called "diamond-like" material, is a new type of electrode material, that has been gaining attention in the scientific world for its superlative properties comparable to BDD. One of the main reasons for its popularity is the fact that t*a*-C:N can be grown at a much lower temperature, allowing for a wider variety of substrate materials.

Carbon microstructure has a significant impact on the electrode's performance, particularly in electrochemical sensing. Therefore, in this Thesis, the microstructure of carbon-based electrodes was discussed, and its effect on the determination of biologically significant compounds (tyrosine, tryptophan, isatin, and pyocyanin) was investigated. The three manuscripts presented in Appendix I-III are primarily focused on BDD and t*a*-C:N, with the goal of highlighting its superior electrochemical performance. These studies aim to demonstrate the advantages of t*a*-C:N and BDD over glassy carbon (GC) electrode. [1–3]

Carbon electrodes have also played a crucial role in advancing our understanding of the central nervous system. In particular, carbon-fiber microelectrodes (CFMEs) have become the gold standard for single-unit recording in neuroscience research. In the second part of this Thesis, several crucial problems related to a detection of neurochemically important compounds were identified, and subsequently addressed using fast scan cyclic voltammetry (FSCV) at CFME. First, a manuscript focused on method development is presented (Appendix IV),[4] describing the development of a FSCV method for the detection of neuropeptide oxytocin at CFME. In Appendix V, a novel method for the quantification of non-electroactive neurotransmitter glutamate, combining the use of electrochemistry and photolysis, is introduced.[5] Finally, CFMEs were employed in a unique study investigating the potential role of dopamine in Alzheimer's disease. In the last study of this Thesis, a possible correlation between cognitive decline and alterations in dopamine levels in AD zebrafish animal model was investigated (Appendix VI).[6]

CHAPTER 2. CARBON ELECTRODES

Carbon is an essential element for life on Earth, and is one of the most abundant elements in the universe. It is found in various forms, including diamond, graphite, and various organic compounds. From a material standpoint, carbon is a fascinating element due to its ability to form a variety of microstructurally unique allotropes. These allotropes include graphite, glassy carbon, single and polycrystalline diamond, and diamond-like carbon, each with its own distinctive properties.

Carbon-based materials are widely employed as electrodes in various electrochemical applications such as electroanalysis, electrosynthesis, and electrochemical storage and conversion.[7–11] This can be attributed to several factors, including their low cost, high mechanical strength, wide working potential window, rich surface chemistry, chemical inertness, and compatibility with a variety of solvents and electrolytes.

To achieve optimal utilization of carbon electrodes, a comprehensive understanding of the factors influencing their surface processes, such as surface capacitance, heterogeneous electron transfer-kinetics, and adsorption is essential. Previously published studies have demonstrated that variations in sp^2 carbon electrode microstructure and surface chemistry significantly impact the heterogeneous electron transfer rate constant for certain redox systems (*e.g.* $Fe(CN)_6^{-3/-4}$), often by orders of magnitude. However, this is not the case for all systems, such as $Ru(NH3)_6^{+3/+2}$, indicating that the effect is highly dependent on the specific system being studied.[12] This finding highlights the importance of careful control and manipulation of carbon electrode surface properties in order to optimize performance in electrochemical applications. Further research into the relation between electrode surface properties and specific redox systems is necessary to fully understand the underlying mechanisms and develop a comprehensive understanding of carbon electrode behavior. [13–18]

2.1. Glassy Carbon

Glassy carbon and *graphite* are the two most common representatives of sp^2-bonded carbon materials. Both materials are composed of carbon atoms that have both σ and π bonds. Graphite exhibits the highest degree of microstructural order among carbon materials, featuring layers on planar polycyclic aromatic sheets arranged in a hexagonal lattice (Figure 1.1A). [19]

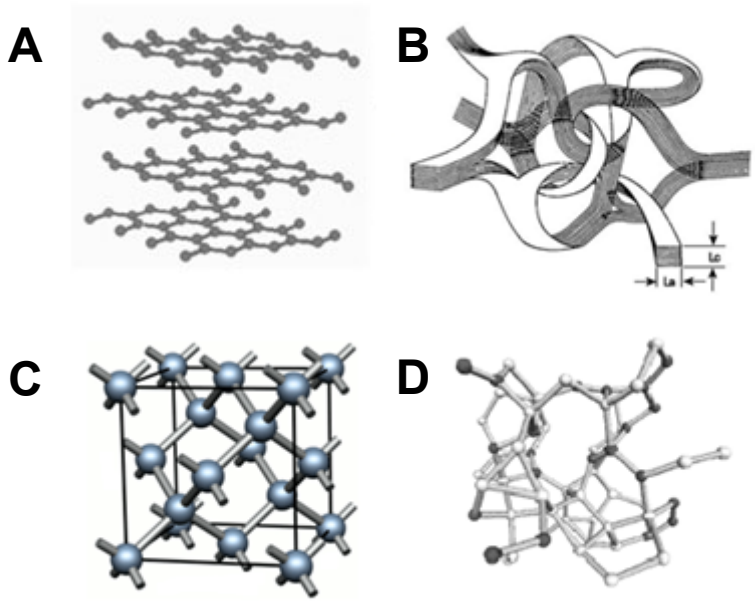

Figure 1.1. Structure of various carbon materials: (**A**) graphite, (**B**) glassy carbon (**C**) diamond and (**D**) tetrahedral amorphous carbon. *(Reprinted with a permission obtained from the Springer Nature).*[19]

Graphitic carbon consists of two distinct surface regions: the basal plane and edge plane. The edge plane sites, which are located at the boundaries between adjacent layers, are highly reactive to adsorption and electron transfer processes. In fact, the carbon atoms at these sites can easily react with oxygen and water, resulting in the formation of a variety of surface oxygen functional groups, including phenols, carbonyls, carboxylic acid, esters, *etc*. The basal plan, which refers to the layer plane surface, lacks functional groups, and has a low density of electronic states. Consequently, the basal plane supports weak molecular adsorption and sluggish electron-transfer kinetics. [20–22] On the other hand, the edge plane is characterized by significantly faster electron transfer kinetics for many redox probes when compared to the basal plane. [23,24] Additionally, the capacitance of the edge plane sites is greater than that of the basal plane sites.

Glassy carbon, in contrast, exhibits a disordered arrangement of graphitic carbon domains, which are intertwined in a random manner to form a ribbon-like structure with nanometer-scale dimensions (Figure 1.1B). The microstructural characteristics of GC are attributed to the production process involving pyrolysis of polymer precursors and subsequent heat treatment, which can influence the degree of microstructural order. The resulting ribbon-like network of entangled graphitic carbon domains provides a high ratio of exposed edge plane sites on the surface of glassy carbon. [19,25,26]

It is important to highlight that glassy carbon possesses electrons in both σ and π orbitals, resulting in a relatively small band gap between the valence and conduction gaps and a high density of electronic states. The existence of π orbitals can give rise to several undesired characteristics, including high background current, structural modifications at high positive potentials, or molecular adsorption. Due to the molecular adsorption, the GC surface is prone to surface deactivation and/or fouling. Achieving optimal performance from a GC electrode requires careful pre-treatment to prepare the surface, microstructure, and chemistry for electrochemical use. One approach to reveal a fresh and active surface on the electrode is to mechanically polish the surface with alumina powder. However, each polishing procedure uncovers a new underlying surface that may have distinct properties, which can lead to changes in the electrochemical activity of the GC electrode.[20,23,27–31] Additionally, the roughness of the electrode surface can influence the electrochemical area, and this may vary with each polishing procedure. As such, it is necessary to carefully consider and understand the unique properties of glassy carbon to effectively utilize it in various scientific applications. [23]

2.2. Boron-Doped Diamond

Diamond is a distinct type of carbon allotrope that represents the opposite end of the spectrum (Figure 1.1.C). Diamond possesses a four-fold, sp3 hybridized carbon lattice composed solely of σ bonds. Diamond is a renowned electrical insulator, with a large band gap of 5.5 eV and a low density of electronic states. Its low electrical conductivity can be attributed to a small number of free charge carriers and limited thermal activation of electron in the conduction band at ambient temperature. In order to enhance the electrical conductivity of diamond, *p*- or *n*- type dopants can be introduced during the growth process. Boron is a frequently used dopant for diamond. It serves as an electron acceptor and creates an impurity

band situated approximately 0.35 eV above the valence band edge. The usual doping levels for diamond films used in electrochemistry vary from 10^{20} to 10^{21} cm^{-3}. [32] The large band gap of diamond allows for optical transparency, which is particularly beneficial for transmission spectroelectrochemical measurements. [33–38]

Boron doped diamond has become a popular choice for carbon electrode materials. [3,39–42] BDD electrodes offer exceptional electrochemical properties, including a wide potential window, low background current and noise, and rapid kinetics of electron transfer processes for many redox analytes. The fundamental electrochemical properties of BDD electrodes have been thoroughly reviewed in numerous publications dating back to the early 1990s. [43–48] In contrast to GC, BDD is morphologically and microstructurally stable, even at potentials higher than +1.4 V. Additionally, due to the absence of π bonds, BDD exhibits limited molecular adsorption, and does not require any extensive surface pre-treatment.

2.3. Nitrogen-Incorporated Tetrahedral Amorphous Carbon

Tetrahedral amorphous carbon (t*a*-C) is a diamond-like allotrope of carbon. Its microstructure consists of randomly arranged sp^2, and sp^3-bonded carbon. The ternary phase diagram (Figure 1.2.) displays the position of t*a*-C reflecting the relationship between the sp^2,

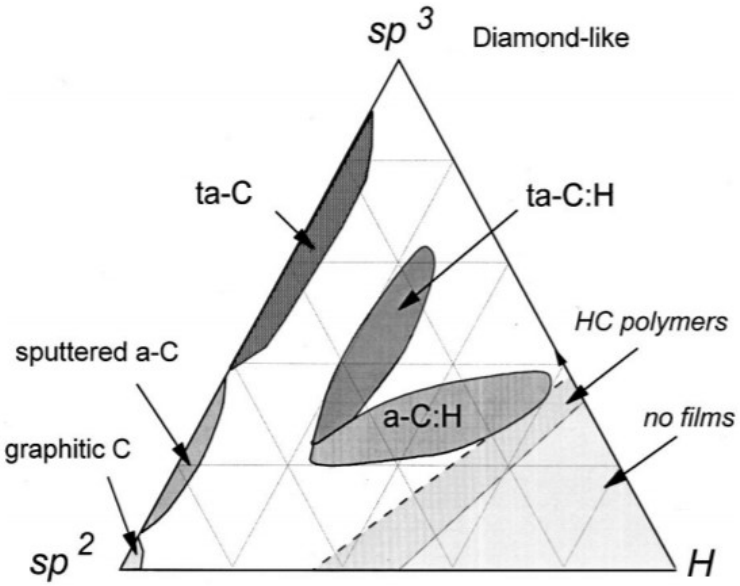

Figure 1.2. Amorphous carbon ternary phase diagram. The corners represent graphite, diamond and hydrocarbons. *(Reprinted with a permission obtained from Elsevier).*[47]

and sp^3-bonded carbon and hydrogen content.[49,50] The amorphous carbon electrodes used in this Thesis contain a high percentage of tetrahedrally bonded sp^3 carbon, typically ranging from 40% to 85%. In t*a-C* films, sp^3 hybridized atoms form a random network with neighboring atoms, connected by strong σ bonds. Interdispersed among these sp^3 carbon regions are sp^2 carbon domains that link them. These sp^2 sites form π states, which are responsible for controlling the electrical and optical properties of the material.

The structural and electronic properties of t*a-C* are primarily determined by the fraction of sp^3-bonded carbon sites, the ordering of sp^2 sites, and the level of hydrogen content. The atomic structure of t*a*-C has been previously described by Robertson *et al.*[51] In this structure, each carbon atom possesses four sp^3 orbitals, which provide four strong σ bonds to neighboring atoms. In contrast, when a carbon atom is in the sp^2 configuration, it forms three trigonal sp^2 orbitals that generate three strong σ bonds in a plane, while the fourth electron is located in a *p* orbital that creates a weaker π bond with an adjacent atom. The incorporation of hydrogen in t*a*-C materials is generally low.

Drawing an analogy with diamond, it is possible to dope t*a*-C material through the incorporation of impurities. Among the various *n*-type dopants employed for this purpose, nitrogen stands out as one of the most commonly used. The incorporation of nitrogen has a profound impact on both the electronic and optical properties of the material. While pure t*a*-C exhibits weak *p*-type semiconductor characteristics, nitrogen doping effectively enhances the material's electrical conductivity, leading to a notable improvement in its performance. [52–55] Finally, nitrogen incorporation affects the sp^2/sp^3 ratio, providing a direct means to fine-tune the material properties through adjustments to sp^2 and sp^3 content. In the first part of this Thesis, the focus is pointed at nitrogen incorporated tetrahedral amorphous carbon (t*a*-C:N) with 30 sccm nitrogen content.

As a result of the significant proportion of sp^3-bonded carbon in this material, t*a*-C:N is frequently compared to diamond, as it boasts of some of diamond's favorable properties, including hardness, chemical inertness, elastic modulus, and optical transparency. Furthermore, previous studies found that t*a*-C:N also possesses exceptional electrochemical behaviors similar to those of BDD. [56–61] While there is an ongoing debate and comparison focused on the properties of both electrode materials, t*a*-C:N electrodes offer an important advantage when compared to BDD as they can be grown at much lower temperatures (25 – 100 °C) while BDD requires

temperatures over 600 °C. This fact opens up new possibilities to a wider range of substrate materials, such as plastics. Furthermore, the deposition of electrodes using t*a*-C:N is considerably more cost-effective, and the process of applying thin films is notably faster compared to the use of BDD.

CHAPTER 3. UTILIZATION OF CARBON-BASED ELECTRODES IN NEUROSCIENCE

The study of the central nervous system has been a fascinating field for researchers for centuries. One of the key components of the nervous system is the neurotransmitter, a chemical messenger that is released by neurons to communicate with other neurons or with other types of cells. Neurotransmitters (*e.g.* dopamine, norepinephrine, serotonin) play a crucial role in regulating a wide range of brain functions, including movement, perception, cognition, and emotion.[62–65] The development of methods for detection of neurotransmitters *in vivo* is a critical tool for studying and understanding the complex mechanism that govern neurotransmission.

The traditional method of measuring neurotransmitter release involves microdialysis,[66–68] an invasive technique that requires significant sample processing, and is not particularly suitable for real-time measurements. Conversely, *in vivo* electrochemical detection of neurotransmitters provides an opportunity for a non-invasive, real-time technique that allows for the detection and quantification of neurotransmitter release in living organisms, organs, and tissues. *In vivo* and *ex vivo* electrochemical detection of neurotransmitters has been used to study a broad spectrum of cerebral activities, including the regulation of mood, addiction, and neurodegenerative disorders.[6,69–72] Additionally, the technique has been also used to study the effects of drugs on neurotransmitter release.[71]

The detection of neurotransmitters using electrochemical methods is not without its challenges. One of the major limitations is the fact that neurotransmitters are present in very low concentrations. Further, the release and uptake of neurotransmitters occur on a millisecond time scale, and their concentration in extracellular fluid changes rapidly, which excludes most of the conventional electrochemical techniques for the possible detection of neurotransmitters in real time. In addition, the presence of other compounds in the extracellular fluid can interfere with the targeted signal. There is also a risk of tissue damage when electrodes are implanted in the tissue, which can affect the accuracy and reliability of the data obtained. Therefore, the method for *in vivo* detection of neurotransmitters requires a sub-second temporal resolution, excellent selectivity, and good sensitivity.

In the second part of this thesis, the application of carbon-based electrodes, specifically carbon-fiber microelectrodes (CFME), in neuroscience research is discussed. Specific challenges are identified under the description of the key molecules in the following chapter.

3.1. Molecules of Interests: Unravelling the Challenges

3.1.1. Oxytocin

Oxytocin is a neuropeptide essential in various physiological and psychological processes in humans and other mammals. It is best known for its role facilitating childbirth and lactation.[73–76] Studies have shown that oxytocin can influence a variety of behaviors and emotions. For example, oxytocin can enhance emotional processing, increase feelings of trust and generosity, as well as reduce negative social behaviors. Additionally, oxytocin has been linked to maternal behavior, bonding between parents and infants.[77–79] Finally, the hormone was linked to stress regulation and anxiety reduction.[77,80]

Given the effects on social behavior and emotions, oxytocin has been investigated as a potential therapeutic agent for various psychiatric disorders (*e.g.* post-traumatic stress disorder, depression),[76,81–83] neurodevelopmental disorders (*e.g.* autism spectrum disorder),[84–88] and investigated for its role in substance abuse [89,90] and addiction.[91–95] However, the dynamics of oxytocin release in living tissue is not fully understood yet. Therefore, there is a significant knowledge gap in understanding and revealing its specific function, as well as its relationship with other neurotransmitters.

The electrochemical behavior of oxytocin have been previously investigated using large scale GC, BDD, and platinum electrodes.[96] The mechanism of the oxytocin redox reaction proposed one electron oxidation on the tyrosine moiety, with a proton loss at the hydroxyl group of the phenol group.[96] The suggested reaction forms a radical susceptible to further nucleophilic attack. The resulting polymerization leads to an adsorption of the reaction product on the electrode surface, fouling the electrode, and consequently leading to a decreased electrode sensitivity.[96]

In vivo based electrochemical methods do not provide possibilities for traditionally used electrode surface cleaning protocols (*e.g.,* polishing and/or chemical cleaning). Hence, there is a critical need for a development of an *in vivo (ex vivo)* method for sensitive detection of oxytocin. This challenge is addressed in Appendix IV.

3.1.2. Glutamate

Glutamate is an amino acid and one of the most abundant excitatory neurotransmitters in the brain. It plays a crucial role in many functions of the brain, including learning, memory, and synaptic plasticity. In addition, glutamate is also involved in various physiological processes, such as metabolism, protein synthesis, and cell proliferation. [97,98]

Dysregulation of glutamate signaling has been implicated in several psychiatric disorders. For example, excessive glutamate release can lead to excitotoxicity, a process in which high levels of glutamate cause damage to neurons and can contribute to the development of neurodegenerative disorders, such as Alzheimer's and Parkinson's disease. On the other hand, decreased glutamate signaling has been linked to depression,[99–101] anxiety,[102–104] and schizophrenia.[105–107] However, the precise role of glutamate in these disorders still not fully understood.

Additionally, there is a complex relationship between glutamate and dopamine in the brain. Dopamine neurons in the brain receive input from glutamate neurons, and the release of dopamine is regulated by glutamate signaling. Specifically, glutamate signaling can either enhance or inhibit the release of dopamine. Importantly, there are several different types of glutamate receptors, each with their own unique functions and effects on neural activity. This diversity makes it challenging to understand the specific effects of glutamate on different brain circuits and behaviors. In addition, it is practically impossible to use traditional methods (tissue perfusion) for investigation of glutamate neural function since glutamate is neurotoxic at high concentrations. To address this knowledge gap, it is crucial to develop a method that would enable for an analysis of glutamate neuronal function. This need is addressed in Appendix V, which describes a newly developed method for *in situ* delivery of glutamate in the living zebrafish brain.[5]

3.1.3. Dopamine

Dopamine is a neurotransmitter that is vital in many brain and body functions. It is involved in a broad variety of processes, including motivation, reward, mood regulation, movement, or attention. [108–110]

Chemically, dopamine belongs to the catecholamine family of neurotransmitters, along with norepinephrine and epinephrine. It is synthesized from the amino acid tyrosine, through a series of enzymatic reactions involving tyrosine hydroxylase, aromatic amino acid decarboxylase, and dopamine beta-hydroxylase. Dopamine is stored in vesicles in dopaminergic

neurons, and released into the synaptic cleft upon depolarization, where it interacts with postsynaptic receptors.

The intricate relationship between dopamine synthesis, storage, release, and uptake has a significant impact on both cognitive and motor function in a range of neurological disorders such as Huntington's disease,[71,111,112] Parkinson's disease, [113–117] and schizophrenia.[118] Despite extensive research, the exact contribution of dopamine dysregulation in the manifestation of cognitive and motor symptoms in Alzheimer's disease remains unclear,[119] creating an important gap in knowledge that needs to be addressed. Understanding the link between dopamine and AD, researchers might be able to develop more effective treatments to slow or prevent the progression of this debilitating condition.

In this thesis, the possible link between dopamine and AD was investigated. Additionally, the correlation between dopamine and cognitive decline commonly observed in AD patients was discussed (Appendix VI).[6]

3.2. Fast-scan Cyclic Voltammetry for Rapid Electrochemical Detection

The utilization of electrochemical methods for a detection of electroactive compounds in brain was pioneered by Ralph N. Adams in 1973. Using cyclic voltammetry (CV) with a carbon paste electrode, Adams attempted to detect neurotransmitters and their metabolites in rat brains.[120–122] Despites of this unquestionable innovation, Adams used conventional cyclic voltammetry with scan rates typically from 0.1 to 1 V s^{-1}, therefore lacking the temporal resolution required for the detection of sub second dynamics of neurotransmitter release. However, his work has led to the invention of FSCV,[123] a method that has been since successfully used for the monitoring of a broad variety of electroactive compounds in the brain (and other tissues) in real time.[112,124–126]

As mentioned, FSCV is a method based on the conventional CV. In both, FSCV and conventional CV, the potential of the working electrode is increased linearly from the holding potential to the switching potential and then back to the holding potential. Such a waveform is specifically chosen based on the analyte of interest. The resulting cyclic voltammogram (plot of current versus the applied potential) provides valuable information that can be used to identify and quantify the target analyte.[127]

The main issue accompanying the detection of neurotransmitters in the brain is the fast rate of the neurotransmitters' release and reuptake, typically on a sub-second scale.[128] This is easily overcome by the utilization of the FSCV. In comparison with conventional CV, FSCV utilizes scan rates on the order of 100 to 1000V/s. As a result, this allows for high frequency measurements, and the technique is therefore characterized by sub-second temporal resolution needed for the detection of neurotransmitters signaling in the brain.[129] Additionally, the waveform parameters, *i.e.* the holding potential, the switching potential, the scan rate, and the frequency, are essential in determining the driving force behind the electrochemical reactions occurring at the electrode surface. Modifying these parameters can improve sensitivity, selectivity, and temporal resolution for a particular analyte.

The typical waveform traditionally used for the detection of dopamine is shown in Figure 3.1., where the potential applied to the working electrode is scanned from -0.4 V to +1.3 V and back to -0.4 V, with a scan rate of 400 V/s. During the forward sweep, dopamine is oxidized to dopamine-*o*-quinone, and reduced back to dopamine on the backward sweep.

For the typical dopamine waveform, 10 Hz frequency is commonly used, and the cycle is therefore repeated every 100 ms.

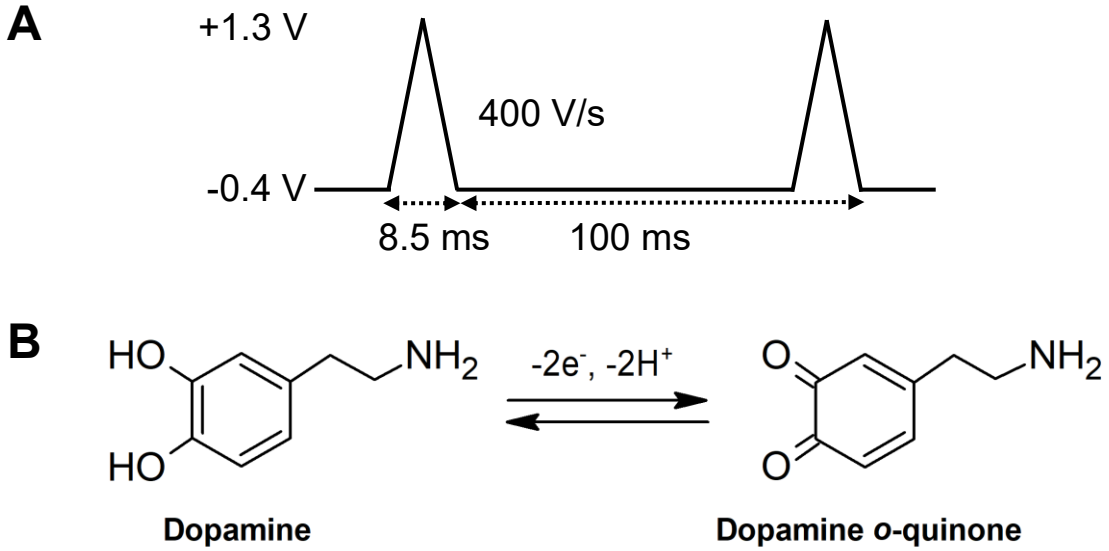

Figure 3.1. (**A**) FSCV waveform for dopamine. (**B**) Dopamine is oxidized to form dopamine-*o*-quinone and reduced back to dopamine.

As mentioned above, FSCV requires an enormously high scan rate in order to capture the neurotransmitters' release. Such a fast scan rate produces a large non-faradaic (*i.e.* background) current, that increases linearly with the used scan rate. [130] As a result, the background current is

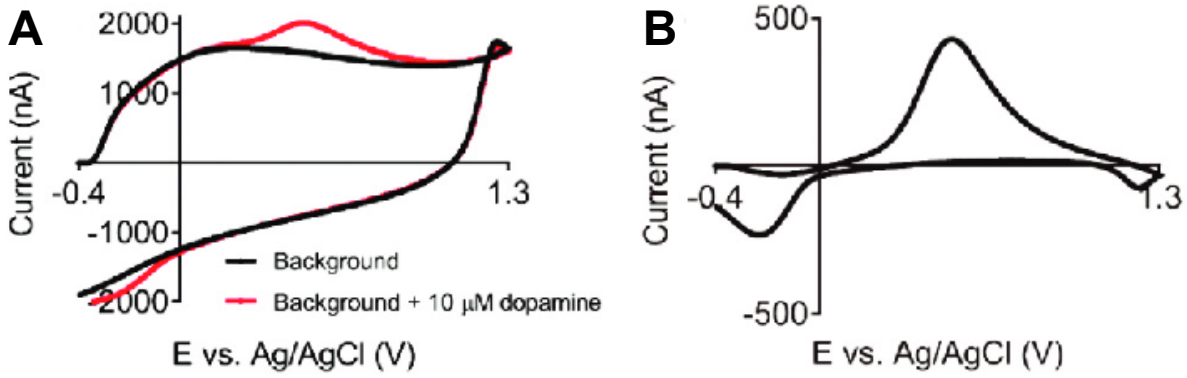

Figure 3.2. FSCV detection of dopamine. (**A**) Background current with (red) and without (black) 10 µM dopamine. (**B**) Background-subtracted FSCV voltammogram for 10 µM dopamine. A waveform from −0.4 to 1.3 V with scan rate of 400 V s^{-1} at 10 Hz was applied to a 7 µm carbon-fiber microelectrode. *Reprinted with permission from Royal Society of Chemistry.*[124]

about 10-100 larger than the measured faradaic current arising from the redox reaction of the target analyte. It is therefore challenging to observe and further evaluate the faradaic current correctly. Nevertheless, the background current for FSCV becomes stable over a short period of continuous cycling, and can be digitally subtracted. The background subtraction is shown in Figure 3.2.

3.2.2. Color Plots

Unlike in the conventional cyclic voltammetry, the typical fast scan cyclic voltammetry experiment lasts about 15 to 30 seconds and produces many voltammograms. Considering the typical high frequency data acquisition at 10 Hz, hundreds of voltammograms are collected. It is therefore impossible to evaluate each individual voltammogram separately. Hence, color plots are used to visualize the large amount of data. the typical cyclic voltammogram for dopamine recorded on CFME is shown in Figure 3.3. On the color plot, the x-axis represents the time (duration of the data collection), and y-axis voltage. Current is represented by different colors. An individual voltammogram at a specific time can be extracted by taking a vertical swipe of the color plot. In order to track the analyte over time, a horizonal swipe should be extracted

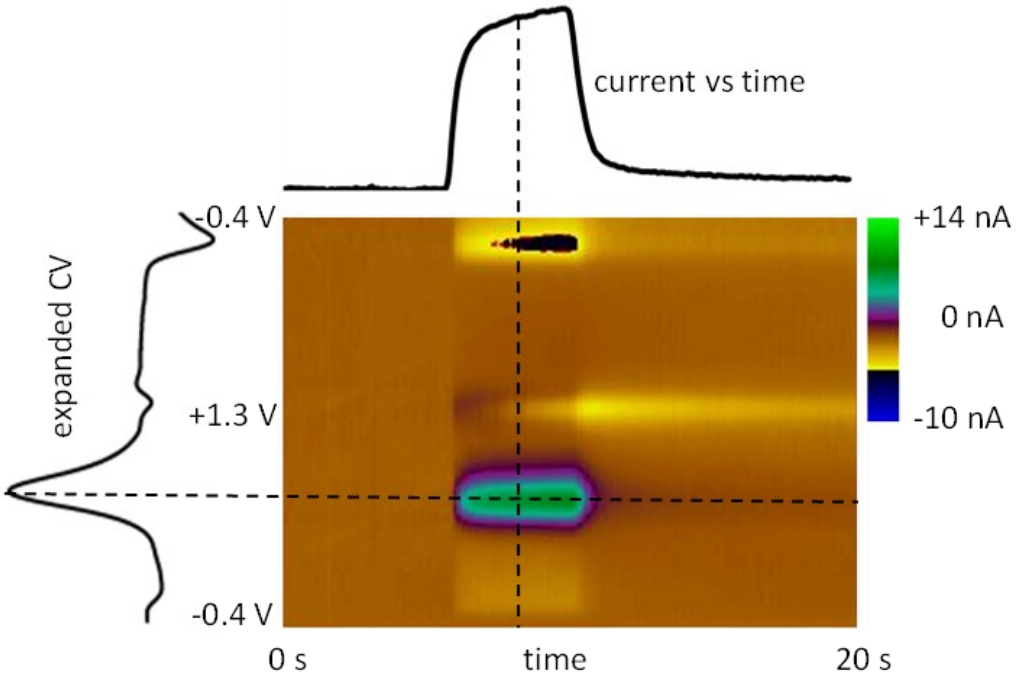

Figure 3.3. FSCV color plot used for data visualization. The x and y axes represent time and voltage applied, and color gradient represents current responses. This plot was generated by injection of 1 µM dopamine at 5 s, the injection was stopped at 10 s. the DA waveform (-0.4 V to +1.3 V and back to -0.4 V at 10 Hz was applied with a scan rate 400 V/s.

to receive a current *vs.* time profile (*I vs. t* trace). FSCV can be used for a real time measurement, however, a manual background subtraction is required to display the redox currents properly.[131]

3.3. Carbon-Fiber Microelectrodes

Conventional electrodes (often called macroelectrodes) described in the first part of this Thesis are not suitable for FSCV applications due to their size. They produce significant charging current, poor spatial resolution, and significantly damage tissue upon their insertion. Microelectrodes have the ability to overcome all of the mentioned barriers. Microelectrodes are generally defined electrodes with at least one characteristic dimension less than 25 μm.[132–134] Due to their small surface area, they generate only small faradaic current, typically smaller than 20 nA. and can be therefore used in a two-electrode arrangement. Furthermore, because of their small size, carbon-based implants are associated with reduced tissue damage during implantation, compared to larger implants. A broad variety of materials have been used for a fabrication of microelectrodes,[135–137] however, carbon based microelectrodes became the most commonly used electrode material used for FSCV applications.[4–6,72,124,138–141]

Carbon-fiber microelectrodes were first introduced by Ponchon et al. in 1979. The team used the electrode for a determination of neurotransmitters (dopamine, norepinephrine,

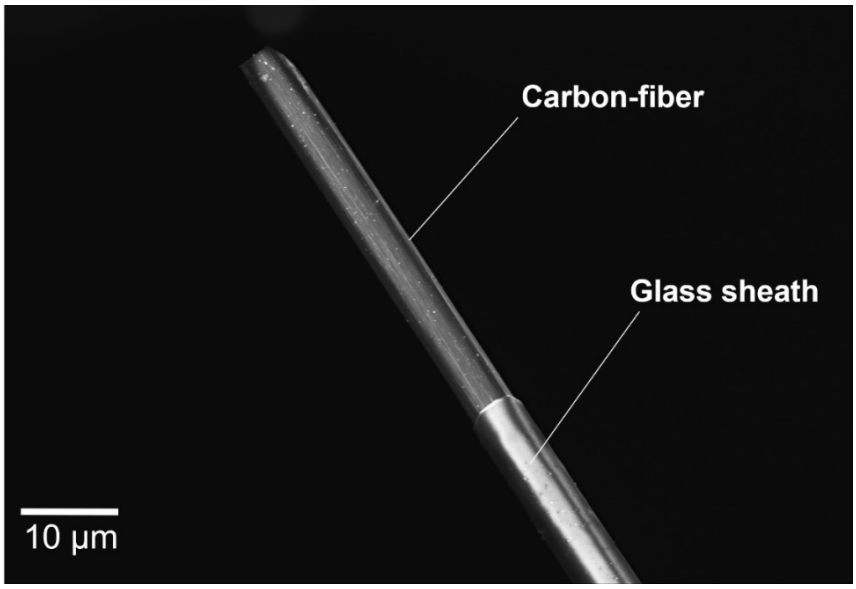

Figure 3.4. SEM image of a carbon-fiber microelectrode. *Obtained from Johnson lab, University of Kansas.*

and serotonin) using normal pulse voltammetry.[142] CFMEs are popular for several reasons: i) biological compatibility with the cellular environment, ii) well characterized electrochemistry, iii) low cost, iv) small size, (v) easy in-house fabrication. Typical size of CFMEs is between 5-10 μm in diameter.[143] In this study, however, the 7 μm (diameter) carbon fiber was used, and the length of the electrode was kept between 50-150 μm. A scanning electron microscope (SEM) image of CFME is shown in Figure 3.4. Detailed information about the CFMEs fabrication process is provided under the Methods sections in Appendix IV-VI.

3.4. Animal Models in Neuroscience

Animal models have been used in neuroscience research for many years to study the structure and function of the nervous system. They are used to provide insight into the cellular and molecular mechanisms underlying brain function, as well as the pathophysiology of neurodegenerative diseases.[144–149] These models are also critical in the discovery of new drugs and therapies, as they allow researchers to study the effects of various compounds and procedures on living organisms.[150–156]

However, despite the extensive research and effort behind the utilization of animal models in neuroscience, using animal models to understand human condition is not fully reliable, mainly due to the difference in biological processes between animal models and humans, Moreover, many brain diseases affecting people do not naturally occur in animals, and modeling might not have the same underlying pathology.

There are numerous animal models used in neuroscience research, including rodents (mice and rats), primates, Drosophila,[157–159] and zebrafish.[160–162] Each animal model has its unique advantages and disadvantages, depending on the research question being investigated. Additionally, when selecting a proper model organism for neuroscience research, a broad variety of factors must be considered; the husbandry cost, genetic ancestry proximity, throughput, as well as moral issues. For example, fruit flies can provide a low cost and high throughput option, however, it is not particularly useful in studies including higher cognitive functions, such as language and memory. On the other side, non-human primates are the exact opposite; while they are excellent models for cognitive related research, their use is extremely expensive, provide only low throughput, and raise serious ethical concerns. In this Thesis, zebrafish (living zebrafish and zebrafish living brain, respectively) was used.

3.4.1. Zebrafish

Zebrafish (*Danio rerio*) are small, tropical freshwater fish that belong to the family Cyprinidae (Figure 3.5.). They are native to the southeastern Himalayan and are widely used as a model organism in scientific research. Over the last decades, zebrafish have become an important model organism in many different areas of research, including developmental biology, genetics, toxicology, neuroscience, and cancer biology.

One of the key advantages of using zebrafish as a model organism is their genetic similarity to humans. Zebrafish share many of the same genes with humans (~70 %), including genes that are associated with diseases like cancer and heart diseases.[163] Additionally, zebrafish have a similar immune system to humans, making them a useful model for studying the immune response to pathogens and potential therapies for immune-related diseases. Another important characteristic of zebrafish is their ability to regenerate tissue. Unlike humans, zebrafish can regenerate damage or lost tissue,[164–166] including fins,[167] heart tissue,[168–170] retina,[171] and even the spinal cord. [172–175]

From the practical point of view, zebrafish are appreciated for several reasons: zebrafish are easy to breed and produce a large number of offspring (generally 100 – 200 per breeding),[176] providing the opportunity for high throughput analyses. Furthermore, housing and maintenance is cheap and does not require extensive housing space. Finally, the transparency of zebrafish embryos and larvae allows researchers to directly observe neural development and activity in real time.

Figure 3.5. Image of adult female zebrafish.

3.4.1.1. Zebrafish as an Animal Model for Alzheimer's Disease

Alzheimer's disease (AD) is a degenerative neurological disorder that progresses over time and impacts millions of individuals globally. It is characterized by the accumulation of abnormal protein aggregates in the brain, including amyloid beta plagues and tau tangles. These aggregates lead to the loss of neurons and consequential cognitive decline. Recent research has demonstrated the effectiveness of okadaic acid (OKA) treatment in developing a robust zebrafish model of AD.[161]

OKA, a polyether fatty acid extracted from marine sponges, has gained widespread use in studies focused on neurotoxicity propagation across various animal models. [177–179] Specifically, OKA has been shown to selectively inhibit protein phosphatases PP1 and PP2A. By blocking PP2A in particular, along with activating several major phosphorylating pathways, OKA trigger the hyperphosphorylation of tau protein, ultimately leading to the formation of tau aggregates. Moreover, although the exact mechanism is not yet fully understood, OKA is believed to contribute to neurodegeneration via oxidative stress and the deposition of Aβ. [180–184] Recent studies have shown that the use of OKA in zebrafish can successfully replicate many of the pathophysiological conditions characteristic of AD. In fact, zebrafish treated with OKA have proven to be a robust model for studying the molecular mechanisms underlying the pathophysiology of AD, as well as for drug discovery targeting this condition. This approach offers a cost-effective and time-efficient way to study AD, as the newly developed OKA-induced AD zebrafish model captures changes in both Aβ-fragments and p-tau protein,[185] reflecting the hallmarks of this disease.

In the final manuscript of this thesis, the OKA-induced AD zebrafish model was used to investigate the possible role of dopamine in AD. In addition, the OKA impact on behavioral changes in adult zebrafish was described.

CHAPTER 4. RESULTS AND DISCUSSION

This chapter provides a summary of the seven scientific publications referenced at the start of this Theses. All of these manuscripts can be found in the Appendix section.

4.1. Boron Doped Diamond and Nitrogen Incorporated Tetrahedral Amorphous Carbon Electrodes: A Critical Comparison of the Electrode's Electroanalytical Performance (Appendix I-III)

The aim of the three enclosed manuscripts is to present a critical evaluation of the analytical performance of BDD and t*a*-C:N electrodes. To achieve this goal, a method for the determination of biologically significant compounds, namely tyrosine and tryptophan,[1] isatin, [2] and pyocyanin, [3] was developed using flow injection analysis (FIA) with amperometric detection at BDD and t*a*-C:N electrodes. The biological importance of each analyte is described in the respective manuscript. The analytical figures of merit for all analytes were determined and used for a direct comparison of the electrochemical performance of both electrodes. Additionally, as BDD and t*a*-C:N are new electrode materials, their results were compared with the historically popular GC electrode. The analytical performance of the electrodes was assessed, and the results presented in this chapter provide valuable insights into the applicability of BDD and t*a*-C:N electrodes in electrochemical sensing applications.

This chapter provides an overview of the results observed in the three manuscripts presented. The first manuscript provides a direct comparison between BDD, t*a*-C:N and GC, while the second publication is focused specifically on t*a*-C:N, and the third on BDD electrode, respectively. To avoid repetitive information, the following text is primarily focused on the comparison of the three electrode materials, with the utilization of tyrosine and tryptophan.

The morphological comparison of both electrodes is shown in Figure 4.1. The SEM images illustrate that the BDD diamond film consists of numerous small, faceted crystallites with lateral dimensions of several hundred nanometers. The film is deposited uniformly over the Si substrate with a thickness of 2-3 μm. On the other hand, the t*a*-C:N film has a nodular morphology, with some larger carbon clusters measuring approximately 50 nm in diameter, and deposited continuously over the silicone substrate at a thickness of 200-400 nm. EDS analysis (not shown here) identified two bright features on the t*a*-C:N film, which were revealed to be adventitious Si particles picked up during handling and use of the film prior to obtaining the micrograph.

The roughness of the t*a*-C:N films is significantly lower, 10-100 times, than the surface roughness of the diamond film.

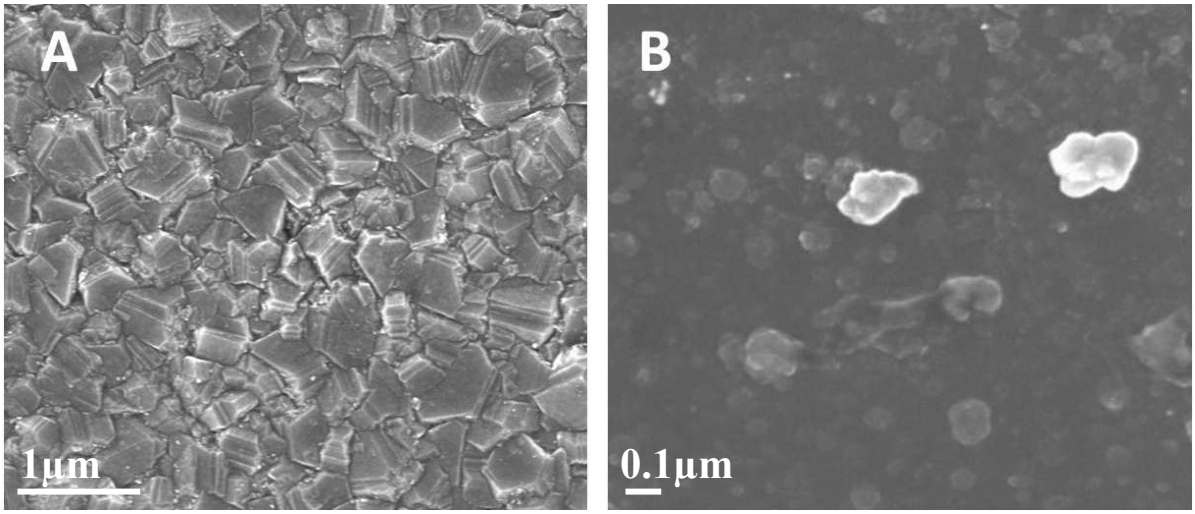

Figure 4.1. SEM micrographs of (**A**) BDD and **B**) t*a*-C:N thin-film electrodes, both deposited on conducting Si substrates. Note the difference in scale bars on the two micrographs: 1µm for BDD and 0.1 µm for t*a*-C:N. *Figure adapted from Appendix III.*[3]

Afterwards, the film microstructure was investigated using Raman imaging spectroscopy. Figure 4.2 displays a representative spectra (Fig 4.2A) and a series of 40 spectra (Fig 4.2B) that were recorded along a several micrometer-long line profile. Each spectrum shown in the line profile is the average of three spectra recorded at each location on the specimen.

In the single spectrum, there are two discernible peaks. The first peak, which is located at 510 cm^{-1}, is intense and appears above a wider scattering signal. The second peak, which is less intense and wider, is observed at approximately 950 cm^{-1}. These peaks are attributed to the silicone substrate's first- and second-order phonon modes. Additionally, there is a broad peak that is observed around 1200 cm^{-1} and a sharp peak at around 1300 cm^{-1}. The latter peak corresponds to the first-order diamond phonon, which is down-shifted from its expected position of 1332 cm^{-1} seen in bulk, single-crystal diamond. The reduced peak intensity, peak broadening, and downward shift of the first-order line are all characteristic features of heavily boron-doped diamond films when compared to bulk diamond.

The shift of the first-order diamond phonon line towards lower wavenumbers is observed when the boron-doping level exceeds 10^{19} boron atoms cm^{-3}. This shift is accompanied

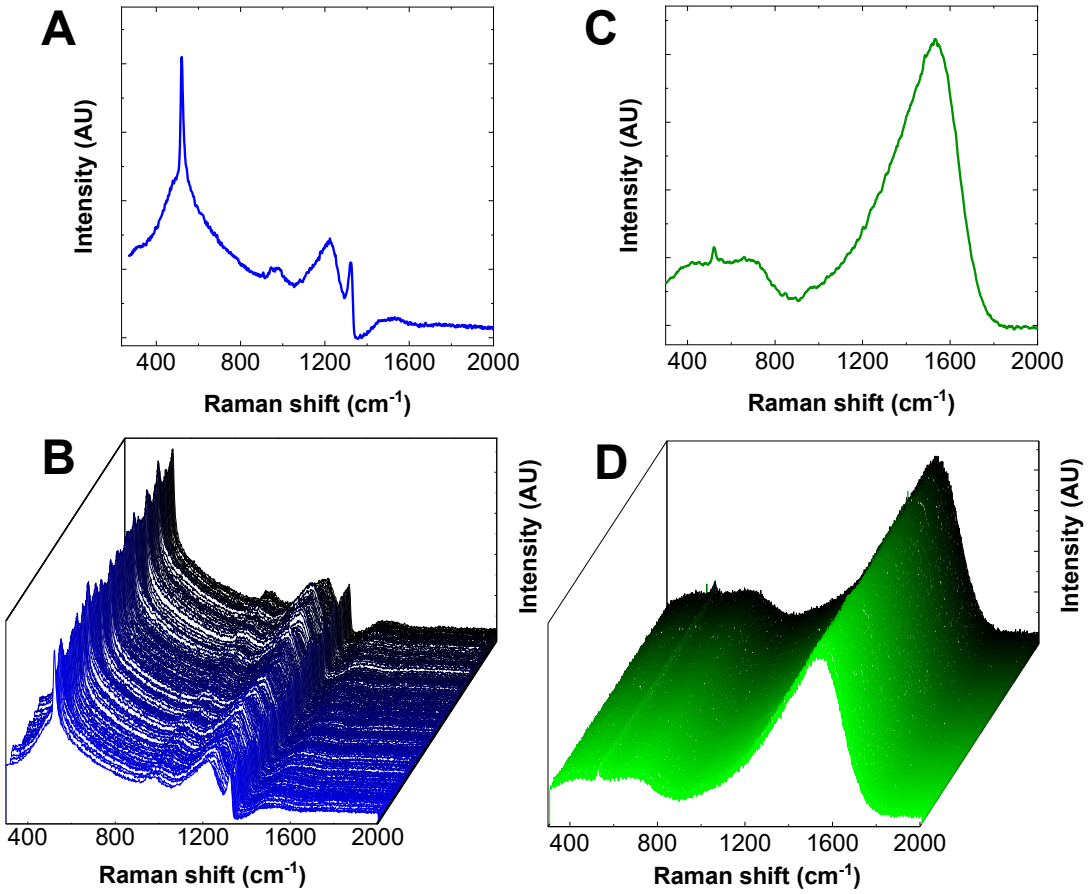

Figure 4.2. Raman spectrum for a (**A**) BDD and (**C**) t*a*-C:N thin-film electrode and multiple spectra for (**B**) BDD and (**D**) t*a*-C:N recorded along a line profile in the center region of the film. The spectra were recorded using an excitation wavelength of 532 nm, 10 mW of power at the sample, and a 3-s integration time for each spectrum. In the line profile, 300 average spectra are presented over a linear distance of a few micrometers. *Figure adapted from Appendix III.*[3]

by increased scattering intensity at around 500 and 1225 cm^{-1}. Additionally, significant scattering intensity is observed around 500 cm^{-1}, alongside the first-order Si phonon, and around 1200 cm^{-1}. The broad scattering at 500 cm^{-1} that tends to increase with boron doping level is believed to arise from the vibrational modes of boron dimers and pairs or clusters. The broad peak around 1200 cm^{-1} is assigned to defects in the diamond lattice caused by high boron doping, possibly boron-carbon complexes.

Finally, a weak scattering intensity is observed near 1510 cm^{-1} in the spectrum, which is attributed to the presence of non-diamond sp^2-bonded carbon impurities located at the interface between the diamond and Si substrate, and/or in some of the grain boundaries. This non-diamond

carbon arises from the disruptions in the diamond lattice caused by the high incorporation of boron atoms.

The Raman spectra for BDD and t*a*-C:N film electrodes are shown in Figure 4.2B and C. The Raman spectrum is characterized by an asymmetrical band centered at approximately 1520 cm^{-1}. Two peaks are of particular interest in the spectra, corresponding to the sp^3 carbon fraction and sp^2 domains, respectively. The line positions are approximately at 1358 cm^{-1} (D band) and 1550 cm^{-1} (G band). The D band can be attributed to the disorder of the graphitic material, while the G band is attributed to the first-order phonon of graphite produced due to the stretching of sp^2 carbon atoms in the rings. In t*a*-C:N films, sp^2 sites typically exist as chains rather than aromatic rings. However, the incorporation of nitrogen in the films adjusts several carbon bonding configurations, resulting in a variety of structures as well as the promotion of the formation of sp^2 sites in the film. As a result, the peak position and shape of the Raman spectra change for t*a*-C:N films deposited with varying levels of incorporated nitrogen.[186] Typically, an increase in the nitrogen flow rate leads to a more asymmetric and broader shape of the Raman band as a result of increased bond-angle and bond-length disorder. Another characteristic feature is the increasing ratio of the peak intensity (I_D/I_G), as well as the decrease of the G band position and the line width of the G peak with increasing nitrogen content.[187] Nitrogen increases the number of sp^2 sites and causes the clustering of existing sp^2 sites in the t*a*-C:N films, leading to a reduced bond gap through graphitization.[187–190]

As mentioned earlier, low background current is one of the crucial electrode properties. An optimal electrode should exhibit a low background current and noise. Additionally, the background current should stabilize quickly upon the application of the detection potential. The data presented in Figure 4.3A confirms that t*a*-C:N electrodes exhibit lower background current and noise, particularly at potentials greater than 1.0 V, as compared to GC, and are comparable to BDD electrodes. It is important to note that this potential range corresponds to the detection range for the tryptophan and tyrosine. A very important trend is seen in this figure; the background current for GC significantly surpasses those for BDD and t*a*-C:N, especially at 1.4 V when an eight-fold difference is observed. Similarly, Figure 4.3B shows that the noise for BDD and t*a*-C:N are comparable, and considerably smaller than that for GC. At the higher potential (at 1.3 V and higher), the noise for BDD and t*a*-C:N is two times smaller than that for GC. It can be concluded that the background current and noise of BDD and t*a*-C:N electrodes are comparable even at high positive potentials and remain stable over time. This contracts with GC, where the background current and noise are expected to progressively increase with time, leading to lower signal-to-noise rations. Thus, these findings provide evidence that the electrochemical properties of ta-C:N resemble those of BDD rather than GC.

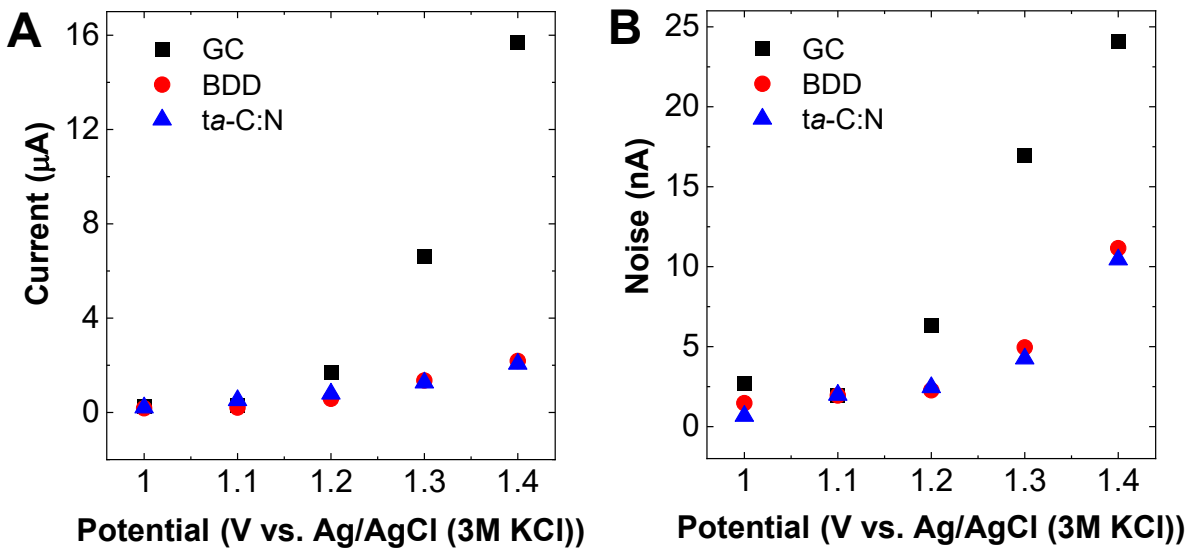

Figure 4.3. Plots of the (**A**) mean background current and (**B**) noise for GC (■), BDD (●) and t*a*-C:N (▲) electrodes as a function of applied potential. Carrier solution = 0.2 mol L^{-1} phosphate buffer (pH 7.4). Flow rate = 1 mL min^{-1}. *Figure adapted from Appendix III.*[3]

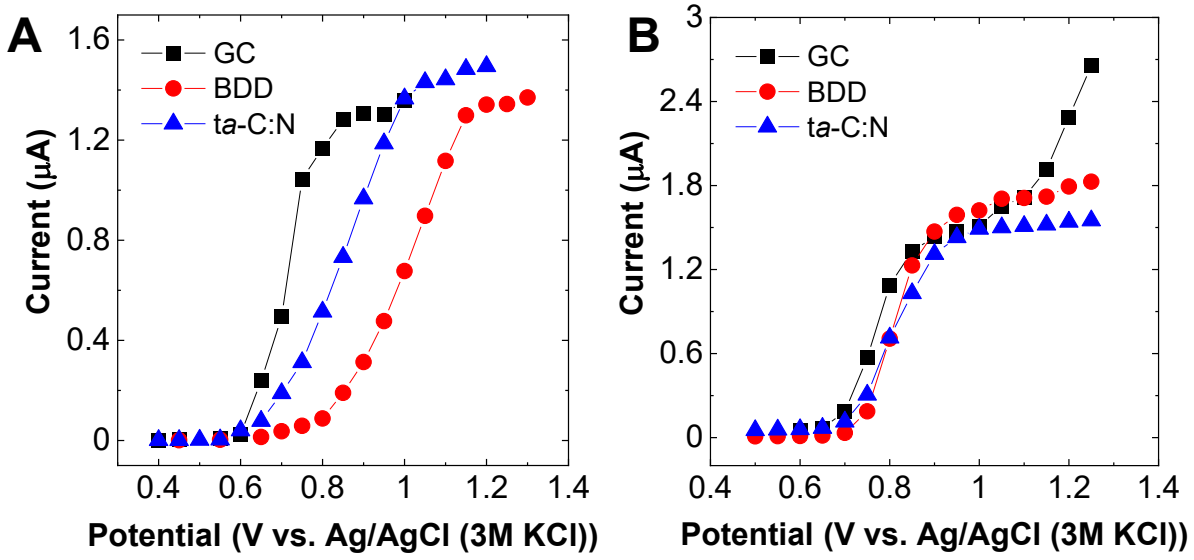

Figure 4.4. Hydrodynamic voltammograms for 100 μmol L^{-1} (**A**) tyrosine and (**B**) tryptophan in 0.2 mol L^{-1} phosphate buffer (pH 7.4) at GC (■), BDD (●) and t*a*-C:N (▲) electrodes. Flow rate = 1 mL min^{-1}. Injection volume = 25 μL. *Figure adapted from Appendix III.*[3]

Following this, hydrodynamic voltammograms were conducted at the three electrodes to determine the optimal detection potential for both analytes and compare the kinetics of electron transfer. The results, as shown in Figure 4.4, indicated that both analytes had a steady-state current of approximately 1.2 μA at all three electrodes. However, there were differences in the rate of electron transfer for tyrosine among the electrodes, as evidenced by the variations in $E_{1/2}$. Specifically, the $E_{1/2}$ at GC was approximately 300 mV less positive than that at BDD, while the $E_{1/2}$ at t*a*-C:N fell between these two values. This suggests that the oxidation reaction kinetics for tyrosine were the slowest at BDD and the fastest at GC, and that the microstructure of the carbon electrode had an impact on the oxidation response for this amino acid. In contrast, nearly identical $E_{1/2}$ values of about 0.8 V were observed for tryptophan at all three electrodes, indicating similar oxidation reaction kinetics for this amino acid irrespective of the carbon electrode type and microstructure. Furthermore, the increase in current at 1.1 V for GC was due to surface oxidation and the initiation of water oxidation, whereas BDD and t*a*-C:N had less current from surface oxidation and higher overpotentials for water oxidation.

The hydrodynamic voltammetric study presented in this work indicates that the oxidation kinetics of tyrosine are fastest at the GC electrode, whereas they are slowest at the BDD electrode, as evidenced by the more positive $E_{1/2}$ value for the latter. The kinetics of tyrosine at the t*a*-C:N

electrode fall between those of the GC and BDD electrodes, based on the $E_{1/2}$ value. These findings suggest that the microstructure of the carbon electrode plays a significant role in the kinetics of this electroactive amino acid. In contrast, the kinetics of tryptophan are comparable at all three electrodes, as evidenced by the similar $E_{1/2}$ values. It is worth noting that achieving the same level of electrode activity for GC requires pretreatment, which is not necessary for BDD and t*a*-C:N electrodes. The latter electrodes have weaker molecular adsorption due to sp^3 carbon bonding, which is responsible for fewer surface carbon-oxygen functional groups and no extended π-electron system, both of which drive molecular adsorption on sp^2 carbon electrodes. The t*a*-C:N electrode, despite having ~37% sp^3 carbon content, is similar to BDD in terms of resistance to fouling and weak molecular adsorption, as demonstrated in this study.

Finally, the short-term electrode response reproducibility was investigated, followed by a construction of calibration curves (plots not shown). The determined figures of merit are sown in Table 4.1. The results indicate that t*a*-C:N has better detection performance than GC, and are comparable to BDD. The linear dynamic range for both tyrosine and tryptophan is more than 4 orders of magnitude with high correlation coefficients ($R^2 > 0.998$) at all three electrodes. The short-term response reproducibility for both analytes at t*a*-C:N was excellent with 1-3% relative standard deviation over 30 injections (about 50 minutes of total analysis time). Although the nominal sensitivity for both amino acids was slightly larger at GC than at BDD and t*a*-C:N, this could be attributed to some adsorption of both amino acids on GC. In contrast, no adsorption is expected on BDD or t*a*-C:N, although this was not explicitly examined.

Analyte	**Electrode**	**Concentration range (µmol L^{-1})**	**Slope (mA $mol^{-1}L$)**	***R^2*** [a]	**Minimum detectable concentration (mol^{-1} L)** [b]
Tryptophan	GC	0.1 – 100	17.7 ± 1.0	0.9991	$(2.51 \pm 0.17) \times 10^{-7}$
	BDD	0.08 – 100	16.7 ± 0.6	0.9989	$(8.26 \pm 0.72) \times 10^{-8}$
	t*a*-C:N	0.08 – 100	12.4 ± 1.2	0.9989	$(8.97 \pm 0.89) \times 10^{-8}$
Tyrosine	GC	0.1 – 100	18.6 ± 0.8	0.9997	$(2.06 \pm 0.19) \times 10^{-7}$
	BDD	0.1 – 100	10.9 ± 1.3	0.9997	$(9.52 \pm 0.41) \times 10^{-8}$
	t*a*-C:N	0.1 – 100	8.3 ± 0.2	0.9996	$(1.20 \pm 0.11) \times 10^{-7}$

Table 4.1. The parameters of the calibration dependences for the detection of tryptophan and tyrosine at GC, BDD and t*a*-C:N electrodes.
[a] Linear regression correlation coefficient. [b] Minimum concentration detectable at S/N = 3. Data are reported as mean ± std. dev. (n = 3 electrodes). *Table adapted from Appendix III.*[3]

The minimum detectable concentration for both amino acids was as good or slightly lower for t*a*-C:N than for BDD and GC. The lower detection limits for tryptophan at BDD and t*a*-C:N were due to the lower noise at the detection potential. The same was observed for tyrosine at BDD compared to GC.

In conclusion, these findings suggest that the t*a*-C:N electrode performs well in the amperometric detection of tryptophan and tyrosine. The electrochemical characteristics of t*a*-C:N are similar to those of BDD, as opposed to those of GC.

4.4. Optimized Sawhorse Waveform for the Measurement of Oxytocin Release in Zebrafish (Appendix IV)

In this methodically oriented manuscript, [4] a fast scan voltametric waveform for detection of oxytocin was developed. Oxytocin is a nonapeptide hormone that serves as an endocrine chemical messenger, and affects a wide range of biological processes, including lactation,[76] sexual behavior,[191] social attachment,[192] maternity care,[78] etc. Furthermore, in the mammalian brain, oxytocin is known to influence the release of a variety of neurotransmitters, including serotonin,[193] dopamine,[194] and GABA.[195] However, the dynamics of oxytocin release on a relevant timescale in living tissue is not fully understood yet, and therefore creates a significant knowledge gap in its specific function in the neurotransmitter regulation system.

Currently, no real-time monitoring method for oxytocin release in the living brain is described in the primary literature. Existing methods for detecting oxytocin rely on sampling approaches, which have a limited temporal resolution on the order of minutes. Although electrochemical methods have the potential to detect oxytocin, electrode fouling is a common issue that poses a challenge to its detection. As mentioned in Chapter 3.1, the proposed redox reaction of oxytocin (Figure 4.5) leads to the formation of highly reactive radicals. This, in turn, leads to polymerization and adsorption on the electrode surface, causing electrode fouling. [96] To address this knowledge gap in the function of oxytocin in the neurotransmitter regulation system, it is critical to develop a sensitive, real-time detection method for oxytocin in living tissues such as the brain.

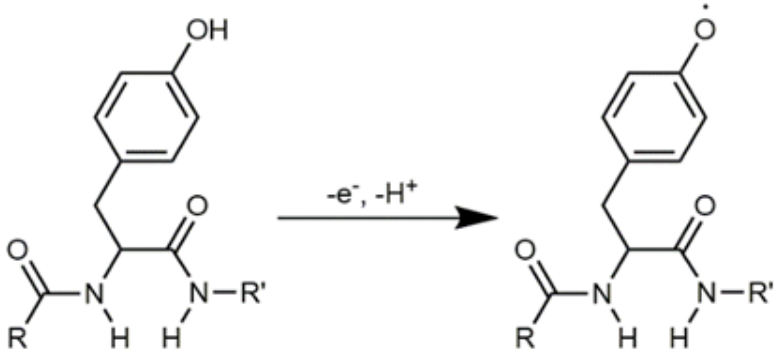

Figure 4.5. the proposed oxidation mechanism of oxytocin oxidation at the tyrosyl moiety. R and R' represents the remaining parts of oxytocin. *Figure adapted from Appendix IV.*[4]

In the manuscript presented in Apendix IV, a waveform optimized for the detection of oxytocin in zebrafish brain was developed. To address the above discussed electrode fouling, a significant effort was devoted to an implementation of a cleaning step into the waveform. In order to maximize the faradaic current arising from the oxidation of oxytocin, the following parameters were optimized: application frequency, switching potential, accumulation potential, and scan rate.[4]

At physiological pH, oxytocin carries a positive charge. Therefore, the negatively charged electrode surface serves as a preconcentration step where the positively charged peptide accumulates. To investigate the impact of waveform frequency changes on oxytocin preconcentration, measurements were collected at selected frequencies, while keeping the remaining parameters constant at the values used by Calhoun et al.[138] The resulting cyclic voltammograms and peak oxidation currents are presented in Figure 4.6A and B, respectively. The peak oxidation current decreased as the frequency and accumulation time increased, indicating that oxytocin preconcentrated at the electrode surface between scans. The negative shift in current observed during the holding potential may be due to factors such as the etching of the electrode surface and/or changes in the electric double layer from oxytocin adsorption. Further research

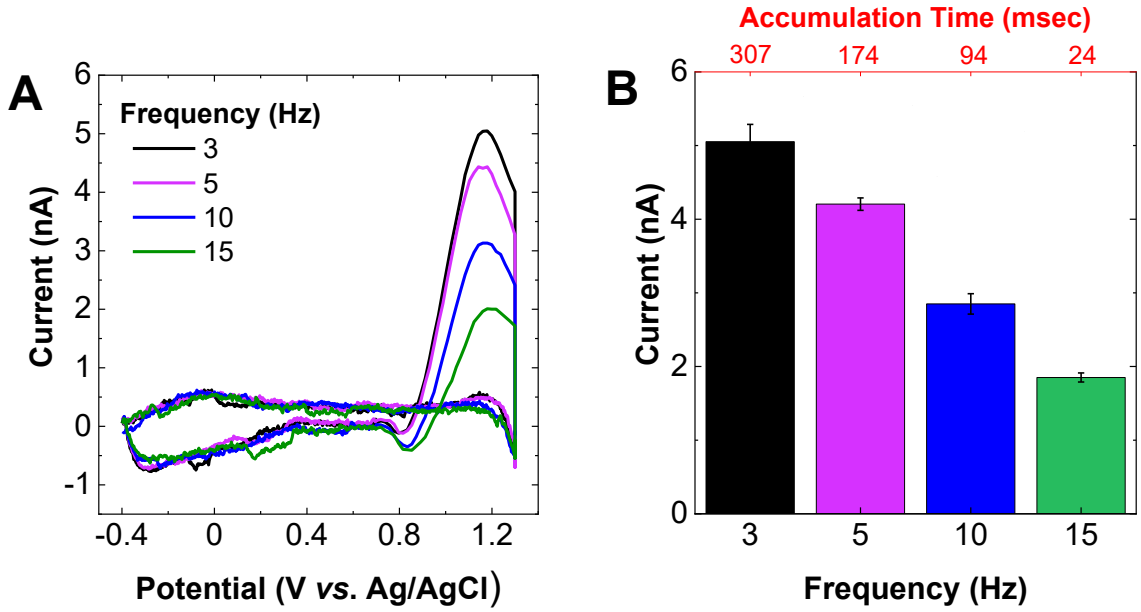

Figure 4.6. Waveform application frequency effects sensitivity to oxytocin. (**A**) Representative voltammograms for 3 µM oxytocin. (**B**) Peak oxidation current decreases with an increasing frequency (decreasing accumulation time, respectively). One-way ANOVA revealed a significant effect of frequency on current ($p < 0.05$). ($n = 3$ electrodes). *Figure adapted from Appendix IV.*[4]

is needed to identify specific contributions. However, the highest current was observed at a frequency of 3 Hz, providing the maximum time for oxytocin adsorption at the holding potential. Finally, a compromise between temporal resolution and sensitivity led to the selection of 5 Hz as the optimal waveform frequency.

In the next step, the effect of switching potential on oxytocin current response was investigated in the range of +1.1 to 1.4 V. The obtained cyclic voltammograms revealed that the oxidation current increases with an increasing switching potential (data not shown). Therefore, the potential of +1.4 V was selected as the optimal switching potential.

The accumulation (holding) potential is one of the most important key parameters in FSCV waveform development. Due to the nature of oxytocin molecules (positively charged), oxytocin is adsorbed onto the electrode surface while the potential is held in the negative values. The changes in the accumulation potential therefore affect the amount of adsorbed oxytocin, and consequently the measured anodic current. The holding potential from 0.0 to -0.6 V was investigated in this part of the study (Figure 4.7). As seen in Figure 4.7B, the peak current increased with more negative accumulation potential. Therefore, the potential of -0.6 V was selected.

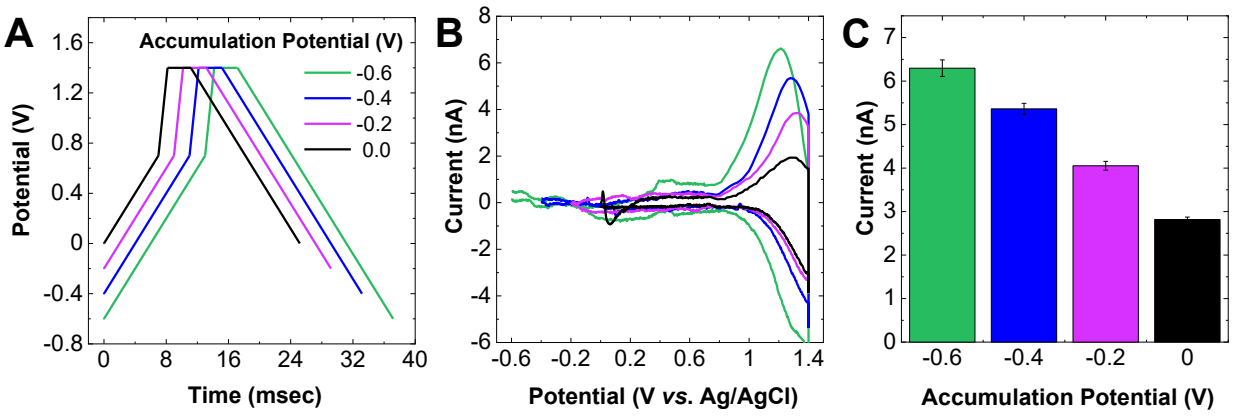

Figure 4.7. Oxytocin voltammetric response is dependent on the accumulation potential. (**A**) Schematic representation of the waveforms used for investigation of the accumulation potential (from 0.0 to -0.6 V) on the oxytocin current response. (**B**) Representative voltammograms for 3 µM oxytocin. (**C**) Peak oxidation potential increases as the holding potential decreases ($n = 3$ electrodes). One-way ANOVA revealed a significant effect of accumulation potential on current ($p < 0.05$). *Figure adapted from Appendix IV.*[4]

To test whether the newly developed waveform overcomes the above-mentioned electrode fouling, electrode response over time was evaluated by administering repeated injections of oxytocin using flow injection analysis. 3 µM oxytocin was injected every 40 s, with a total of 10 injections (Figure 4.8A). In order to observe any significant changes in current, the evaluated faradaic current was normalized to the first injection (Figure 4.8B). The current *vs* time record for 10 consecutive injections, as well as cyclic voltammograms of the first and last injections of oxytocin revealed no significant change in peak current and/or voltammogram shape (Figure 4.8B, inset). The RSD for 10 injections was 3.19%, implying that the electrodes exhibited considerable stability when utilizing this waveform for detection of oxytocin. In addition, no discernible trend, indicating a gradual decline in signal over time, was observed. Hence, it was proven that the developed waveform for oxytocin detection did not cause fouling of the CFME surface when subjected to multiple oxytocin injections.

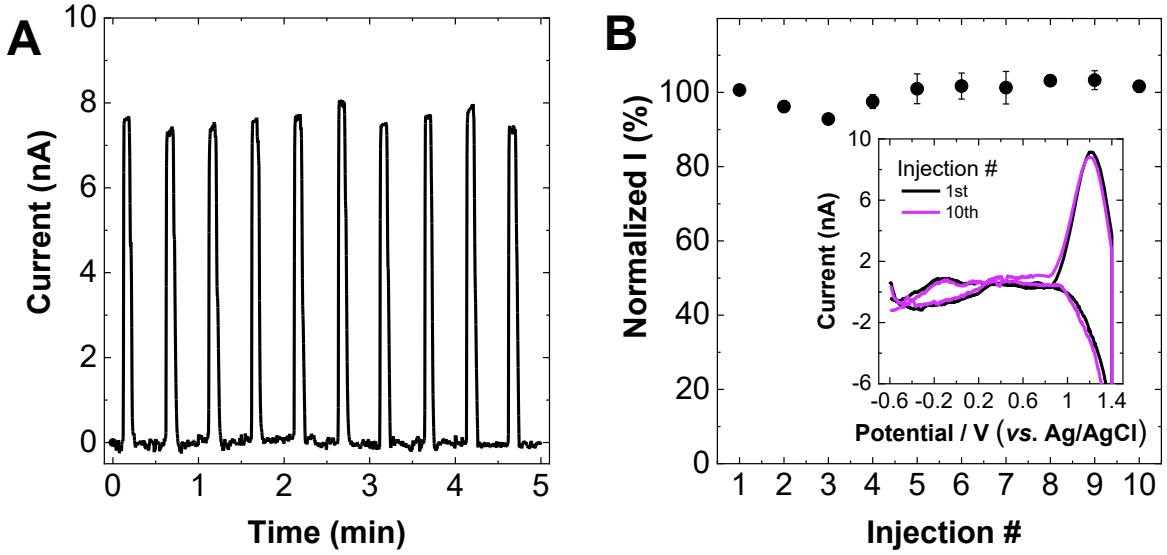

Figure 4.8. Electrode stability. Electrode fouling resistance was determined by injecting 3 µM oxytocin every 40 seconds for 10 times. **(A)** Current-time responses to illustrate the stability of the response. **(B)** Normalized current (to the first injection) with SEM error bars. the RSD = 3.19%, and there is no significant difference between the first and the last injections. **Inset:** the CVs for the first and last injections. *Figure adapted from Appendix IV.*[4]

The calibration dependences were obtained in the concentration range from 0.4 to 10 μM under the optimized waveform parameters. The limit of quantification, obtained at S/N = 10, was 0.34 ± 0.02 μM. Importantly, a high degree of linearity (R^2 = 9994) was obtained, which indicates that the optimized waveform can be utilized for a quantification of oxytocin release at low concentration.

Finally, the developed FSCV method was used to measure light-evoked oxytocin release in living, whole zebrafish brains. The fish used in this experiment were genetically modified to express channel rhodopsin and yellow fluorescent protein on oxytonergic neurons. Figure 4.9 shows an epifluorescence image of CFME in close proximity to oxytocinergic neurons, located in the preoptic nucleus of the hypothalamus.

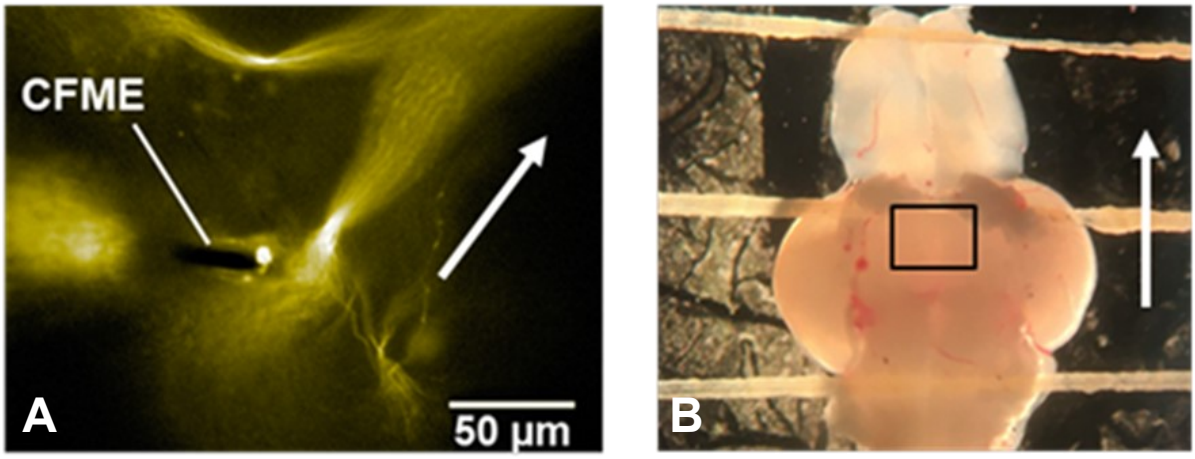

Figure 4.9. Epifluorescence image of a whole brain from an adult *OXT-Gal4; UAS-ChREYFP* zebrafish (**A**) and brightfield image of zebrafish brain with approximate field of view (**B**). The white arrows indicate relative orientation. Imaging (**A**): Nikon E600fn epifluorescence microscope Plan Fluor 40X/0.80 NA water immersion objective. *Figure adapted from Appendix IV.*[4]

After placing the electrode, the brain was subjected to a 200 ms pulse of ~480 nm light from a xenon lamp source. The current time-trace profile (data not shown) detected a temporary increase, which was followed by a sharp decrease. The cyclic voltammogram was similar to those acquired by FIA, indicating that the current increase was due to oxytocin release. The average concentration of light-stimulated oxytocin release was determined to be 0.40 ± 0.04 nM (n = 3 separate measurement locations in two brains).

Interestingly, the plot (Figure 4.10) reveals that the stimulated release was superimposed upon transient oxytocin release events, with the current declining below the original baseline level

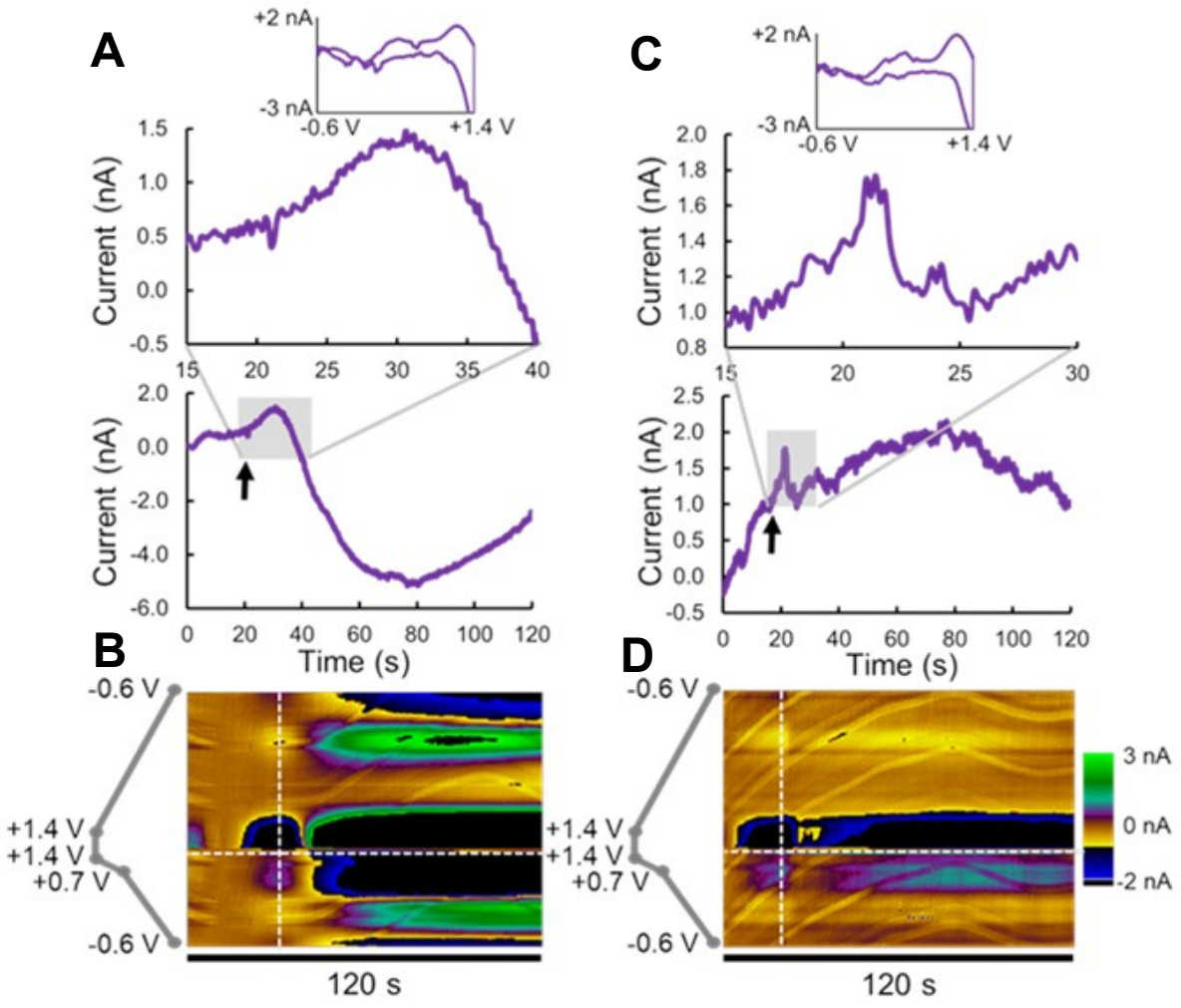

Figure 4.10. Stimulated and spontaneous OXT release in adult zebrafish brains. **A and C,** current time plots of light (**A**) and mechanically induced (**C**) OXT release. Inset, CVs of OXT confirm the identity of OXT. Stimulated release is short term and is superimposed over longer term OXT transient concentration changes. **B and D**, respective color plots of light- and mechanically evoked OXT release. *Figure adapted from Appendix IV.*[4]

and dropping to a minimum at arounds 80 s before increasing again. The color plot current signal occurring after about 40 s resembled an inverse of the currents obtained at 30 s, which provided additional support for the idea that these currents originated from oxytocin. Multiple measurements were carried out in two additional brains, and analogous transient oxytocin release patterns were observed.

To stimulate oxytocin release, the CFME was mechanically moved laterally ~5 μm over ~0.5 s, a method that had previously been employed to evoke adenosine release in brain tissue.

A sharp increase in current was observed, indicating the occurrence of oxytocin release. Files were also collected in the absence of stimulation, and transient changes in oxytocin release were observed over the course of seconds. While acknowledging the possibility that mechanical stimulation may induce the release of other electroactive compounds, it should be mentioned that sub-population oxytonergic neurons located in hypothalamus are known to be mechanosensitive. Therefore, it can be presumed that oxytocin is likely to co-occur with other tyrosine -containing peptides.

Release of oxytocin from terminals that project to different brain regions, as well as somatodendritic release from oxytocinergic cell bodies and dendrites, is a well-established phenomenon in various species. The recorded current in zebrafish, given its location in the brain, could potentially originate from somatodendritic release or from axonal projections over short distances. It is crucial to investigate whether the observed transients result from the manipulation of the tissue (*e.g.*, use of light for imaging) or occur spontaneously.

In conclusion, a novel waveform was developed in this study to optimize the measurement of oxytocin, a nonapeptide that plays a crucial role in various biological functions but presents measurement challenges due to fouling of the carbon-fiber electrode surface. Furthermore, oxytocin was successfully measured in zebrafish genetically modified to express channel rhodopsin and yellow fluorescent protein specifically in oxytocinergic neurons. The findings of this study demonstrate the ability to measure both stimulated and spontaneous oxytocin release. Future research should aim to validate this method in more complex species, such as rodents.

4.5. In situ Electrochemical Monitoring of Caged Compound Photochemistry: An Internal Actinometer for Substrate Release (Appendix V)

Caged compounds are a class of molecules that can liberate a biologically active substrate by releasing a protective substrate upon exposure to light of sufficient energy and duration. A key challenge associated with this approach is the difficulty in quantifying the degree of photoactivation as in tissues or opaque solutions as the light reaching the desired location is obstructed. To overcome this challenge, an *in-situ* electrochemical method that leverages FSCV at CFME to determine the amount of caged molecule photorelease was developed.[5] Using this approach, a precise delivery of a specific compound is possible, with a high spatial, and temporal resolution. This work represents a significant breakthrough in electrochemical monitoring of caged compound photochemistry in brain tissue, which could potentially facilitate analysis of neuronal function.

In this work, a *p*-hydroxyphenacyl cage (*p*HP) was used as a protective cage for glutamate. The *p*Hp class of cages provides high quantum yields and rapid release on a nanosecond timescale. Moreover, they can be converted into biologically benign 4-hydroxyphenylacet acid (4HPAA) via a deep-seated rearrangement of the caging chromophore (Figure 4.11). 4HPAA can be easily detected using FSCV, and distinguished from other biologically active compounds, such as monoamine neurotransmitters. Therefore, this approach provides an excellent candidate for targeted drug delivery with minimal side effects.

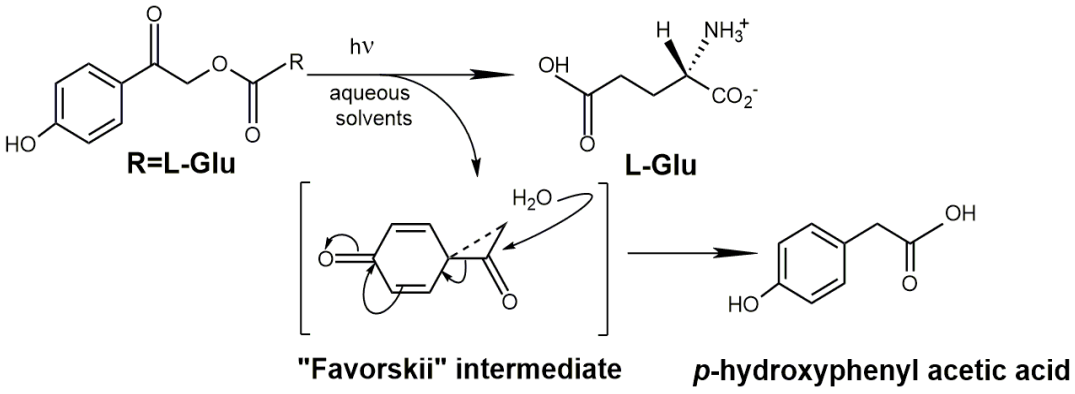

Figure 4.11. Reaction mechanism of uncaging *p*-hydroxyphenacyl-based compounds. *Figure adapted from Appendix V.*[5]

A previously published study has demonstrated that 4HPAA can be measured using FSCV.[196] This study aimed to show that *p*HP based compounds could be used to measure the formation of 4HPAA. The goal of this part of the manuscript was to demonstrate that the resulting bioactive molecule (glutamate) can be quantified by liberating 4HPAA from the caged compound. A cyclic voltammogram of 4HPAA obtained by flow injection analysis and FSCV showed two well-resolved peaks, indicating the occurrence of two electrochemical processes. The first peak was around +1.23 V on the forward scan, while the second peak occurred at +1.12 V on the back scan. The electrochemical response to 4HPAA evaluated from the primary peak (at +1.23 V) was found to be linear from 10 μM up to at least 1000 μM, demonstrating the feasibility of quantifying the amount of photo-released 4HPAA.

It is important to note that the electroactivity of the caged form of the compound was a concern, as it could complicate the interpretation of the electrochemical data. Despite this concern, it was still possible to distinguish between the two voltammograms. Cyclic voltammograms of 4HPAA and caged glutamate were obtained, and it was found that the oxidation peak of the 4HPAA did not interfere with any response correlated to caged glutamate oxidation. When subtracting the two cyclic voltammograms, a measurable signal proportional to the amount of 4HPAA formed by photo-uncaging can be derived. This demonstrates that the cyclic voltammograms for the two species are qualitatively different and result in characteristic voltammograms upon subtraction.

Next, the artificial light artifact complication was addressed. It has been found that current generated by photons hitting the CFME surface produced a voltammogram similar to those of 4HPAA. To address this issue, the effect of subtracting the signal produced by photo activation of caged compound from the overall electrochemical signal was investigated. It was found that a large photo-induced current was observed even in the absence of caged glutamate and increases linearly with increasing exposure time up to 600 ms. The carried-out studies (more details in chapter *Removing the artifactual light signal from the 4HPAA signal* of Appendix V.) suggested that the light artifact can be removed from the overall electrochemical signal, and the remaining currents can be used to monitor the formation of 4HPAA.

Up to this point, the study demonstrated the possibility of quantifying 4HPAA in a solution via the isolation of currents generated by photolysis. However, to achieve accurate quantification of 4HPAA, it is crucial to account for other electrochemically active species that may be present.

To address this issue, a microliter reaction vessel was developed (Figure 2, Appendix V), which enables a direct comparison between oxidation current that occur during photoreaction (using FSCV) and the actual concentration of 4HPAA release via photoreaction (determined using HPLC).

The change in concentration of 4HPAA under different UV exposure times was determined by combining FSCV and HPLC. First, a light intensity independent curve was generated. The photo uncaging of caged glutamate was measured with FSCV as a function of exposure time. Subsequently, the sample solution was moved to HPLC-UV. In addition, the artificial light artefact was removed by the above discussed method. Two linear plots were constructed, which plotted current and 4HPAA concentration against exposure time. Combining these graphs yielded a third plot that directly related current to 4HPAA concentration. The direct quantification of 4HPAA, coupled with the knowledge that 0.95 molecule of 4HPAA are released for every molecule of glutamate, enabled the quantification of glutamate generated by photoactivation of caged glutamate. This method represented a more direct means of quantifying the release, biologically active glutamate, than actinometry.

Finally, an experiment in a living zebrafish brain was performed to validate the newly developed method for *in situ* electrochemical detection of photoreleased 4HPAA. Following the brain dissection, the CFME and optic fiber were positioned in the telencephalon in close

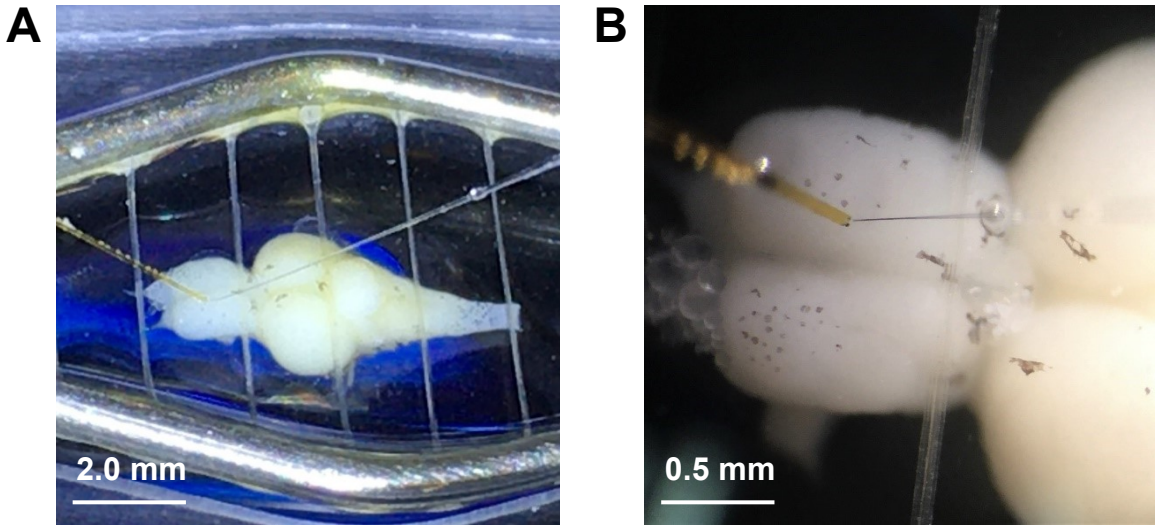

Figure 4.12. The placement of the carbon-fiber working electrode and optic fiber in the telencephalon of zebrafish brain. *Figure adapted from Appendix V.*[5]

proximity (Figure 4.12). 1000 ms light pulses were applied to measure the current responsible for the above discussed light artifact. Then, the brain was perfused with 1000 µM *p*Hp-glutamate in aCSF, and light (1000 ms in duration) was applied. A characteristic cyclic voltammogram reflecting the oxidation of 4HPAA (Figure 4.13A) proves the successful uncaging process in whole living zebrafish brain. In addition, the photo-released current vs. time plot showed a significant increase in current at the time of light exposure (Figure 4.13B). This increase in current can be attributed to the appearance of photo-released 4HPAA. After subtracting the photo-induced current, the resulting current was determined to be 1.23 ± 0.06 nA. This current corresponds to the formation of 21.1 ± 0.9 µM of 4HPAA and 22.2 ± 1.0 µM of glutamate. Lower signal was obtained for experiments carried out in whole brain, indicating a lower uncaging power of the system in opaque brain tissue. Nonetheless, this method provides proof-of-concept for *in situ* monitoring of caged compound photochemistry.

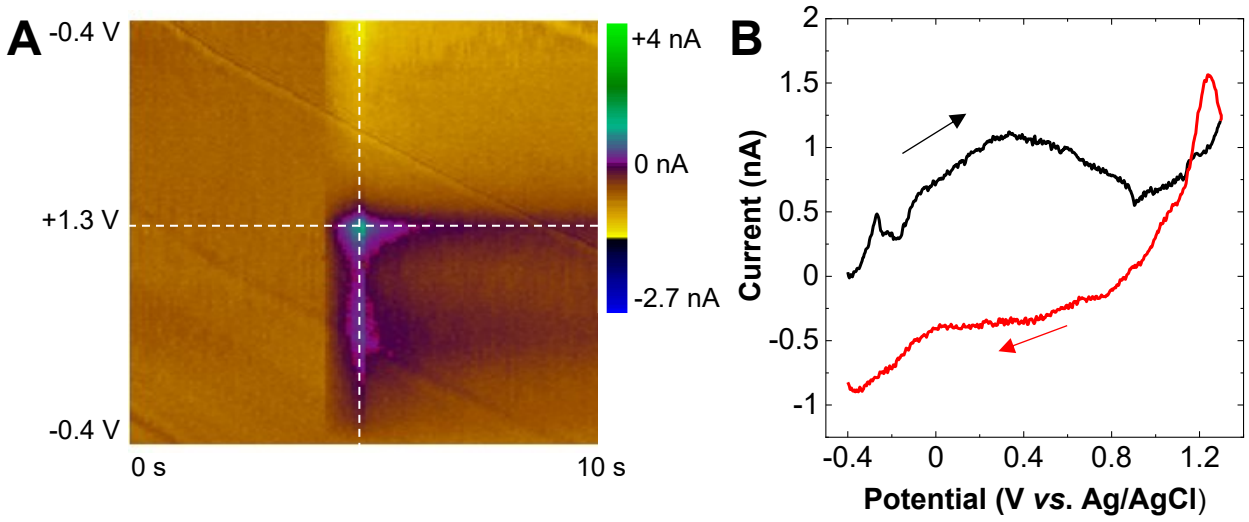

Figure 4.13. Representative data of 4HPAA detection in zebrafish whole brain after *p*Hp-glutamate photo uncaging. (**A**) Color plot and (**B**) corresponding cyclic voltammogram are shown. 1000 µM of *p*HP-glutamate in aCSF was perfused through the brain for 30 minutes. Direction of the potential sweep is indicated by arrows. Duration of light exposure: 1000 ms. *Figure adapted from Appendix V.*[5]

The uncaging capacity of this method is powerful enough to release an amount of glutamate that exceeds its estimated extracellular concentration range. Furthermore, the amount of photo-released glutamate can be controlled by adjusting the length of uncaging time and light intensity.

In conclusion, a new method for quantifying the degree of caged compound photolysis *in situ* with FSCV was developed. This method is independent of the light source and depends only on the electroactivity of the photo-released cage. While further validation in higher species is needed, this method is expected to have broad applicability, particularly in cases where quantitation of photons is difficult. In future studies, adapting this method for *in vivo* application with a combined electrode, light-guide, and caged compound delivery method will be crucial for maximizing its utility.

4.6. Impaired Dopamine Release and Latent Learning in Alzheimer's Disease Model Zebrafish (Appendix VI)

The aim of this publication is to describe the impact of OKA on adult zebrafish behavior and neurochemistry, and to investigate the possible role of dopamine in Alzheimer's disease (AD). To model AD, zebrafish were treated with OKA, and their behavioral and neurochemical changes were evaluated.[6]

First, the latent learning paradigm was used to investigate the effect of OKA on zebrafish memory and cognitive function.[197] the detailed information about the latent learning maze used in this learning paradigm, as well as the learning protocol,[198] are described in Appendix VI. Figure 4.14 shows the representative heatmaps monitoring the movement of individual zebrafish (for chemically naive, vehicle and OKA-treated zebrafish). The analysis of the heatmaps revealed that OKA treated fish tend to spend the majority of their time in the blind-ended tunnel, close to the start box. This can be attributed to a lower motivation to shoal, and/or lower interest to explore the maze, possibly arising from anxiety. Next, the effect of the OKA treatment on zebrafish learning was examined. It was found that the treatment caused learning impairment in zebrafish. These results were in agreement with previously published literature reporting that OKA treatment induces learning and memory impairment in rats. [199–201]

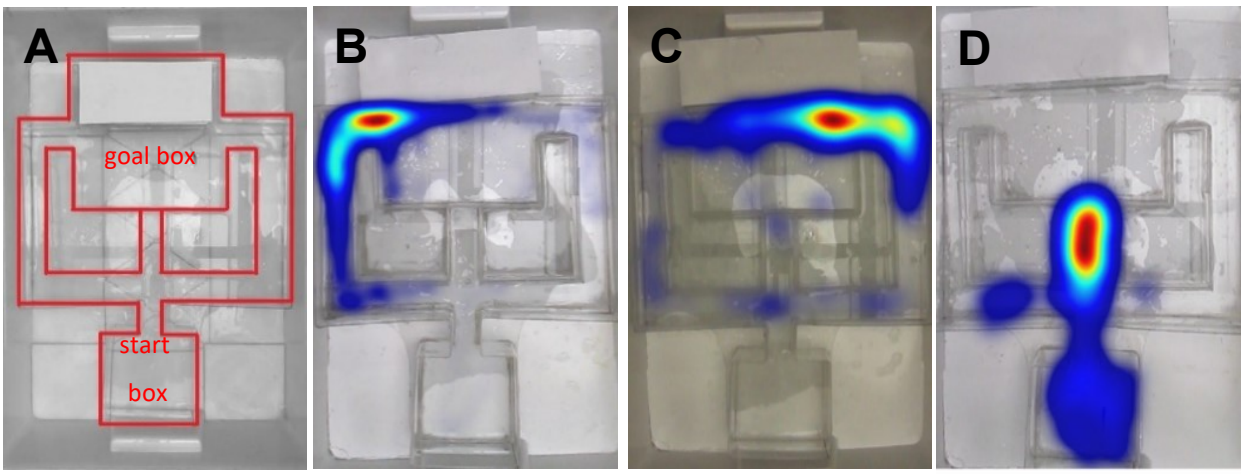

Figure 4.14. the maze for latent learning **(A)**. Heatmaps of zebrafish activity in the maze on the probe trial. **(B)** Chemically naive, **(C)** vehicle treated, and **(D)** okadaic acid treated fish. All fish were trained to the left tunnel. A heatmap of the location of the fish over 10 min trial. The colors represent the duration of time the fish spent in each pixel. Red indicates the longest time, while blue represents the shortest time. *Figure adapted from Appendix VI.*[6]

Next, the effect of OKA treatment on zebrafish learning was analyzed in this study (Figure 4.15). The correct tunnel, i.e. the tunnel that was opened during the training session was chosen by 86% of chemically naive and 92% of vehicle-treated fish (details about the fish training provided in Appendix VI, *Experimental section*), while OKA treated fish tended to choose the incorrect tunnel (56%). These findings support the hypothesis that OKA induced learning impairment in zebrafish. Numerous studies have reported that OKA treatment in rodents causes deficit in learning and memory. The ultimate mechanism for the cognitive decline in AD pathology had been identified as the inhibition of protein phosphatase 2A. [180] Given that OKA is a potent and selective inhibitor of PP1 and PP2A activity,[202] these results are consistent with previous research that showed OKA-induced impairments in rodents.

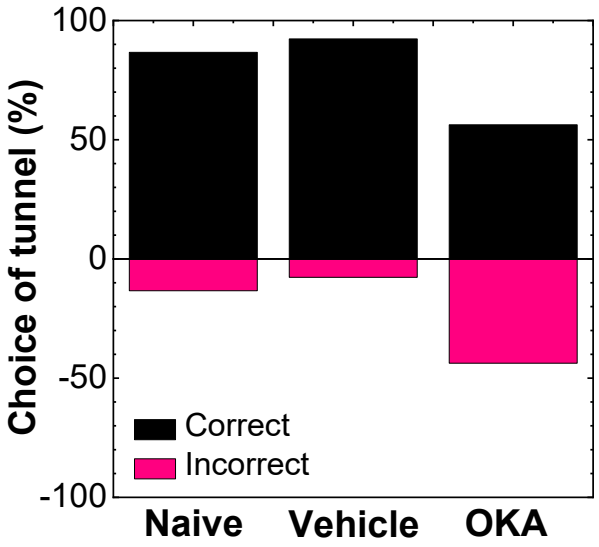

Figure 4.15. The percentage of individual fish choosing the correct and incorrect tunnel the first time they encounter this choice point when they come out of the start box during the probe trial. The fish treated with OKA tend to choose the incorrect tunnel compared to the naive and vehicle treated fish. Sample size n = 14 fish for each treatment condition. *Figure adapted from Appendix VI.*[6]

A series of behavioral tests was further carried out, and the following behavioral parameters were evaluated: latency to leave the start box, time to reach the goal box, swimming velocity, moved distance, and freezing. A detailed description of the performed test and analyzed behavioral patterns are provided in Appendix VI.

An example of behavioral oriented results can be described as freezing (immobility). Previous research has linked freezing with aversive or painful events,[203] and anxiety-related behavior in zebrafish. [198,204,205] Figure 4.16 shows the freezing response of each group throughout the probe trial, confirming that OKA-treated fish displayed significantly higher immobility values than chemically naive and vehicle-treated fish. It is speculated that this increased freezing may be related to fear or fear-induce anxiety, potentially affected by dopaminergic impairment. Although the role of dopamine in fear and anxiety is often overlooked, recent evidence suggests that it may have greater significance in inducing anxious states, and is one of the most potent neurotransmitters modulating the underlying mechanism of fear and anxiety.[206,207]

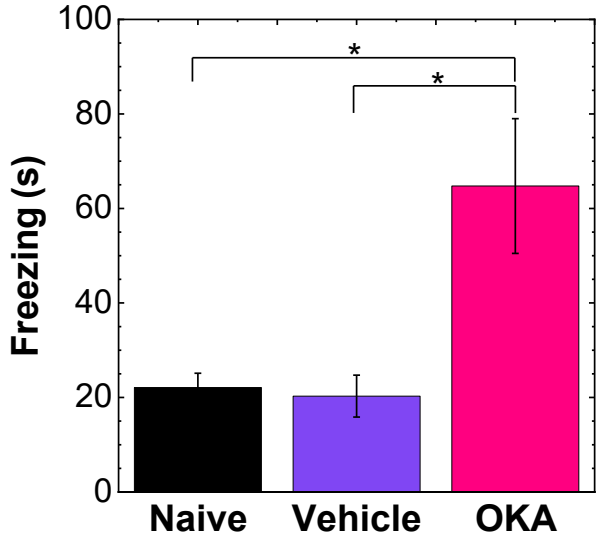

Figure 4.16. Duration of time freezing during the probe trial is affected by the treatment condition. Fish treated with the OKA showed significant immobility as compared with the chemically naive and vehicle treated zebrafish (one way ANOVA with *Tukey post-hoc* test, $p < 0.05$, $n = 14$). *$p < 0.05$. Mean ± SEM are depicted in the chart. $N = 14$ fish for each treatment condition. *Figure adapted from Appendix VI.*[6]

The second part of the study focused on the correlation between dopamine release and behavioral deficits. Electrically stimulated DA release in live brain harvested from zebrafish was measured using FSCV at CFME. The study found that zebrafish treated with OKA had significantly less dopamine release (one-way ANOVA with *Tukey post-hoc* analysis, $p < 0.05$, $n = 14$) than chemically naive and vehicle-treated fish (Figure 4.17). To investigate the possible effect of sex, the results were further analyzed by sex. However, no correlation was found between treatment condition and/or sex on evoked dopamine release.

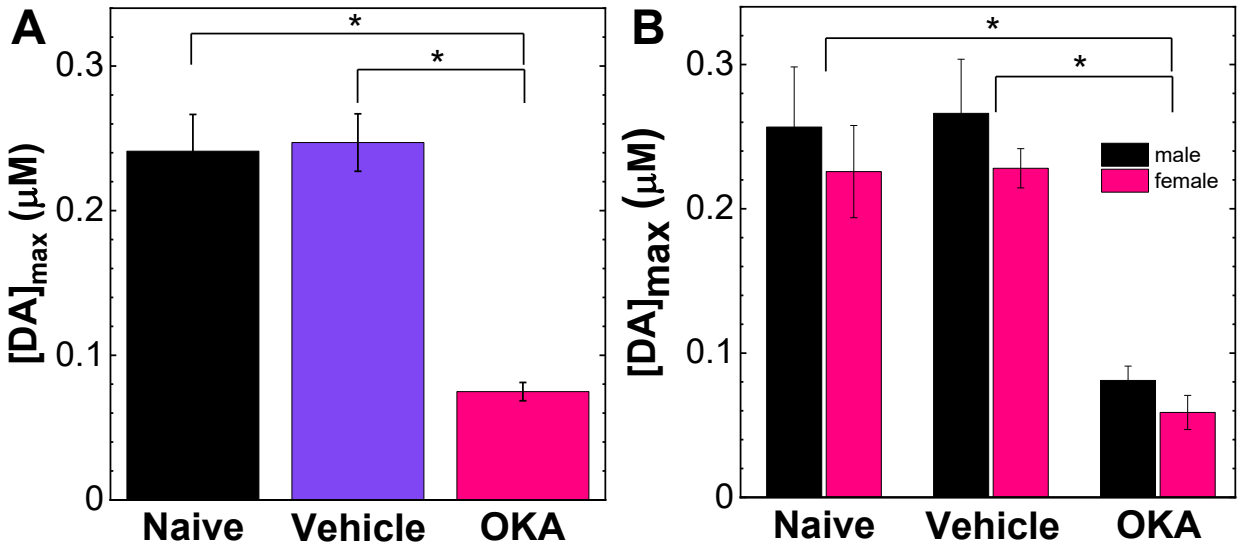

Figure 4.17. Effect of OKA treatment on evoked dopamine release. **(A)** OKA treatment has a significant effect on evoked dopamine release in zebrafish whole brains ($p < 0.05$, t-test, $n = 14$). **(B)** There was no significant difference in the DA release in male *vs* female zebrafish in each treatment group ($p < 0.05$, 2-way ANOVA, $n = 7$). $p < 0.05$. Mean ± SEM are depicted in the chart. Sample size $n = 14$ for each treatment condition. *Figure adapted from Appendix VI.*[6]

Taken collectively, it has been found that OKA treatment causes major cognitive decline in adult zebrafish. Additionally, the observed deficiencies were accompanied by a decrease in DA release levels. DA release in the dorsal striatum [112,208] and nucleus accumbens in rodents [209] play essential roles in motor control and learning. Hence, it was concluded that dopamine release plays a role in locomotion and cognitive impairment in this AD model organism.

The study demonstrates the benefits of using zebrafish as a model organism for detecting neurochemical and behavioral changes in models of Alzheimer's disease (AD) and other neurological conditions. These benefits include improved efficiency in behavioral experiments compared to rodents, lower costs, and ease of neurochemical measurements. Thus, the research represents a promising advance towards the accurate detection of such changes using zebrafish models. Furthermore, this approach will be useful in future evaluations of therapeutic compounds with higher throughput for behavioral and neurochemical analyses.

CHAPTER 5. CONCLUSION

In this Thesis, the utilization of carbon-based electrodes was discussed.

The first part of this Thesis investigates the use of carbon-based electrodes and their electrochemical performance in detection of biologically significant compounds. The focus is on the microstructure-analyte relationship of two novel carbon materials, BDD and t*a*-C:N, and their comparison with GC. The electrode performance was compared *via* a development of electrochemical methods (FIA with ameprometric detection) for determination of tyrosine, tryptophan, isatin, and pyocyanin.

The results show that both BDD and t*a*-C:N electrodes exhibit lower and stable background current and noise at high positive potentials when compared with GC, owing to their microstructural stability and low reactivity. Additionally, both electrodes are suitable for detecting electroactive compounds that require high positive potentials. The active t*a*-C:N and BDD electrode response is obtained without the time-consuming surface pretreatment that is necessary for GC activation. Furthermore, both BDD and t*a*-C:N exhibit good short-term response reproducibility for all analytes used (less than 5% RSD). Finally, when comparing the figures of merit for detection of tyrosine and tryptophan, BDD and t*a*-C:N provided significantly lower minimum detectable concentrations for both analytes than GC, due to their lower background current and noise. In conclusion, these findings suggest that BDD and t*a*-C:N electrodes hold promise for detecting biologically significant compounds and offer advantages over GC. In addition, the importance of a proper electrode material selection for a specific analyte of interest was highlighted.

The second part of this Thesis was focused on a utilization of carbon-based electrodes in neuroscience.

First, a novel FSCV waveform for a detection of oxytocin was introduced. For ages, oxytocin was a challenge molecule to detect in real time. In this study, a method for detecting this neuropeptide with sub-second temporal resolution was developed. The focus of the research was to optimize individual parameters of the applied FSCV waveform, such as application frequency, accumulation potential, switching potential, and scan rate. The resulting waveform was able to prevent electrode fouling, which occurs due to the polymerization of the product of the redox reaction on the electrode surface. The calculated figures of merit showed

that the newly developed method is also highly sensitive. Moreover, the method was used to detect oxytocin in a living zebrafish brain and demonstrated the ability to measure both stimulated and spontaneous oxytocin release.

In the next study, the CFME was employed to develop a novel approach for quantification of glutamate. Glutamate, unlike other commonly occurring neurotransmitters, can be neurotoxic at high concentrations, thus hindering its use in perfusion methods for studying its neural functions. Moreover, glutamate is not electrochemically active and, therefore, cannot be detected on bare electrodes without additional surface modification.

To overcome these challenges, a unique concept that combined electrochemistry and light activation was introduced. The use of caged glutamate, a complex that enabled a precise delivery of glutamate to the telencephalon of zebrafish brain, was the key innovation in this work. Upon activation of the caged glutamate by light, an electroactive byproduct (4HPAA) was released, which could be measured using FSCV at the CFME electrode and used for quantification of photoreleased glutamate.

Importantly, it has been demonstrated that 4HPAA can be easily detected and quantified in the telencephalon of whole zebrafish brain. Therefore, the feasibility of photo-delivering biologically active compounds in living tissues has been demonstrated by this work. This novel approach provided excellent spatial and temporal resolution, allowing for the precise delivery of a neurotoxic compound. Overall, this approach provides an innovative and powerful tool for investigating the functions of glutamate in the nervous system, which may ultimately lead to a better understanding of neurological disorders associated with glutamate dysregulation.

In the final study presented in this Thesis, the CFME was utilized to investigate the correlation between dopamine and Alzheimer's disease. The study involved treating zebrafish with OKA to simulate the symptoms typical of AD patients, and conducting behavioral and electrochemical analyses. The results showed that OKA treatment caused significant cognitive decline, deficits in learning and locomotion, and a notable decrease in stimulated dopamine release. This research represents a promising step towards improved understanding of AD and provides an important tool for future evaluations of potential therapeutic interventions on both behavioral and neurochemical levels.

CHAPTER 6. REFERENCES

1. Jarošová, R.; Rutherford, J.; Swain, G. M. Evaluation of a Nitrogen-Incorporated Tetrahedral Amorphous Carbon Thin Film for the Detection of Tryptophan and Tyrosine Using Flow Injection Analysis with Amperometric Detection. *Analyst* **2016**, *141* (21), 6031–6041.

2. Jarošová, R.; Sanchez, S.; Haubold, L.; Swain, G. M. Isatin Analysis Using Flow Injection Analysis with Amperometric Detection – Comparison of Tetrahedral Amorphous Carbon and Diamond Electrode Performance. *Electroanalysis* **2017**, *29* (9), 2147–2154.

3. Jarosova, R.; Irikura, K.; Rocha-Filho, R.; Swain, G. Detection of Pyocyanin with a Boron-Doped Diamond Electrode Using Flow Injection Analysis with Amperometric Detection and Square Wave Voltammetry. *Electroanalysis* **2021**, *34*, 1–12.

4. Jarosova, R.; Douglass, A. D.; Johnson, M. A. Optimized Sawhorse Waveform for the Measurement of Oxytocin Release in Zebrafish. *Anal. Chem.* **2022**, *94* (6), 2942-2949. PMCID: PMC9087480.

5. Jarosova, R.; Kaplan, S. V.; Field, T. M.; Givens, R. S.; Senadheera, S. N.; Johnson, M. A. In Situ Electrochemical Monitoring of Caged Compound Photochemistry: An Internal Actinometer for Substrate Release. *Anal. Chem.* **2021**, *93* (5), 2776-2784. PMCID: PMC8177719.

6. Jarosova, R.; Niyangoda, S. S.; Hettiarachchi, P.; Johnson, M. A. Impaired Dopamine Release and Latent Learning in Alzheimer's Disease Model Zebrafish. *ACS Chem. Neurosci.* **2022**, *13* (19), 2924–2931.

7. McCreery, R. L. Carbon Electrodes: Structural Effects on Electron Transfer Kinetics. In *Electroanalytical Chemistry*; Bard, A. J., Ed.; Marcel Dekker Inc: New York, 1991; pp 221–374.

8. Svancara, I.; Vytras, K.; Barek, J.; Zima, J. Carbon Paste Electrodes in Modern Electroanalysis. *Crit. Rev. Anal. Chem.* **2001**, *31* (4), 311–345.

9. Xu, C.; Xu, B.; Gu, Y.; Xiong, Z.; Sun, J.; Zhao, X. S. Graphene-Based Electrodes for Electrochemical Energy Storage. *Energy Environ. Sci.* **2013**, *6* (6), 1388–1414.

10. McDonough, J. K.; Gogotsi, Y. Carbon Onions: Synthesis and Electrochemical Applications. *Interface Mag.* **2013**, *22* (3), 61–66.

11. Power, A. C.; Gorey, B.; Chandra, S.; Chapman, J. Carbon Nanomaterials and Their Application to Electrochemical Sensors: A Review. *Nanotechnol. Rev.* **2018**, *7* (1), 19–41.

12. Jarošová, R.; De Sousa Bezerra, P. M.; Munson, C.; Swain, G. M. Assessment of Heterogeneous Electron-Transfer Rate Constants for Soluble Redox Analytes at Tetrahedral Amorphous Carbon, Boron-Doped Diamond, and Glassy Carbon Electrodes. *Phys. Status Solidi Appl. Mater. Sci.* **2016**, *213* (8), 2087–2098.

13. Bowling, R. J.; Packard, R. T.; McCreery, R. L. Activation of Highly Ordered Pyrolytic Graphite for Heterogeneous Electron Transfer: Relationship between Electrochemical Performance and Carbon Microstructure. *J. Am. Chem. Soc.* **1989**, *111* (4), 1217–1223.

14. Rice, R. J.; McCreery, R. L. Quantitative Relationship between Electron Transfer Rate and Surface Microstructure of Laser-Modified Graphite Electrodes. *Anal. Chem.* **1989**, *61* (15), 1637–1641.

15. Rice, R. J.; Pontikos, N. M.; McCreery, R. L. Quantitative Correlations of Heterogeneous Electron-Transfer Kinetics with Surface Properties of Glassy Carbon Electrodes. *J. Am. Chem. Soc.* **1990**, *112* (12), 4617–4622.

16. Kneten, K. R.; McCreery, R. L. Effects of Redox System Structure on Electron-Transfer Kinetics at Ordered Graphite and Glassy Carbon Electrodes. *Anal. Chem.* **1992**, *64* (21), 2518–2524.

17. Chen, P.; Fryling, M. A.; McCreery, R. L. Electron Transfer Kinetics at Modified Carbon Electrode Surfaces: The Role of Specific Surface Site. *Anal. Chem.* **1995**, *67* (18), 3115–3122.

18. Chen, P.; McCreery, R. L. Control of Electron Transfer Kinetics at Glassy Carbon Electrodes by Specific Surface Modification. *Anal. Chem.* **1996**, *68* (22), 3958–3965.

19. Cavalheiro, É. T. G.; Brett, C. M. A.; Oliveira-Brett, A. M.; Fatibello-Filho, O. Bioelectroanalysis of Pharmaceutical Compounds. *Bioanal. Rev.* **2012**, *4* (1), 31–53.

20. Ranganathan, S.; Kuo, T. C.; McCreery, R. L. Facile Preparation of Active Glassy Carbon Electrodes with Activated Carbon and Organic Solvents. *Anal. Chem.* **1999**, *71* (16), 3574–3580.

21. Barrière, F.; Downard, A. J. Covalent Modification of Graphitic Carbon Substrates by Non-Electrochemical Methods. *J. Solid State Electrochem.* **2008**, *12* (10), 1231–1244.

22. Yang, H. H.; McCreery, R. L. Effects of Surface Monolayers on the Electron-Transfer Kinetics and Adsorption of Methyl Viologen and Phenothiazine Derivatives on Glassy Carbon Electrodes. *Anal. Chem.* **1999**, *71* (18), 4081–4087.

23. McCreery, R. L. Advanced Carbon Electrode Materials for Molecular Electrochemistry. *Chem. Rev.* **2008**, *108* (7), 2646–2687.

24. Banks, C. E.; Compton, R. G. New Electrodes for Old: From Carbon Nanotubes to Edge Plane Pyrolytic Graphite. *Analyst* **2006**, *131* (1), 15–21.

25. McDermott, M. T.; McCreery, R. L. Scanning Tunneling Microscopy of Ordered Graphite and Glassy Carbon Surfaces: Electronic Control of Quinone Adsorption. *Langmuir* **1994**, *10* (11), 4307–4314.

26. McDermott, M. T.; McCreery, C. A.; McDermott, R. L. Scanning Tunneling Microscopy

of Carbon Surfaces: Relationships between Electrode Kinetics, Capacitance, and Morphology for Glassy Carbon Electrodes. *Anal. Chem.* **1993**, *65* (7), 937–944.

27. Morteza Najarian, A.; Chen, R.; Balla, R. J.; Amemiya, S.; McCreery, R. L. Ultraflat, Pristine, and Robust Carbon Electrode for Fast Electron-Transfer Kinetics. *Anal. Chem.* **2017**, *89* (24), 13532–13540.

28. Hoogvliet, J. C.; van den Beld, C. M. B.; van der Poel, C. J.; van Bennekom, W. P. Influence of Polishing and of Electrochemical Pretreatment on the Performance of Glassy-Carbon Electrodes in Electrochemical Detection. *J. Electroanal. Chem. Interfacial Electrochem.* **1986**, *201* (1), 11–21.

29. Engstrom, R. C.; Strasser, V. A. Characterization of Electrochemically Pretreated Glassy Carbon Electrodes. *Anal. Chem.* **1984**, *56* (2), 136–141.

30. Fagan, D. T.; Hu, I. F.; Kuwana, T. Vacuum Heat Treatment for Activation of Glassy Carbon Electrodes. *Anal. Chem.* **1985**, *57* (14), 2759–2763.

31. Poon, M.; Mccreery, R. L. In Situ Laser Activation of Glassy Carbon Electrodes. *Anal. Chem* **1986**, *58*, 2745–2750.

32. Asmussen, J.; Reinhard, D. K. *Diamond Films Handbook*; Dekker, Marcel, I., Ed.; New York, 2002.

33. Swain, G. M.; Show, Y.; Zak, J.; Stotter, J.; Behler, Z. Optical and Electrochemical Properties of Optically Transparent, Boron-Doped Diamond Thin Films Deposited on Quartz. *Anal. Chem.* **2002**, *74* (23), 5924–5930.

34. Haymond, S.; Zak, J. K.; Show, Y.; Butler, J. E.; Babcock, G. T.; Swain, G. M. Spectroelectrochemical Responsiveness of a Freestanding, Boron-Doped Diamond, Optically Transparent Electrode toward Ferrocene. *Anal. Chim. Acta* **2003**, *500* (1–2), 137–144.

35. Stotter, J.; Show, Y.; Wang, S.; Swain, G. Comparison of the Electrical, Optical, and Electrochemical Properties of Diamond and Indium Tin Oxide Thin-Film Electrodes. *Chem. Mater.* **2005**, *17* (19), 4880–4888.

36. Wächter, N.; Munson, C.; Jarošová, R.; Berkun, I.; Hogan, T.; Rocha-Filho, R. C.; Swain, G. M. Structure, Electronic Properties, and Electrochemical Behavior of a Boron-Doped Diamond/Quartz Optically Transparent Electrode. *ACS Appl. Mater. Interfaces* **2016**, *8* (42), 28325–28337.

37. Zak, J. K.; Butler, J. E.; Swain, G. M. Diamond Optically Transparent Electrodes: Demonstration of Concept with Ferri/Ferrocyanide and Methyl Viologen. *Anal. Chem.* **2001**, *73* (5), 908–914.

38. Dai, Y.; Proshlyakov, D. A.; Zak, J. K.; Swain, G. M. Optically Transparent Diamond Electrode for Use in IR Transmission Spectroelectrochemical Measurements. *Anal. Chem.*

2007, *79* (19), 7526–7533.

39. Tafur, J.; Espinoza-Montero, P.; Manciati, C.; Fierro-Naranjo, C.; Swain, G. M.; Fernández, L. Evaluation of BDD Electrode in the Determination of Cd(II), Pb(II) and Hg(II) in Wastewater Mining (Portovelo - Zaruma, Provincia de El Oro, Ecuador). *Rev. Tec. la Fac. Ing. Univ. del Zulia* **2018**, *41* (2), 104–112.

40. Dong, H.; Wang, S.; Galligan, J. J.; Swain, G. M. Boron-Doped Diamond Nano/Microelectrodes for Biosensing and in Vitro Measurements. *Front. Biosci. (Schol. Ed).* **2011**, *3*, 518–540.

41. Show, Y.; Quaiserová, V.; Cvačka, J.; Muck, A.; Swain, G. M.; Park, J. Boron-Doped Diamond Microelectrodes for Use in Capillary Electrophoresis with Electrochemical Detection. *Anal. Chem.* **2003**, *75* (11), 2678–2687.

42. Benešová, L.; Klouda, J.; Bláhová, E.; Nesměrák, K.; Kočovský, P.; Nádvorníková, J.; Barták, P.; Skopalová, J.; Schwarzová-Pecková, K. Non-Enzymatic Electrochemical Determination of Cholesterol in Dairy Products on Boron-Doped Diamond Electrode. *Food Chem.* **2022**, *393*.

43. Hupert, M.; Muck, A.; Wang, J.; Stotter, J.; Cvackova, Z.; Haymond, S.; Show, Y.; Swain, G. M. Conductive Diamond Thin-Films in Electrochemistry. *Diam. Relat. Mater.* **2003**, *12* (10–11), 1940–1949.

44. Compton, R. G.; Foord, J. S.; Marken, F. Electroanalysis at Diamond-like and Doped-Diamond Electrodes. *Electroanalysis* **2003**, *15* (17), 1349–1363.

45. Nebel, C. E.; Rezek, B.; Shin, D.; Uetsuka, H.; Yang, N. Diamond for Bio-Sensor Applications. *J. Phys. D. Appl. Phys.* **2007**, *40* (20), 6443–6466.

46. Pecková, K.; Musilová, J.; Barek, J. Boron-Doped Diamond Film Electrodes-New Tool for Voltammetric Determination of Organic Substances. *Crit. Rev. Anal. Chem.* **2009**, *39* (3), 148–172.

47. Einaga, Y.; Foord, J. S.; Swain, G. M. Diamond Electrodes: Diversity and Maturity. *MRS Bull.* **2014**, *39* (6), 525–532.

48. Macpherson, J. V. A Practical Guide to Using Boron Doped Diamond in Electrochemical Research. *Phys. Chem. Chem. Phys.* **2015**, *17* (5), 2935–2949.

49. Robertson, J. Structural Models of A-C and a-C:H. *Diam. Relat. Mater.* **1995**, *4* (4), 297–301.

50. Das, D. Nanocrystalline Diamond: A High-Impact Carbon Nanomaterial for Multifunctional Applications Including as Nanofiller in Biopolymeric Matrices. *Carbon-Based Nanofillers and Their Rubber Nanocomposites: Carbon Nano-Objects* **2019**, 123–181.

51. Robertson, J.; Oreilly, E. P. Electronic and Atomic Structure of Amorphous Carbon. *Phys. Rev. B* **1987**, *35* (6), 2946–2957.

52. Jones, D. I.; Stewart, A. D. Properties of Hydrogenated Amorphous Carbon Films and the Effects of Doping. *Philos. Mag. B* **1982**, *46* (5), 423–434.

53. Thiele, J. U.; Rubarth, B.; Hammer, P.; Helmbold, A.; Kessler, B.; Rohwer, K.; Meissner, D. Ambiguous Doping Effects in Amorphous Hydrogenated Carbon Films Prepared by PACVD. *Diam. Relat. Mater.* **1994**, *3* (8), 1103–1106.

54. Hamblin, D.; Qiu, J.; Haubold, L.; Swain, G. M. The Performance of a Nitrogen-Containing Tetrahedral Amorphous Carbon Electrode in Flow Injection Analysis with Amperometric Detection. *Anal. Methods* **2015**, *7* (11), 4481–4485.

55. Shi, J. R.; Liu, E. J.; Silva, S. R. P.; Shi, X.; Cheah, L. K. Properties of Nitrogen Doped Tetrahedral Amorphous Carbon Films Prepared by Filtered Cathodic Vacuum Arc Technique. *J. Non. Cryst. Solids* **1998**, *242* (1), 40–48.

56. McKenzie, D. R.; Muller, D.; Pailthorpe, B. A.; Wang, Z. H.; Kravtchinskaia, E.; Segal, D.; Lukins, P. B.; Swift, P. D.; Martin, P. J.; Amaratunga, G.; et al. Properties of Tetrahedral Amorphous Carbon Prepared by Vacuum Arc Deposition. *Diam. Relat. Mater.* **1991**, *1* (1), 51–59.

57. Veerasamy, V. S.; Yuan, J.; Amaratunga, G. A. J.; Milne, W. I.; Gilkes, K. W. R.; Weiler, M.; Brown, L. M. Nitrogen Doping of Highly Tetrahedral Amorphous Carbon. *Phys. Rev. B* **1993**, *48* (24), 17954–17959.

58. Chhowalla, M.; Robertson, J.; Chen, C. W.; Silva, S. R. P.; Davis, C. A.; Amaratunga, G. A. J.; Milne, W. I. Influence of Ion Energy and Substrate Temperature on the Optical and Electronic Properties of Tetrahedral Amorphous Carbon (Ta-C) Films. *J. Appl. Phys.* **1997**, *81* (1), 139–145.

59. Elinson, V. M.; Sleptsov, V. V.; Laymin, A. N.; Potraysay, V. V.; Kostuychenko, L. N.; Moussina, A. D. Barrier Properties of Carbon Films Deposited on Polymer-Based Devices in Aggressive Environments. *Diam. Relat. Mater.* **1999**, *8* (12), 2103–2109.

60. Mehta, B. R.; Ogryzlo, E. A. Room-Temperature Deposition of Diamond-like Carbon Films by the Microwave Plasma Jet Method. *Diam. Relat. Mater.* **1994**, *3* (1–2), 10–13.

61. Beghi, M. G.; Robertson, J.; Bottani, C. E.; Libassi, A.; Teo, K. B. K.; Tanner, B. K.; Ferrari, A. C. Bonding and Mechanical Properties of Ultrathin Diamond-like Carbon Films. *Appl. Phys. Lett.* **2002**, *81* (20), 3804–3806.

62. El-Ghundi, M.; O'Dowd, B. F.; George, S. R. Insights into the Role of Dopamine Receptor Systems in Learning and Memory. *Rev. Neurosci.* **2007**, *18* (1), 37–66.

63. Volkow, N. D.; Fowler, J. S.; Wang, G. J.; Baler, R.; Telang, F. Imaging Dopamine's Role in Drug Abuse and Addiction. *Neuropharmacology* **2009**, *56* (SUPPL. 1), 3–8.

64. Schultz, W. Multiple Dopamine Functions at Different Time Courses. *Annu. Rev. Neurosci.* **2007**, *30*, 259–288.

65. Macedo-Lima, M.; Remage-Healey, L. Dopamine Modulation of Motor and Sensory Cortical Plasticity among Vertebrates. *Integr. Comp. Biol.* **2021**, *61* (1), 316–336.

66. Su, Y.; Bian, S.; Sawan, M. Real-Time: In Vivo Detection Techniques for Neurotransmitters: A Review. *Analyst* **2020**, *145* (19), 6193–6210.

67. Olive, M. F.; Mehmert, K. K.; Hodge, C. W. Microdialysis in the Mouse Nucleus Accumbens: A Method for Detection of Monoamine and Amino Acid Neurotransmitters with Simultaneous Assessment of Locomotor Activity. *Brain Res. Protoc.* **2000**, *5* (1), 16–24.

68. Pan, L. Y.; Wang, Y.; Liu, X. H.; Jia, Y. Q. Simultaneous Determination of 11 Neurotransmitters in Brain Microdialysis Samples from Rats by UPLC-MS/MS. *Zhongguo Zhongyao Zazhi* **2022**, *47* (12), 3242–3250.

69. Yuen, J.; Goyal, A.; Rusheen, A. E.; Kouzani, A. Z.; Berk, M.; Kim, J. H.; Tye, S. J.; Blaha, C. D.; Bennet, K. E.; Jang, D.-P.; et al. Cocaine-Induced Changes in Tonic Dopamine Concentrations Measured Using Multiple-Cyclic Square Wave Voltammetry in Vivo. *Front. Pharmacol.* **2021**, *12*, 705254.

70. Yuen, J.; Goyal, A.; Rusheen, A. E.; Kouzani, A. Z.; Berk, M.; Kim, J. H.; Tye, S. J.; Blaha, C. D.; Bennet, K. E.; Lee, K. H.; et al. Cocaine Increases Stimulation-Evoked Serotonin Efflux in the Nucleus Accumbens. *J. Neurophysiol.* **2022**, *127* (3), 714–724.

71. Ortiz, A. N.; Kurth, B. J.; Osterhaus, G. L.; Johnson, M. A. Dysregulation of Intracellular Dopamine Stores Revealed in the R6/2 Mouse Striatum. *J. Neurochem.* **2010**, *112* (3), 755–761.

72. Hettiarachchi, P.; Niyangoda, S. S.; Jarosova, R.; Johnson, M. A. Dopamine Release Impairments Accompany Locomotor and Cognitive Deficiencies in Rotenone-Treated Parkinson's Disease Model Zebrafish. *Chem. Res. Toxicol.* **2022**, *35* (11), 1974–1982.

73. Kernberg, A.; Caughey, A. B. Augmentation of Labor: A Review of Oxytocin Augmentation and Active Management of Labor. *Obstet. Gynecol. Clin. North Am.* **2017**, *44* (4), 593–600.

74. Owen, J.; Hauth, J. C. Oxytocin for the Induction or Augmentation of Labor. *Clin. Obstet. Gynecol.* **1992**, *35* (3), 464–475.

75. Bell, A. F.; Erickson, E. N.; Carter, C. S. Beyond Labor: The Role of Natural and Synthetic Oxytocin in the Transition to Motherhood. *J. Midwifery Women's Heal.* **2014**, *59* (1), 35–42.

76. Whitley, J.; Wouk, K.; Bauer, A. E.; Grewen, K.; Gottfredson, N. C.; Meltzer-Brody, S.; Propper, C.; Mills-Koonce, R.; Pearson, B.; Stuebe, A. Oxytocin during Breastfeeding and

Maternal Mood Symptoms. *Psychoneuroendocrinology* **2020**, *113*.

77. Olff, M.; Frijling, J. L.; Kubzansky, L. D.; Bradley, B.; Ellenbogen, M. A.; Cardoso, C.; Bartz, J. A.; Yee, J. R.; van Zuiden, M. The Role of Oxytocin in Social Bonding, Stress Regulation and Mental Health: An Update on the Moderating Effects of Context and Interindividual Differences. *Psychoneuroendocrinology* **2013**, *38* (9), 1883–1894.

78. Ogi, A.; Mariti, C.; Pirrone, F.; Baragli, P.; Gazzano, A. The Influence of Oxytocin on Maternal Care in Lactating Dogs. *Animals* **2021**, *11* (4).

79. Walum, H.; Young, L. J. The Neural Mechanisms and Circuitry of the Pair Bond. *Nat. Rev. Neurosci.* **2018**, *19* (11), 643–654.

80. Winter, J.; Jurek, B. The Interplay between Oxytocin and the CRF System: Regulation of the Stress Response. *Cell Tissue Res.* **2019**, *375* (1), 85–91.

81. McQuaid, R. J.; McInnis, O. A.; Abizaid, A.; Anisman, H. Making Room for Oxytocin in Understanding Depression. *Neurosci. Biobehav. Rev.* **2014**, *45*, 305–322.

82. Cardoso, C.; Ellenbogen, M. A.; Linnen, A. M. Acute Intranasal Oxytocin Improves Positive Self-Perceptions of Personality. *Psychopharmacology (Berl).* **2012**, *220* (4), 741–749.

83. Nawijn, L.; van Zuiden, M.; Koch, S. B. J.; Frijling, J. L.; Veltman, D. J.; Olff, M. Intranasal Oxytocin Increases Neural Responses to Social Reward in Post-Traumatic Stress Disorder. *Soc. Cogn. Affect. Neurosci.* **2017**, *12* (2), 212–223.

84. Lawson, S. K.; Gray, A. C.; Woehrle, N. S. Effects of Oxytocin on Serotonin 1B Agonist-Induced Autism-like Behavior in Mice. *Behav. Brain Res.* **2016**, *314*, 52–64.

85. Yamasue, H.; Domes, G. Oxytocin and Autism Spectrum Disorders. *Curr. Top. Behav. Neurosci.* **2018**, *35*, 449–465.

86. Sikich, L.; Kolevzon, A.; King, B. H.; McDougle, C. J.; Sanders, K. B.; Kim, S.-J.; Spanos, M.; Chandrasekhar, T.; Trelles, M. D. P.; Rockhill, C. M.; et al. Intranasal Oxytocin in Children and Adolescents with Autism Spectrum Disorder. *N. Engl. J. Med.* **2021**, *385* (16), 1462–1473.

87. Hörnberg, H.; Pérez-Garci, E.; Schreiner, D.; Hatstatt-Burklé, L.; Magara, F.; Baudouin, S.; Matter, A.; Nacro, K.; Pecho-Vrieseling, E.; Scheiffele, P. Rescue of Oxytocin Response and Social Behaviour in a Mouse Model of Autism. *Nature* **2020**, *584* (7820), 252–256.

88. Huang, Y.; Huang, X.; Ebstein, R. P.; Yu, R. Intranasal Oxytocin in the Treatment of Autism Spectrum Disorders: A Multilevel Meta-Analysis. *Neurosci. Biobehav. Rev.* **2021**, *122*, 18–27.

89. King, C. E.; Gano, A.; Becker, H. C. The Role of Oxytocin in Alcohol and Drug Abuse. *Brain Res.* **2020**, *1736*.

90. Che, X.; Cai, J.; Liu, Y.; Xu, T.; Yang, J.; Wu, C. Oxytocin Signaling in the Treatment of Drug Addiction: Therapeutic Opportunities and Challenges. *Pharmacol. Ther.* **2021**, *223*.

91. Leong, K. C.; Cox, S.; King, C.; Becker, H.; Reichel, C. M. Oxytocin and Rodent Models of Addiction. *Int. Rev. Neurobiol.* **2018**, *140*, 201–247.

92. Sundar, M.; Patel, D.; Young, Z.; Leong, K. C. Oxytocin and Addiction: Potential Glutamatergic Mechanisms. *Int. J. Mol. Sci.* **2021**, *22* (5), 1–17.

93. Sanna, F.; De Luca, M. A. The Potential Role of Oxytocin in Addiction: What Is the Target Process? *Curr. Opin. Pharmacol.* **2021**, *58*, 8–20.

94. Zanos, P.; Georgiou, P.; Weber, C.; Robinson, F.; Kouimtsidis, C.; Niforooshan, R.; Bailey, A. Oxytocin and Opioid Addiction Revisited: Old Drug, New Applications. *Br. J. Pharmacol.* **2018**, *175* (14), 2809–2824.

95. Pedersen, C. A. Oxytocin, Tolerance, and the Dark Side of Addiction. *Int. Rev. Neurobiol.* **2017**, *136*, 239–274.

96. Asai, K.; Ivandini, T. A.; Einaga, Y. Continuous and Selective Measurement of Oxytocin and Vasopressin Using Boron-Doped Diamond Electrodes. *Sci. Rep.* **2016**.

97. Zhou, Y.; Danbolt, N. C. Glutamate as a Neurotransmitter in the Healthy Brain. *J. Neural Transm.* **2014**, *121* (8), 799–817.

98. Meldrum, B. S. Glutamate as a Neurotransmitter in the Brain: Review of Physiology and Pathology. *J. Nutr.* **2000**, *130* (4 SUPPL.).

99. Deutschenbaur, L.; Beck, J.; Kiyhankhadiv, A.; Mühlhauser, M.; Borgwardt, S.; Walter, M.; Hasler, G.; Sollberger, D.; Lang, U. E. Role of Calcium, Glutamate and NMDA in Major Depression and Therapeutic Application. *Prog. Neuro-Psychopharmacology Biol. Psychiatry* **2016**, *64*, 325–333.

100. Murrough, J. W.; Abdallah, C. G.; Mathew, S. J. Targeting Glutamate Signalling in Depression: Progress and Prospects. *Nat. Rev. Drug Discov.* **2017**, *16* (7), 472–486.

101. Abdallah, C. G.; Sanacora, G.; Duman, R. S.; Krystal, J. H. The Neurobiology of Depression, Ketamine and Rapid-Acting Antidepressants: Is It Glutamate Inhibition or Activation? *Pharmacol. Ther.* **2018**, *190*, 148–158.

102. Riaza Bermudo-Soriano, C.; Perez-Rodriguez, M. M.; Vaquero-Lorenzo, C.; Baca-Garcia, E. New Perspectives in Glutamate and Anxiety. *Pharmacol. Biochem. Behav.* **2012**, *100* (4), 752–774.

103. Bergink, V.; Van Megen, H. J. G. M.; Westenberg, H. G. M. Glutamate and Anxiety. *Eur. Neuropsychopharmacol.* **2004**, *14* (3), 175–183.

104. Cortese, B. M.; Phan, K. L. The Role of Glutamate in Anxiety and Related Disorders. *CNS*

Spectr. **2005**, *10* (10), 820–830.

105. Buck, S. A.; Quincy Erickson-Oberg, M.; Logan, R. W.; Freyberg, Z. Relevance of Interactions between Dopamine and Glutamate Neurotransmission in Schizophrenia. *Mol. Psychiatry* **2022**, *27* (9), 3583–3591.

106. Howes, O.; McCutcheon, R.; Stone, J. Glutamate and Dopamine in Schizophrenia: An Update for the 21st Century. *J. Psychopharmacol.* **2015**, *29* (2), 97–115.

107. Egerton, A.; Grace, A. A.; Stone, J.; Bossong, M. G.; Sand, M.; McGuire, P. Glutamate in Schizophrenia: Neurodevelopmental Perspectives and Drug Development. *Schizophr. Res.* **2020**, *223*, 59–70.

108. Schallert, T.; Fleming, S. M. Dopamine and Motor Function in Rat and Mouse Models of Parkinson's Disease. In *Dopamine Handbook*; Oxford University Press, New York, 2010; pp 279–285.

109. Cools, R.; D'Esposito, M. Dopaminergic Modulation of Flexible Cognitive Control in Humans. In *Dopamine Handbook*; Oxford University Press, New York, 2010; Vol. 14, pp 249–261.

110. Lelos, M. J.; Dunnett, S. B. Aberrant Dopamine Transmission and Cognitive Dysfunction in Animal Models of Parkinson's Disease. *J. Parkinsons. Dis.* **2011**, *1* (2), 151–165.

111. Ortiz, A. N.; Osterhaus, G. L.; Lauderdale, K.; Mahoney, L.; Fowler, S. C.; Von Hörsten, S.; Riess, O.; Johnson, M. A. Motor Function and Dopamine Release Measurements in Transgenic Huntington's Disease Model Rats. *Brain Res.* **2012**, *1450*, 148–156.

112. Ortiz, A. N.; Kurth, B. J.; Osterhaus, G. L.; Johnson, M. A. Impaired Dopamine Release and Uptake in R6/1 Huntington's Disease Model Mice. *Neurosci. Lett.* **2011**, *492* (1), 11-14. PMCID: PMC3677767.

113. Masoud, S. T.; Vecchio, L. M.; Bergeron, Y.; Hossain, M. M.; Nguyen, L. T.; Bermejo, M. K.; Kile, B.; Sotnikova, T. D.; Siesser, W. B.; Gainetdinov, R. R.; et al. Increased Expression of the Dopamine Transporter Leads to Loss of Dopamine Neurons, Oxidative Stress and l-DOPA Reversible Motor Deficits. *Neurobiol. Dis.* **2015**, *74*, 66–75.

114. Masato, A.; Plotegher, N.; Boassa, D.; Bubacco, L. Impaired Dopamine Metabolism in Parkinson's Disease Pathogenesis. *Mol. Neurodegener.* **2019**, *14* (1).

115. Latif, S.; Jahangeer, M.; Maknoon Razia, D.; Ashiq, M.; Ghaffar, A.; Akram, M.; El Allam, A.; Bouyahya, A.; Garipova, L.; Ali Shariati, M.; et al. Dopamine in Parkinson's Disease. *Clin. Chim. Acta* **2021**, *522*, 114–126.

116. Segura-Aguilar, J.; Paris, I.; Muñoz, P.; Ferrari, E.; Zecca, L.; Zucca, F. A. Protective and Toxic Roles of Dopamine in Parkinson's Disease. *J. Neurochem.* **2014**, *129* (6), 898–915.

117. Warren, N.; O'Gorman, C.; Lehn, A.; Siskind, D. Dopamine Dysregulation Syndrome in

Parkinson's Disease: A Systematic Review of Published Cases. *J. Neurol. Neurosurg. Psychiatry* **2017**, *88* (12), 1060–1064.

118. Howes, O. D.; Williams, M.; Ibrahim, K.; Leung, G.; Egerton, A.; McGuire, P. K.; Turkheimer, F. Midbrain Dopamine Function in Schizophrenia and Depression: A Post-Mortem and Positron Emission Tomographic Imaging Study. *Brain* **2013**, *136* (Pt 11), 3242–3251.

119. Martorana, A.; Koch, G. Is Dopamine Involved in Alzheimer's Disease? *Front. Aging Neurosci.* **2014**, *6* (SEP), 252.

120. Kissinger, P. T.; Hart, J. B.; Adams, R. N. Voltammetry in Brain Tissue — a New Neurophysiological Measurement. *Brain Res.* **1973**, *55* (1), 209–213.

121. Wightman, R. M.; Strope, E.; Plotsky, P. M.; Adams, R. N. Monitoring of Transmitter Metabolites by Voltammetry in Cerebrospinal Fluid Following Neural Pathway Stimulation. *Nature* **1976**, *262* (5564), 145–146.

122. Wightman, R. M. Probing Cellular Chemistry in Biological Systems with Microelectrodes. *Science (80-.).* **2006**, *311* (5767), 1570–1574.

123. Stamford, J. A.; Kruk, Z. L.; Millar, J.; Wightman, R. M. Striatal Dopamine Uptake in the Rat: In Vivo Analysis by Fast Cyclic Voltammetry. *Neurosci. Lett.* **1984**, *51* (1), 133–138.

124. Kaplan, S. V.; Limbocker, R. A.; Gehringer, R. C.; Divis, J. L.; Osterhaus, G. L.; Newby, M. D.; Sofis, M. J.; Jarmolowicz, D. P.; Newman, B. D.; Mathews, T. A.; et al. Impaired Brain Dopamine and Serotonin Release and Uptake in Wistar Rats Following Treatment with Carboplatin. *ACS Chem. Neurosci.* **2016**, *7* (6), 689–699.

125. Spanos, M.; Gras-Najjar, J.; Letchworth, J. M.; Sanford, A. L.; Toups, J. V.; Sombers, L. A. Quantitation of Hydrogen Peroxide Fluctuations and Their Modulation of Dopamine Dynamics in the Rat Dorsal Striatum Using Fast-Scan Cyclic Voltammetry. *ACS Chem. Neurosci.* **2013**, *4* (5), 782–789.

126. Lim, G. N.; Regan, S. L.; Ross, A. E. Subsecond Spontaneous Catecholamine Release in Mesenteric Lymph Node Ex Vivo. *Journal of Neurochemistry*. 2020, pp 417–429.

127. Keithley, R. B.; Wightman, R. M. Assessing Principal Component Regression Prediction of Neurochemicals Detected with Fast-Scan Cyclic Voltammetry. *ACS Chem. Neurosci.* **2011**, *2* (9), 514–525.

128. Venton, B. J.; Wightman, R. M. Psychoanalytical Electrochemistry: Dopamine and Behavior. *Anal. Chem.* **2003**, *75* (19).

129. Swamy, B. E. K.; Venton, B. J. Subsecond Detection of Physiological Adenosine Concentrations Using Fast-Scan Cyclic Voltammetry. *Anal. Chem.* **2007**, *79* (2), 744–750.

130. Bard, A. J.; Faulkner, L. R. *Electrochemical Methods: Fundamentals and Applications*, 2nd

ed.; John Wiley & Sons, Ltd, 2000.

131. Venton, B. J.; Cao, Q. Fundamentals of Fast-Scan Cyclic Voltammetry for Dopamine Detection. *Analyst* **2020**, *145* (4), 1158–1168.

132. Molina, A.; González, J.; Laborda, E.; Compton, R. G. Analytical Solutions for Fast and Straightforward Study of the Effect of the Electrode Geometry in Transient and Steady State Voltammetries: Single- and Multi-Electron Transfers, Coupled Chemical Reactions and Electrode Kinetics. *J. Electroanal. Chem.* **2015**, *756*, 1–21.

133. Heinze, J. Ultramicroelectrodes in Electrochemistry. *Angew. Chemie Int. Ed. English* **1993**, *32* (9), 1268–1288.

134. Forster, R. J. Microelectrodes—Retrospect and Prospect. *Encycl. Electrochem.* **2003**.

135. Zachek, M. K.; Hermans, A.; Wightman, R. M.; McCarty, G. S. Electrochemical Dopamine Detection: Comparing Gold and Carbon Fiber Microelectrodes Using Background Subtracted Fast Scan Cyclic Voltammetry. *J. Electroanal. Chem. (Lausanne. Switz).* **2008**, *614* (1–2), 113–120.

136. Kim, D.; Kang, H.; Nam, Y. Lab on a Chip Compact 256-Channel Multi-Well Microelectrode Array System for in Vitro Neuropharmacology Test. **2020**, *20*, 3410.

137. Danis, L.; Polcari, D.; Kwan, A.; Gateman, S. M.; Mauzeroll, J. Fabrication of Carbon, Gold, Platinum, Silver, and Mercury Ultramicroelectrodes with Controlled Geometry. *Anal. Chem* **2015**, *87*, 18.

138. Calhoun, S. E.; Meunier, C. J.; Lee, C. A.; McCarty, G. S.; Sombers, L. A. Characterization of a Multiple-Scan-Rate Voltammetric Waveform for Real-Time Detection of Met-Enkephalin. *ACS Chem. Neurosci.* **2019**, *10* (4), 2022–2032.

139. Kraft, J. C.; Osterhaus, G. L.; Ortiz, A. N.; Garris, P. A.; Johnson, M. A. In Vivo Dopamine Release and Uptake Impairments in Rats Treated with 3-Nitropropionic Acid. *Neuroscience* **2009**, *161* (3), 940–949.

140. Maina, F. K.; Khalid, M.; Apawu, A. K.; Mathews, T. A. Presynaptic Dopamine Dynamics in Striatal Brain Slices with Fast-Scan Cyclic Voltammetry. *J. Vis. Exp.* **2012**, No. 59, 1–6.

141. Sanford, A. L.; Morton, S. W.; Whitehouse, K. L.; Oara, H. M.; Lugo-Morales, L. Z.; Roberts, J. G.; Sombers, L. A. Voltammetric Detection of Hydrogen Peroxide at Carbon Fiber Microelectrodes. *Anal. Chem.* **2010**, *82* (12), 5205–5210.

142. Ponchon, J. L.; Cespuglio, R.; Gonon, F.; Jouvet, M.; Pujol1, J. F. Normal Pulse Polarography with Carbon Fiber Electrodes for in Vitro and in Vivo Determination of Catecholamines. *Anal. Chem.* **1979**, *51* (9), 1483–1486.

143. Bucher, E. S.; Wightman, R. M. Electrochemical Analysis of Neurotransmitters. *Annu. Rev. Anal. Chem.* **2015**, *8*, 239–261.

144. Strickland, J. C.; Smith, M. A. Animal Models of Resistance Exercise and Their Application to Neuroscience Research. *J. Neurosci. Methods* **2016**, *273*, 191–200.

145. Bovenkerk, B.; Kaldewaij, F. The Use of Animal Models in Behavioural Neuroscience Research. *Curr. Top. Behav. Neurosci.* **2015**, *19*, 17–46.

146. Romanova, E. V.; Sweedler, J. V. Animal Model Systems in Neuroscience. *ACS Chem. Neurosci.* **2018**, *9* (8), 1869–1870.

147. Sarnyai, Z.; Guest, P. C. Connecting Brain Proteomics with Behavioural Neuroscience in Translational Animal Models of Neuropsychiatric Disorders. *Adv. Exp. Med. Biol.* **2017**, *974*, 97–114.

148. Yartsev, M. M. The Emperor's New Wardrobe: Rebalancing Diversity of Animal Models in Neuroscience Research. *Science (80-.).* **2017**, *358* (6362), 466–469.

149. Markou, A.; Chiamulera, C.; Geyer, M. A.; Tricklebank, M.; Steckler, T. Removing Obstacles in Neuroscience Drug Discovery: The Future Path for Animal Models. *Neuropsychopharmacology* **2009**, *34* (1), 74–89.

150. Löscher, W. Animal Models of Seizures and Epilepsy: Past, Present, and Future Role for the Discovery of Antiseizure Drugs. *Neurochem. Res.* **2017**, *42* (7), 1873–1888.

151. Hermann, D. M.; Popa-Wagner, A.; Kleinschnitz, C.; Doeppner, T. R. Animal Models of Ischemic Stroke and Their Impact on Drug Discovery. *Expert Opin. Drug Discov.* **2019**, *14* (3), 315–326.

152. Bisht, S.; Feldmann, G. Animal Models for Modeling Pancreatic Cancer and Novel Drug Discovery. *Expert Opin. Drug Discov.* **2019**, *14* (2), 127–142.

153. Barker-Haliski, M.; Steve White, H. Validated Animal Models for Antiseizure Drug (ASD) Discovery: Advantages and Potential Pitfalls in ASD Screening. *Neuropharmacology* **2020**, *167*.

154. Kaliyaperumal, S.; Wilson, K.; Aeffner, F.; Dean, C. Animal Models of Peripheral Pain: Biology Review and Application for Drug Discovery. *Toxicol. Pathol.* **2020**, *48* (1), 202–219.

155. Pandey, U. B.; Nichols, C. D. Human Disease Models in Drosophila Melanogaster and the Role of the Fly in Therapeutic Drug Discovery. *Pharmacol. Rev.* **2011**, *63* (2), 411–436.

156. Singh, V. K.; Seed, T. M. How Necessary Are Animal Models for Modern Drug Discovery? *Expert Opin. Drug Discov.* **2021**, *16* (12), 1391–1397.

157. Souidi, A.; Jagla, K. Drosophila Heart as a Model for Cardiac Development and Diseases. *Cells* **2021**, *10* (11).

158. Tsuda, L.; Lim, Y. M. Alzheimer's Disease Model System Using Drosophila. *Adv. Exp.*

Med. Biol. **2018**, *1076*, 25–40.

159. Saitoe, M.; Horiuchi, J.; Tamura, T.; Ito, N. Drosophila as a Novel Animal Model for Studying the Genetics of Age-Related Memory Impairment. *Rev. Neurosci.* **2005**, *16* (2), 137–149.

160. Kalueff, A. V.; Stewart, A. M.; Gerlai, R. Zebrafish as an Emerging Model for Studying Complex Brain Disorders. *Trends Pharmacol. Sci.* **2014**, *35* (2), 63–75.

161. Koehler, D.; Williams, F. E. Utilizing Zebrafish and Okadaic Acid to Study Alzheimer's Disease. *Neural Regen. Res.* **2018**, *13* (9), 1538–1541.

162. Stewart, A. M.; Nguyen, M.; Wong, K.; Poudel, M. K.; Kalueff, A. V. Developing Zebrafish Models of Autism Spectrum Disorder (ASD). *Prog. Neuro-Psychopharmacology Biol. Psychiatry* **2014**, *50*, 27–36.

163. Howe, K.; Clark, M. D.; Torroja, C. F.; Torrance, J.; Berthelot, C.; Muffato, M.; Collins, J. E.; Humphray, S.; McLaren, K.; Matthews, L.; et al. The Zebrafish Reference Genome Sequence and Its Relationship to the Human Genome. *Nature* **2013**, *496* (7446), 498–503.

164. Bohaud, C.; Johansen, M. D.; Jorgensen, C.; Ipseiz, N.; Kremer, L.; Djouad, F. The Role of Macrophages During Zebrafish Injury and Tissue Regeneration Under Infectious and Non-Infectious Conditions. *Front. Immunol.* **2021**, *12*.

165. Gemberling, M.; Bailey, T. J.; Hyde, D. R.; Poss, K. D. The Zebrafish as a Model for Complex Tissue Regeneration. *Trends Genet.* **2013**, *29* (11), 611–620.

166. Marques, I. J.; Lupi, E.; Mercader, N. Model Systems for Regeneration: Zebrafish. *Dev.* **2019**, *146* (18).

167. Lebedeva, L.; Zhumabayeva, B.; Gebauer, T.; Kisselev, I.; Aitasheva, Z. Zebrafish (Danio Rerio) as a Model for Understanding the Process of Caudal Fin Regeneration. *Zebrafish* **2020**, *17* (6), 359–372.

168. Jopling, C.; Sleep, E.; Raya, M.; Martí, M.; Raya, A.; Belmonte, J. C. I. Zebrafish Heart Regeneration Occurs by Cardiomyocyte Dedifferentiation and Proliferation. *Nature* **2010**, *464* (7288), 606–609.

169. Poss, K. D.; Wilson, L. G.; Keating, M. T. Heart Regeneration in Zebrafish. *Science (80-.).* **2002**, *298* (5601), 2188–2190.

170. Hu, B.; Lelek, S.; Spanjaard, B.; El-Sammak, H.; Simões, M. G.; Mintcheva, J.; Aliee, H.; Schäfer, R.; Meyer, A. M.; Theis, F.; et al. Origin and Function of Activated Fibroblast States during Zebrafish Heart Regeneration. *Nat. Genet.* **2022**, *54* (8), 1227–1237.

171. Wan, J.; Goldman, D. Retina Regeneration in Zebrafish. *Curr. Opin. Genet. Dev.* **2016**, *40*, 41–47.

172. Ghosh, S.; Hui, S. P. Axonal Regeneration in Zebrafish Spinal Cord. *Regen. (Oxford, England)* **2018**, *5* (1), 43–60.

173. Cigliola, V.; Becker, C. J.; Poss, K. D. Building Bridges, Not Walls: Spinal Cord Regeneration in Zebrafish. *DMM Dis. Model. Mech.* **2020**, *13* (5).

174. Alper, S. R.; Dorsky, R. I. Unique Advantages of Zebrafish Larvae as a Model for Spinal Cord Regeneration. *Front. Mol. Neurosci.* **2022**, *15*, 983336.

175. Chang, W.; Pedroni, A.; Bertuzzi, M.; Kizil, C.; Simon, A.; Ampatzis, K. Locomotion Dependent Neuron-Glia Interactions Control Neurogenesis and Regeneration in the Adult Zebrafish Spinal Cord. *Nat. Commun.* **2021**, *12* (1).

176. Babin, P. J.; Goizet, C.; Raldúa, D. Zebrafish Models of Human Motor Neuron Diseases: Advantages and Limitations. *Prog. Neurobiol.* **2014**, *118*, 36–58.

177. Vieira, A. C.; Rubiolo, J. A.; López-Alonso, H.; Cifuentes, J. M.; Alfonso, A.; Bermúdez, R.; Otero, P.; Vieytes, M. R.; Vega, F. V.; Botana, L. M. Oral Toxicity of Okadaic Acid in Mice: Study of Lethality, Organ Damage, Distribution and Effects on Detoxifying Gene Expression. *Toxins (Basel).* **2013**, *5* (11), 2093.

178. Emery, H.; Traves, W.; Rowley, A. F.; Coates, C. J. The Diarrhetic Shellfish-Poisoning Toxin, Okadaic Acid, Provokes Gastropathy, Dysbiosis and Susceptibility to Bacterial Infection in a Non-Rodent Bioassay, Galleria Mellonella. *Arch. Toxicol.* **2021**, *95* (10), 3361–3376.

179. Tubaro, A.; Sosa, S.; Altinier, G.; Soranzo, M. R.; Satake, M.; Della Loggia, R.; Yasumoto, T. Short-Term Oral Toxicity of Homoyessotoxins, Yessotoxin and Okadaic Acid in Mice. *Toxicon* **2004**, *43* (4), 439–445.

180. Kamat, P. K.; Rai, S.; Swarnkar, S.; Shukla, R.; Nath, C. Molecular and Cellular Mechanism of Okadaic Acid (OKA)-Induced Neurotoxicity: A Novel Tool for Alzheimer's Disease Therapeutic Application. *Mol. Neurobiol.* **2014**, *50* (3), 852–865.

181. Cohen, P.; Holmes, C. F. B.; Tsukitani, Y. Okadaic Acid: A New Probe for the Study of Cellular Regulation. *Trends Biochem. Sci.* **1990**, *15* (3), 98–102.

182. Choi, J. Y.; Ryoo, H. M.; Lee, B. H.; Kim, H. J.; Sohn, K. Y.; Jo, J. S. Okadaic Acid Inhibits Alkaline Phosphatase Activity in MC3T3-E1 Cells. *Biochem. Mol. Biol. Int.* **1995**, *37* (5), 943–947.

183. Meštrović, V.; Pavela-Vrančič, M. Inhibition of Alkaline Phosphatase Activity by Okadaic Acid, a Protein Phosphatase Inhibitor. *Biochimie* **2003**, *85* (7), 647–650.

184. Murata, T.; Shirakawa, S.; Takehara, T.; Kobayashi, S.; Haneji, T. Protein Phosphatase Inhibitors, Okadaic Acid and Calyculin A, Induce Alkaline Phosphatase Activity in Osteoblastic Cells Derived from Newborn Mouse Calvaria. *Biochem. Mol. Biol. Int.* **1995**, *36* (2), 365–372.

185. E. Nada, S.; E. Williams, F.; A. Shah, Z. Development of a Novel and Robust Pharmacological Model of Okadaic Acid-Induced Alzheimer's Disease in Zebrafish. *CNS Neurol. Disord. - Drug Targets* **2016**, *15* (1), 86–94.

186. Ferrari, A. C.; Robertson, J. Resonant Raman Spectroscopy of Disordered, Amorphous, and Diamondlike Carbon. *Phys. Rev. B - Condens. Matter Mater. Phys.* **2001**, *64* (7).

187. Ferrari, A. C.; Robertson, J. Raman Spectroscopy of Amorphous, Nanostructured, Diamond-like Carbon, and Nanodiamond. *Philos. Trans. R. Soc. A Math. Phys. Eng. Sci.* **2004**, *362* (1824), 2477–2512.

188. Khun, N. W.; Liu, E.; Guo, H. W. Cyclic Voltammetric Behavior of Nitrogen-Doped Tetrahedral Amorphous Carbon Films Deposited by Filtered Cathodic Vacuum Arc. *Electroanalysis* **2008**, *20* (17), 1851–1856.

189. Roy, S. S.; McCann, R.; Papakonstantinou, P.; Maguire, P.; McLaughlin, J. A. The Structure of Amorphous Carbon Nitride Films Using a Combined Study of NEXAFS, XPS and Raman Spectroscopies. *Thin Solid Films* **2005**, *482* (1–2), 145–150.

190. Ferrari, A. C.; Rodil, S. E.; Robertson, J.; Rodil, S. E.; Robertson, J. Interpretation of Infrared and Raman Spectra of Amorphous Carbon Nitrides. *Phys. Rev. B - Condens. Matter Mater. Phys.* **2003**, *67* (15).

191. Oti, T.; Sakamoto, T.; Sakamoto, H. Systemic Effects of Oxytocin on Male Sexual Activity via the Spinal Ejaculation Generator in Rats. *Commun. Integr. Biol.* **2021**, *14* (1), 55.

192. Kosfeld, M.; Heinrichs, M.; Zak, P. J.; Fischbacher, U.; Fehr, E. Oxytocin Increases Trust in Humans. *Nature* **2005**, *435* (7042), 673–676.

193. Flight, M. H. Oxytocin and Serotonin Make It Worthwhile. *Nat. Rev. Neurosci. 2013 1411* **2013**, *14* (11), 740–741.

194. Love, T. M. Oxytocin, Motivation and the Role of Dopamine. *Pharmacol. Biochem. Behav.* **2014**, *119*, 49–60.

195. Tyzio, R.; Nardou, R.; Ferrari, D. C.; Tsintsadze, T.; Shahrokhi, A.; Eftekhari, S.; Khalilov, I.; Tsintsadze, V.; Brouchoud, C.; Chazal, G.; et al. Oxytocin-Mediated GABA Inhibition during Delivery Attenuates Autism Pathogenesis in Rodent Offspring. *Science (80-.).* **2014**, *343* (6171), 675–679.

196. Shin, M.; Kaplan, S. V.; Raider, K. D.; Johnson, M. A. Simultaneous Measurement and Quantitation of 4-Hydroxyphenylacetic Acid and Dopamine with Fast-Scan Cyclic Voltammetry. *Analyst* **2015**, *140* (9), 3039–3047.

197. Gómez-Laplaza, L. M.; Gerlai, R. Latent Learning in Zebrafish (Danio Rerio). *Behav. Brain Res.* **2010**, *208* (2), 509-515. PMCID: PMC2831165.

198. Luchiari, A. C.; Salajan, D. C.; Gerlai, R. Acute and Chronic Alcohol Administration:

Effects on Performance of Zebrafish in a Latent Learning Task. *Behav. Brain Res.* **2015**, *282*, 76-83. PMCID: PMC4339105.

199. Hamidi, N.; Nozad, A.; Sheikhkanloui Milan, H.; Amani, M. Okadaic Acid Attenuates Short-Term and Long-Term Synaptic Plasticity of Hippocampal Dentate Gyrus Neurons in Rats. *Neurobiol. Learn. Mem.* **2019**, *158*, 24–31.

200. Kamat, P. K.; Tota, S.; Saxena, G.; Shukla, R.; Nath, C. Okadaic Acid (ICV) Induced Memory Impairment in Rats: A Suitable Experimental Model to Test Anti-Dementia Activity. *Brain Res.* **2010**, *1309*, 66–74.

201. Kaushal, A.; Wani, W. Y.; Bal, A.; Gill, K. D.; Kaur, J. Okadaic Acid and Hypoxia Induced Dementia Model of Alzheimer's Type in Rats. *Neurotox. Res.* **2019**, *35* (3), 621–634.

202. Garcia, L.; Garcia, F.; Llorens, F.; Unzeta, M.; Itarte, E.; Gómez, N. PP1/PP2A Phosphatases Inhibitors Okadaic Acid and Calyculin A Block ERK5 Activation by Growth Factors and Oxidative Stress. *FEBS Lett.* **2002**, *523* (1–3), 90–94.

203. Gerlai, R.; Ahmad, F.; Prajapati, S. Differences in Acute Alcohol-Induced Behavioral Responses among Zebrafish Populations. *Alcohol. Clin. Exp. Res.* **2008**, *32* (10), 1763-1773. PMCID: PMC2709829.

204. Faustino, A. I.; Tacão-Monteiro, A.; Oliveira, R. F. Mechanisms of Social Buffering of Fear in Zebrafish. *Sci. Rep.* **2017**, *7*, PMCID: PMC5374490.

205. Agetsuma, M.; Aoki, T.; Aoki, R.; Okamoto, H. Cued Fear Conditioning in Zebrafish (Danio Rerio). In *Zebrafish Protocols for Neurobehavioral Research*; Humana Press, Totowa, NJ, 2012; Vol. 66, pp 257–264.

206. De Souza Caetano, K. A.; De Oliveira, A. R.; Brandão, M. L. Dopamine D2 Receptors Modulate the Expression of Contextual Conditioned Fear: Role of the Ventral Tegmental Area and the Basolateral Amygdala. *Behav. Pharmacol.* **2013**, *24* (4), 264–274.

207. de Vita, V. M.; Zapparoli, H. R.; Reimer, A. E.; Brandão, M. L.; de Oliveira, A. R. Dopamine D2 Receptors in the Expression and Extinction of Contextual and Cued Conditioned Fear in Rats. *Exp. brain Res.* **2021**, *239* (6), 1963–1974.

208. Johnson, M. A.; Rajan, V.; Miller, C. E.; Wightman, R. M. Dopamine Release Is Severely Compromised in the R6/2 Mouse Model of Huntington's Disease. *J. Neurochem.* **2006**, *97* (3), 737–746.

209. Phillips, P. E. M.; Stuber, G. D.; Helen, M. L. A. V.; Wightman, R. M.; Carelli, R. M. Subsecond Dopamine Release Promotes Cocaine Seeking. *Nature* **2003**, *422* (6932), 614–618.

APPENDIX I

Evaluation of Nitrogen-Incorporated Tetrahedral Amorphous Carbon Thin-Film for the Detection of Tryptophan and Tyrosine Using Flow Injection Analysis with Amperometric Detection

Romana Jarošová, Joy Rutherford, and Greg M. Swain

ANALYST

141 (2016) 6031-6041

Analyst

PAPER

View Article Online
View Journal | View Issue

Cite this: *Analyst*, 2016, **141**, 6031

Evaluation of a nitrogen-incorporated tetrahedral amorphous carbon thin film for the detection of tryptophan and tyrosine using flow injection analysis with amperometric detection

Romana Jarošová,[a,b] Joy Rutherford[a] and Greg M. Swain*[a]

Received 17th June 2016,
Accepted 7th September 2016

DOI: 10.1039/c6an01379a

www.rsc.org/analyst

We report on the analytical performance of a tetrahedral amorphous carbon (ta-C:N) thin-film electrode in flow injection analysis with amperometric detection. Two model redox analytes were used to evaluate the electrode response because of their positive detection potentials and propensity (*i.e.*, reaction products) to adsorb and foul sp^2 carbon electrodes: tyrosine and tryptophan. ta-C:N electrodes are attractive for electroanalytical applications because they possesses many of the excellent properties of boron-doped nanocrystalline diamond (BDD) and they can be deposited at or near room temperature. The results show that the ta-C:N electrode exhibits lower background current and noise than glassy carbon (GC). The electrode was stable microstructurally at the positive potentials used for detection, ~1.1 V, of these two amino acids and it exhibited superior analytical detection figures of merit as compared to GC and as good or superior to BDD. The linear dynamic range for both analytes at ta-C:N was from 0.1 to 100 μmol L^{-1}, the sensitivity was 8–12 mA L mol^{-1}, the short-term response variability was 1–2%, and the minimum detectable concentration was 89.7 ± 0.9 nM (18.3 μg L^{-1} or 0.46 ng) for tryptophan and 120 ± 11 nM (21.7 μg L^{-1} or 0.54 ng) for tyrosine. The analytical detection figures of merit for these amino acids at GC and BDD are also presented for comparison as is characterization data for the chemical composition and microstructure of the ta-C:N film.

1. Introduction

Liquid chromatography (LC) and flow injection analysis (FIA) with electrochemical detection are versatile techniques used for the determination of easily oxidizable or reducible analytes.[1–3] Major contributions have been made by Lunte and colleagues over the years on coupling novel electrochemical detection strategies to LC,[4,5] CE[6] and microchip-CE.[7] Detection limits for oxidizable analytes are generally sub-picomole but are often higher for reducible analytes because of interference by dissolved oxygen. There are three methods of electrochemical detection used: amperometric, coulometric and voltammetric.[1,8] The most popular of these being amperometric detection in a cross-flow thin-layer electrochemical cell. Typically, single electrodes are used in these measurements but as Lunte *et al.* have elegantly described, there are situations where dual electrodes[4] or combinations of voltammetric and amperometric detection[5] are useful. Series, parallel-adjacent and parallel-opposed are the most common dual-electrode configurations[4] Each of these configurations has been shown to improve the selectivity and extend the versatility of electrochemical detection.[4] That said, in practice, the detector performance can vary widely with the analyte type, the mobile phase or carrier solution composition, and the electrode material.

Carbon electrodes have been routinely used for electrochemical detection for over five decades now. These include glassy carbon, pyrolytic graphite and polycrystalline diamond. Glassy carbon (GC) is attractive for electroanalysis because of its chemical inertness, wide working potential window (at least compared to many metals), good activity for a wide range of redox analytes, and renewable surface.[9] Boron-doped diamond (BDD) is another type of carbon electrode that performs well in electrochemical detection often providing superior detection figures of merit compared with GC.[10–15] The basic electrochemical properties of BDD have been reviewed extensively in publications dating back to the 1990s.[10–15] In addition, BDD can function as an optically transparent electrode for transmission spectroelectrochemical measurements in the UV/Vis[16–20] and mid-IR[21] regions of the electromagnetic spec-

[a]*Department of Chemistry, 578 S. Shaw Lane, Michigan State University, East Lansing, Michigan 48824-1226, USA. E-mail: swain@chemistry.msu.edu*
[b]*Department on Analytical Chemistry, UNESCO Laboratory of Environmental Electrochemistry, Albertov 6, Charles University in Prague, 128 43 Prague 2, Czech Republic*

trum. The use of this carbon electrode makes possible novel dual detection (electrochemical and spectroscopic) strategies for complex analytes.

Another type of carbon electrode that shows promise in electroanalysis is nitrogen-incorporated tetrahedral amorphous carbon (*ta*-C:N).[22,23] Thin-film *ta*-C:N is diamond-like and consists of a mixture of sp^2 and sp^3-bonded carbon. The hardness, optical properties and electronic structure can be tailored from graphite to diamond by controlling the ratio of non-diamond (sp^2) to diamond (sp^3) carbon atom bonding as well as the hydrogen content in the film. Depending on the deposition method, *ta*-C films can have high hardness (~70 GPa), a wide bandgap (~3.5 eV) and a high proportion of sp^3-bonded carbon (~80% max.).[24–34] There is always some residual sp^2-bonded carbon in *ta*-C.[26] This is important because this carbon "impurity" increases the π states in the bandgap and thus influences the electronic properties of the material.[22,26,27,30,31] In other words, increasing the sp^2 carbon content in *ta*-C films has the tendency to increase the electrical conductivity. The sp^3 hybridized atoms form a random network in which neighboring atoms are connected by strong σ bonds.[24] An sp^3 site forms tetrahedral σ bonds with four adjacent atoms. This gives the material its "diamond" character.[24] An sp^2 site forms trigonal σ bonds with three neighboring atoms in a plane and a weaker π bond normal to the plane.

The electronic properties of the thin-film *ta*-C can also be altered by impurity incorporation. Nitrogen is a common impurity incorporated during the film deposition. The addition of N, by adding N_2 gas flow to the deposition chamber, can have at least two effects. First, adding the element dopes the film making it an n-type semiconductor.[25–27] Second, adding the element can increase the amount of sp^2-bonded carbon in the film, which adds π electronic states in the bandgap.[25–27] Hence, nitrogen incorporation also alters the electronic properties of *ta*-C (*i.e.*, increases the electrical conductivity).

We recently reported on some of the basic electrochemical properties of *ta*-C:N thin-film electrodes,[22] and on the application of this electrode in flow injection analysis with amperometric detection for norepinephrine.[23] The use of *ta*-C electrodes in electroanalyis is an underexplored area of research. There have been a few recent studies reported[35–40] but the original papers were from Miller and co-workers back in the 1990s.[41,42] *ta*-C films are formed by filtered cathodic vacuum arc or laser arc plasma deposition. The *ta*-C:N electrodes investigated so far by our group have consisted of 40–60% sp^3 carbon.[22,23] Even with this level of sp^2 carbon, the films exhibit electrochemical properties more closely resembling those of BDD rather than GC:[22,23,38] excellent microstructural stability, low background current and noise, weak molecular adsorption and good activity for several redox systems without conventional pretreatment. The electrochemical behavior of the *ta*-C:N films bear some similarities to the nanocarbon films reported on extensively by Niwa and co-workers.[43–46] One advantage of *ta*-C:N over BDD is that it can be deposited at or near room temperature on a wider variety of substrate materials.

Two other advantages of *ta*-C:N electrodes, as compared to GC, are the stability of the surface chemistry and microstructure over time at the positive potentials required for the detection of difficult to oxidize analytes, and the fact that they can be used without conventional pretreatment because of a resistance to fouling. The latter is time consuming and can add to the electrode response variability if not performed carefully. The microstructural stability of *ta*-C:N at positive potentials should lead to lower and more stable background current and noise, as compared to GC.[23] At high potentials, the GC surface will undergo oxidation and microstructural alterations that will trend toward reduce signal-to-noise ratios over time. In this paper, we report on an evaluation of the *ta*-C:N electrode performance at high potentials for the detection of two amino acids: tryptophan and tyrosine. These analytes require potentials of 1 V, or greater, for detection and generally have a propensity (*i.e.*, reaction products) to adsorb on and foul sp^2 carbon electrodes. Flow injection analysis (FIA) with amperometric detection in a cross-flow, thin-layer cell was used to evaluate the electrode performance in terms of the detection figures of merit. Comparison detection figures of merit are presented for BDD and GC. Given the fact that *ta*-C:N films possess a mixed sp^2/sp^3 carbon microstructure, an important question is, *does the film behave electrochemically more like GC or BDD?*

2. Experimental

2.1. Reagents

Stock solutions (0.1 mmol L^{-1}) of tryptophan (CAS no. 73-22-3, ≥98%, Sigma Aldrich, USA) and tyrosine (CAS no. 60-18-4, ≥98%, Sigma Aldrich, USA) were prepared by dissolving the exact amount of the analyte in 0.2 mol L^{-1} phosphate buffer pH 7.4. The solutions used for generating the calibration curves were prepared by serial dilution of the stock solutions.

The carrier solution was the same phosphate buffer prepared with 0.2 mol L^{-1} K_2HPO_4 and 0.2 mol L^{-1} KH_2PO_4. The resulting buffer pH was 7.4. Both salts were high purity (>98% pure, Sigma Aldrich, USA). All aqueous solutions were prepared using ultrapure water (~18 M ohm cm) from the MilliQ plus system (Millipore, USA). Stock solutions were stored in glass vessels in the dark at 5 °C when not in use.

2.2. Electrode preparation

Glassy carbon electrode. The glassy carbon (GC) working electrode (GC-20, Tokai Ltd) was pretreated prior to use by a three-step procedure. This involved polishing with successively smaller grades of alumina powder (1.0, 0.3 and 0.05 μm diameter). The powder was slurried with ultrapure water and the polishing was performed by hand on separate felt polishing pads. After each polishing step, the electrode was rinsed copiously with ultrapure water and then ultrasonically cleaned

for 10–20 minutes in ultrapure water to remove the polishing debris.

Nitrogen-incorporated tetrahedral amorphous carbon electrode. The *ta*-C:N film was grown on a boron-doped Si (111) substrate (Virginia Semiconductor, Fredericksburg, VA; $\sim 10^{-3}$ Ω cm) using Laser-Arc physical vapor deposition system at the Fraunhofer Center for Coatings and Diamond Technologies, Michigan State University. The technology is based on laser-controlled, high-current cathodic vacuum arc deposition.[29,47] In the process, a pulsed-laser beam is rastered across a rotating high purity graphite target that serves as the cathode. Each laser pulse generates a small localized plasma that delivers free charge carriers for the arc discharge. The arc discharge lasts only 125 μs before the laser triggers a new, staggered plasma across the graphite cathode. This deposition method produces highly ionized C atoms and small carbon clusters that are accelerated toward the substrate (grounded anode). This process produces hard (30–60 GPa) and dense *ta*: C films. The substrate-target distance was approximately 30 cm. The arc evaporation is associated with the emission of macro particles originating from the cathode surface.[48] The particles can be incorporated into the growing film. The nitrogen-incorporated films were deposited in the presence of N_2 gas at a flow rate of 30 sccm (*ta*-C:N) with a pulse rate of 350 Hz and a peak arc current of 1200 A. The substrate temperature during the deposition was below 100 °C. This contrasts with the 700–800 °C substrate temperature during typical CVD diamond growth. The film growth rate was approximately 2–3 μm h^{-1}. The film (ML15122201) tested electrochemically had a nominal thickness of *ca.* 200 nm, as determined by a Dektak profilometer, with an electrical resistivity between 0.01–0.04 ohm cm (room temperature). The film had a Young's modulus (YM) of 270 GPa, which is reflective of an sp^3 carbon content of ~37%. The sp^3 content tracks the YM according to the following relationship, $\sim sp^3\% = YM/800$.

A second *ta*-C:N film (ML1306301), also grown with 30 sccm of N_2 flow, was used for XPS analysis. Survey scans were performed to determine the O/C and N/C atomic ratios, depth profiling was performed to determine the nitrogen level with depth in the film and deconvolution of the C 1s peak was performed to estimate the sp^3/sp^2 carbon ratio.

Boron-doped diamond electrode. The boron-doped nanocrystalline diamond (BDD) film (GMS040716 and GMS041416) was deposited on a boron-doped Si (111) substrate ($\sim 10^{-3}$ ohm cm) by microwave-assisted chemical vapor deposition. A 1.5 kW reactor from Seki Technotron was used for the diamond growth. A 1% CH_4/H_2 source gas was used with 10 ppm of B_2H_6 added for boron doping. The microwave power was 800 W and the system pressure was 35 torr. These conditions produced a diamond film that was ~2–3 μm thick with a doping level in the low 10^{21} cm^{-3} range, based on Raman spectroscopic analysis,[49–51] and an electrical resistivity of 0.01 ohm cm. At the end of the deposition, the CH_4 and B_2H_6 flows were stopped. The specimen was then cooled in the presence of atomic hydrogen (plasma remained ignited with only H_2) by slowly low lowering the power and pressure over a 30 min period to reduce the substrate temperature to the 400 °C range. This post-growth cooling is essential for maintaining a hydrogen surface termination and prohibiting surface reconstruction from sp^3 to sp^2 hybridization.

As a final cleaning step, all electrodes were pretreated by a 20 min immersion in ultrapure isopropanol daily.[52,53] The isopropanol was purified by distillation and storage over activated carbon. This ultraclean solvent cleans the surface and activates the electrode by dissolving adventitious contaminants.

2.3. Material characterization

The boron-doped diamond and *ta*-C:N film morphology was examined using a field-emission scanning electron microscope (JSM-7500F, JEOL, Ltd, Tokyo, Japan) at the Center for Advanced Microscopy, Michigan State University. Images of the *ta*-C:N films have been presented elsewhere.[22,54] An accelerating voltage of 10–15 kV was used with secondary electron images generated. Raman spectroscopy was performed using a Renishaw *inVia* Reflex spectrometer. The instrument consisted of a confocal microscope connected to a continuous wave, diode-pumped solid-state laser with a fundamental emission at 532 nm. The sample was positioned under the laser light using a motorized stage. The stage position was controlled and spectral data acquired with commercial software (WiREInterface). This software allows for control over the laser power, exposure time, spectral range covered, and stage positioning for mapping a sample. The parameters used were a laser power of 10 mW at the sample and an integration time of 10 s. Each spectrum was generated from an average of 5 spectral acquisitions at each point. A Leica (100×/0.85) objective lens was used for focusing the excitation light and collecting the scattered radiation. A 1800 lines per mm holographic grating was used.

The XPS was performed courtesy of Kratos Analytical Ltd using the Axis Supra™ instrument. The surface science station was equipped with XPS and an Ar^+ gas cluster ion source for depth profiling. The ion source was operated at 4 kV for the depth profiling of the *ta*-C:N film. X rays were generated from an Al/Mg Kα X-ray source and emitted photoelectrons were analyzed using a hemispherical analyzer. The X-ray power was 600 W and scans were acquired over a 700 μm × 300 μm area. The pass energy was 160 eV and the acquisition time was 120 s per survey scan. The samples were analyzed as received after evacuation to the base pressure of $\sim 10^{-10}$ Torr. A combined Gaussian/Lorentzian lineshape was used to deconvolute the C 1s and N 1s core level peaks. The low binding energy side of the C 1s peak was fit first by adjusting the height and half-width. Once that was done, additional components were added based on knowledge of the different types of carbon–oxygen functional groups and their respective binding energy shifts from the base peak. Some survey scans, from which the sp^3/sp^2 carbon ratio was determined, were recorded using a Perkin Elmer Phi 5600 ESCA system with a Mg Kα X-ray source at a take-off angle of 45°.

Fitting of the C 1s core level peak was used to determine the sp^3 carbon atom content in the film according to literature

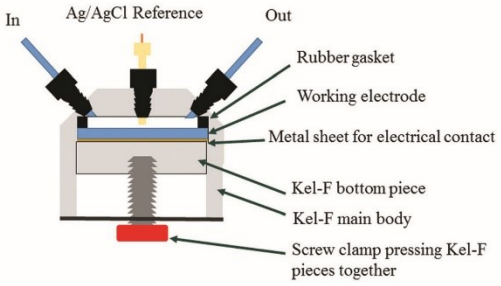

Fig. 1 Diagram of the thin-layer, cross-flow flow cell for the FIA measurements.

procedures.[55,56] The peak was fit to the two main components, 284.6 eV for sp^2 carbon (graphite) and 285.4 eV for sp^3 carbon (diamond). Since the sensitivity factor for the XPS core-level spectra depends only on atomic factors and is independent of the chemical state of the atoms, it should be the same for the two peaks.[56] The sp^3 carbon content was then estimated as the ratio of the sp^3 carbon peak area to the total C 1s peak area.

2.4. Flow injection apparatus

The flow injection analysis system consisted of Alltech HPLC pump (Model 3012, Grace) and a six-port injection valve Model 7125 (Rheodyne) with 25 μL injection loop, connected to the home-made, thin-layer flow cell. The flow cell was a cross-flow design as shown in Fig. 1. This is similar to the design used in prior work.[23,57] The electrochemical flow cell consisted of a two-piece Kel-f body with the top piece having entrance and exit ports for the carrier solution and a port for the no-leak Ag/AgCl reference electrode (Dionex). A stainless tube on the exit port served as the auxiliary electrode. The working electrode was placed between the bottom and top piece of the cell with a thin rubber gasket defining the flow channel. Electrical contact was made using a thin piece of copper foil placed against the back side of the electrode (conducting Si substrate). The area of the working electrode was defined by a rectangular channel (1.05 × 0.1 × 0.1 cm) cut out of the rubber (neoprene) gasket. This gives rise to a cell volume of ~10 μL assuming no compression of the gasket when the cell is tightened. Electrical noise was reduced by placing the cell inside a Faraday cage that was electrically grounded. All measurements were made using a Model 832A electrochemical work station (CH Instruments, USA).

3. Results and discussion

Raman and EELs data for *ta*-C:N films similar to the one used herein have been reported previously.[22] Fig. 2A shows an XPS survey scan for a *ta*-C:N film deposited with 30 sccm N_2. Three major peaks are present for C 1s (285.0 eV), N 1s (395.0 eV) and O 1s (532.6 eV). The O/C atomic ratio was 0.162 and the N/C atomic ratio was 0.094 in this particular film. These determinations are based on known sensitivity factors for C, O and N. This film was exposed to the atmosphere for a lengthy period of time prior to the analysis so this is the reason for the relatively high O/C ratio. We have not studied this yet but it is likely that the *ta*-C:N films will pick up oxygen over time when exposed to the atmosphere. A shown below, this oxygen exists in the near surface region of the film and not the bulk. The C 1s spectrum is asymmetrically shaped with broadening on the high energy side of the peak due to the presence of C–O and C–N functional groups. The C 1s peak was fit to four components: 284.66 eV (65.55% area), 285.91 eV (24.75% area), 287.46 eV (6.44% area) and 288.65 eV (3.26% area). The 284.66 eV peak is assumed to be associated with sp^2 bonded carbon (*e.g.*, graphite) and the 285.91 eV peak is assumed to be associated with sp^3 bonded carbon (*e.g.* diamond).[55,56] The sp^3 carbon was estimated to be 25%. This is lower than the 38% content determined from the Young's modulus. The XPS method for estimating the sp^3 carbon content is most accurate when there is little C 1s peak area from higher binding energy components arising from surface functional groups (*i.e.*, carbon–oxygen). For this film, about 10% of the total C 1s

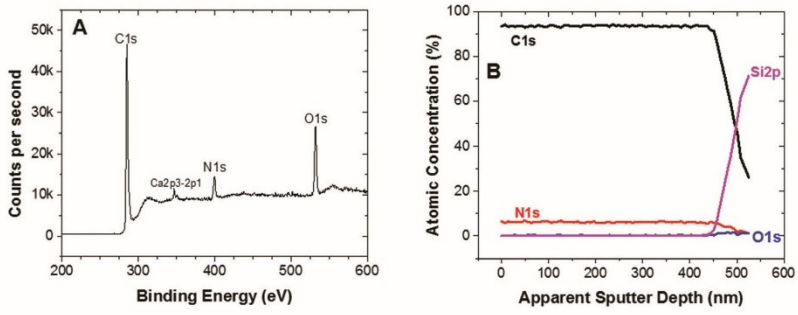

Fig. 2 XPS (A) survey spectrum for a ta-C:N thin film deposited in the presence of 30 sccm N_2 on a Si substrate and (B) depth profiling data for C 1s, O 1s, N 1s and Si 2p through the film. Ar^+ sputtering at 4 kV was used for the profiling.

peak area was associated with these functional groups. Therefore, we suppose that the 25% sp^3 carbon content is an underestimate and it is probably closer to the 38% value.

The N 1s peak was deconvoluted and fit to three components with the following areas: 398.56 (39.11%), 399.91 (52.73%) and 401.41 (8.16%). This result suggests that the N in the film exists in three different chemical environments. According to Rodil *et al.*[58] the peaks are assigned to N bonded to sp^3 carbon (398.56 eV), CN triple bonds (399.91 eV) and N-sp^2 carbon (401.41 eV). By way of comparison, the peak at 398.6 eV has been assigned to pyridinic-like N and the peak at 401.8 eV to graphitic N in nitrogen-doped carbon nanotubes.[59]

Fig. 2B shows XPS depth profiles recorded for the t*a*-C:N film using 4 kV Ar^+ sputtering. The sputter depth is apparent but this particular film appears to be thicker than most others deposited under these conditions, *ca.* 200 nm. The C atomic concentration is constant with depth at about 93%. The Si concentration begins to increase once the substrate is reached. The N atomic concentration is constant at ~6% through the film. The O atomic concentration is less than 1% through the film. These results indicate that the nitrogen content is relatively constant with depth in the t*a*-C:N film. The 6% atomic concentration corresponds to ~60 000 ppm (6 at% – 10 000 ppm) or 2.6×10^{21} atoms N cm^{-3}.

Fig. 3 shows visible Raman microprobe spectra for one of the BDD films used in the work. Both BDD films were deposited using the same conditions and therefore exhibited identical Raman spectral features. Similar spectra were acquired in the five quadrants probed on this film reflective of a uniform microstructure across the substrate surface. Multiple peaks are seen in the spectrum at 519, 1137, 1215, 1321 and 1510 cm^{-1}. These spectral features are consistent with the film being heavily boron doped.[49–51,60] For heavily boron-doped films, the first-order diamond phonon line shifts from 1332 cm^{-1} to lower wavenumbers with increasing boron concentration. This shift is typically accompanied by increases in scattering intensity at *ca.* 500 and *ca.* 1225 cm^{-1}.[49–51,60] In these spectra, the diamond phonon peak is shifted down to 1321 cm^{-1}. The 519 cm^{-1} peak (Si phonon mode) is actually superimposed on broad scattering intensity centered at *ca.* 500 cm^{-1}. The presence of the Si substrate peak is consistent with a thin diamond film. The broad scattering at 500 cm^{-1} dominates the spectrum at all positions. Given that this intensity increases with boron doping level, this peak has been assigned to the vibrational modes of boron dimers[61–63] and pairs or clusters.[64] The 1215 cm^{-1} peak has been assigned to defects in the diamond lattice brought about by the high boron doping, possibly boron–carbon complexes.[51,60] The 1137 cm^{-1} peak has been assigned to polymeric sp^2 carbon species in the grain boundaries.[65] Finally, the 1510 cm^{-1} peak is caused by some non-diamond carbon that becomes more prominent with increasing boron concentration.[51,60]

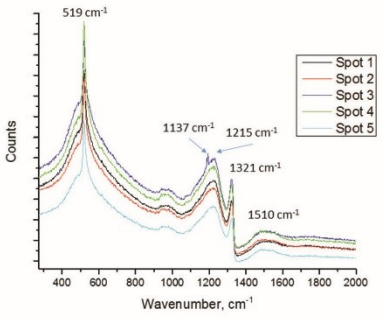

Fig. 3 Raman spectra recorded at different quadrants on a boron-doped nanocrystalline diamond (GMS040716) thin-film electrode.

Ideally, an electrode used for electrochemical detection should exhibit low background current and noise (standard deviation of the mean background current), and the background current should quickly stabilize after application of the detection potential.[66,67] In order to obtain this information, 0.1 mol L^{-1} phosphate buffer pH 7.4 was used as the carrier solution and different potentials from 1.0 to 1.4 V *vs.* Ag/AgCl were applied to the working electrode for 30 min periods. Fig. 4 shows the background current and noise (mean values) recorded for GC, BDD and t*a*-C:N electrodes. The data were obtained at the end of a 60 min measurement period. Importantly, this is the potential range where tryptophan and tyrosine are detected. It can be seen in Fig. 4A that the background current (notice the scale is μA) for GC starts to become significantly higher than that for BDD or t*a*-C:N. This is especially noticeable at 1.4 V, a potential at which an 8× difference exists. A similar trend is seen for the noise as a function of potential. In Fig. 4B, it can be seen that the noise for GC becomes significantly larger than BDD and t*a*-C:N starting at 1.2 V. This difference grows at 1.3 and 1.4 V. At 1.4 V, the noise for GC is 2.5× larger than BDD and t*a*-C:N. The BDD and t*a*-C:N electrodes exhibit comparable responses in terms of background current and noise at these positive potentials, and they are stable with time. This is different from the trend expected for GC. At these positive potentials, the background current and noise are expected to progressively increase with time leading to reduced signal-to-noise ratios.[68] This is just one example showing that the electrode properties of t*a*-C:N are more like those of BDD rather than GC.

In order to determine the optimum detection potential for tyrosine and tryptophan, hydrodynamic voltammograms were recorded over a potential range from +0.5 to 1.3 V at all three electrodes. Fig. 5 shows resulting hydrodynamic voltammograms for 100 μmol L^{-1} (A) tyrosine and (B) tryptophan in 0.2 mol L^{-1} phosphate buffer (pH 7.4) at GC, BDD and t*a*-C:N electrodes. Steady-state currents of *ca.* 1.2 μA are seen for both analytes at all three electrodes. There are differences in the rate of electron transfer for tyrosine (Fig. 5A) at the three electrodes as evidenced by the differences in $E_{1/2}$. The $E_{1/2}$ at GC is ~300 mV less positive than at BDD. The $E_{1/2}$ at t*a*-C:N falls in between these two values. These results indicate that the oxidation reaction kinetics for this amino acid are the most sluggish at BDD and the most rapid at GC. The microstructure

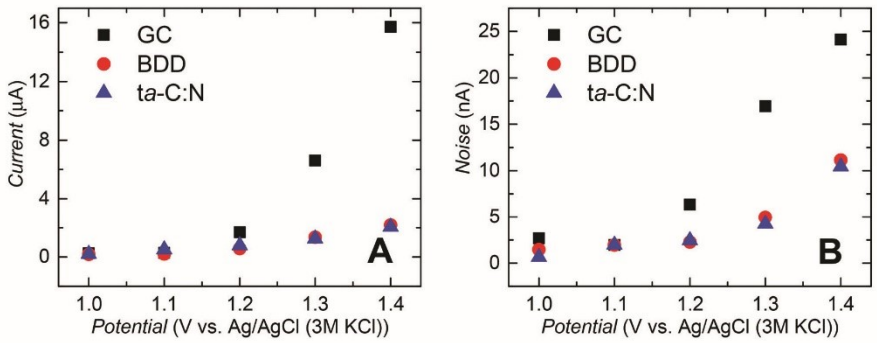

Fig. 4 Plots of the (A) mean background current and (B) noise for GC (■), BDD (●) and ta-C:N (▲) electrodes a function of applied potential from +1.0 to 1.4 V. Carrier solution = 0.2 mol L^{-1} phosphate buffer (pH 7.4). Flow rate = 1 mL min^{-1}.

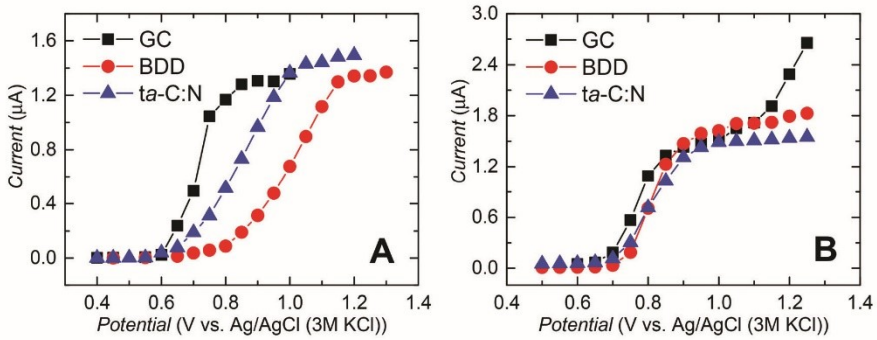

Fig. 5 Hydrodynamic voltammograms for 100 μmol L^{-1} (A) tyrosine and (B) tryptophan in 0.2 mol L^{-1} phosphate buffer (pH 7.4) at GC (■), BDD (●) and ta-C:N (▲) electrodes. Flow rate = 1 mL min^{-1}. Injection volume = 25 μL.

of the carbon electrode clearly has an impact on the oxidation response for this amino acid. In contrast, nearly identical $E_{1/2}$ values of ~0.8 V are seen for tryptophan at the three electrodes (Fig. 5B). This indicates similar oxidation reaction kinetics for this amino acid regardless of the carbon electrode type and microstructure. The increase in current at 1.1 V for GC is due to a combination of surface oxidation and the onset of water oxidation. BDD and ta-C:N have less current from surface oxidation and higher overpotentials for water oxidation.[22]

Fig. 6 shows the short-term response reproducibility for 30 injections of 100 μmol L^{-1} tryptophan at (A) GC, (B) BDD and (C) ta-C:N electrodes. Similar data were obtained for tyrosine at the three electrodes (data not shown). The optimum detection potentials, selected based on the maximum signal-to-background, $\frac{i_{total} - i_{bkg}}{i_{bkg}}$, ratios were 0.90, 1.00 and 1.05 V for the three electrodes, respectively. Good reproducibility is seen for all three electrodes over this short-term period of sample injection. Table 1 presents quantitative data for the reproducibility (peak height) at the three electrodes. Excellent reproducibility is seen at all three electrodes with relative standard deviations in the 1–2.5% range. All three electrodes provide reproducible responses for both amino acids with no significant differences between them. No evidence for any electrode fouling was observed at any of the electrodes under these conditions. This is particularly surprising for GC.

Fig. 7 shows replicate injections (3×) of different concentrations of (A) tryptophan and (B) tyrosine at a ta-C:N electrode. The concentrations injected ranged from 1 to 0.1 μmol L^{-1} in 0.2 mol L^{-1} phosphate buffer (pH 7.4). Reproducible signals are seen at each concentration and the peak height increases proportionally with the concentration injected. The signal-to-noise ratio at the lowest concentration injected, 0.1 μmol L^{-1}, is ~4 and ~3 for tryptophan and tyrosine, respectively.

Fig. 8 shows log–log plots of the detector responses for (A) tyrosine and (B) tryptophan at all three electrodes. Good linearity is seen for both analytes at all three. Over the concentration range from 0.1 to 100 μmol L^{-1}, linear regression correlation coefficients are high ranging from 0.9989 to 0.9997. Clearly, the linear dynamic range for all three

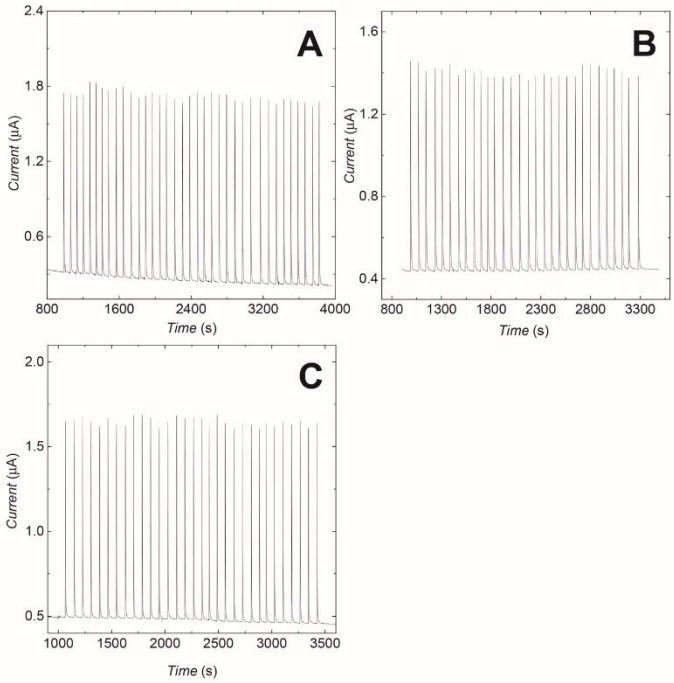

Fig. 6 Short-term (~40 min) response reproducibility over 30 injections of 100 μmol L^{-1} tryptophan in 0.2 mol L^{-1} phosphate buffer (pH 7.4) for (A) GC, (B) BDD and (C) ta-C:N electrodes. Flow rate = 1 mL min^{-1}. Injection volume = 25 μL.

Table 1 Optimum detection potentials and short-term response reproducibility (30 injections) for tryptophan and tyrosine detection at GC, BDD and ta-C:N electrodes

Analyte	Electrode	Detection Potential [V]	Reproducibility [RSD %]
Tryptophan	GC	0.95	1.81
	BDD	1.05	2.11
	ta-C:N	1.00	1.23
Tyrosine	GC	0.90	2.14
	BDD	1.20	2.48
	ta-C:N	1.10	0.92

electrodes is at least 4 orders of magnitude. Similar current magnitudes and slopes are seen for both analytes at the three electrodes. Table 2 provides a summary of the linear dynamic range, regression analysis correlation coefficient, sensitivity and minimum concentration detectable (signal-to-noise ≥3) for each of the analytes at the three electrodes. It can be seen that the slopes of the response curves are slightly higher for both analytes at GC, ~18 mA L mol^{-1}. Slightly lower slopes were observed for BDD and ta-C:N, but nominally by less than a factor of 2. This difference may be due to some adsorption on GC, which likely does not occur on BDD or ta-C:N.[22] The minimum concentration detectable (C_{min}) with GC was 2.5×10^{-7} mol L^{-1} (51.1 μg L^{-1} or 1.3 ng) for tryptophan and 2.1×10^{-7} mol L^{-1} (37.3 μg L^{-1} or 0.93 ng) for tyrosine. C_{min} values were 2–3× lower for tryptophan at both ta-C:N and BDD. C_{min} for tryptophan with BDD and ta-C:N was (avg.) 8.3×10^{-8} mol L^{-1} (16.9 μg L^{-1} or 0.42 ng) and 9.0×10^{-8} mol L^{-1} (18.4 μg L^{-1} or 0.46 ng), respectively. C_{mim} values were also 2–3× lower for tyrosine at both BDD and ta-C:N. C_{min} for tyrosine with BDD and ta-C:N was 9.5×10^{-8} mol L^{-1} (17.2 μg L^{-1}, 0.43 ng) and 1.2×10^{-7} mol L^{-1} (21.7 μg L^{-1}, 0.54 ng), respectively.

4. Discussion

ta-C:N thin-film electrodes are of interest for electroanalysis for several reasons. First, these electrodes possess many of the excellent attributes of BDD electrodes and they can be deposited near room temperature. The number of potential substrate materials is therefore greater given the milder deposition conditions. Even with an sp^3 carbon content on the order of 37%, the ta-C:N electrode exhibits properties more closely aligned with BDD than with GC. These include low background current, wide working potential window and weak molecular adsorption.[22] The present FIA-EC data further confirm this. The background current magnitude and noise,

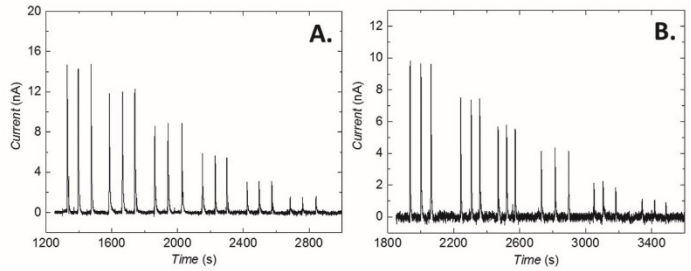

Fig. 7 Detector responses for (A) tryptophan and (B) tyrosine for different injected concentrations from 1 to 0.1 μmol L^{-1} in phosphate buffer (pH 7.4) at a ta-C:N thin-film electrode. Flow rate = 1 mL min^{-1}. Injection volume = 25 μL. Injected concentrations were 1, 0.8, 0.6, 0.4, 0.2 and 0.1 μmol L^{-1}.

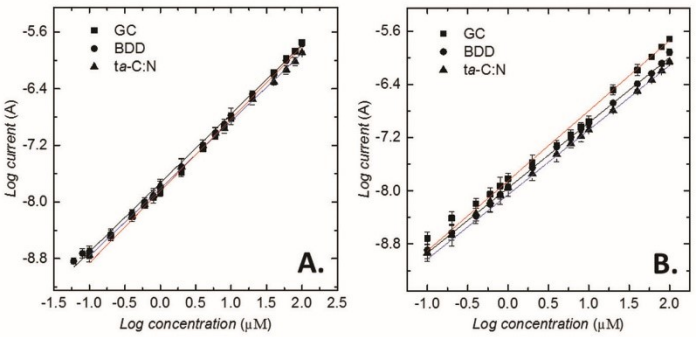

Fig. 8 Response curves for (A) tryptophan and (B) tyrosine in 0.2 mol L^{-1} phosphate buffer (pH 7.4) for injected concentrations from 0.1 to 100 μmol L^{-1} at GC (■), BDD (●) and ta-C:N electrodes (▲). Flow rate = 1 mL min^{-1}. Injection volume = 25 μL.

Table 2 The parameters of the calibration dependences for the detection of tryptophan and tyrosine at GC, BDD and ta-C:N electrodes

Analyte	Electrode	Concentration range (μmol L^{-1})	Slope (mA mol^{-1} L)	R^2 [a]	Minimum concentration detectable[b] (C_{min}, mol L^{-1})
Tryptophan	GC	0.1–100	17.7 ± 1.0	0.9991	$(2.51 \pm 0.17) \times 10^{-7}$
	BDD	0.08–100	16.7 ± 0.6	0.9989	$(8.26 \pm 0.72) \times 10^{-8}$
	ta-C:N	0.08–100	12.4 ± 1.2	0.9989	$(8.97 \pm 0.89) \times 10^{-8}$
Tyrosine	GC	0.1–100	18.6 ± 0.8	0.9997	$(2.06 \pm 0.19) \times 10^{-7}$
	BDD	0.1–100	10.9 ± 1.3	0.9997	$(9.52 \pm 0.41) \times 10^{-8}$
	ta-C:N	0.1–100	8.3 ± 0.2	0.9996	$(1.20 \pm 0.11) \times 10^{-7}$

[a] Linear regression correlation coefficient. [b] Minimum concentration detectable at S/N = 3. Data are reported as mean ± std. dev. (n = 3 electrodes of each type).

especially at potentials positive of 1.0 V, are lower for ta-C:N than for GC and are comparable to BDD.[23] What we did not investigate in this work is the stability of the background current and noise at the three electrodes over longer periods of time at the positive detection potentials. Based on prior results,[68] a progressive increase in the background current and noise for GC with time at potentials positive of 1.2 V is expected while the current and noise should be stable with time (multiple hours) for BDD and ta-C:N.

Second, good electrochemical activity is seen for the ta-C:N electrode without the time-consuming pretreatment that is typically necessary to activate GC.[22,23,53] The ta-C:N and BDD electrodes used in this work were only pretreated by soaking in ultrapure isopropanol. In contrast, GC was pretreated by mechanical polishing plus the isopropanol soak. Additonally, the ta-C:N electrode had been used for many measurements prior to these so it had an extensive past history. Even so, the electrode exhibited an active response for these two amino acids

similar to what is only achieved at freshly activated GC. Using these electrodes in FIA-EC analysis means less frequent electrode removal for pretreatment, recalibration and revalidation. The hydrodynamic voltammograms reveal that the electrode kinetics for tyrosine are most rapid at GC and slowest at BDD based on the more positive $E_{1/2}$ at the latter. The kinetics at t*a*-C:N fall in between these two electrodes based on the $E_{1/2}$. It is clear the kinetics for this electroactive amino acid are sensitive to the microstructure of the carbon electrode. In contrast, similar electrode kinetics are observed for tryptophan at all three electrodes based on the similarity of the $E_{1/2}$ values. This level of electrode activity for GC would not have been possible without pretreatment. BDD and t*a*-C:N electrodes typically exhibit good electrochemical activity without conventional pretreatment. Maintenance of the high activity results because the electrodes are less susceptible to molecular adsorption than is GC because of the sp^3 carbon bonding. These electrodes have no extended π-electron system and fewer surface carbon–oxygen functional groups; both of which drive molecular adsorption on sp^2 carbon electrodes. Even with the ~37% sp^3 carbon content, t*a*-C:N electrode resembles BDD in terms of weak molecular adsorption[22] and resistance to fouling based on the results presented herein.

Tryptophan and tyrosine are electroactive amino acids that can be oxidatively detected sp^2 carbon and metal electrodes.[69–74] There are also examples of using BDD films and nanowires for the detection of tyrosine and tryptophan,[75–81] tyrosine derivatives[80,81] and peptide and proteins containing these amino acids.[80,81] There is published work showing that the simultaneous voltammetric detection of tryptophan and tyrosine at BDD and BDD nanowires is possible with detection limits in the low micromolar range.[77,79] Selective detection is possible given the slight different redox potentials of the two amino acids. The oxidation potentials for these amino acids strongly depend on the electrochemical conditions namely the pH and carbon electrode material. It is generally easier to oxidize tryptophan than tyrosine, and E_p^{ox} for both shifts negative with increasing solution pH. The electrooxidation of both compounds proceeds initially by a one or two-electron transfer reaction to produce reactive intermediates that can undergo further reaction to form polymeric films that can passivate the electrode.[69,70,72–74] No evidence was observed for any fouling of the t*a*-C:N or BDD electrodes, as expected. More interesting is the fact that no fouling was observed for GC at least under the conditions employed in this work.

Overall, the detection figures of merit for t*a*-C:N are superior to GC and as good as BDD. The linear dynamic range for both tryptophan and tyrosine was at least 4 orders of magnitude (R^2 > 0.998) at all three electrodes. The short-term response reproducibility for both analytes at t*a*-C:N was 1–3% RSD over 30 injections (about 50 min of total analysis time). The nominal sensitivity for both tryptophan and tyrosine at GC was slightly larger than the sensitivity at BDD and t*a*-C:N. This could be due to the fact that there is some adsorption of both amino acids on GC. No adsorption is expected on BDD or t*a*-C:N, although this was not explicitly studied. The minimum concentration detectable (C_{min}) for both amino acids are as good or slightly lower for t*a*-C:N than for BDD and GC. The lower detection limits for tryptophan at BDD and t*a*-C:N arise from the lower noise at the detection potential. The same holds true for tyrosine at BDD compared to GC.

There is little published data on the FIA-EC or LC-EC detection of these two amino acids at BDD and none for t*a*-C:N electrodes. Ivandini *et al.*[80] reported on the FIA-EC and LC-EC detection of the peptide, leucine-enkephalinamide, and its metabolites, including tyrosine, using a BDD electrode. The linear dynamic range for tyrosine was from 0.06 to 30 μmol L^{-1} with a limit of detection (S/N = 3) of 3 nM. In another recent paper describing the HPLC-EC analysis of multiple bioanalytes using a BDD electrode,[82] the authors report mass limits of detection (S/N = 3) of 0.06 ng for tryptophan and 1.6 ng for tyrosine. Our C_{min} values are slightly higher for tryptophan at BDD (0.42 ng) and t*a*-C:N (0.45 ng). The authors reported mass limits of detection (S/N = 3) of 1.6 ng for tyrosine. Our C_{min} values are lower for both BDD (0.43 ng) and t*a*-C:N (0.54 ng).

5. Conclusions

Overall, the results indicate that the t*a*-C:N electrode functions well in the amperometric detection of tryptophan and tyrosine. The electrochemical properties of t*a*-C:N resemble those of BDD more so than those of GC. The following conclusions can be reached based on the results presented.

1. At potentials positive of 1.0 V where tryptophan and tyrosine are oxidatively detected, the t*a*-C:N electrode exhibits low and stable background current and noise that are significantly lower as compared to GC. Like BDD, the lower background current and noise result from the microstructural stability and low reactivity of the t*a*-C:N electrode.

2. The oxidation potential of tyrosine is slightly more positive of the oxidation potential of tryptophan at all three electrodes. The $E_{1/2}$ for tyrosine is sensitive to the carbon electrode type and microstructure with the most positive value seen at BDD (~1.0 V) and the least positive seen at GC (~0.70 V). The $E_{1/2}$ at t*a*-C:N (~0.82 V) falls in between. In contrast $E_{1/2}$ for tyrosine at all three electrodes is similar (~0.75 V).

3. The t*a*-C:N electrode is suitable for the detection of electroactive amino acids that require positive potentials for detection. The active t*a*-C:N electrode response is obtained without the time consuming surface pretreatment that is necessary to activate GC.

4. The linear dynamic range for both tyrosine and tryptophan all three electrodes is at least 4 orders of magnitude from 0.1–100 μmol L^{-1} (R^2 > 0.998). The short-term response reproducibility of both amino acids at all three electrodes is 1–3% RSD.

5. Lower minimum detectable concentrations are found for tryptophan (0.42 and 0.45 ng) and tyrosine (0.43 and 0.54 ng) at t*a*-C:N and BDD electrodes, respectively, as compared to GC

(1.3 and 0.93 ng). The lower detection limits result from the lower background current and noise of the *ta*-C:N and BDD electrodes.

Acknowledgements

This article is dedicated to Prof. Craig Lunte who exemplified excellence in teaching, research and service. Much of what this author knows about electrochemical detection was learned from Craig in my first graduate course. We thank Lars Haubold of the Fraunhofer CCD – Center for Coatings and Diamond Technologies at Michigan State University for depositing the *ta*-C:N films. This research was carried out under the framework of project W911NF-12-R-0011 funded by the Army Research Office (GMS). RJ thanks Charles University in Prague (SVV260317) for their financial support. We acknowledge Dr Jonathan Counsell of Kratos Analytical Ltd for acquiring the XPS results using the AXIS Supra XPS instrument. We also thank Dr Per Askeland (Composite Materials and Structures Center, MSU) for his assistance with the XPS measurements and the peak deconvolution.

References

1 P. T. Kissinger, C. Refshaug, R. Dreiling and R. N. Adams, *Anal. Lett.*, 1973, **6**, 465–477.
2 R. M. Riggin and P. T. Kissinger, *Anal. Chem.*, 1977, **49**, 2109–2111.
3 P. H. Jemdahl, M. Daleskog and T. Kahan, *Life Sci.*, 1979, **25**, 131–138.
4 C. E. Lunte, P. T. Kissinger and R. E. Shoup, *Anal. Chem.*, 1985, **57**, 1541–1546.
5 C. E. Lunte, T. H. Ridgway and W. R. Heineman, *Anal. Chem.*, 1987, **59**, 761–766.
6 S. Park, M. J. McGrath, M. R. Smyth, D. Diamond and C. E. Lunte, *Anal. Chem.*, 1997, **69**, 2994–3001.
7 U. Backofen, F. M. Matysik and C. E. Lunte, *Anal. Chem.*, 2002, **74**, 4054–4059.
8 P. T. Kissinger, *Anal. Chem.*, 1977, **49**, 447A–456A.
9 R. L. McCreery, Carbon Electrode Surface Chemistry: Optimization of Bioanalytical Performance, in *Voltammetric Methods in Brain Systems*, ed. A. A. Boulton, G. B. Baker and R. N. Adams, Humana Press, Totowa, NJ, 1995, pp. 1–26.
10 M. C. Granger, J. Xu, J. W. Strojek and G. M. Swain, *Anal. Chim. Acta*, 1999, **397**, 145–161.
11 R. G. Compton, J. S. Foord and F. Marken, *Electroanalysis*, 2003, **15**, 1349–1363.
12 C. E. Nebel, B. Rezek, D. Shin and H. Uetsuka, *J. Phys. D: Appl. Phys.*, 2007, **40**, 6443–6466.
13 K. Peckova, J. Musilova and J. Barek, *Crit. Rev. Anal. Chem.*, 2009, **39**, 148–172.
14 Y. Einaga, J. S. Foord and G. M. Swain, *MRS Bull.*, 2014, **39**, 525–532.
15 J. V. Macpherson, *Phys. Chem. Chem. Phys.*, 2015, **17**, 2935–2949.
16 J. Stotter, J. Zak, Z. Behler, Y. Show and G. M. Swain, *Anal. Chem.*, 2002, **74**, 5924–5930.
17 S. Haymond, J. K. Zak, Y. Show, J. E. Butler, G. T. Babcock and G. M. Swain, *Anal. Chim. Acta*, 2003, **500**, 137–144.
18 J. Stotter, Y. Show, S. Wang and G. M. Swain, *Chem. Mater.*, 2005, **17**, 4880–4888.
19 N. Wächter, C. A. Munson, R. Jarosová, I. Berkun, T. Hogan, R. Rocha-Filo and G. M. Swain, *ACS Appl. Mater. Interfaces*, 2016, DOI: 10.1021/acsami.6b02467 (Forum Article).
20 J. K. Zak, J. E. Butler and G. M. Swain, *Anal. Chem.*, 2001, **73**, 908–914.
21 Y. Dai, D. A. Proshlyakov, J. K. Zak and G. M. Swain, *Anal. Chem.*, 2007, **79**, 7526–7533.
22 X. Yang, L. Haubold, G. DeVivo and G. M. Swain, *Anal. Chem.*, 2012, **84**, 6240–6248.
23 D. Hamblin, J. Qiu, L. Haubold and G. M. Swain, *Anal. Methods*, 2015, **7**, 4481–4485.
24 J. Robertson, *Diamond Relat. Mater.*, 1997, **6**, 212–218.
25 B. Kleinsorge, A. C. Ferrari, J. Robertson and W. I. Milne, *J. Appl. Phys.*, 2000, **88**, 1149–1157.
26 S. Waidmann, M. Knupfer, J. Fink, B. Kleinsorge and J. Robertson, *Diamond Relat. Mater.*, 2000, **9**, 722–727.
27 S. Waidmann, M. Knupfer, J. Fink, B. Kleinsorge and J. Robertson, *J. Appl. Phys.*, 2001, **89**, 3783–3792.
28 O. Kutsay, I. Bello, Y. Lifshitz, C. W. Lam, W. Y. Luk, S. T. Lee, X. Meng and V. Kremnican, *Diamond Relat. Mater.*, 2003, **12**, 2051–2056.
29 H.-J. Scheibe and B. Schultrich, 2004 Society of Vacuum Coaters, *47th Ann. Tech. Conf. Proceed*, April 24–29, 2004, Dallas, TX, pp. 501–508.
30 S. S. Roy, R. McCann, P. Papakonstantinou, P. Maguire and J. A. McLaughlin, *Thin Solid Films*, 2005, **482**, 145–150.
31 N. Soin, S. S. Roy, S. C. Ray, P. Lemoine, M. A. Rahman, P. D. McGuire, S. K. Mitra and J. A. McLaughlin, *Thin Solid Films*, 2012, **520**, 2909–2915.
32 D. R. Mckenzie, D. Muller, B. A. Pailthorpe, Z. H. Wang, E. Kravtchinskaia, D. Segal, P. B. Lukins, P. D. Swift, P. J. Matu, G. Amaratunga, P. H. Gaskell and A. Saeed, *Diamond Relat. Mater.*, 1991, **1**, 51–59.
33 V. S. Veerasamy, J. Yuan, G. A. J. Amaratunga, W. I. Milne, K. W. R. Gilkes, M. Weiler and L. M. Brown, *Phys. Rev. B: Condens. Matter*, 1993, **48**, 17954–17959.
34 M. Chhowalla, J. Robertson, C. W. Chen, S. R. P. Silva, C. A. Davis, G. A. J. Amaratunga and W. I. Milne, *J. Appl. Phys.*, 1997, **81**, 139–145.
35 J. J. Lee, B. Miller, X. Shi, R. Kalish and K. A. Wheeler, *J. Electrochem. Soc.*, 2001, **148**, C183–C190.
36 D. Sopchak, B. Miller, R. Kalish, Y. Avygal and X. Shi, *Electroanalysis*, 2002, **14**, 473–478.
37 N. W. Khun, E. Liu and H. W. Guo, *Electroanalysis*, 2008, **20**, 1851–1856.
38 R. F. Brocenschi, R. C. Rocha-Filho, L. Li and G. M. Swain, *J. Electroanal. Chem.*, 2014, **712**, 207–214.

39 A. Zeng, V. F. Neto, J. J. Gracio and Q. H. Fan, *Diamond Relat. Mater.*, 2014, **43**, 12–22.
40 T. Laurila, V. Protopopova, S. Rhode, S. Saino, T. Palomaki, M. Moran, J. Feliu and J. Koskinen, *Diamond Relat. Mater.*, 2014, **49**, 62–71.
41 K. S. Yoo, B. Miller, R. Kalish and X. Shi, *Electrochem. Solid-State Lett.*, 1999, **2**, 233–235.
42 N. C. Yee, Q. F. Shi, W. D. Cai, D. A. Scherson and B. Miller, *Electrochem. Solid-State Lett.*, 2001, **4**, E42–E44.
43 O. Niwa, J. Jai, Y. Sato, D. Kato, R. Kurita, K. Maruyama, K. Suzuki and S. Hirono, *J. Am. Chem. Soc.*, 2006, **128**, 7144–7145.
44 T. Kamata, D. Kato, S. Hirone and O. Niwa, *Anal. Chem.*, 2013, **85**, 9845–9851.
45 T. Kamata, D. Kato, H. Ida and O. Niwa, *Diamond Relat. Mater.*, 2014, **49**, 25–32.
46 T. Kamata, D. Kato, S. Umemura and O. Niwa, *Anal. Sci.*, 2015, **31**, 651–656.
47 H.-J. Scheibe and B. Schultrich, *Thin Solid Films*, 2004, **A78**, 675–679.
48 D. Drescher, J. Koskinen, H.-J. Scheibe and A. Mensch, *Diamond Relat. Mater.*, 1998, 7, 1375–1380.
49 P. Gonon, E. Gheeraert, A. Deneuville and F. Fontaine, *J. Appl. Phys.*, 1995, **78**, 7059–7062.
50 A. Deneuville, C. Baron, S. Ghodbane and C. Agnès, *Diamond Relat. Mater.*, 2007, **16**, 915–920.
51 P. W. May, W. J. Ludlow, M. Hannaway, P. J. Heard, J. A. Smith and K. N. Rosser, *Diamond Relat. Mater.*, 2008, **17**, 105–117.
52 S. Ranganthan, T.-C. Kuo and R. L. McCreery, *Anal. Chem.*, 1999, **71**, 3574–3580.
53 M. C. Granger, M. Witek, J. S. Xu, J. Wang, M. Hupert, A. Hanks, M. D. Koppang, J. E. Butler, G. Lucazeau, M. Mermoux and G. M. Swain, *Anal. Chem.*, 2000, **72**, 3793–3804.
54 R. Jarošová, P. M. De Sousa Bezerra, C. Munson and G. M. Swain, *Phys. Status Solidi A*, 2016, **8**, 2087–2098.
55 P. Mérel, M. Tabbal, M. Chaker, S. Moisa and J. Margot, *Appl. Surf. Sci.*, 1998, **136**, 105–110.
56 T. Y. Leung, W. F. Man, P. K. Lim, W. C. Cnan, F. Gaspari and S. Zukotynski, *J. Non-Cryst. Solids*, 1999, **254**, 156–160.
57 S. Jolley, M. Koppang, T. Jackson and G. M. Swain, *Anal. Chem.*, 1997, **69**, 4099–4107.
58 S. E. Rodil, N. A. Morrison, J. Robertson and W. I. Milne, *Phys. Status Solidi A*, 1999, **174**, 25–37.
59 M. I. Ionescu, Y. Zhang, R. Li, H. Abou-Rachid and X. Sun, *Appl. Surf. Sci.*, 2012, **258**, 4563–4568.
60 P. Szirmai, T. Pichler, O. A. Williams, S. Mandal, C. Bäuerle and F. A. Simon, *Phys. Status Solidi*, 2012, **249**, 2656–2659.
61 E. Bourgeois, E. Bustarret, P. Achatz, F. Omnès and X. Blasé, *Phys. Rev. B: Condens. Matter*, 2006, **74**, 094509.
62 M. Bernard, C. Baron and A. Deneuville, *Diamond Relat. Mater.*, 2004, **13**, 896–899.
63 V. Sidorov and E. Ekimov, *Diamond Relat. Mater.*, 2010, **19**, 351–357.
64 J. P. Goss and P. R. Briddon, *Phys Rev. B: Condens. Matter*, 2006, **73**, 085204.
65 A. C. Ferrari and J. Robertson, *Phys Rev. B: Condens. Matter*, 2001, **63**, 121405.
66 D. W. Morgan and S. G. Weber, *Anal. Chem.*, 1984, **56**, 2560–2567.
67 S. G. Weber and J. T. Long, *Anal. Chem.*, 1988, **60**, A903–A913.
68 J. Xu and G. M. Swain, *Anal. Chem.*, 1998, **70**, 1502–1510.
69 B. Malfoy and J. A. Reynaud, *J. Electroanal. Chem.*, 1980, **114**, 213–223.
70 N. G. Nguyen, M. Z. Wrona and G. Dryhurst, *J. Electroanal. Chem.*, 1986, **199**, 101–126.
71 A. Harriman, *J. Phys. Chem.*, 1987, **91**, 6102–6104.
72 M. Faraggi, M. R. DeFellipis and M. H. Klapper, *J. Am. Chem. Soc.*, 1989, **111**, 5141–5145.
73 M. R. DeFellipis, M. Faraggi and M. H. Klapper, *J. Am. Chem. Soc.*, 1990, **112**, 5640–5642.
74 S. M. MacDonald and S. G. Roscoe, *Electrochim. Acta*, 1997, **42**, 1189–1200.
75 J. S. Foord and A. Chatterjee, *Phys. Status Solidi A*, 2005, **202**, 2110–2115.
76 G.-P. Jin and X.-Q. Lin, *Electrochem. Commun.*, 2004, **6**, 454–460.
77 G. Zhao, Y. Qi and Y. Tian, *Electroanalysis*, 2006, **18**, 830–834.
78 S. Szunerits, Y. Coffinier, E. Galopin and J. Brenner, *Electrochem. Commun.*, 2010, **12**, 438–441.
79 Q. Wang, A. Vasilescu, P. Subramanian, A. Vezeanu, V. Andrei, Y. Coffinier, M. Li, R. Boukherroub and S. Szunerits, *Electrochem. Commun.*, 2013, **35**, 84–87.
80 T. A. Ivandini, B. V. Sarada, C. Terashima, T. N. Rao, D. A. Tryk, H. Ishiguro, Y. Kubota and A. Fujishima, *J. Chromatogr., B: Biomed. Appl.*, 2003, **791**, 63–72.
81 M. Chiku, T. A. Ivandini, A. Kamiya, A. Fujishima and Y. Einaga, *J. Electroanal. Chem.*, 2008, **612**, 201–207.
82 L. Zhang, J. Yang, Y. Luo, J. Shang and X. Jiang, *J. Pharm. Biomed. Anal.*, 2016, **118**, 41–51.

APPENDIX II

Isatin Analysis Using Flow Injection Analysis with Amperometric Detection: Comparison of Tetrahedral Amorphous Carbon and Diamond Electrode Performance

Romana Jarošová, Simon Sanchez, Lars Haubold, and Greg M. Swain

ELECTROANALYSIS

29 (2017) 2147-2154

Full Paper Wiley Online Library ELECTROANALYSIS

DOI: 10.1002/elan.201700272

Isatin Analysis Using Flow Injection Analysis with Amperometric Detection – Comparison of Tetrahedral Amorphous Carbon and Diamond Electrode Performance

Romana Jarošová,[a, d] Simon Sanchez,[b] Lars Haubold,[c] and Greg M. Swain[c, d]

Abstract: Isatin is an endogenous indole compound in humans and rodents that has a wide range of biological activity. In rat models, isatin concentrations have been shown to increase in the heart, brain, blood plasma, and urine with stress. Studies on patients suffering from Parkinson's disease have indicated a correlation between progress of the disease and urinary output of the molecule. Isatin is electrochemically active and can therefore be detected with electrochemical techniques. In this work, we compared the performance of a nitrogen-incorporated tetrahedral amorphous carbon (*ta*-C:N) and a boron-doped nanocrystalline diamond thin-film electrode for the oxidative detection of this biomolecule using flow injection analysis with amperometric detection. The measurements were performed in 0.1 phosphate buffer pH 7.2. The *ta*-C:N electrode, like boron-doped nanocrystalline diamond, exhibits some excellent properties for electroanalytical measurements including (i) low background current and noise, (ii) microstructural stability at positive detection potentials, and (iii) good activity for a wide range of bioanalytes without conventional surface pretreatment. The results reveal that both electrodes exhibit a linear dynamic range from 100 to 0.1 μmol L^{-1}, a short-term response variability 3–4 % RSD (30 injections), a sensitivity of 18 mA M^{-1}, and a limit of detection (S/N = 3) of 1.0×10^{-7} mol L^{-1} (14 ng mL^{-1} or 2.5 fmol).

Keywords: Isatin · boron-doped diamond electrodes · tetrahedral amorphous carbon electrodes · flow injection analysis and amperometric detection

1 Introduction

Indoles are heterocyclic organic compounds that have diverse and wide-ranging biological activity and properties. Some of these properties include anti-inflammatory, antibacterial, anticonvulsant, and antioxidant properties [1,2]. They are made up of a two-ring (bicyclic) structure containing a six-carbon (benzene) ring fused to a five membered nitrogen-containing ring (pyrrole). Isatin (Figure 1 below) is an indole found endogenously in humans and rodents [3–5]. It is a modulator of different biochemical processes and a neurochemical regulator in the brain. Isatin has been detected in blood, urine, and tissue samples in mammals. Highest concentrations in the brain are found in the hippocampus and cerebellum [6]. In the rat, highest concentrations are in the vas deferens and seminal vesicles with levels in the heart somewhat higher than in the brain [6]. Isatin is also shown to have prominent behavioral and metabolic effects. Of these, isatin can act as an inhibitor of monoamine oxidase (MAO) B [5–9]. Monoamine oxidase (MAO) B inhibitors have been used as antidepressants in symptom relief treatment for patients with Parkinson's disease. It can also act as an inhibitor of atrial natriuretic peptide (ANP) receptor binding and ANP-stimulated guanylate cyclase activity [10,11]. Notably, isatin concentrations in urine samples of patients with Parkinson's disease have been shown to increase with the severity of the disease [12,13]. Isatin could also serve as an indicator of stress and anxiety. In rat models, isatin concentrations have been shown to increase with stress in the heart, brain, blood and urine [14,15]. The detection of isatin therefore is potentially important for assessing stress levels in humans and rodents, and diagnosing the progress of maladies like Parkinson's disease.

Isatin is electrochemically active, which means it can be detected voltammetrically or amperometrically. There is limited literature reporting on the electrochemical detection of this biomolecule. One key paper by Diculescu et al. reported on the electrochemistry is isatin using cyclic, square wave, and differential pulse voltammetry with a glassy carbon electrode [16]. Xu et al. reported on HPLC-EC analysis of isatin and other monoamine neurotransmitters [17]. The authors used a palladium hexacyanoferrate-modified glassy carbon electrode for detection.

[a] R. Jarošová
Charles University, Department of Analytical Chemistry, Prague 128 4, Czech Republic
[b] S. Sanchez
Department of Biological Sciences, 1 Camino Santa Maria, St. Mary's University, San Antonio, Texas 78228, United States
[c] L. Haubold, G. M. Swain
Fraunhofer Center for Coatings and Diamond Technologies, 1449 Engineering Research Center, Michigan State University, East Lansing, MI 48823
[d] R. Jarošová, G. M. Swain
Department of Chemistry, 578 S. Shaw Lane, Michigan State University, East Lansing, Michigan 48824-1226, United States

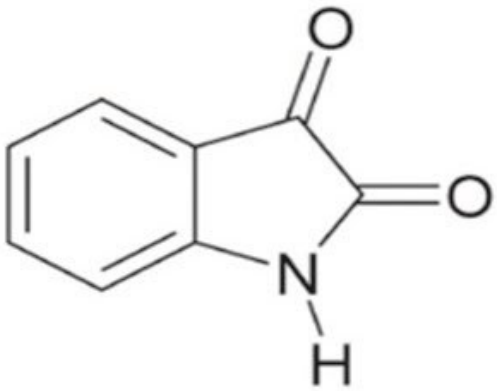

Fig. 1. Chemical structure of isatin.

The analytical method was applied to the measurement of isatin in Parkinsonian rats. A detection limit of 2.5×10^{-8} mol L^{-1} (S/N 3) was found. Baumann et al. used HPLC-ESI-MS to analyze the metabolism of non-labeled and radiolabeled isatin [18]. Electrochemical oxidation was used to predict metabolites found in tissues. There has also been work reporting on the detection of isatin in serum, urine and tissue samples using gas chromatography with mass spectrometry [19,20]. HPLC with UV absorption detection has also been reported for isatin analysis [21]. Sommer et al. developed and applied a fluorescence-based enzymatic assay to quantify isatin in blood samples [22]. The key enzyme is isatin hydrolase. A detection limit of 3×10^{-9} mol L^{-1} (S/N 2) was reported and the method was applied to a 96-well plate format.

Overall there has been limited work using electrochemical detection for the analysis of isatin. Therefore, the objective of the project was to investigate the detection of isatin in standard solutions using flow injection analysis with amperometric detection. Two new carbon electrodes were compared: boron-doped nanocrystalline diamond and nitrogen-incorporated tetrahedral amorphous carbon. These two carbon electrodes exhibit some excellent properties and offer good sensitivity, reproducibility and stability for analytes such as amino acids [23], serotonin [24] and pharmaceuticals [25]. Boron-doped diamond has been used extensively and researched for two decades now, and is well known for its excellent properties such as a low stable background current, a wide working potential window, weak molecular absorption and resistance to electrode fouling, and good microstructural stability during the imposition of high currents and potentials [26–28]. However, this carbon material requires high temperatures for growth (700–800 °C), which limits the types of substrates that can be coated. In contrast, ta-C:N electrodes have many of these properties and can be deposited at or near room temperature (< 100 °C).

2 Experimental Methods

FIA System and Electrochemical Detection Cell. A home-built flow injection analysis (FIA) system was used in the measurements [23–25]. The carrier solution flow was regulated with an Alltech Model 301 HPLC pump (Grace). Samples were manually injected into the carrier solution for transport to the flow cell using a six-port injection valve (Model 7125 (Rheodyne)) with a 25-μL injection loop. A Model LP-21 pulse dampener was placed in series between the pump and the injection valve to reduce pump noise (flow fluctuations). The entire system was electrically grounded and the electrochemical detection cell was housed in a grounded Faraday cage to reduce electrical noise. The home-made, cross-flow electrochemical detection cell was constructed with two pieces of Kel-f [23–25]. The top piece contained the entrance and exit ports for the carrier solution and a port for the no-leak Ag/AgCl mini-reference electrode (ET072-1, eDAQ). The exit port was fitted with a short piece of stainless steel tubing (~6 cm in length) that served as the counter electrode. The bottom piece supported the boron-doped diamond and ta-C:N working electrodes. Electrical contact was made to these electrodes with a thin piece of clean copper foil placed against the backside of the electrode (conducting Si substrate). The backside of the Si substrate was first lightly sanded with fine SiC paper, wiped clean with isopropanol and a cotton swab, and coated with carbon from a graphite pencil prior to making ohmic contact with the copper foil. A 0.1 cm thick neoprene rubber gasket separated the surface of the working electrode from the top piece of the cell. A rectangular groove (1.1 cm × 0.1 cm × 0.1 cm) was manually cut out of the rubber (neoprene) gasket to define the flow channel. Assuming no compression of the gasket when the two pieces of the cell are clamped together, the cell volume is estimated to be ~10 μL. No experiments were performed to actually measure this volume.

Prior to the initial use, the boron-doped diamond or the ta-C:N thin-film electrode surface was cleaned with ultrapure isopropanol (20 min soak) and dried with N_2. The isopropanol was purified by storage over activated carbon for one week followed by distillation. The two pieces of Kel-f and the soft neoprene rubber gasket were also cleaned with the ultrapure isopropanol and dried with N_2. When in use, the working electrode surface was cleaned while mounted in the flow cell by flowing through a small volume of ultrapure isopropanol.

Potentials were controlled and currents measured using a Model 823A electrochemical workstation (CH Instruments, USA). The carrier solution was 0.1 mol L^{-1} phosphate buffer (pH 7.2) prepared with a mixture of 0.2 mol L^{-1} sodium phosphate monobasic (NaH_2PO_4, J.T. Baker) and 0.2 mol L^{-1} sodium phosphate dibasic (Na_2HPO_4, Jade Scientific). A stock solution (0.1 mmol L^{-1}) of isatin (Sigma Aldrich) was prepared by dissolving the exact amount of the analyte in 0.2 mol L^{-1} phosphate buffer pH 7.2. The solutions used for generating the

calibration curves were prepared by serial dilution of the stock solution. All aqueous solutions were prepared using ultrapure water (~18 Mohm-cm) from a Barnstead E-Pure system (distilled, deionized and passed over activated carbon). The stock isatin solution was stored in a glass vessel in the refrigerator when not in use. The electrolyte solution was purged with N_2 for ~15 min prior to a measurement and blanketed with the gas during a measurement to minimize the contribution of dissolved oxygen.

Nitrogen-incorporated tetrahedral amorphous carbon thin-film electrode. The *ta*-C:N film was grown on a boron-doped Si (111) substrate (Virginia Semiconductor, Fredericksburg, VA; $\sim 10^{-3}$ Ω-cm) using a Laser-Arc physical vapor deposition system at the Fraunhofer Center for Coatings and Diamond Technologies (MSU). The method is based on laser-controlled, high-current cathodic vacuum arc deposition [29,30]. In the process, a pulsed-laser beam is rastered across a rotating high-purity graphite target that serves as the cathode. Each laser pulse generates a small localized plasma that delivers free charge carriers for the discharge. The arc discharge lasts only 125 μs before the laser triggers a new, staggered plasma across the graphite cathode. This discharge consists of ionized C atoms and small carbon atom clusters that are accelerated toward the substrate (grounded). This process produces hard (30–60 GPa) and dense *ta*-C films. The substrate-target distance is approximately 30 cm. The conducting Si substrate is rotated during the deposition to promote uniform film deposition. The arc evaporation is associated with the emission of particulates of carbon originating from the graphite drum (*i.e.*, cathode surface) [31]. These particulates can be incorporated into the growing film and will enhance the film roughness. The nitrogen-incorporated film was deposited in the presence of N_2 gas at a flow rate of 30 sccm (*ta*-C:N), a pulse rate of 350 Hz and a peak arc current of 1200 A. Increased levels of added N_2 in the chamber lead to increased nitrogen incorporation into the films and increased electrical conductivity [32–35]. The substrate temperature during the deposition was below 100 °C. This contrasts with the ~800 °C substrate temperature during a typical CVD diamond growth. The film growth rate was approximately 2–3 μm/h. The film used in this work had a nominal thickness in the 200–300 nm range, as determined by a contact profilometer (Dektak), and an electrical resistivity between 0.01–0.04 ohm-cm (room temperature). The film exhibited a Young's modulus (YM) of 270 GPa, which is reflective of an sp^3 carbon content of ~37 %. The sp^3 content generally tracks the YM according to the following relationship, ~% sp^3 = YM/800.

Boron-doped diamond thin-film electrode. The boron-doped nanocrystalline diamond (BDD) thin film was deposited on a boron-doped Si (111) substrate (~10^{-3} ohm-cm) by microwave-assisted chemical vapor deposition (CVD). A 1.5 kW reactor from Seki Technotron was used for the diamond growth. A 1 % CH_4/H_2 source gas was employed with 10 ppm of B_2H_6 added for boron doping. The microwave power was 800 W and the system pressure was 35 torr. The apparent substrate temperature during the deposition was *ca.* 825 °C, as measured with a disappearing filament optical pyrometer. These deposition conditions produced a diamond film that was ~2–4 μm thick with a doping level in the low 10^{21} cm^{-3} range, based on Raman spectroscopic analysis [36–38], and an electrical resistivity of ≤0.01 ohm-cm. At the end of the deposition, the CH_4 and B_2H_6 flows were stopped. The specimen was then cooled in the presence of atomic hydrogen (H_2 plasma) by slowly lowering the power and pressure over a 30-min period to reduce the substrate to an estimated temperature below 400 °C. This post-growth cooling is essential for maintaining a hydrogen surface termination and minimizing surface reconstruction from an sp^3 to sp^2 hybridization. The XPS oxygen-to-carbon atomic ratio after this post-treatment is typically ≤0.03.

3 Results

Cyclic Voltammetry Studies. Figure 2A shows that both the oxidation and reduction peaks increase in magnitude proportionally with the scan rate. Plots of i_p vs. *scan rate*$^{1/2}$ shown in Figure 2B reveal that both redox reactions are diffusion controlled based on the response linearity ($R^2 >$ 0.998). The currents for the oxidation peak at 1.0 V are larger than those for the reduction peak at −0.65 V. This is due to the fact that the oxidation peak is superimposed on a rising background current due to the onset of water oxidation. No background correction was used when measuring the peak magnitude. For a glassy carbon electrode, it has been reported that the oxidation peak current decreases with scan number at a given scan rate, which has been attributed to surface adsorption of isatin oxidation reaction product(s) [16]. For diamond and *ta*-C:N electrodes (latter data not shown), no such peak current decrease was observed so the adsorption of reaction product(s) (*i.e.*, fouling) appears minimal. The electrochemical response of isatin involves the two redox processes at diamond similar to that reported for glassy carbon [16]. The two redox reactions are distinct as isatin can be both oxidized and reduced. The following redox reactions have been reported for glassy carbon and we presume the same reactions are occurring at both diamond and *ta*-C:N [16]:

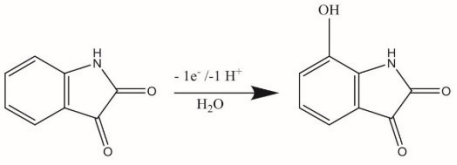

(1)

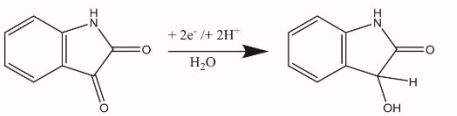

(2)

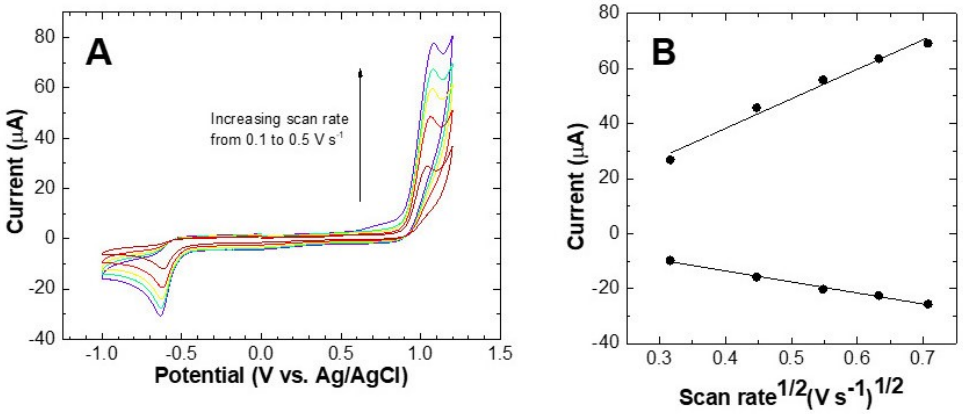

Fig. 2. (A) Cyclic voltammetric *i-E* curves for a boron-doped nanocrystalline diamond thin-film electrode in 0.25 mmol L ^{1} isatin in 0.1 mol L ^{1} phosphate buffer pH 7.2 as a function of scan rate from 0.1 to 0.5 V s ^{1}. (B) Randles-Sevcik plots (i_p vs $v^{1/2}$) generated from cyclic voltammetric *i-E* curves at scan rates from 0.1 to 0.5 V s ^{1} for a positive initial scan polarity from 0 V. Geometric area = 0.2 cm^2.

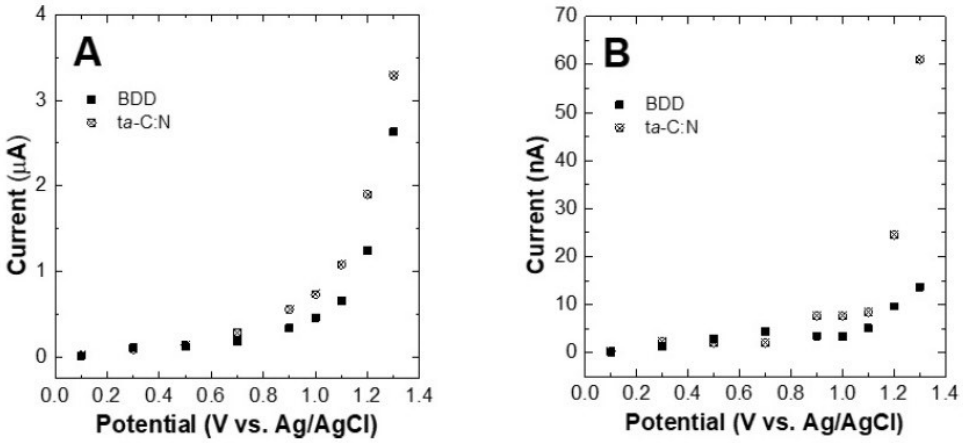

Fig. 3. Plots of the (A) mean background current and (B) noise for boron-doped nanocrystalline diamond (BDD) and ta-C:N thin-film electrodes as a function of the applied potential. Measurements were made in the thin-layer flow cell with 0.1 mol L ^{1} phosphate buffer (pH 7.2). Flow rate = 1 mL min ^{1}.

Flow Injection Analysis Measurements. Figure 3A and B show plots of the mean background current, determined from the last 5 min of a 30-min recording, and the noise (standard deviation about the mean for the 5-min current data) for the nanocrystalline diamond and ta-C:N electrodes as a function of the applied potential from 0.1 to 1.3 V vs Ag/AgCl. These data were obtained in the thin-layer flow cell with a flowing carrier solution of 0.1 mol L^{-1} phosphate buffer, pH 7.2. One of the advantages of both ta-C:N and diamond electrodes for the measurement of analytes that require positive potentials for detection is their microstructural stability [23–25]. Normally, sp^2 carbon electrodes experience oxidation processes at positive potentials that lead to surface roughening and microstructural alterations. These structural changes generally cause increasing and drifting background currents and noise with time. ta-C:N and diamond electrodes are not plagued by these problems [23–25]. Recall that the oxidation potential for isatin in this buffer is −1.0 V. The background currents for both electrodes stabilized quickly after application of the potential. This rapid stabilization time is a characteristic feature of ta-C:N and diamond thin-film electrodes. Data are presented for single electrodes of each type so no statistical analysis was performed. In fact, the behavior of these two electrodes is very consistent with data reported for other ta-C:N and

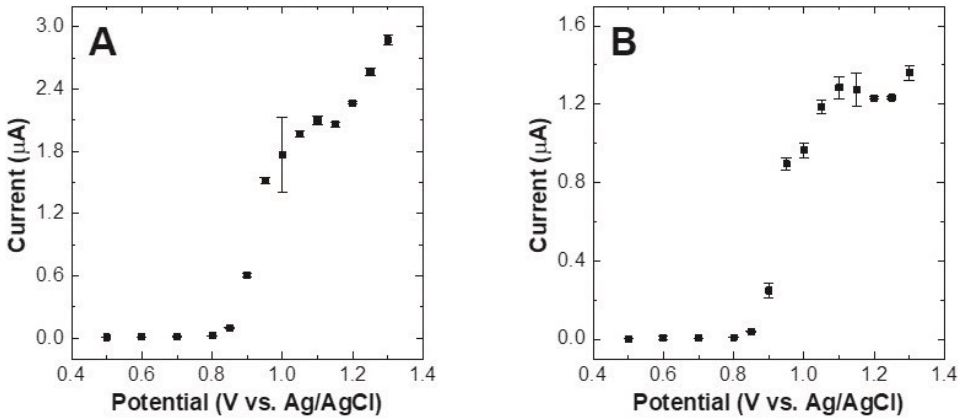

Fig. 4. Hydrodynamic voltammograms for 100 μmol L^{-1} isatin in 0.1 mol L^{-1} phosphate buffer (pH 7.2) at a (A) boron-doped nanocrystalline diamond and (B) *ta*-C:N thin-film electrode. Flow rate – 1 mL min^{-1}. Injection volume – 25 μL. Data are presented as mean ± std.dev. (n – 3 injections at each potential).

diamond thin-film electrodes deposited under identical conditions [23–25]. The magnitude of the background current for both electrodes increases with the potential. At the most positive potentials, the nominal background current for the diamond electrode is slightly lower than that for the *ta*-C:N electrode. The difference in background current between the two electrodes starts at 0.9 V. The noise also increases with the potential. The values (1–4 nA) are similar for both electrodes up to 0.9 V at which potential the values for *ta*-C:N exceed those for diamond. There is a substantial difference at the most positive potentials as the noise at 1.2 V is 2.5 × greater and at 1.4 V is 6× greater for *ta*-C:N. The signal-to-background and signal-to-noise ratios are important in analytical measurements as the smaller these values are, the lower the minimum concentration or mass detectable is.

Figure 4 shows hydrodynamic voltammograms for 100 μmol L^{-1} isatin in 0.1 mol L^{-1} phosphate buffer (pH 7.2) at (A) boron-doped nanocrystalline diamond and (B) *ta*-C:N thin-film electrodes. The flow rate was 1 mL min^{-1} and the injection volume was 25 μL. Isatin is oxidized at a positive potential so good microstructural stability of the two electrodes is imperative for this measurement. A half-wave, $E_{1/2}$, potential of 0.92 V is seen for both electrodes indicating that isatin oxidation occurs with similar kinetics at both electrodes. Steady-state currents are seen between 1.0 to 1.2 V for both electrodes, consistent with the oxidation peak potential in the cyclic voltammetric data (see Figure 2). The steady-state current for the diamond electrode is slightly larger, 2.0 μA, than the value for the *ta*-C:N electrode, 1.3 μA. We believe this disparity in values is likely due to a difference in the channel height of the thin-layer gasket for the two electrodes. The gasket is compressible and its thickness depends on how tight the cell is manually tightened by the user. Therefore, there can be some variability with user. Most often when comparing these two electrode materials in FIA-EC studies; however, similar limiting currents are observed for the same analyte molecule [23–25]. At potentials from 1.0–1.2 V, the oxidation current for isatin is limited by mass transport of the analyte to the electrode surface.

Figure 5 presents short-term reproducibility data for thirty 25-μL injections of 100 μmol L^{-1} isatin in 0.1 mol L^{-1} phosphate buffer (pH 7.2) at the (A) boron-doped nanocrystalline diamond and (B) *ta*-C:N thin-film electrodes. The detection potential for both electrodes was 1.1 V (see Figure 4). Unlike the hydrodynamic voltammetric data in Figure 4, the peak currents are similar for both electrodes in this set of data, consistent with comparable tightness of the flow cell. The results demonstrate that the *ta*-C:N electrode provides as good short-term response reproducibility as does the diamond electrode. The relative standard deviation of the peak height was 3.2 % for diamond and 4.2 % for *ta*-C:N.

Figure 6 shows response curves for the two electrodes to different injected concentrations of isatin. Replicate measurements were made (n = 3) at each concentration. The response curves for both electrodes are essentially the same with good linearity over this narrow range of concentrations. In fact, good linearity was observed for both electrodes over three orders of magnitude (r^2 > 0.990) from 100 to 0.1 μM. The lowest injected concentration that could be detected was 0.1 μmol L^{-1} (S/N > 3). Table 1 summarizes the detection figures of merit for the two electrodes. As can be seen, the detection figures of merit are nearly identical for the two electrode materials.

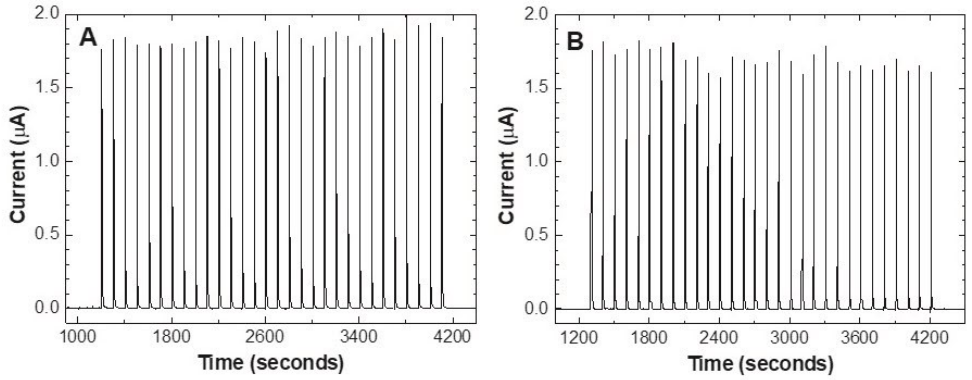

Fig. 5. Repeat injections (30) of 100 μmol L^{-1} isatin in 0.1 mol L^{-1} phosphate buffer (pH 7.2) at a (A) boron-doped nanocrystalline diamond and (B) *ta*-C:N thin-film electrode. Detection potential = 1.1 V. Flow rate = 1 mL min^{-1}. Injection volume = 25 μL.

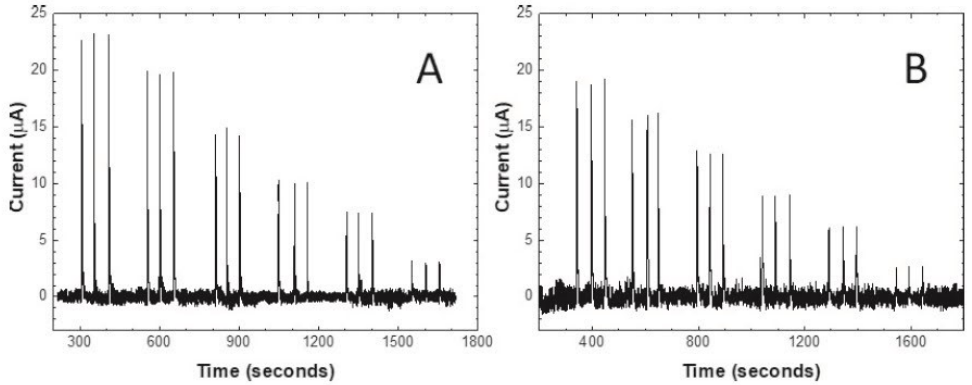

Fig. 6. Injected concentrations of isatin from 1 to 0.1 μmol L^{-1} in 0.1 mol L^{-1} phosphate buffer (pH 7.2) at a (A) boron-doped nanocrystalline diamond and (B) *ta*-C:N thin-film electrode. Three injections of each concentration were made. Flow rate = 1 mL min^{-1}.

Table 1. Detection figures of merit for isatin using a boron-doped nanocrystalline diamond (BDD) and a *ta*-C:N thin-film electrode.

Detection figure of merit	BDD	*ta*-C:N
Sensitivity (mA M^{-1})	19.7	18.1
Linear dynamic range (μmol L^{-1})	100-0.1	100-0.1
Response variability (RSD, %)	3.2	4.2
Limit of detection (S/N = 3) (mol L^{-1})	1.0×10^{-7}	1.0×10^{-7}
Limit of detection (S/N = 3) (ng mL^{-1})	14	14
Limit of detection (S/N = 3) (fmol)	2.5	2.5

4 Discussion

One goal of this work was to evaluate the properties of nitrogen-incorporated tetrahedral amorphous carbon electrodes, specifically ones grown with 30 sccm N_2 in the source gas, and to compare these properties with those of the more well-studied boron-doped nanocrystalline diamond. Recall prior work revealed that some of the basic electrochemical properties of these two electrodes are very similar including (i) low and stable background current, (ii) good activity for redox systems without time-consuming conventional surface pretreatment, (iii) weak molecular adsorption and (iv) microstructural stability at positive potentials [26–28]. A major advantage of the *ta*-C:N electrode is the fact that it can be deposited at or near room temperature as compared to diamond, which is typically deposited at 700–800 °C. The lower temperature makes possible the deposition of this material on a wide variety of substrates, such as flexible polymers.

Even though the *ta*-C:N electrode consists of a mixed sp^2–sp^3 bonded carbon microstructure, the electrochemical properties more resemble those of diamond rather than glassy carbon [23–25, 39–41]. The surface chemistry of the *ta*-C:N electrode grown with 30 sccm N_2 consists of some surface oxygen and nitrogen. XPS survey scans of the elemental composition in the top 10 nm or so reveal an

atomic oxygen-to-carbon ratio in the 0.10–0.16 range and a nitrogen-to-carbon ratio of ~0.09. The surface nitrogen concentration is slightly higher than the concentration in the bulk as XPS depth profiles reveal a uniform nitrogen concentration with depth of ~6 at. % for a film grown with 30 sccm N_2 in the source gas. This corresponds to a nitrogen concentration of 60,000 ppm or $\sim 3 \times 10^{21}$ cm $^{-3}$. Oxygen is only present in the near-surface region. Careful examination of the line shapes of the C1s and N1s peaks reveals that for the latter, the chemical environment around the nitrogen is uniform with depth. In contrast, there is more sp^2 carbon at the surface than in the bulk based on slight changes in the C1s peak shape with depth, specifically the intensity at 284.4 eV (sp^2 graphite) and 285.1 eV (sp^3 diamond) [42,43]. In the surface region, the ratio of sp^3 to sp^2 bonded carbon is *ca.* 30 %. In the bulk, the ratio is greater closer to 40 %. This is based on the measured Young's modulus (YM) of 270 GPa for the film used in this work, which is indicative of an sp^3 carbon content of ~37 %. The sp^3 content generally tracks the YM according to the following relationship, ~% sp^3 = YM/800. The sp^2-bonded carbon content increases with increasing nitrogen incorporation with the electrical conductivity following the same trend [32–35,39]. Deconvolution of the N1s peak from the near-surface region and the bulk suggests nitrogen in three different chemical states: (i) 398.6 eV (39%) pyridinic-O, (ii) 399.9 eV (53 %) pyrrolic and (iii) 401.4 eV (8 %) quarternary N within an extended aromatic structure [44].

The FIA-EC data presented herein for isatin, and prior data such as for tryptophan and tyrosine and other analytes [23–25], all reveal that the t*a*-C:N electrode compares quite favorably with the nanocrystalline diamond electrode in terms of the detection figures of merit they provide for analytes that require positive potentials for detection. At these positive potentials, good microstructural stability is a must as surface oxidation, microstructural alterations and carbon corrosion would all lead to increasing background current and noise during the measurement. Both t*a*-C:N and nanocrystalline diamond exhibit excellent microstructural stability at these detection potentials.

A second goal of this work was the initial testing of a simple, sensitive and reproducible measurement assay for isatin. Ultimately, the goal is to use the assay to measure isatin in biological fluids and tissues. The initial results reported herein suggest that an electrochemical-based assay using t*a*-C:N or diamond electrodes affords simplicity, sensitivity and reproducibility for the detection of isatin at physiologically-relevant concentrations. Cyclic voltammetric results indicated that the molecule can be oxidized at ca. 1.0 V or reduced at −0.7 V via diffusion-controlled reactions on both diamond and t*a*-C:N electrodes. There is no evidence of adsorption on either electrode or any electrode fouling over time. The oxidation and reduction potentials are essentially the same for both electrodes indicating that both possess equivalent activity. By comparison, one report showed an oxidation potential of 1.0 V and a less negative reduction potential at −0.5 V for isatin at glassy carbon in a similar pH 7 electrolyte [16]. In another paper, it was reported that oxidation of isatin at glassy carbon occurs more positive than 1.2 V in a neutral electrolyte with no well resolved peak [17].

The FIA results presented herein demonstrate that the t*a*-C:N electrode performs as well as the diamond electrode for the detection of isatin in terms of sensitivity, reproducibility, linear dynamic range and limit of detection. Both electrodes have background currents that stabilize quickly at the positive detection potential after detector turn on. The background current and noise μexceed those for diamond. Well defined hydrodynamic voltammograms are observed with limiting currents for isatin oxidation at 1.0–1.2 V for both electrodes. The short-term response reproducibility is excellent for both electrodes over 30 injections with variabilities of less than 5 % RSD. Importantly, the detection figures of merit are obtainable without conventional pretreatment as no polishing or anodic/cathodic polarization is required for optimum electrode performance. The linear dynamic range is from 100 to 0.1 μmol L $^{-1}$ ($R^2 > 0.998$) and the experimentally-determined limit of detection for both electrodes is 0.10 μmol L $^{-1}$ (2.5 fmol or 14 ng mL $^{-1}$) at a signal-to-noise ratio of 3. The linear dynamic range of 0.1 to 100 μmol L $^{-1}$ covers the physiological relevant concentration range in tissues and body fluids of 0.1 to 10 μmol L $^{-1}$. While the current detection figures of merit are adequate for measuring physiological levels of isatin, improvements can be achieved by reducing the volume in the detector cell. Future work will involve testing a new flow cell design and combining electrochemical detection with HPLC for use in the analysis of isatin in biological fluids and tissues.

5 Conclusions

The analytical performance of a t*a*-C:N and a boron-doped nanocrystalline diamond thin-film electrode was compared for the detection of isatin using flow injection analysis with amperometric detection. The following are the key findings from the work:

1. Both electrodes exhibit a diffusion-controlled oxidation peak for isatin at 1.0 V and a diffusion-controlled reduction peak at −0.7 V in 0.1 mol L $^{-1}$ phosphate buffer pH 7.2. No evidence for electrode fouling was observed.
2. The background current and noise for both electrodes up to *ca.* 0.9 V are comparable. At more positive potentials, the background current and noise are slightly greater for t*a*-C:N.
3. Both electrodes exhibit similar hydrodynamic voltammetric *i-E* curves with an $E_{1/2}$ of 0.92 V and a limiting current from 1.0–1.2 V.
4. Both electrodes exhibit excellent short-term response reproducibility with variabilities less than 5 % RSD over 30 consecutive injections (100 μmol L $^{-1}$).

5. The linear dynamic range for both electrodes is 100 to 0.1 μmol L^{-1} ($R^2 > 0.998$) and the limit of detection (S/N = 3) is similar at 0.10 μmol L^{-1} (2.5 fmol or 14 ng mL^{-1}). This dynamic range and limit of detection is adequate for typical levels of isatin found in biological fluids.

Acknowledgements

This research was carried out in the framework of project W911NF-12-R-0011 funded by the Army Research Office (G.M.S.) (Dr. Robert A. Mantz, Program Manager). We acknowledge Michal Sobaszek (University of Gdansk) for his isatin voltammetric measurements on optically transparent diamond electrodes. R.J. thanks the Grant Agency of the Czech Republic (Project P206/12/G151) and Charles University in Prague (SVV260440) for their financial support. S.S. acknowledges financial support through the *Bridge to the PhD in Neuroscience* program at Michigan State University under the auspices of the NIH NINDS ENDURE Program (R25 NS090989) (Prof. William Atchison, Program Director).

References

[1] V. Sharma, P. Kumar, D. Pathak, *J. Heterocyclic Chem.* **2010**, *47*, 491-502.
[2] S. Biswal, U. Sahoo, S. Sethy, H.K.S Kumar, M. Banerjee, *Asian J. Pharm. Clin. Res.* **2012**, *5*, 1-6.
[3] P. A. Maroñas, R. T. Sudo, M. B. Corrêa, A. C. Pinto, S. J. Garden, M. N. Trachez, G. Zapata-Sudo, *Clin. Exp. Pharmacol. Physiol.* **2008**, *35*, 1091-1096.
[4] P. Pakravan, S. Kashanian, M.M. Khodaei, F. J. Harding, *Pharmacol. Rep.* **2013**, *65*, 313-35.
[5] Justo LA, Durán R, Alfonso M, Fajardo D, Faro LR. , *Neurochem. Int.* **2016**, *99*, 147-57.
[6] A. Medvedev, O. Buneeva, V. Glover, *Biol.: Targets Ther.* **2001**, *1*, 151-162.
[7] P. Watkins, A. Clow, V. Glover, J. Halket, A. Przyborowska, M. Sandler, *Neurochem. Int.* **1990**, *17*, 321–323.
[8] S. Carradori, R. Silvestri, New Frontiers in Selective Human MAO-B Inhibitors . *J. Med. Chem.* **2015**, *58*, 6717–6732.
[9] P. Phogat, P. Singh, A Mini Review on Central Nervous System Potential of Isatin Derivatives. *Cent. Nerv. Syst. Agents Med. Chem.* **2015**, *15*, 28–31.
[10] A. E. Medvedev, M. Sandler, V. Glover, *Life Sci.* **1998**, *62*, 2391–2398.
[11] A. E. Medvedev, A. Clow, M. Sandler, V. Glover, *Biochem. Pharmacol.* **1996**, *52*, 385–391.
[12] Y. Zhou, Z. Zhao, J. Xie, *Brain Res.* **2001**, *917*, 127–132.
[13] N. Hamaue, N. Yamazaki, M. Terado, M. Minami, K. Ohno, H. Ide, A. Ogata, S. Honma, K. Tashiro, *Res. Commun. Mol. Pathol. Pharmacol.* **2000**, *108*, 63–73.
[14] A. Medvedev, N. Igosheva, M. Crumeyrolle-Arias, V. Glover, *Stress* **2005**, *8*, 175-183.
[15] N. Igosheva, C. Lorz, E. O'Conner, V. Glover and H. Mehmet, *Physiol. Behav.* **2004**, *80*, 665–668.
[16] V. C. Diculescu, S. Kumbhat, A. M. Oliveira-Brett, *Anal. Chim Acta* **2006**, *575*, 190–197.
[17] H. Xu, D. Wang, W. Zhang, W. Zhu, K. Yamamoto, L. Jin, *Anal. Chim. Acta* **2006**, *577*, 207–213.
[18] A. Baumann, A. Faust, M. P. Law, M. T. Kuhlmann, K. Kopka, M. Schafers, U. Karst, *Anal. Chem.* **2011**, *83*, 5415–5421.
[19] M. Unger, W. Jacobsen, U. Holzgrabe, L. Z. Benet, *J Chromatogr B Analyt Technol Biomed Life Sci.* **2002**, *767*, 245–253.
[20] P. Zou, H. L. Koh, *Rapid Commun. Mass. Spectrom.* **2007**, *21*, 1239–1246.
[21] S. Manabe, Q. Gao, J. Yuan, T. Takahashi, A. Ueki, *J. Chromatogr. B*, **1997**, *691*, 197–202.
[22] T. Sommer, K. Bjerregaard-Andersen, S. M. Simensen, J. K. Jensen, B. Jochimsen, P. J. Riss, M. Etzerodt, J. Preben Morth, *ACS Chem. Neurosci* **2015**, *6*, 1353–1360.
[23] R. Jarošová, J. Rutherford, G. M. Swain, *Analyst* **2016**, *141*, 6031–6041.
[24] D. Hamblin, J. Qiu, L. Haubold, G. M. Swain, *Anal. Meth.* **2015**, *7*, 4481–4485.
[25] B. C. Lourencao, T. A. Silva, O. Fatibello-Filho, G. M. Swain, *Electrochim. Acta* **2014**, *143*, 398–406.
[26] N. Yang, G. M. Swain, X. Jiang, *Electroanal.* **2016**, *28*, 27–34.
[27] J. V. Macpherson, *Phys. Chem. Chem. Phys.* **2015**, *17*, 2935–2949.
[28] M. C. Granger, M. Witek, J.S. Xu, J. Wang, M. Hupert, A. Hanks, M. D. Koppang, J. E. Butler, G. Lucazeau, M. Mermoux, J. W. Strojek, G. M. Swain, *Anal. Chem.* **2000**, *72*, 3793–3804.
[29] H. J. Scheibe, D. Drescher, B. Schultrich, M. Falz, G. Leonhardt, R. Wilberg, *Surf. Coat. Technol.* **1996**, *85*, 209–214.
[30] H. J. Scheibe, B. Schultrich, D. Drescher, *Surf. Coat. Technol.* **1995**, *74–75*, 813–818.
[31] D. Drescher, J. Koskinen, H.-J. Scheibe, A. Mensch, *Diamond. Relat. Mater.* **1998**, *7*, 1375–1380.
[32] S. Waidmann, M. Knupfer, J. Fink, B. Kleinsorge, J. Robertson, *J. Appl. Phys.* **2001**, *89*, 3783–3792.
[33] B. Kleinsorge, A. C. Ferrari, J. Robertson, W. I. Milne, *J. Appl. Phys.* **2000**, *88*, 1149–1157.
[34] S. E. Rodil, N. A. Morrison, J. Robertson, W. I Milne, *Phys. Stat. Sol. A* **1999**, *174*, 25–37.
[35] P. Stumm, D. A. Drabold, P. A. Fedders, *J. Appl. Phys.* **1997**, *81*, 1289–1295.
[36] V. Mortet, Z. Vlčková Živcová, A. Taylor, O. Frank, P. Hubík, D. Trémouilles, F. Jomard, J. Barjon, L. Kavan, *Carbon* **2017**, *115*, 279–284.
[37] A. Deneuville, C. Baron, S. Ghodbane and C. Agnès, *Diamond Relat. Mater.* **2007**, *16*, 915–920.
[38] P. Gonon, E. Gheeraert, A. Deneuville, F. Fontaine, *J. Appl. Phys.*, **1995**, *78*, 705–7062.
[39] X. Yang, L. Haubold, G. DeVivo and G. M. Swain, *Anal. Chem.* **2012**, *84*, 6240–6248.
[40] R. Jarošová, P. M. De Sousa Bezerra, C. Munson, G. M. Swain, *Phys. Status Solidi A*, **2016**, *213*, 2087–2098.
[41] N. C. Yee, Q. F. Shi, W. D. Cai, D. A. Scherson, B. Miller, *Electrochem. Solid-State Lett.* **2001**, *4*, E42–44.
[42] P. Mérel, M. Tabbal, M. Chaker, S. Moisa, J. Margot, *Appl. Surf. Sci.* **1998**, *136*, 105–110.
[43] T. Y. Leung, W. F. Man, P. K. Lim, W. C. Cnan, F. Gaspari, S. Zukotynski, *J. Non-Crystal. Solids* **1999**, *254*, 156–160.
[44] T. M. Byrne, X. Gu, P. Hou, F. S. Cannon, N. R. Brown, C. Nieto-Delgado, *Carbon* **2014**, *73*, 1–12

Received: May 11, 2017
Accepted: May 29, 2017
Published online on June 13, 2017

APPENDIX III

Detection of Pyocyanin with a Boron-Doped Diamond Electrode Using Flow Injection Analysis with Amperometric Detection and Square Wave Voltammetry

Romana Jarosova, Kallyni Irikura, Romeu Rocha-Filho, and Greg M. Swain

ELECTROANALYSIS

34 (2021) 1-12

Research Article Wiley Online Library ELECTROANALYSIS

doi.org/10.1002/elan.202100562

Detection of Pyocyanin with a Boron-doped Diamond Electrode Using Flow Injection Analysis with Amperometric Detection and Square Wave Voltammetry

Romana Jarosova,*[a, c] Kallyni Irikura,[b, c] Romeu C. Rocha-Filho,[b] and Greg M. Swain*[c]

Abstract: We report on the analytical performance of boron-doped diamond thin-film electrodes for the detection of the virulence factor, pyocyanin (PYO). The results reported herein confirm the utility of diamond electrodes for the sensitive and reproducible detection of pyocyanin in a 0.1 mol L^{-1} phosphate buffer (pH 7.4) when using amperometric detection coupled with flow injection analysis (FIA) or square wave voltammetry (SWV). Pyocyanin was reductively detected by hydrodynamic voltammetry in FIA at an $E_{1/2}$ of −0.31 V vs. Ag/AgCl (3 mol L^{-1} KCl). The detection figures of merit were a linear dynamic range from 100 to 0.08 μmol L^{-1}, a response reproducibility of 1.3 % (RSD), and a limit of detection of 0.09 μmol L^{-1} (S/N = 3). A comparable linear dynamic range, response reproducibility and limit of detection were observed in preliminary square wave voltammetry measurements. Importantly, these detection figures of merit were obtained using boron-doped diamond electrodes that received no conventional pretreatment. Some comparison data are presented for nitrogen-incorporated tetrahedral amorphous carbon (*ta*-C:N) and glassy carbon (GC) electrodes.

Keywords: pyocyanin detection · diamond electrodes · *ta*-C:N electrodes · flow injection analysis

1 Introduction

Carbon materials (sp^2 bonded) have served as important electrodes in fundamental and applied electrochemistry for over 50 years [1–9]. Over the years, a variety of carbon materials have been employed in electroanalytical measurements, including highly oriented pyrolytic graphite, glassy carbon, carbon fibers, carbon nanotubes and graphene. All these materials are sp^2 hybridized with both σ and π-bonded carbon atoms. Capacitance, molecular adsorption, and electron-transfer kinetics of these carbons are largely controlled by the exposed surface microstructure (*i. e.*, graphitic edge plane) and surface chemistry (*i. e.*, carbon-oxygen functional groups) [1–9]. Sp^2 carbon materials with a high fraction of exposed clean graphitic edge plane generally exhibit the most rapid electron-transfer kinetics for soluble redox systems [1–9]. In other words, the active site on these electrodes (highest capacitance – C_{dl}, strongest adsorption and highest molecular coverage – Γ, and largest heterogeneous electron-transfer rate constant – k^o) is generally the exposed edge plane. Recent work, however, has shown that fast outer-sphere electron-transfer kinetics for ferrocene derivatives ($k^o > 10$ cm/s) can be observed on carbon surfaces prepared under ultraclean conditions [10–12]. Additionally, recent work has provided evidence for larger than expected heterogeneous electron-transfer rate constants on low-defect HOPG [13–15]. Carbon electrodes generally exhibit a wider potential window compared with metal electrodes, like Au and Pt. Carbon electrodes are chemically stable, highly conductive, and low in cost [1, 16].

This author's (GMS) indoctrination to carbon electrodes occurred in the period from 1984–87 during undergraduate research work with Professor Wayne Britton. It was during this time that this author learned about the importance of carbon electrode surface activation for achieving high rates of electron transfer with soluble redox systems, and about controlled surface modification and its impact on electron transfer. Specifically, the research involved covalently attaching ferrocenemethylamine molecules to an oxidized glassy carbon surface. The linkage was through amide bond formation and the goal was to use this modified electrode as a pH sensor based on the shift of the half-wave potential for ferrocene oxidation as a function of the hydrogen ion concentration in solution. It was during this time, as well, that this author became familiar with the carbon electrode research being conducted in the laboratory of Professor Ted Kuwana, and ultimately decided to conduct graduate studies with TK at the University of Kansas.

[a] R. Jarosova
Department of Analytical Chemistry, UNESCO Laboratory of Environmental Electrochemistry, Charles University, 12843 Prague 2, Czech Republic
E-mail: jarosora@ucmail.uc.edu
[b] K. Irikura, R. C. Rocha-Filho
Department of Chemistry, Universidade Federal de São Carlos (UFSCar), C.P. 676, 13560-970 São Carlos, SP, Brazil
[c] R. Jarosova, K. Irikura, Dr. G. M. Swain
Department of Chemistry, Michigan State University, 48824-1322 East Lansing, MI, United States
E-mail: swain@chemistry.msu.edu

The idea for using diamond as an analytical electrode came to this author as a graduate student in the Kuwana group in about 1989. There was a nice article published in Chemical and Engineering News by Peter Bachmann and Russell Messier on the emerging technology of CVD diamond [17]. At the time, there did not appear to be much published in the scientific literature on conducting (*i.e.*, boron-doped) diamond. Impurity-free diamond is one of Mother Nature's best electrical insulators. Additionally, some very interesting work from the Kodak company in the form of a patent emerged around this time that further spawned interest in diamond electrodes [18,19]. Researchers at the company reported on the effective electrochemical degradation of phenolic waste from the film making process using diamond anodes [18,19]. A fortuitous meeting between this author and Dr. Rajeshuni Ramesham in the Department of Electrical Engineering at Auburn University in 1991 lead to the first boron-doped diamond films being prepared and used in electroanalytical measurements [20]. Since those early days, and in particular over the past 20 years, electrochemical studies of boron-doped diamond (BDD) electrodes have become commonplace [21–40]. This is because of the electrode's excellent properties and the fact that the materials have become commercially available from multiple vendors.

In electroanalytical measurements, BDD electrodes generally provide significant improvements over conventional sp^2 carbon electrodes (*e.g.*, glassy carbon) in terms of linear dynamic range, limits of detection, response precision, and response stability [21–26,40]. BDD exhibits an extremely wide potential window due to its stability and lower background current and noise than other electrodes [21–26,40]. This gives the material an inherent signal-to-background and signal-to-noise ratio advantage, as compared to conventional sp^2 carbon electrodes. Other properties include (i) microstructural stability at high potentials, (ii) relatively rapid electron-transfer kinetics without conventional pretreatment, (iii) low capacitance, (iv) weak molecular adsorption, and (v) optical transparency in the near-UV/Vis and mid to far IR regions of the electromagnetic spectrum. BDD electrodes are quite useful for detecting various species including heavy metal ions [41,42], chlorinated phenols [43,44], histamine and serotonin [45,46], redox proteins [47,48], and bisphenols [49,50]. In fact, BDD electrodes have been successfully used for the determination of a large number of organic compounds and biomolecules [40,51], in many instances after an electrochemical pretreatment of the electrode [52] or using flow-based systems [53]. A limitation of diamond materials, however, is the high temperature (600–800 °C) needed for their deposition that limits the substrate materials to thermally stable Si, Ti, W, and quartz.

The work reported on herein focused on the detection of pyocyanin (PYO) in a standard buffer solution using boron-doped nanocrystalline diamond electrodes combined with flow injection analysis (FIA) and amperometric detection. The molecular structure and redox reaction of PYO (5-methylphenazin-1-one) is shown in Figure 1.

PYO is a virulence factor solely produced by the pathogenic bacterium *Pseudomonas aeruginosa* (PA). PYO is redox-active toxin that can be directly detected by electrochemical sensing. It can be reduced via a $2H^+/2e^-$ reversible redox reaction as shown in Figure 1 [54–57]. Polymerization of PYO is avoided by limiting the positive-going scan in voltametric measurements to 0.2 V vs. Ag/AgCl, as was the case for the work reported on herein [54].

There has been literature published over the past decade or so on the electrochemical detection of PYO either as an indicator of the presence of PA in samples or as a tool for quantifying its virulence, as reviewed by Alatraktchi et al. [57] who provided an overview of the advances in the electrochemical detection of PYO. The same group reported on the electrochemical detection of PYO in standard solutions and artificial sputum [58] and in sputum specimens collected from cystic fibrosis patients [59], with detection limits in the range of 100–200 nmol L^{-1}. Elkhawaga et al. [60] reported on the application of an ITO electrode decorated with polyaniline/gold nanoparticles for rapid and sensitive PYO detection in supernatants of PA cultures with and without different electrochemically active interferents, including vitamin C, uric acid, and glucose. The Goluch group has been active and somewhat pioneering reporting on the electrochemical sensing of PYO in clinical isolates [61], human fluids [62], and wound exudates [63]. Additionally, the Stevenson group has reported on the application of ultrathin transparent carbon electrodes for the detection of PYO [54], PYO and phenazine metabolites in supernatants from different PA strains [64], and PYO in a

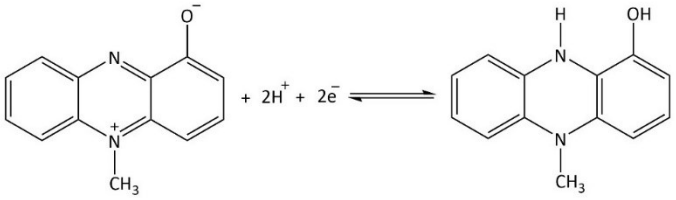

Fig. 1. The molecular structure and redox reaction mechanism of pyocyanin (PYO) (5-methylphenazin-1-one).

wound fluid simulant to demonstrate the performance of the electrodes on a flexible sensing platform [65]. Others have reported on the electrochemical detection of PYO using carbon fiber and glassy carbon electrodes [55,56].

BDD electrodes have been used in a limited manner for the detection of PYO in standard and clinically relevant samples so far. For example, Buzid et al. [66] described the rapid and sensitive detection of PYO in PA culture supernatants using differential pulse voltammetry (DPV) at a BDD electrode. Buzid et al. [67] also reported the use of differential pulse voltammetry and a BDD electrode for the simultaneous detection of 2-heptyl-3-hydroxy-4-quinolone (PQS), 2-heptyl-4-hydroxyquinoline (HHQ) and PYO. PQS and its precursor HHQ are two important signal molecules produced by PA, while PYO is a toxin involved in virulence and pathogenesis. For PYO, a linear dynamic range of 2–100 $\mu mol\,L^{-1}$ and a limit of detection of 50 $nmol\,L^{-1}$ were reported. Previously, Zhou et al. [68] described the use of coated capillary zone electrophoresis and amperometric detection with a BDD electrode for the analysis of chemically synthesized HHQ, PQS, and 2-methyl analogues.

Herein, we present results demonstrating that boron-doped nanocrystalline diamond electrodes can be used to measure PYO in a standard buffer solution (pH 7.4), detected at negative potentials as a reduction current, from 100 to 0.08 $\mu mol\,L^{-1}$ ($R^2 > 0.998$), with a sensitivity of $11.6 \pm 0.2\ mA\,L\,mol^{-1}$, response reproducibility $< 2\%$ RSD, and a limit of detection (signal-to-noise = 3) of 0.09 $\mu mol\,L^{-1}$. Additionally, the BDD electrodes provide a low background current and noise, a rapidly stabilizing background current after detection potential turn-on, and proved to be relatively insensitive to the presence of dissolved oxygen. Some limited comparison data for nitrogen-incorporated tetrahedral amorphous carbon (*ta*-C:N) and glassy carbon (GC) electrodes are also presented. This work is important for the field of electroanalytical chemistry because it shows the excellent qualities of diamond electrodes, without any conventional pretreatment, for the rapid and reproducible detection of PYO by flow injection analysis.

2 Experimental

Chemicals. The stock solution of PYO (CAS No. 85–66-5, ≥ 98 %, Sigma-Aldrich, USA) was prepared by dissolving the exact amount of the analyte in a 0.1 $mol\,L^{-1}$ phosphate buffer pH 7.4. The solutions used for generating the calibration curves were prepared by serial dilution of this stock solution. The phosphate buffer was prepared with 0.1 $mol\,L^{-1}$ Na_2HPO_4 and 0.1 $mol\,L^{-1}$ NaH_2PO_4. Both salts were high purity (> 98 % pure, Sigma-Aldrich, USA). Solution pH adjustments were made with HCl or NaOH solutions, as required. All aqueous solutions were prepared using ultrapure water (~ 18 MΩ cm) from a MilliQ plus system (Millipore, USA). All the solutions were stored in glass vessels and refrigerated at ~ 5 °C when not in use.

Electrochemical Measurements. For all the square-wave voltammetric measurements, a model 650B electrochemical workstation (CH Instruments, Austin, Texas) was used. A single-compartment, glass electrochemical cell was used in a three-electrode measurement configuration consisting of a BDD thin-film working electrode mounted in the bottom of the cell, a carbon rod counter electrode, and a commercial Ag/AgCl (3 $mol\,L^{-1}$ KCl) reference electrode. All potentials are reported versus this reference. The working electrode area of 0.2 cm^2 was defined by a Viton *o*-ring. The square-wave voltametric measurement parameters were as follows: step potential = 1 mV, pulse amplitude = 25 mV, and frequency = 15 Hz.

Flow Injection Analysis System. For the FIA system, an Alltech HPLC pump (model 301, Grace) was used in series with a six-port injection valve (model 7125, Rheodyne) fitted with a 25 µL injection loop. The amperometric detector was a crossflow design, as described previously [69,70]. The flow cell was constructed with a two-piece Kel-F body. The entrance and exit ports were incorporated into the top piece, along with a port for a no-leak Ag/AgCl (3 $mol\,L^{-1}$ KCl) electrode. The counter electrode was a stainless-steel tube that served as the exit port. The bottom part of the cell provided the physical support for the rubber gasket defining the volume of the flow channel (1.05 cm long × 0.1 cm wide × 0.1 cm thick), and importantly a support for the BDD working electrode. Electrical contact was made by pressing a piece of clean copper foil against the back side of the cleaned, conducting Si substrate of the BDD thin-film electrode. A model 832 A electrochemical workstation (CH Instruments) was used for potential control and current measurement. Upon tightening the flow cell, a gasket compression of *ca.* 50 % occurs. This yields a channel height and cell volume on the order of 500 µm and 10 µL, respectively. This type of compressible gasket is needed with the polycrystalline diamond films in order to produce a tight seal.

All electrochemical measurements were performed in an electrically grounded Faraday cage to reduce any extraneous electrical noise pickup. All measurements were repeated at least in triplicate, if not mentioned otherwise. Calibration curves were measured in triplicate and analyzed using linear regression analysis. All electrochemical measurements were carried out at 25 °C.

Boron-Doped Diamond Electrodes. The boron-doped nanocrystalline diamond (BDD) thin-film (GMS040716 and GMS041416) electrodes were deposited on a boron-doped Si (111) substrate (~ 10^{-3} Ω cm) by microwave-assisted chemical vapor deposition. A 1.5 kW reactor from Seki Technotron was used for the diamond growth. A 1 % (v/v) CH_4/H_2 source gas was used with 10 ppm of B_2H_6 added for boron doping. The microwave power was 800 W, and the system pressure was 35 Torr. These conditions produced a diamond film that was ~ 2–3 µm thick with a doping level in the low 10^{21} cm^{-3} range, based on Raman spectroscopic analysis [71–73], and an electrical resistivity of ~ 0.01 Ω cm. At the end of the deposition, the

CH_4 and B_2H_6 flows were stopped. The specimen was then cooled in the presence of atomic hydrogen (the plasma remained ignited with only H_2) by slowly lowering the power and pressure over a 30 min period to reduce the substrate temperature to the 400 °C range. This post-growth cooling is essential for maintaining a hydrogen surface termination and prohibiting surface reconstruction from sp^3 to sp^2 hybridization.

As a final cleaning step, all electrodes were pretreated by a daily 20 min immersion in ultrapure isopropanol [74]. The isopropanol was purified by distillation, and stored over activated carbon. This ultraclean solvent cleans the surface and activates the electrode by dissolving adventitious contaminants.

Glassy Carbon Electrode. The glassy carbon (GC) working electrode (GC-20, Tokai Ltd.) was pretreated prior to use by a three-step protocol. This involved polishing with successively smaller grades of alumina powder (1.0, 0.3 and 0.05 μm diameter). The powder was slurried with ultrapure water, and the polishing was performed by hand on separate felt polishing pads. After each polishing step, the electrode was rinsed copiously with ultrapure water and then ultrasonically cleaned for ~20 min in ultrapure water to remove polishing debris.

Nitrogen-Incorporated Tetrahedral Amorphous Carbon Electrode. The *ta*-C:N film was grown on a boron-doped Si (111) substrate (Virginia Semiconductor, Fredericksburg, VA; ~10^{-3} Ω cm) using a Laser-Arc physical vapor deposition system at the Fraunhofer Center for Coatings and Diamond Technologies, Michigan State University. The technology is based on laser-controlled, high-current cathodic vacuum arc deposition [75,76]. In the process, a pulsed-laser beam is rastered across a rotating high purity graphite target that is biased negatively as the cathode. Each laser pulse generates a small, localized plasma that delivers free charge carriers for the arc discharge. The arc discharge lasts a brief period (μs–ms) before the laser triggers a new, staggered plasma across the graphite cathode. This deposition method produces highly ionized C atoms and carbon atom clusters that are accelerated toward the substrate (grounded anode). This process produces hard (30–60 GPa) and dense *ta*:C films. The substrate-target distance was approximately 30 cm. The arc evaporation is associated with the emission of macro particles of carbon originating from the cathode surface [77]. The particles are incorporated into the growing film, and enhance the surface roughness. The nitrogen-incorporated films were deposited in the presence of N_2 gas at a flow rate of 30 sccm (*ta*-C:N) with a pulse rate of 350 Hz (~3 ms) and a peak arc current of 1200 A. The substrate temperature during the deposition was below 100 °C. This contrasts with the 700–800 °C substrate temperature during typical CVD diamond growth. The film growth rate was approximately 2–3 μm h^{-1}. The film (ML15122201) tested electrochemically had a nominal thickness of *ca.* 200 nm, as determined by a Dektak profilometer, with an electrical resistivity between 0.01–0.04 Ω cm (room temperature). The film had a Young's modulus (YM) of 270 GPa, which is reflective of a sp^3 carbon content of ~37 %. The sp^3 content approximately tracks the YM according to the following approximation, $sp^3\ \% \approx YM/800$.

3 Results and Discussion

Figure 2 shows plain view SEM micrographs of (A) boron-doped nanocrystalline (scale bar 1 μm) and (B) *ta*-C:N (scale bar 100 nm), deposited with 30 sccm of N_2, thin-film electrodes. As can be seen, the diamond film consists of small, faceted crystallites that are a few hundred nanometers in lateral dimension. The diamond film deposited continuously over the Si substrate at a thickness of 2–3 μm, under the deposition conditions used. In contrast, the *ta*-C:N film has a nodular morphology with some of the larger carbon clusters being about 50 nm in diameter. There are two brighter features on this particular film near the center and center right of the micrograph. EDS analysis revealed these to be adventitious Si particles. These are normally not present on *ta*-C:N films and were picked up during handling and use of this film prior to obtaining the micrograph. The *ta*-C:N film thickness was 200–400 nm and deposited continuously over the Si substrate. The surface roughness of the *ta*-C:N films is 10–100× lower than the surface roughness of the diamond film.

Figure 3 presents visible Raman spectral data recorded for a boron-doped nanocrystalline film. The figure includes (A) a single representative spectrum and (B) a series of spectra recorded along a several micrometer-long line profile. Each spectrum shown in the line profile is the average of three spectra recorded at each location on the specimen. The spectrum in Figure 3A consists of an intense peak at 510 cm^{-1} on top of a broader scattering signal, and a broader, less intense peak at *ca.* 950 cm^{-1}. These two peaks are assigned to the first- and second-order phonon modes of the Si substrate. These two substrate bands are often present when boron-doped diamond films are relatively thin, less than a few micrometers. There is also a broad peak around 1200 cm^{-1} and a sharp peak near 1300 cm^{-1}. The latter peak is the first-order diamond phonon that is down-shifted from the expected 1332 cm^{-1} position observed for bulk, single crystal diamond. The downward shift of the first-order line, the peak broadening, and the reduced peak intensity, as compared to bulk diamond, is characteristic of heavily boron-doped diamond films [71–73,78,79]. This shift starts to happen at boron-doping levels above 10^{19} boron atoms cm^{-3} with the first-order diamond phonon line shifting from 1332 cm^{-1} toward lower wavenumbers with increasing boron concentration. This shift is typically accompanied by increases in scattering intensity at *ca.* 500 and 1225 cm^{-1} [78,79]. In this spectrum, there is also significant scattering intensity around 500 cm^{-1}, along with the first-order Si phonon, and 1200 cm^{-1}. The broad scattering at 500 cm^{-1} that tends to increase with boron doping level, has been assigned to the vibrational modes

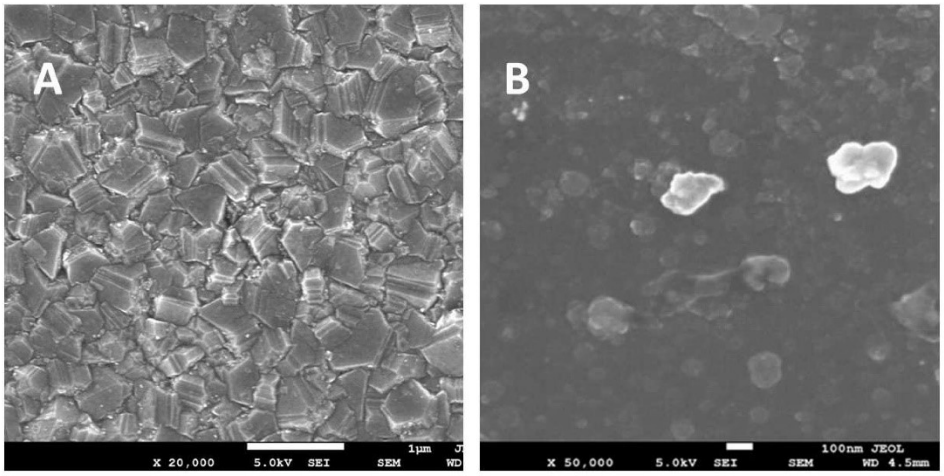

Fig. 2. SEM micrographs of (A) boron-doped nanocrystalline diamond (BDD) and (B) nitrogen-incorporated tetrahedral amorphous carbon (*ta*-C:N) thin-film electrodes, both deposited on conducting Si substrates. Note the difference in scale bars on the two micrographs: 1 µm for BDD and 0.1 µm for *ta*-C:N.

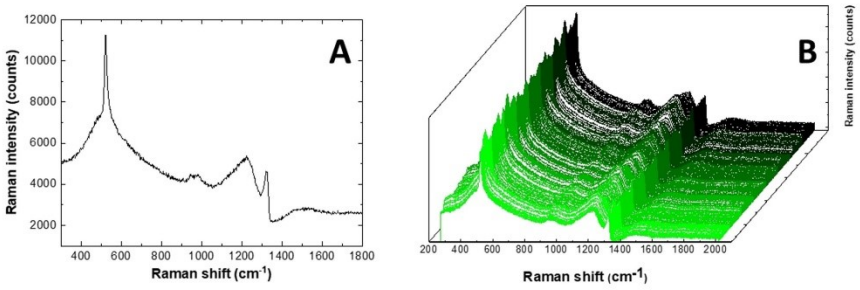

Fig. 3. Raman spectrum (A) for a boron-doped nanocrystalline diamond thin-film electrode and multiple spectra (B) recorded along a line profile in the center region of the film. The spectra were recorded using an excitation wavelength of 532 nm, 10 mW of power at the sample, and a 3-s integration time for each spectrum. In the line profile, 317 average spectra are presented over a linear distance of a few micrometers.

of boron dimers [80–82] and pairs or clusters [83]. The broad peak around 1200 cm^{-1} peak has been assigned to defects in the diamond lattice brought about by the high boron doping, possibly boron-carbon complexes [78, 79].

Finally, there is some weak scattering intensity near 1510 cm^{-1} and this is assigned to non-diamond sp^2-bonded carbon impurity located at the interface between the diamond and Si substrate, and or in some of the grain boundaries. This non-diamond carbon forms due to the disruptions in the diamond lattice because of the high boron atom incorporation. Figure 3B shows similar spectral features along the line profile. Similar spectra (not shown) were recorded at different quadrants of multiple diamond films indicating uniformity of the microstructure, boron-doping level, and optical properties across a film. In summary, the boron-doped diamond thin-film electrodes used in this work were heavily boron-doped (mid 10^{20} to low 10^{21} boron atoms cm^{-3} range), consisted of nanometer dimension crystallites of diamond, and were continuous over the substrate surface.

Figure 4 presents a typical cyclic voltammogram for 0.1 mmol L^{-1} PYO in 0.1 mol L^{-1} phosphate buffer, pH 7.4. Replicate scans are presented (5×) showing good stability of the oxidation and reduction peaks. The curves were recorded at 0.1 $V s^{-1}$, starting at an initial potential of 0.2 V, and scanning initially in the negative potential direction. A well resolved reduction peak is observed at −0.11 V vs. Ag/AgCl, and a corresponding well resolved oxidation peak is observed at −0.060 V vs. Ag/AgCl. The ΔE_p is 0.050 V, and the midpoint potential, ~ $E_{1/2}$, value is

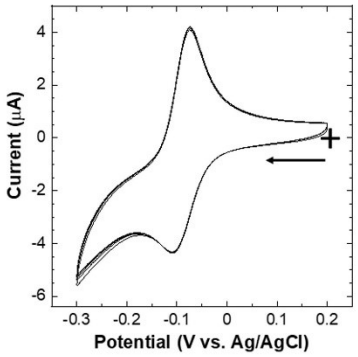

Fig. 4. Cyclic voltametric *i-E* curves for 0.1 mmol L^{-1} pyocyanin (PYO) in 0.1 mol L^{-1} phosphate buffer (pH 7.4) at a boron-doped nanocrystalline diamond thin-film electrode. Scan rate = 0.1 Vs^{-1}. Replicate scans are shown (5×).

−0.085 V vs. Ag/AgCl. The reversible $2H^+/2e^-$ reduction and oxidation reaction (see Figure 1) proceeds on diamond in a diffusion-controlled manner as there was no evidence for any surface adsorption [54–57]. This was evidenced by the fact that the reduction peak current varied linearly with the scan rate$^{1/2}$. There was also no evidence of residual electroactive PYO on the electrode surface after running some cyclic voltametric scans in the presence of the molecule and then repeating the scans after replacement of the solution with fresh electrolyte devoid of the molecule.

Flow Injection Analysis. Initial measurements were performed to assess the background current and noise for the BDD electrode over the potential range used for PYO detection as a reduction current. Figure 5A shows plots of the mean background current measured over the last 5 min of a 30 min potential step to each designated potential. The figure also includes data for a t*a*-C:N thin-film and GC, for comparison. Data are presented for a single electrode of each type. It should be noted that in these measurements, the background current for the BDD and t*a*-C:N electrodes stabilized within 2–5 min at each potential while a much longer time was required (10–30 min) for GC. This is because of the redox active functional group formation, surface oxidation, and associated microstructural changes that take place on GC over a wide potential range. As can be seen, the background currents are similar for all three electrodes at potentials between 0 and −0.3 V. More negative of −0.3 V, the current for GC increases more than the currents for BDD and t*a*-C:N. At these negative potentials, where PYO is detected as a reduction current, the background current for GC is *ca.* 4× greater than for BDD and *ca.* 3x greater than for t*a*-C:N. This additional current for GC likely arises from two sources: the reduction of redox-active surface carbon oxygen functional groups (quinone→hydroquinone) at this pH, which the BDD and t*a*-C:N surfaces are largely devoid of, and the onset of the reduction of dissolved oxygen as the carrier solution was not deaerated. The BDD and t*a*-C:N electrodes exhibit more sluggish oxygen reduction reaction kinetics, so the onset current is at potentials more negative of −0.6 V. The lower background current and reduced sensitivity to

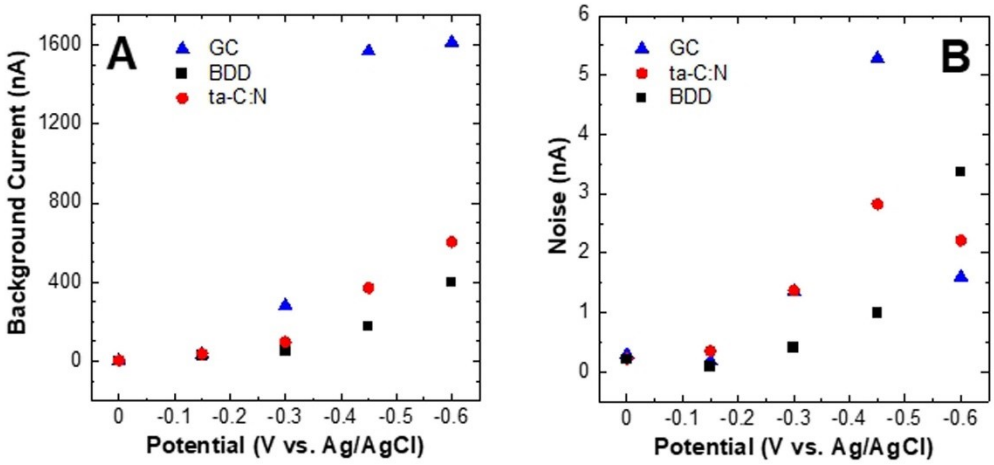

Fig. 5. Plots of the (A) mean background current and (B) noise as a function of applied potential for representative BDD, t*a*-C:N and GC electrodes recorded amperometrically in the thin-layer flow cell. The measurements were performed in a naturally aerated carrier solution of a 0.1 mol L^{-1} phosphate buffer (pH 7.4) at a flow rate of 1.0 mL min^{-1}. The geometric area for all three electrodes exposed in the flow cell was 0.11 cm^2. The current recorded at these negative potentials is plotted as a positive value.

dissolved oxygen are two advantages of BDD electrodes in electroanalytical measurements at negative potentials.

Figure 5B presents plots of the noise (*i.e.*, time-dependent fluctuations of the background current) for the three electrodes as a function of the applied potential. These values were determined from the standard deviation around the mean of the background current recorded over the last 5 min of the potential step. At potentials positive of 0.3 V, the noise for all three electrodes is similar at *ca.* 0.3 nA. At potentials between 0.3 and 0.6 V, the noise for GC is 1.5–3× higher than the noise for BDD and t*a*-C:N, similar to the background current differences. Interesting though, at 0.6 V, the noise for BDD or t*a*-C:N exceeds that for GC in this set of measurements. This is not typically what is observed though. Generally, the background current and noise data at these negative applied potentials trend as previously reported data at more positive potentials [69,70]. The background current and noise are lowest for BDD, followed by t*a*-C:N, and then GC.

Figure 6A presents a representative hydrodynamic voltammogram for PYO reduction at a BDD electrode with more negative potentials going to the right. Error bars are presented with the data markers, which represent the mean and standard deviation of three successive injections of the analyte at each potential. A sigmoidal-shaped curve is seen with an $E_{1/2}$ value of 0.310 V. The current magnitude at each potential was quite reproducible at this BDD electrode as evidenced by the small error bars. Figure 6B presents a comparison hydrodynamic voltammogram for a t*a*-C:N electrode. The $E_{1/2}$ value for t*a*-C:N is similar to that for BDD at 0.320 V. In fact, the $E_{1/2}$ values for different t*a*-C:N and GC electrodes (n 3 of each) were similar with values in the range of 0.320 to 0.360 V (data not shown). These results demonstrate that the electrode reaction kinetics for the redox-active PYO are essentially the same at all three carbon electrodes, regardless of their differences in carbon bonding, microstructure, and surface chemistry. This $E_{1/2}$ for BDD is shifted negative from the midpoint potential of the cyclic voltammogram presented in Figure 4 due to differences in the absolute potential of the different Ag/AgCl reference electrodes used in the two measurements.

Figure 7 presents the electrode response for repeated injections (31 total in this example) of 100 µmol L ^{1} PYO in a 0.1 mol L ^{1} phosphate buffer (pH 7.4), at a detection potential of 0.45 V. At this potential (see Figure 6), PYO is reduced at a diffusion-limited rate. As can be seen, reproducible peak heights were recorded for the different injections. The response variability was 1.3 % (RSD). By way of comparison, the response variability for 30 injections of the same analyte concentration at t*a*-C:N and GC electrodes was 1.3 and 3.7 % (RSD), respectively (data not shown). In fact, the response reproducibility for all three electrodes in this measurement was quite good. Excellent response reproducibility is a typical trait of BDD electrodes even without any conventional pretreatment; a characteristic that often distinguishes them from other traditional carbon electrodes in electroanalytical measurements.

Figure 8 shows (A) the responses for replicate injections of PYO as a function of the injected concentration from 1 down to 0.08 µmol L ^{1} and (B) an associated log-log response curve showing the mean current as a function of the injected concentration over the full

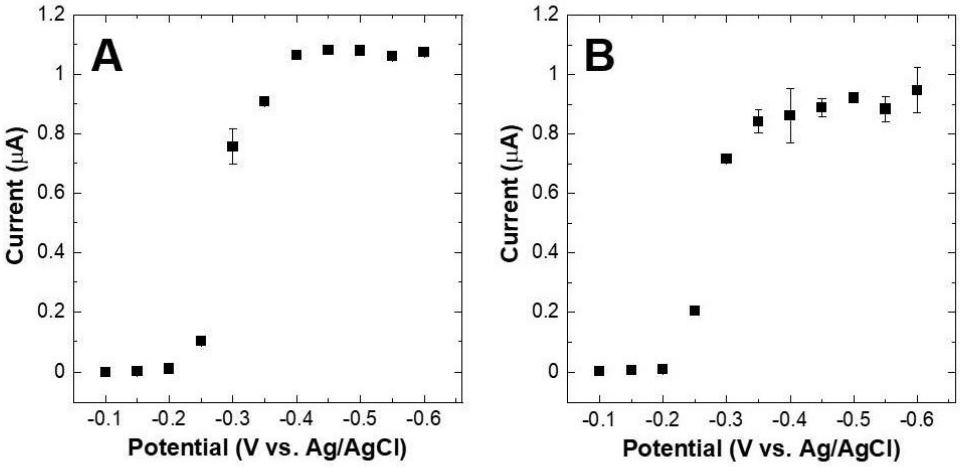

Fig. 6. Hydrodynamic voltammograms for 100 µmol L^{-1} pyocyanin (PYO) in a 0.1 mol L^{-1} phosphate buffer (pH 7.4) at a (A) BDD and (B) t*a*-C:N thin-film electrode. Flow rate = 1 mL min^{-1}. Injection volume = 25 µL. Data are presented as mean ± standard deviation for the BDD and t*a*-C:N electrodes (n = 3 injections at each potential). Cathodic current is presented as a positive value.

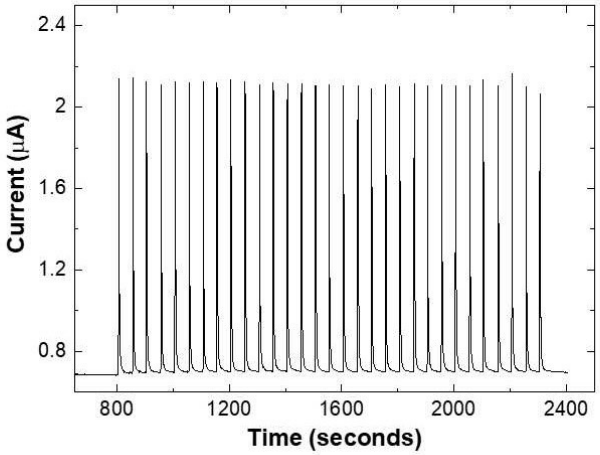

Fig. 7. FIA records of 31 repeat injections of 100 μmol L^{-1} pyocyanin (PYO) in a 0.1 mol L^{-1} phosphate buffer (pH 7.4) at a BDD electrode. Detection potential = −0.45 V. Flow rate = 1 mL min^{-1}. Injection volume = 25 μL.

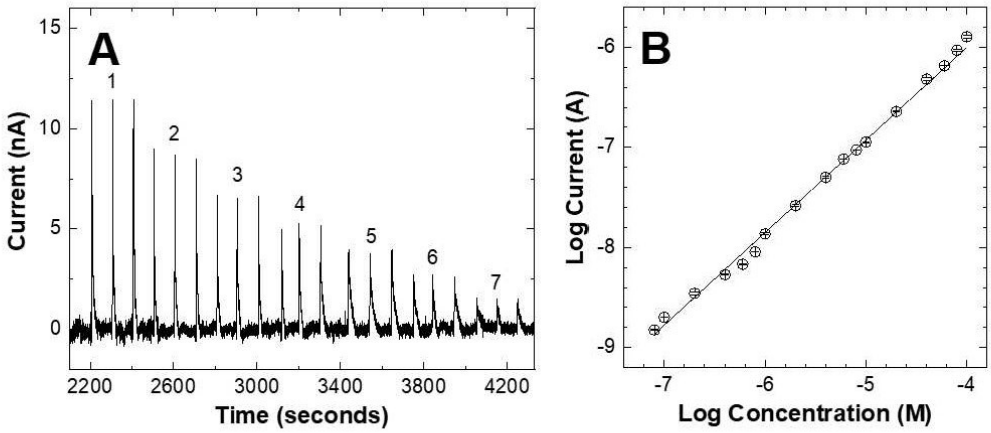

Fig. 8. (A) Detector response for pyocyanin (PYO) at different injected concentrations in a naturally aerated 0.1 mol L^{-1} phosphate buffer (pH 7.4) at a BDD thin-film electrode. (B) Associated log-log response curve showing the mean peak current as a function of the injected concentration over the full dynamic range. Data are presented as mean ± standard deviation (n = 3 injections at each potential). Error bars are within the size of the data marker. Flow rate = 1 mL min^{-1}. Injection volume = 25 μL. Injected concentrations were 1 (**1**), 0.8 (**2**), 0.6 (**3**), 0.4 (**4**), 0.2 (**5**), 0.1 (**6**) and 0.08 (**7**) μmol L^{-1}.

dynamic range from 100 to 0.08 μmol L^{-1}. Again, the triplicate response reproducibility was quite good for the BDD electrode, and a concentration dependent response is seen in terms of the increasing peak height with increasing concentration. The experimentally determined minimum concentration detectable was found to be 0.09 μmol L^{-1} (S/N 3). The upper limit of the linear dynamic range is 100 μmol L^{-1} under these conditions. At higher concentrations, the response curve starts to roll off toward unchanging current with injected concentration.

In addition to the rapid, reproducible, and sensitive measurement of PYO using FIA coupled with amperometric detection and a BDD electrode, the analyte can be detected with square wave voltammetry (SWV), as well. Figure 9 presents preliminary SWV measurements in a quiescent solution outside the flow cell. The measurements were made in a naturally aerated 0.1 mol L^{-1} phosphate buffer (pH 7.4) using PYO concentrations ranging from 0.02 to 1 μmol L^{-1}. By way of comparison, we have previously reported on the response of inkjet-

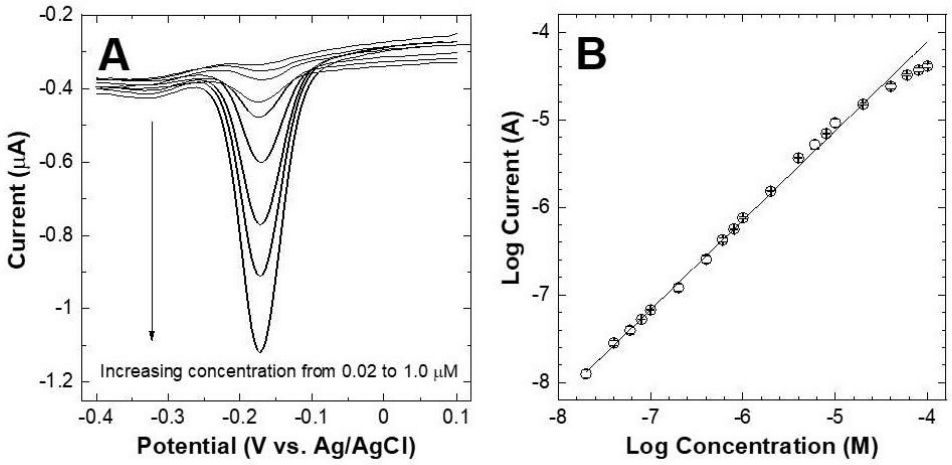

Fig. 9. (A) Square wave voltammograms for different concentrations of pyocyanin (PYO) in a naturally aerated 0.1 mol L^{-1} phosphate buffer (pH 7.4) at a BDD electrode. Curves for concentrations ranging from 0.02 to 1 μmol L^{-1} are presented. Step potential = 1 mV. Pulse amplitude = 25 mV. Frequency = 15 Hz. (B) Associated log-log response curve showing the mean peak current as a function of the pyocyanin concentration in a 0.1 mol L^{-1} phosphate buffer (pH 7.4) over the concentration range from 100 to 0.02 μmol L^{-1}. The peak current measured at −0.18 V is plotted versus the concentration. Data are presented as mean ± standard deviation (n = 3 injections at each potential). Error bars are within the size of the data marker.

printed carbon electrodes for PYO detection (reduction current) in a 0.1 mol L^{-1} phosphate buffer and a wound fluid simulant, both at pH 7.2 [84]. The inkjet-printed carbon nanotube electrodes and electrical contacts were stable with unchanging physical and electrochemical properties in the wound fluid simulant over a 7–8-day period of continuous immersion at 37 °C. The detection figures of merit for PYO in the simulant at 37 °C by SWV were: linear dynamic range 0.10 to 100 μmol L^{-1} (R^2 0.9992), limit of detection 0.10 μmol L^{-1} (S/N 3), sensitivity 35.6 ± 0.8 mA $L mol^{-1}$, and response reproducibility ≤ 4 % RSD. Improved detection figures of merit were observed using BDD. Figure 9A shows a well defined reduction peak at 0.18 V and a peak current that increases with increasing PYO concentration. Figure 9B presents a log-log plot of the mean peak current versus the PYO concentration. Excellent linearity is seen over the concentration range of multiple orders of magnitude. Above 20 μmol L^{-1}, there is the start of some roll-off in the response curve. The data for the BDD electrode reveal excellent response linearity from 20 to 0.02 μmol L^{-1} with a linear regression correlation coefficient of $R^2 > 0.990$. The response variability measured for 100 μmol L^{-1} PYO using multiple BDD electrodes was 4.3 % (RSD).

Table 1 presents a summary of the detection figures of merit for PYO at BDD electrodes as determined by FIA with amperometric detection and SWV in quiescent solution. The FIA data were recorded at a detection potential of 0.45 V, where the reduction reaction is mass transport limited (see Figure 6). For the square wave voltametric measurements, the detection figures of merit were determined from the peak current measured at the reduction peak potential, $E_{p,red}$. Comparable detection figures of merit were found for BDD using both techniques. Importantly, these detection figures of merit are observed for the BDD electrodes without any conventional pretreatment.

Table 1. Detection figures of merit for pyocyanin (PYO) at BDD electrodes as determined by FIA with amperometric detection and SWV in a naturally aerated 0.1 mol L^{-1} phosphate buffer (pH 7.4).

Detection figure of merit	FIA-EC	SWV
Detection potential (V vs. Ag/AgCl (3 M KCl))	−0.45	−0.18 V ($E_{p,red}$)
Response variability (RSD, %)	1.3	4.3
Linear dynamic range (μmol L^{-1})	100–0.08	20–0.02
Sensitivity (mA $L mol^{-1}$)	11.6 ± 0.2	79.1 ± 0.3
Limit of detection (μmol L^{-1}) (S/N = 3)	0.09	0.02

4 Conclusions

The results reported herein confirm the utility of BDD electrodes for the sensitive and reproducible detection of PYO in a 0.1 mol L^{-1} phosphate buffer (pH 7.4) using amperometric detection coupled with FIA. The data are consistent with the other limited data in the scientific literature for BDD electrodes [66–68]. BDD electrodes generally exhibit lower background current and noise than traditional carbon electrodes, like GC, and diamond-like carbon electrodes, such as *ta*-C:N. PYO was reductively detected by hydrodynamic voltammetry at an $E_{1/2}$ of −0.31 V vs. Ag/AgCl for BDD. Similar $E_{1/2}$ values were observed for *ta*-C:N and GC electrodes. This indicates that the redox reaction is insensitive to the carbon bonding, electrode microstructure and surface chemistry of the different carbon electrodes. For detection of analytes at negative potentials, BDD is useful because of its low sensitivity to dissolved oxygen reduction. The detection figures of merit for PYO with BDD electrodes in FIA-EC are impressive with a linear dynamic range from 100 to 0.08 µmol L^{-1}, a response reproducibility of 1.3% (RSD), and a limit of detection of 0.09 µmol L^{-1} (S/N = 3). Comparable detection figures of merit were observed in preliminary SWV measurements. Importantly, these detection figures of merit were obtained at BDD electrodes receiving no conventional pretreatment. Finally, the current for BDD electrodes rapidly stabilizes after potential application in the amperometric detection mode.

Acknowledgements

The research was carried out under the framework of project #W911-NF-14-10063 funded by the Army Research Office. Funding for this research also came, in part, from a Tier II Starter Grant from the Michigan Translational Research and Commercialization (MTRAC) AgBio Program. R. J. acknowledges the support from the Specific Charles University Research (SVV 260560) program. K. I. acknowledges support from CAPES – Coordination for the Improvement of Higher Education Personnel, Brazil (grant AUXPE no. 499/2013), for her visit to MSU. The authors acknowledge the contributions of Gary Yaklic and Sarah McFall-Boegeman for their work investigating the reproducibility of some of the background current and noise data. GMS gratefully acknowledges the critical role that Ted Kuwana played in the development of his academic career. His enthusiasm for science, creativity, mentorship, and friendship were instrumental in helping to prepare me for a career in academia. I thank T. K. for teaching me that "carbon" is the only electrode material!

R. J. conducted the experiments, data analysis and contributed to the writing of the manuscript. K. I. also contributed to some of the experiments. R. J., K. I., R. R. and G. M. S. contributed to the design of the experiments, review of the experimental results, and review of the manuscript. All authors approved this submission.

Data Availability Statement

All data from this study will be made available upon reasonable request.

References

[1] R. L. McCreery in *Electroanalytical Chemistry* (Ed.: A. J. Bard), Marcel Dekker, **1991**, Vol. 17, pp. 221–374.
[2] R. L. McCreery, *ChemPhysChem* **2009**, *10*, 2387–2391.
[3] S. Ranganathan, R. L. McCreery, *Anal. Chem.* **2001**, *73*, 893–900.
[4] H.-H. Yang, R. L. McCreery, *Anal. Chem.* **1999**, *71*, 4081–4087.
[5] S. Hunt-Duvall, R. L. McCreery, *Anal. Chem.* **1999**, *71*, 4594–4602.
[6] P. Chen, R. L. McCreery, *Anal. Chem.* **1996**, *68*, 3958–3965.
[7] K. R. Kneten, R. L. McCreery, *Anal. Chem.* **1992**, *64*, 2518–2524.
[8] R. J. Rice, N. M. Pontikos, R. L. McCreery, *J. Am. Chem. Soc.* **1990**, *112*, 4617–4622.
[9] R. Bowling, R. T. Packard, R. L. McCreery, *Langmuir* **1989**, *5*, 683–688.
[10] A. Morteza Najarian, R. Chen, R. J. Balla, S. Amemiya, R. L. McCreery, *Anal. Chem.* **2017**, *89*, 13532–13540.
[11] R. Chen, A. M. Nazarian, N. Kurapati, R. J. Balla, A. Oleinick, I. Svir, C. Amatore, R. L. McCreery, S. Amemiya, *Anal. Chem.* **2018**, *90*, 11115–11123.
[12] N. Kurapati, P. Pathirathna, R. Chen, S. Amemiya, *Anal. Chem.* **2018**, *90*, 13632–13639.
[13] S. Y. Tan, R. A. Lazenby, K. Bano, J. Zhang, A. M. Bond, J. V. Macpherson, P. R. Unwin, *Phys. Chem. Chem. Phys.* **2017**, *19*, 8726–8734.
[14] G. Zhang, S. Y. Tan, A. N. Patel, P. R. Unwin, *Phys. Chem. Chem. Phys.* **2016**, *18*, 32387–32395.
[15] P. R. Unwin, A. G. Güell, G. Zhang, *Acc. Chem. Res.* **2016**, *49*, 2041–2048.
[16] S. Shiba, T. Kamata, D. Kato, O. Niwa in *Nanocarbons for Electroanalysis* (Eds.: S. Szunerits, R. Boukherroub, A. Downard, J.-J. Zhu), John Wiley and Sons, **2017**, pp. 1–25.
[17] P. K. Bachmann, R. Messier, *Chem. Eng. News* **1989**, *67*(20), 24–39.
[18] S. N. Lowery, J. J. Carey, C. S. Christ, Method of Electrolysis Employing a Doped Diamond Anode to Oxidize Solutes in Wastewater, U.S. Patent # 5,399,247. Issued: March 21, **1995**.
[19] J. J. Carey, C. S. Christ, S. N. Lowery, D. R. English, *International Symposium on Silver Halide Imaging: Recent Advances and Future Opportunities in Silver Halide Imaging*, Victoria, Canada, **1997**, pp. 262–263.
[20] G. M. Swain, R. Ramesham, *Anal. Chem.* **1992**, *65*, 345–351.
[21] G. M. Swain in *Electroanalytical Chemistry* (Eds.: A. J. Bard, I. Rubinstein), Marcel Dekker, **2004**, vol. 22, pp. 182–277.
[22] M. Hupert, A. Muck, J. Wang, J. Stotter, Z. Cvackova, S. Haymond, Y. Show, G. M. Swain, *Diamond Relat. Mater.* **2003**, *12*, 1940–1949.
[23] G. M. Swain in *Thin-Film Diamond II (Semiconductors and Semimetals)* (Eds.: C. E. Nebel, J. Ristein), Elsevier, **2004**, vol. 77, pp. 121–148.
[24] J. V. Macpherson, *Phys. Chem. Chem. Phys.* **2015**, *17*, 2935–2949.
[25] N. Yang, G. M. Swain, X. Jiang, *Electroanalysis* **2016**, *28*, 27–34.

APPENDIX IV

Optimized Sawhorse Waveform for the Measurement of Oxytocin Release in Zebrafish

Romana Jarošová, Adam D. Douglass, and Michael A. Johnson

ANALYTICAL CHEMISTRY

94 (2022) 2942-2949

analytical chemistry

pubs.acs.org/ac Article

Optimized Sawhorse Waveform for the Measurement of Oxytocin Release in Zebrafish

Romana Jarosova, Adam D. Douglass, and Michael A. Johnson*

Cite This: *Anal. Chem.* 2022, 94, 2942−2949 Read Online

ACCESS | Metrics & More | Article Recommendations | Supporting Information

ABSTRACT: Oxytocin is a nonapeptide hormone involved in numerous physiological functions. Real-time electrochemical measurements of oxytocin in living tissue are challenging due to electrode fouling and the large potentials needed to oxidize the tyrosine residue. Here, we used fast-scan cyclic voltammetry at carbon-fiber microelectrodes and flow injection analysis to optimize a waveform for the measurement of oxytocin. This optimized waveform employed an accumulation potential of −0.6 V, multiple scan rates, and a 3 ms holding potential at a positive, oxidizing potential of +1.4 V before linearly scanning the potential back to −0.6 V (versus Ag/AgCl). We obtained a limit of quantitation of 0.34 ± 0.02 μM, and our electrodes did not foul upon multiple injections. Moreover, to demonstrate the utility of our method, we measured the release of oxytocin, evoked by light application and mechanical perturbation, in whole brains from genetically engineered adult zebrafish that express channelrhodopsin-2 selectively on oxytocinergic neurons. Collectively, this work expands the toolkit for the measurement of peptides in living tissue preparations.

Oxytocin is a nonapeptide hormone that acts as an endocrine chemical messenger, playing roles in numerous functions, including parturition,[1] lactation,[2] pair-bonding,[3] maternal care,[4] sexual behavior,[5] social attachment,[6] and the relief of fear and anxiety.[7] In the mammalian brain, oxytocin is synthesized mainly in the hypothalamic periventricular nucleus (PVN) and the magnocellular hypothalamic supraoptic nucleus (SON).[6,8−10] Oxytocin influences the release of multiple neurotransmitters, including dopamine,[11] serotonin,[12] and GABA[13] through its interactions with receptors in several brain regions, including the thalamus, hypothalamus, brainstem, basal ganglia, limbic system, and select cortical areas.[9,14] Thus, given its specific functions in regulating neurotransmitter systems, understanding the dynamics of oxytocin release on relevant timescales and with sufficient sensitivity in living brain tissue is a critical need.

Current methods of measuring oxytocin in living brain described in the primary literature are limited mostly to sampling approaches, including microdialysis[15] and push−pull perfusion,[16] used in conjunction with select detection schemes, such as radioimmunoassay (RIA),[16] derivatization and fluorescence detection,[17] and mass spectrometry.[18,19] While these sampling methods have the advantage of analyzing a wide variety of molecule types, the temporal resolution is limited by the amount of material collected, and usually is on the order of minutes.[20] Another detection method employed molecularly imprinted polymers (MIPs) with quartz crystal microbalance (QCM);[21] however, the utility of this method for the measurement of oxytocin in microdialysate samples has not yet been demonstrated.

Electrochemical methods represent a potentially fruitful avenue for measuring oxytocin with a subsecond timescale resolution. However, the electrochemical measurement of oxytocin can be challenging. Although the tyrosine residue in oxytocin is electroactive, it has been previously reported that the oxidation of tyrosine-containing neuropeptides tends to

Received: November 9, 2021
Accepted: January 21, 2022
Published: February 2, 2022

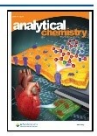

https://doi.org/10.1021/acs.analchem.1c04879
Anal. Chem. 2022, 94, 2942−2949

foul the electrode surface due to adsorption of oxidized or polymerized protein molecules, causing low reproducibility.[22,23] Additionally, there is a need for a higher oxidation potential in comparison with traditionally detected molecules (*e.g.*, catecholamines), which leads to additional problems with interferents.[24] To overcome these limitations, Schmidt et al.[23] designed a modified sawhorse waveform (MSW), consisting of two distinct scan rates in each anodic and cathodic sweep, and a short holding period at the switching potential. This approach, termed multiple scan rate voltammetry (MSRV), not only mitigates electrode fouling but also improves chemical resolution in the detection of tyrosine-containing peptides.[23,25]

Despite growing interest, many functional aspects of oxytocin in the brain have not yet been fully described due largely to the lack of analytical tools that allow its quantitative measurement in intact tissue on fast (subsecond) timescales. Here, we adapted MSRV to measure oxytocin through the oxidation of the tyrosine residue. Our results show that we can quantitatively measure oxytocin in a flow cell with good limits of detection and subsecond temporal resolution. Furthermore, we demonstrated the feasibility of our method by measuring the light-evoked release of oxytocin in live, intact whole brains acutely harvested from zebrafish engineered to express channelrhodopsin on oxytocin-containing neurons. In this model, exposure of oxytocinergic neurons to light of the proper wavelength can induce the release of oxytocin. Additionally, we demonstrated that the release of oxytocin may be induced by mechanical stimulation of the brain tissue.

EXPERIMENTAL SECTION

Chemicals. All chemicals were purchased from Sigma-Aldrich (St. Louis, MO) and used as received. A stock solution of 20 μM oxytocin (CAS no. 50-56-6, ≥97.0%) was prepared by dissolving the appropriate amount of analyte in artificial cerebrospinal fluid (aCSF; 126 mM NaCl, 2.5 mM KCl, 1.2 mM NaH_2PO_4, 2.4 mM $CaCl_2$, 1.2 mM $MgCl_2$, 25 mM $NaHCO_3$, and 20 mM HEPES, adjusted to pH 7.4 with 10 M NaOH). The solutions used for generating the calibration curves were prepared by serial dilution on the stock solution. The stock solution was stored at 5 °C in the dark and used within 48 h of preparation. All solutions were made using ultrapure water (~18 MΩ cm).

Microelectrode Fabrication. Carbon-fiber working electrodes were constructed following the previously published procedure.[26] Briefly, a 7 μm diameter carbon fiber (Goodfellow Cambridge Ltd., Huntingdon, U.K.) was aspirated into a glass capillary tube (1.2 mm outer diameter, 0.68 mm inner diameter, A-M system, Inc., Carlsborg, WA) and fixed in the position by sealing the glass capillary around the fiber using a heated coil puller (PE-22, Narishige Int., East Meadow, NY). Next, the exposed carbon fiber was trimmed to approximately 40 μm from the end of pulled glass capillary, and an epoxy seal was created (EPON resin 815C, EPIKURE 3234 curing agent, Miller-Stephenson, Danbury, CT). The microelectrode was further cured at 100 °C for 1 h and cleaned by soaking in ultrapure isopropanol for 30 min. To ensure electrical connection between the carbon fiber and electrode holder, all electrodes were backfilled by ionic solution (0.5 M potassium acetate) and a silver wire was inserted.

Electrochemical Data Acquisition *In Vitro*. All *in vitro* experiments were carried out in a homemade flow injection cell, housed within a custom-built faraday cage. A Chem Clamp potentiostat (Dagan, Minneapolis, MN) modified to enhance the range of available gain settings was used. TarHeel CV software (M.L.A.V. Heien and R.M. Wightman, University of North Carolina, Chapel Hill, NC) with data acquisition PCI 6711 multifunction I/O board (National Instruments, Austin, TX) was used to collect and analyze all data. The modified sawhorse waveform (MSW)[23,25] was originally used and further optimized. Specifically, the waveform started at a holding potential of −0.2 V and scanned to +0.6 at 100 V/s. Then, the potential was ramped to +1.2 V at 400 V/s and held for 3 ms. Finally, the potential was scanned back to −0.2 V at a scan rate of 100 V/s, at a frequency of 10 Hz.

Animals. Zebrafish embryos *Danio rerio*, transgenic line *Tg(oxt:Gal4-VP16; uas:chr2-eyfp)* were raised until adulthood (~90 days). The fish were housed in the Shankel Structural Biology Center, University of Kansas, in 3 L tanks (20 fish per 3 L system rack tank) and connected to a recirculation filtration system. All tanks were maintained under constant chemical, biological, and mechanical filtration, as well as a UV sterilizing unit to ensure adequate conditions. The following quality parameters of the reverse osmosis purified system water were controlled and adjusted using Multiparameter Monitoring and Control Instrument 5200A (YSI, Yellow Springs, OH): conductivity (~700 μS/cm), pH (7.2), and temperature (28 °C). The fish were fed twice a day and maintained on a 14:10 h light/dark cycle. All protocols and procedures involving zebrafish were approved by the Animal Care and Use Committee of the University of Kansas.

Electrochemical Detection of Oxytocin in Zebrafish Whole Brain. All zebrafish were euthanized by hypothermic shock followed by decapitation. Immediately following euthanasia, whole brains were harvested using previously described methods[26] and transferred to a superfusion chamber. The viability of the brain was ensured by a continuous flow of oxygenated and heated (28 °C) aCSF. Prior to any experiment, the brain was equilibrated in the chamber for 40 min. The carbon-fiber microelectrode was positioned into the preoptic area of the hypothalamus where epifluorescence imaging showed dense oxytocinergic innervation. Oxytocin in zebrafish is also known as isotocin and differs slightly in amino acid composition compared to mammalian oxytocin.[27]

For the optogenetics activation of cells, ADD created the UAS line using the H134R variant of ChR2, which was originally described.[28] The peak excitation is ~460 nm, which may vary slightly depending on where it is expressed and pH. ChR2 is expressed only in oxytocinergic neurons, which has previously been verified.[29] Ambient light generally contains insufficient blue light to activate cells expressing this ChR2 variant. However, experiments were performed in the dark as a precaution. For stimulated release measurements, light from a xenon source (~480 nm) was applied for 200 ms and the oxidation current was used against a calibration to determine concentration.

Microscopy. Epifluorescence images were obtained with a Nikon E600FN Epifluorescence microscope using a Fluor 40X/0.80 NA water immersion objective. Images were collected and analyzed with Metamorph software (Molecular Devices, San Jose, CA).

Statistics and Graphics. All data are presented as mean ± standard error of the mean (SEM) unless mentioned otherwise. Statistical differences were determined using one-way ANOVA with a Bonferonni post hoc test. Significance was designated at $p < 0.05$. All statistical analysis and graphical depictions were carried out using OriginPro Software, version

https://doi.org/10.1021/acs.analchem.1c04879
Anal. Chem. 2022, 94, 2942−2949

2021 (OriginLab Corp., Northampton, MA) and Microsoft Excel.

RESULTS AND DISCUSSION

The electrochemistry of oxytocin has been previously studied using carbon macroelectrodes.[30] The oxidation of oxytocin occurs at the tyrosine moiety, the only electroactive amino acid presented in the oxytocin structure. The proposed mechanism involves one-electron oxidation and loss of a proton at the hydroxyl group of the phenol group (Figure 1).[30] The resulting

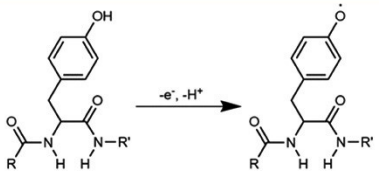

Figure 1. Proposed oxidation mechanism of oxytocin oxidation at the tyrosyl moiety. R and R′ represent the remaining parts of oxytocin.

radical is highly reactive and susceptible to further nucleophilic attack, leading to polymerization and formation of a complex mixture of substances. Such polymerization results in subsequent adsorption of the reaction products on the electrode surface, leading to electrode fouling and a significant reduction of the electrode sensitivity.[31,32] Traditionally, the FSCV waveform for the detection of electrochemically active analytes has employed a simple triangular shape (ranging from a holding potential of −0.4 V to a switching potential of 1.3 V and back at a scan rate of 400 V/s and frequency of 10 Hz, Figure 2A). However, using this waveform for the detection of peptides results in passivation of the electrode surface and loss of faradaic signal, as illustrated by the color plot (Figure 2A) and cyclic voltammograms at selected time points (Figure 2B). To address this issue, Schmidt et al. introduced a modified sawhorse waveform that incorporated multiple scan rate steps that mitigate fouling upon oxidation of met-enkephalin, a pentapeptide that also possesses a tyrosine residue. This waveform incorporated a linear scan from −0.2 to +0.6 V at a rate of 100 V/s and then to +1.2 V at 400 V/s. After a 3 ms holding time, the potential was linearly decreased to −0.2 V at 100 V/s.[23] Oxidation of the hydroxyl group was observed during the scan from +0.6 to +1.2 V. The higher scan rate increases the faradaic current measured, while holding the electrode at a potential above +1.1 V decreases the adsorption of tyrosine, thereby decreasing fouling.[33]

Oxytocin Waveform Optimization. Key waveform parameters were optimized to maximize the faradaic current resulting from the oxidation of oxytocin. The investigated parameters include waveform application frequency, upper limit of the potential window, switching potential, and scan rate. Because oxytocin possesses tyrosine, the previously published modified sawhorse waveform[14] was used as an initial starting point and further modified.

Waveform Frequency. Oxytocin possesses a positive charge at a physiological pH; thus, the negative holding potential between scans serves as a preconcentration step in which the positively charged peptide accumulates at the negatively charged electrode surface. Because changes in the waveform frequency alter the duration of this preconcentration step, we collected measurements at selected frequencies, with the remaining parameters held constant at the values used by Calhoun et al.[25]

Figure 3A,B shows CVs resulting from this change in frequencies and the peak oxidation currents, respectively. Oxidation current decreased with increasing frequency and accumulation time (indicated in red at the top of Figure 3B), suggesting that oxytocin is preconcentrating at the electrode surface between scans. The negative shift in current that occurs while holding potential constant may be caused by a

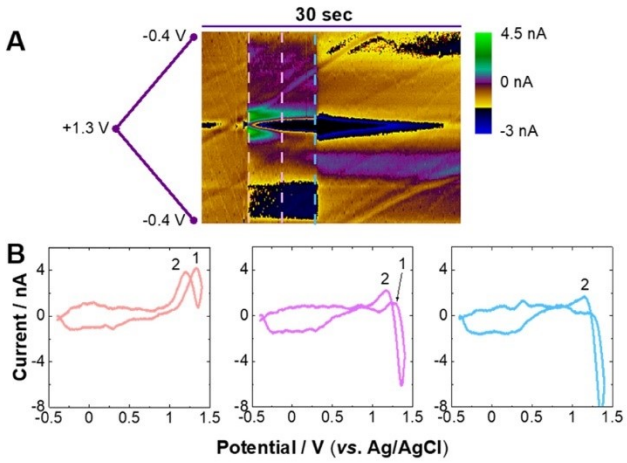

Figure 2. Oxytocin fouls the carbon-fiber microelectrode surface when the traditional FSCV waveform is used (holding potential −0.4 V, switching potential +1.3 V, scan rate 400 V/s, frequency 10 Hz). (A) Color plot representing the change in current as a function of time and applied potential. Oxytocin is injected at approximately 5.5 s, and the injection port is closed approximately at 13 s. (B) Voltammetric response for oxytocin is unstable over time. Representative CVs are shown for t = 5.6, 8.8, and 12.5 s. The oxidation peaks are labeled on the CVs.

https://doi.org/10.1021/acs.analchem.1c04879
Anal. Chem. 2022, 94, 2942−2949

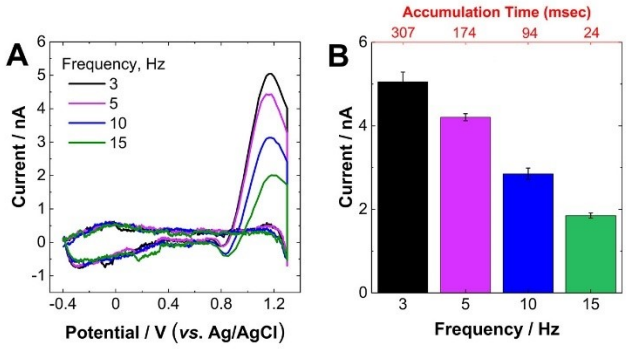

Figure 3. Waveform frequency affects sensitivity to oxytocin. (A) Representative voltammograms for 3 μM oxytocin. (B) Peak oxidation current decreases with increasing frequency (decreasing accumulation time, respectively). One-way ANOVA revealed a significant effect of frequency on current ($p < 0.05$, $n = 3$ electrodes).

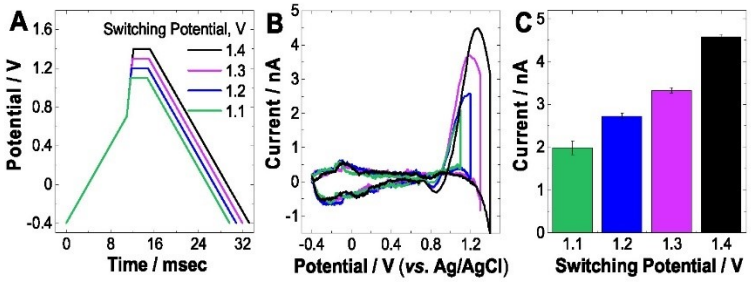

Figure 4. Oxytocin voltammetric response is dependent on the switching potential. (A) Schematic representation of the waveforms used for the investigation of the switching potential (from +1.1 to +1.4 V) on the oxytocin current response. (B) Representative voltammograms for 3 μM oxytocin. A high switching potential (+1.4 V) is required for a well-defined oxidation peak. (C) Peak anodic potential increases as the switching potential increases ($n = 3$ electrodes).

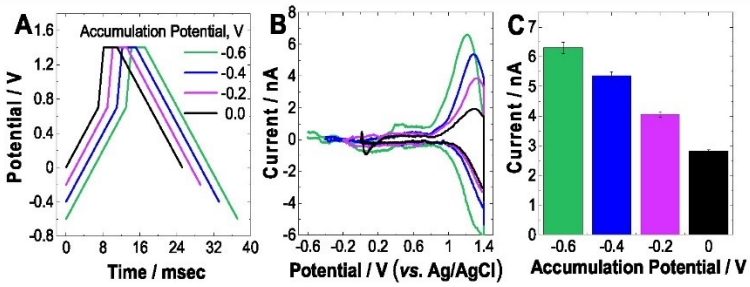

Figure 5. Oxytocin voltammetric response is dependent on the accumulation potential. (A) Schematic representation of the waveforms used for the investigation of the accumulation potential (from 0.0 to −0.6 V) on the oxytocin current response. (B) Representative voltammograms for 3 μM oxytocin. (C) Peak oxidation potential increases as the holding potential decreases ($n = 3$ electrodes). One-way ANOVA revealed a significant effect of accumulation potential on current ($p < 0.05$).

combination of factors, including etching of the electrode surface and changes in the electric double layer from adsorption of oxytocin. More work is needed to elucidate particular contributions. The lowest frequency of 3 Hz resulted in the highest current as the maximum time was available for the adsorption at the holding potential. However, as a compromise between temporal resolution and sensitivity, 5 Hz was chosen as the optimal waveform frequency.

Switching Potential. The effect of switching potential on oxytocin current response was studied by obtaining CVs with selected switching potentials ranging from +1.1 to +1.4 V (Figure 4A). The representative CVs in Figure 4B reveal that the higher switching potentials of +1.3 and +1.4 V yielded well-defined oxidation peaks, while +1.1 and +1.2 V did not. In addition, the anodic peak current increased significantly with increasing switching potential, demonstrating higher sensitivity

https://doi.org/10.1021/acs.analchem.1c04879
Anal. Chem. 2022, 94, 2942−2949

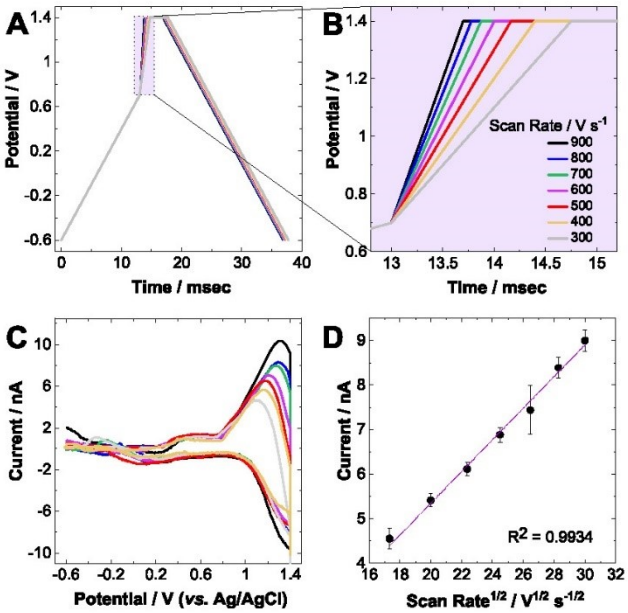

Figure 6. Effect of scan rate on oxytocin oxidation. (A) Graphical representation of the investigated waveforms. (B) Highlighted region of interest. (C) Cyclic voltammograms of 3 μM oxytocin recorded as a response of scan rate from 300 to 900 V/ s. The current response increased linearly as a function of both (D) square root of scan rate and (E) scan rate. Error bars represent mean ± SEM (n = 3 electrodes).

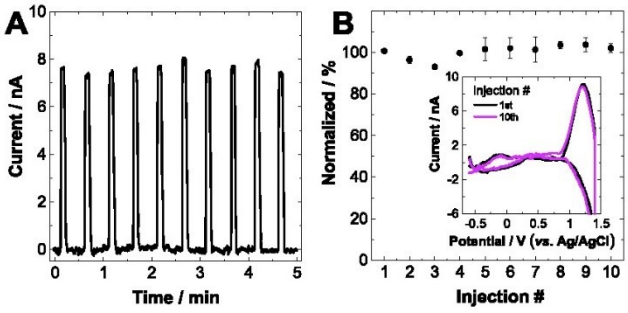

Figure 7. Electrode stability. Electrode fouling resistance was determined by injecting 3 μM oxytocin 10 times every 40 s. (A) Current−time responses for a single electrode to illustrate the stability of the response. (B) Normalized current (to the first injection) with SEM error bars (n = 3 electrodes). RSD = 3.19 %, and there is no significant difference between the first and last injections. Inset: CVs for the first and last injections.

to oxytocin (p < 0.05; n = 3 electrodes). Therefore, the potential of +1.4 V was chosen as an optimal switching potential and further used for any consequent waveform optimization steps.

Accumulation Potential. The adsorption of oxytocin molecules, which are positively charged at a physiological pH, to the electrode surface occurs due to the negative holding potential. It is, therefore, a key waveform parameter due to its significant role in the preconcentration process. The amount of adsorbed analyte and, consequently, the measured current, should be affected by changes in the holding potential. To optimize this parameter, we obtained CVs using selected holding potentials ranging from 0.0 to −0.6 V (Figure 5A). More negative holding potentials resulted in significant increases of peak current. The maximum oxidation signal was observed at −0.6 V; therefore, we chose this value for subsequent measurements.

Scan Rate. The kinetics of the electron transfer reaction were further investigated. According to the Randles−Sevcik equation, the faradaic current response increases linearly with the increasing square root of scan rate for diffusion-controlled reactions.[34] To study the nature of the oxytocin's interaction on the surface of the electrode, the scan rate was systematically varied from 200 to 900 V/s (Figure 6A,B), and the current response obtained from the resulting CVs was plotted as a function of the square root of scan rate (Figure 6C,D). The linearity of this plot (R^2 = 0.9934) suggests that the current measured is faradaic and diffusion-limited.

https://doi.org/10.1021/acs.analchem.1c04879
Anal. Chem. 2022, 94, 2942−2949

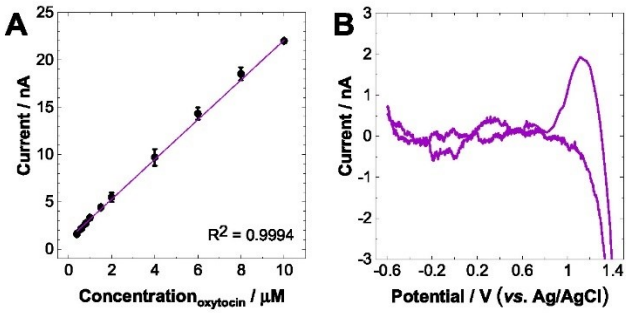

Figure 8. Detection of oxytocin using MSW exhibits nanomolar detection limits. (A) Calibration curve generated by flow injection analysis of increasing concentrations of oxytocin. (B) Representative CV for 0.4 μM oxytocin demonstrates the ability for low concentration detection. Error bars represent mean ± SEM ($n = 3$ electrodes).

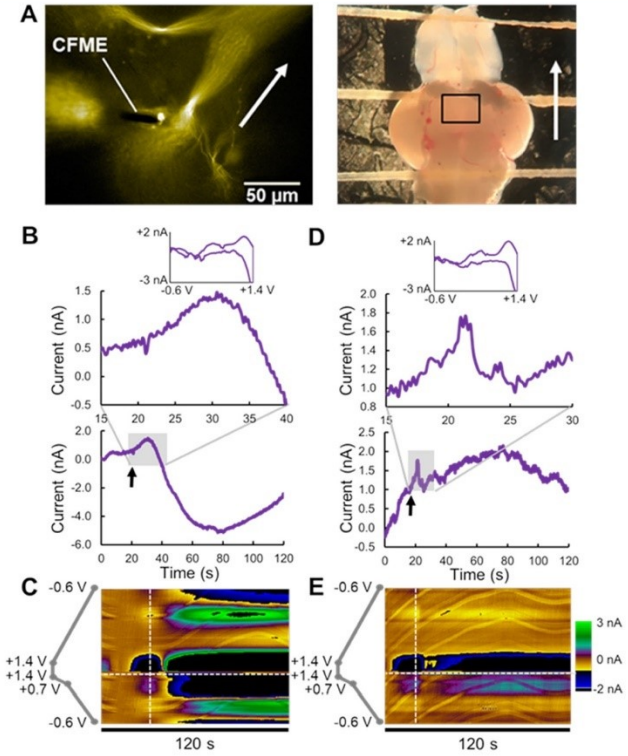

Figure 9. Stimulated and spontaneous oxytocin release in adult zebrafish brains. (A) Epifluorescence image of whole brain from adult *OXT-Gal4; UAS-ChREYFP* zebrafish (left) and bright-field image of zebrafish brain with approximate field of view in the left panel represented by the rectangle (right). The white arrows indicate relative orientation. Imaging (left): Nikon E600FN epifluorescence microscope Plan Fluor 40X/0.80 NA water immersion objective. (B, C) Current−time plots of light-induced oxytocin release and putative mechanically induced oxytocin release. Inset: CVs suggesting that the identity of measured species is oxytocin. The stimulated release is short term and is superimposed over longer-term oxytocin transient concentration changes. (C, E) Respective color plots of light- and mechanically evoked oxytocin release.

To determine the optimum scan rate value, both the current response and peak oxidation potential must be taken into consideration. As mentioned, the response current is increasing with increasing scan rate, providing the highest oxidation current at the rate of 900 V/s. However, at the fastest investigated scan rate (900 V/s), the oxidation peak occurred near the switching potential, suggesting that oxidation cannot be fully completed before scanning toward the negative

https://doi.org/10.1021/acs.analchem.1c04879
Anal. Chem. 2022, 94, 2942−2949

potential. As the scan rate decreases, the position of the oxytocin oxidation peak shifted to the less positive potential values, with a more defined peak shape. As a trade-off to providing a well-defined peak while also maximizing the oxidation current, we chose a scan rate of 600 V/s.

Electrode Stability. To measure oxytocin release consistently, it is necessary for the electrode to provide the same response over multiple measurements and extended periods of time. Electrode stability and resistance to fouling were investigated by applying repeated injections of 3 μM oxytocin every 40 s by flow injection analysis, with a total of 10 injections (Figure 7A). To visualize any significant changes in current, the evaluated faradaic current was normalized to the first injection (Figure 7B). The current *vs* time record for 10 consecutive injections, as well as CVs of the first and last injections of oxytocin showed no significant degradation in peak current and/or change in the shape of the CV (Figure 7B, inset). The relative standard deviation (RSD) for 10 injections was 3.19%, indicating that the electrodes have good stability when applying this waveform. Furthermore, no trend showing the progressive decrease of the signal over time was observed, and the newly developed waveform for the detection of oxytocin did not foul the CFE surface when exposed to repeated oxytocin injections.

Oxytocin Limit of Quantitation. We generated a calibration curve for oxytocin using the optimized waveform by plotting the current response (collected at +1.15 V) and the analyte concentration ranging from 0.4 to 10 μM (Figure 8). We found that the limit of quantitation, obtained at S/N = 10, was 0.34 $\pm$ 0.02 μM. Furthermore, regression analysis indicated a high degree of linearity (R^2 = 0.9994), indicating that the application of this optimized waveform can be used to quantitate the release of oxytocin at low concentrations.

Oxytocin Release in *Ex Vivo* Zebrafish Brain. To demonstrate the utility of our approach, we measured the light-evoked release of oxytocin in *ex vivo* whole brains harvested from transgenic zebrafish expressing fluorescently tagged channelrhodopsin-2 within oxytocinergic neurons (*Tg-[oxt:Gal4-VP16; uas:chr2-eyfp]*).

Figure 9A (left) shows an epifluorescence image of a carbon-fiber microelectrode placed in the vicinity of oxytocinergic neurons, located in the preoptic nucleus of the hypothalamus. The overall orientation of the electrode placement is indicated in Figure 9A (right). After placing the electrode, we exposed the brain to a 200 ms pulse of ~480 nm light from a xenon lamp source. The current–time trace in Figure 9B shows a temporary increase in current. The current then dropped sharply. The CV (Figure 9B, top) was sampled at 30 s, and an averaged set of five background scans obtained at 15 s was subtracted from the entire set of CVs. The CV in Figure 9B closely resembles those obtained by flow injection analysis (*e.g.*, Figure 8), suggesting that the current increase arises from oxytocin release. The average concentration of light-stimulated oxytocin release was estimated to be 0.40 $\pm$ 0.04 nM (n = 3 separate measurement locations in two brains).

Interestingly, in this plot, our stimulated release appears to be superimposed upon transient oxytocin release events, with the current decreasing below the initial baseline value, reaching a minimum at about 80 s, and then increasing. Further supporting the idea that these currents arise from the presence of oxytocin, the color plot current signal occurring after about 40 s resembles an inverse of the currents obtained at 30 s. We have carried out multiple measurements in two other brains and have noted similar patterns of transient oxytocin release.

To our knowledge, the electrochemical measurement of oxytocin release directly from the brains of any organism has not been published in the peer-reviewed literature. Oxytocin has been measured *in vivo* from the paraventricular nucleus of anesthetized rats by microdialysis sampling with detection by liquid chromatography–mass spectrometry.[18] Using this method, it was determined that the basal concentration of oxytocin in the microdialysates was 5.4 $\pm$ 1.3 pM and that this value increased 530% upon stimulation by injection of aCSF that contains 75 mM K^+. Possible factors that contribute to the greater concentration determined by our methods (several orders of magnitude) include measurement of oxytocin levels directly at the site of the neurons on faster timescales, low oxytocin recoveries in the microdialysates, differences in stimulation regimens, and differences in species.

Next, we attempted stimulation by mechanically moving the microelectrode laterally ~5 μm over ~0.5 s (Figure 9D,E). This method of stimulation had been applied previously to evoke adenosine release in brain tissue.[35] We noted a sharp increase in current, suggesting that oxytocin release occurred. We also collected files in the absence of stimulation and found what appeared to be transient changes in oxytocin release that occurred over the course of seconds, like those superimposed on stimulated release currents in the dataset shown in Figure 9B,C. While it is possible that other electroactive components are released due to mechanical stimulation, it is important to note that a subpopulation of oxytonergic neurons in the hypothalamus is mechanosensitive.[36] Thus, we speculate that oxytocin is likely present along with other tyrosine-containing peptides.

Stimulated and transient release from terminals that project to various brain regions as well as release from oxytocinergic cell bodies and dendrites (somatodendritic release) is known to occur in multiple species.[37−39] The current we measured in zebrafish, given the location in the brain, arises possibly from somatodendritic release or from short-range axonal projections. It will be important to determine if the transients arise from our handling of the tissue (*e.g.*, application of light for imaging) or if they occur naturally.

■ CONCLUSIONS

In this research, we developed a waveform optimized for the measurement of oxytocin, a nonapeptide that is an important player in numerous biological functions. However, it is difficult to measure because it tends to foul the carbon-fiber electrode surface. We also demonstrated the measurement of oxytocin in genetically altered zebrafish that express channelrhodopsin and yellow fluorescent protein selectively in oxytocinergic neurons. Our findings demonstrate that we can measure stimulated release as well as spontaneously occurring oxytocin transients. In the future, it will be important to further validate our method in more complex species, including rodents.

■ ASSOCIATED CONTENT

Supporting Information

The Supporting Information is available free of charge at https://pubs.acs.org/doi/10.1021/acs.analchem.1c04879.

Alternative representation of data and current plotted against time for a typical cyclic voltammogram (PDF)

https://doi.org/10.1021/acs.analchem.1c04879
Anal. Chem. 2022, 94, 2942−2949

AUTHOR INFORMATION

Corresponding Author

Michael A. Johnson − *Department of Chemistry and R.N. Adams Institute for Bioanalytical Chemistry, University of Kansas, Lawrence, Kansas 66045, United States;* orcid.org/0000-0001-5078-9896; Phone: 785-864-4269; Email: johnsonm@ku.edu

Authors

Romana Jarosova − *Department of Chemistry and R.N. Adams Institute for Bioanalytical Chemistry, University of Kansas, Lawrence, Kansas 66045, United States; Department of Analytical Chemistry, UNESCO Laboratory of Environmental Electrochemistry, Charles University, Prague 2 12843, Czech Republic;* Present Address: University of Cincinnati, Cincinnati, Ohio 45221, United States

Adam D. Douglass − *Department of Neurobiology and Anatomy, University of Utah, Salt Lake City, Utah 84112, United States*

Complete contact information is available at: https://pubs.acs.org/10.1021/acs.analchem.1c04879

Author Contributions

M.A.J. and R.J. conceived all experiments. R.J. performed all experiments. A.D.D. developed and supplied Tg*[oxt:Gal4-VP16; uas:chr2-eyfp]*. The manuscript was written through contributions of all authors. All authors have given approval to the final version of the manuscript.

Notes

The authors declare no competing financial interest.

ACKNOWLEDGMENTS

Support for this research was provided by grants from the National Institutes of Health, R21NS109659 (MAJ), P20GM103638 (MAJ), and R01NS111067-01 (ADD); the University of Kansas (MAJ); the National Science Foundation, IOS10043082 (ADD); and Charles University in Prague under Award Number SVV260560 (RJ).

REFERENCES

(1) Mauri, A.; Argiolas, A.; Ticconi, C.; Piccione, E. *Reprod., Fertil. Dev.* **1995**, *7*, 1481−1484.
(2) Drewett, R. F.; Bowen-Jones, A.; Dogterom, J. *Horm. Behav.* **1982**, *16*, 245−248.
(3) Liu, Y.; Wang, Z. X. *Neuroscience* **2003**, *121*, 537−544.
(4) Ogi, A.; Mariti, C.; Pirrone, F.; Baragli, P.; Gazzano, A. *Animals* **2021**, *11*, No. 1130.
(5) Oti, T.; Sakamoto, T.; Sakamoto, H. *Commun. Integr. Biol.* **2021**, *14*, 55−60.
(6) Kosfeld, M.; Heinrichs, M.; Zak, P. J.; Fischbacher, U.; Fehr, E. *Nature* **2005**, *435*, 673−676.
(7) Smith, A. S.; Wang, Z. *Biol. Psychiatry* **2014**, *76*, 281−288.
(8) Zimmerman, E. A.; Nilaver, G.; Hou-Yu, A.; Silverman, A. J. *Fed. Proc.* **1984**, *43*, 91−96.
(9) Gimpl, G.; Fahrenholz, F. *Physiol. Rev.* **2001**, *81*, 629−683.
(10) Rossoni, E.; Feng, J.; Tirozzi, B.; Brown, D.; Leng, G.; Moos, F. *PLoS Comput. Biol.* **2008**, *4*, No. e1000123.
(11) Love, T. M. *Pharmacol., Biochem. Behav.* **2014**, *119*, 49−60.
(12) Flight, M. H. *Nat. Rev. Neurosci.* **2013**, *14*, 740−741.
(13) Tyzio, R.; Nardou, R.; Ferrari, D. C.; Tsintsadze, T.; Shahrokhi, A.; Eftekhari, S.; Khalilov, I.; Tsintsadze, V.; Brouchoud, C.; Chazal, G.; Lemonnier, E.; Lozovaya, N.; Burnashev, N.; Ben-Ari, Y. *Science* **2014**, *343*, 675−679.
(14) Yoshimura, R.; Kiyama, H.; Kimura, T.; Araki, T.; Maeno, H.; Tanizawa, O.; Tohyama, M. *Endocrinology* **1993**, *133*, 1239−1246.
(15) de Moura Oliveira, V. E.; Lukas, M.; Wolf, H. N.; Durante, E.; Lorenz, A.; Mayer, A. L.; Bludau, A.; Bosch, O. J.; Grinevich, V.; Egger, V.; de Jong, T. R.; Neumann, I. D. *Nat. Commun.* **2021**, *12*, No. 2900.
(16) Landgraf, R.; Neumann, I.; Russell, J. A.; Pittman, Q. J. *Ann. N. Y. Acad. Sci.* **1992**, *652*, 326−339.
(17) Gozdowska, M.; Kulczykowska, E. *J. Chromatogr. B: Anal. Technol. Biomed. Life Sci.* **2004**, *807*, 229−233.
(18) Mabrouk, O. S.; Kennedy, R. T. *J. Neurosci. Methods* **2012**, *209*, 127−133.
(19) Wang, L.; Marti, D. W.; Anderson, R. E. *Molecules* **2019**, *24*, 3079.
(20) Kendrick, K. M. *J. Neurosci. Methods* **1990**, *34*, 35−46.
(21) Lin, C. Y.; Tsai, S. H.; Tai, D. F. *J. Pept. Sci.* **2019**, *25*, No. e3150.
(22) Lane, R. F.; Hubbard, A. T. *Anal. Chem.* **1976**, *48*, 1287−1292.
(23) Schmidt, A. C.; Dunaway, L. E.; Roberts, J. G.; McCarty, G. S.; Sombers, L. A. *Anal. Chem.* **2014**, *86*, 7806−7812.
(24) Shen, H.; Lada, M. W.; Kennedy, R. T. *J. Chromatogr. B: Biomed. Sci. Appl.* **1997**, *704*, 43−52.
(25) Calhoun, S. E.; Meunier, C. J.; Lee, C. A.; McCarty, G. S.; Sombers, L. A. *ACS Chem. Neurosci.* **2019**, *10*, 2022−2032.
(26) Kraft, J. C.; Osterhaus, G. L.; Ortiz, A. N.; Garris, P. A.; Johnson, M. A. *Neuroscience* **2009**, *161*, 940−949.
(27) Landin, J.; Hovey, D.; Xu, B.; Lagman, D.; Zettergren, A.; Larhammar, D.; Kettunen, P.; Westberg, L. *Sci. Rep.* **2020**, *10*, 5435.
(28) Nagel, G.; Brauner, M.; Liewald, J. F.; Adeishvili, N.; Bamberg, E.; Gottschalk, A. *Curr. Biol.* **2005**, *15*, 2279−2284.
(29) Wee, C. L.; Nikitchenko, M.; Wang, W. C.; Luks-Morgan, S. J.; Song, E.; Gagnon, J. A.; Randlett, O.; Bianco, I. H.; Lacoste, A. M. B.; Glushenkova, E.; Barrios, J. P.; Schier, A. F.; Kunes, S.; Engert, F.; Douglass, A. D. *Nat. Neurosci.* **2019**, *22*, 1477−1492.
(30) Asai, K.; Ivandini, T. A.; Einaga, Y. *Sci. Rep.* **2016**, *6*, No. 32429.
(31) Jackson, B. P.; Dietz, S. M.; Wightman, R. M. *Anal. Chem.* **1995**, *67*, 1115−1120.
(32) Cooper, S. E.; Venton, B. J. *Anal. Bioanal. Chem.* **2009**, *394*, 329−336.
(33) Ogura, K.; Kobayashi, M.; Nakayama, M.; Miho, Y. *J. Electroanal. Chem.* **1999**, *463*, 218−223.
(34) Bard, A. J.; Faulkner, L. R. *Electrochemical Methods: Fundamentals and Applications*; 2nd ed.; John Wiley & Sons, Ltd., 2000.
(35) Wang, Y.; Venton, B. J. *Neurochem. Int.* **2019**, *124*, 46−50.
(36) Wee, C. L.; Nikitchenko, M.; Wang, W. C.; Luks-Morgan, S. J.; Song, E.; Gagnon, J. A.; Randlett, O.; Bianco, I. H.; Lacoste, A. M. B.; Glushenkova, E.; Barrios, J. P.; Schier, A. F.; Kunes, S.; Engert, F.; Douglass, A. D. *Nat. Neurosci.* **2019**, *22*, 1477−1492.
(37) Althammer, F.; Eliava, M.; Grinevich, V. *Handb. Clin. Neurol.* **2021**, *180*, 25−44.
(38) Ludwig, M.; Stern, J. *Philos. Trans. R. Soc., B* **2015**, *370*, No. 20140182.
(39) Pow, D. V.; Morris, J. F. *Neuroscience* **1989**, *32*, 435−439.

APPENDIX V

In situ Electrochemical Monitoring of Caged Compound Photochemistry: An Internal Actinometer for Substrate Release

Romana Jarošová, Sam V. Kaplan, Thomas M. Field, Richard S. Givens, Sanjeewa N. Seaheera, and Michael A. Johnson

ANALYTICAL CHEMISTRY

93 (2021) 2776-2784

Published in final edited form as:

Anal Chem. 2021 February 09; 93(5): 2776–2784. doi:10.1021/acs.analchem.0c03452.

In situ Electrochemical Monitoring of Caged Compound Photochemistry: An Internal Actinometer for Substrate Release

Romana Jarosova[†,‡], **Sam V. Kaplan**[†], **Thomas M. Field**[†], **Richard S. Givens**[†], **Sanjeewa N. Senadheera**[§], **Michael A. Johnson**[*,†,‖]

[†]Department of Chemistry and R.N. Adams Institute for Bioanalytical Chemistry, University of Kansas, Lawrence, Kansas 66045

[‡]Department of Analytical Chemistry, UNESCO Laboratory of Environmental Electrochemistry, Charles University, Prague 2, Czech Republic 12843

[§]Department of Pharmaceutical Chemistry, University of Kansas, Lawrence, Kansas 66045

[‖]Graduate Program in Neuroscience, University of Kansas, Lawrence, Kansas 66045

Abstract

Caged compounds are molecules that release a protective substrate to free a biologically active substrate upon treatment with light of sufficient energy and duration. A notable limitation of this approach is difficulty in determining the degree of photoactivation in tissues or opaque solutions because light reaching the desired location is obstructed. Here, we have addressed this issue by developing an *in situ* electrochemical method in which the amount of caged molecule photo-release is determined by fast-scan cyclic voltammetry (FSCV) at carbon-fiber microelectrodes. Using *p*-hydroxyphenyl glutamate (*p*HP-Glu) as our model system, we generated a linear calibration curve for oxidation of 4-hydroxyphenylacetic acid (4HPAA), the group from which the glutamate molecule leaves, up to a concentration of 1000 μM. Moreover, we are able to correct for the presence of residual *p*HP-Glu in solution as well as the light artifact that is produced. A corrected calibration curve was constructed by photo-activation of *p*HP-Glu in a 3 μL photoreaction vessel and subsequent analysis by high performance liquid chromatography. This approach has yielded a linear relationship between 4HPAA concentration and oxidation current, allowing the determination of released glutamate independent of the amount of light reaching the chromophore. Moreover, we have successfully validated the newly developed method by *in situ* measurement in whole, intact zebrafish brain. This work demonstrates, for the first time, the *in situ* electrochemical monitoring of caged compound photochemistry in brain tissue with FSCV, thus facilitating analyses of neuronal function.

Keywords

voltammetry; caged compound; photoactivation; glutamate; zebrafish

[*]**Corresponding Author** Michael A. Johnson, johnsonm@ku.edu. Tel. 785-864-4269.

Author Contributions

Michael A. Johnson conceived of the work. This manuscript was written by Michael A. Johnson, Sam V. Kaplan, Romana Jarosova and Richard S. Givens. Experiments were carried out by Romana Jarosova, Michael A. Johnson, Sam V. Kaplan, and Thomas M. Field. Compounds were synthesized by Sanjeewa N. Senadheera and the Synthetic Chemical Biology Core.

The use of light-driven approaches to manipulate biological systems has grown dramatically over the past decade. One such approach, caged compound photoactivation, allows the application of biologically active molecules with micrometer spatial and sub-second temporal resolution. When treated with light of sufficient energy, the photo-removable protecting group on a caged compound separates from the biologically active form of the molecule.[1-6] This photochemical delivery method has been used to activate biologically dormant or inactive bio-systems such as neurons and sensory cells in *ex vivo* and *in vivo* tissue platforms as well as reactions at the molecular level such as enzymatic reactions and protein folding. Moreover, the protecting group's rapid release occurs within ns to μs depending on the protecting group and the substrate[7], making this photo-activation process compatible for probing temporal and spatial parameters by electrophysiological and electrochemical detection methods. For example, caged substrate photo-activation combines the photo-release process with patch clamp detection to examine the influence of the amino acids glutamate and GABA as agonists and antagonists for neuronal function.[2,3,5,8-13] The function of dopaminergic neurons and circuits can be explored using recently developed caged dopamine and its caged receptor antagonists.[14,15]

A major challenge of this approach, as well as others that employ photo-activation strategies, is quantitation of photo-released substrate when sample variability is not controlled. Traditionally, the amount of photo-released substrate has been determined indirectly by measuring the photon flux impinging on the sample using actinometry methods, e.g. potassium ferrioxalate solutions[16] and the quantum yield (the ratio of yield to photons absorbed) for substrate release upon exposure to the light source. Knowing the quantum yield, one can determine the number of moles released when the number of photons absorbed by the sample is known. This approach is reliable as long as the photon delivery system and the substrate photolysis reaction are identical for both the actinometry and substrate release measurements.

Determination of yields of photo-released substrate in complex biological and tissue entrainments present additional confounding variables. Such complications arise because actinometer solutions are homogeneous and contain only the reactive chromophore in physiological media. Conversely, in actual physiological experiments, there may be several competing chromophores as well as opaque materials that competitively absorb light or reflect it away from the caged material. This interference diminishes the amount of light reaching the caged compound, thereby resulting in an overestimation of substrate release.

A direct, *in situ* measurement of photo-release of the substrate, which is independent of interferences of the incident light and the nature of the biological sample, would mitigate many of the inherent complications associated with traditional actinometer methods. We propose a remedy for quantifying the photoreaction by employing a doubly responsive photoreaction that couples substrate release with the generation of a separate electroactive byproduct. This concept parallels the photo-generation of active fluorophores with substrate release that uses fluorescence intensities to quantify the release.[3]

FSCV is a technique of choice for measuring chemicals secreted from individual cells,[16,17] in acutely dissociated brain sections,[12,16,18-22] and in whole animals.[23-28] This method is compatible with caged compound photo-activation studies because it has good temporal resolution (sub-second to millisecond), selectivity (a characteristic cyclic voltammogram, or CV, is formed), and spatial resolution (nanometer to micrometer). Here, we report a new synergistic approach using FSCV to quantify photo-activation of substrate release and caged compound decomposition simultaneously with an *in situ* single probe. The concept requires that the byproduct of the caging chromophore be electroactive, but preferably not the caged compound itself. However, as demonstrated here, the starting material signal can be subtracted to remove it from interfering with the product analyses.

In this work, we use a *p*-hydroxyphenacyl cage to demonstrate proof of concept for the electrochemical monitoring of photoactivation. The use of this cage for a wide variety of substrates has several inherent advantages for FSCV based analyses. The *p*HP class of caged compounds offer high quantum yields, nanosecond timescales of release, and deep-seated rearrangement of the caging chromophore into biologically benign 4-hydroxyphenylacetic acid (4HPAA; Fig. 1). This molecule can be measured electrochemically and distinguished from other biologically active compounds such as monoamine neurotransmitters.[29]

The method described here uses a microliter photoreaction vessel to generate a calibration curve that relates the electrochemical oxidation signal of photo-released 4HPAA measured by FSCV to the concentration of 4HPAA obtained by HPLC with ultraviolet-visible detection. We have previously demonstrated the simultaneous, electrochemical quantitation of 4HPAA versus dopamine by FSCV.[30] Thus, the method proposed here extends our capability to include the direct measurement of caged compound degradation in conjunction with dopamine release.

Experimental

Reagents.

Stock solution (0.1 mmol L^{-1}) of 4HPAA (CAS No. 156-38-7, 98%, Sigma-Aldrich, St Louis, MO) and *p*HP-Glu (synthesized by the Synthetic Chemical Biology Core of the Center for the Molecular Analysis of Disease Pathways at The University of Kansas, Lawrence) were prepared by dissolving the appropriate analyte mass in artificial cerebrospinal fluid (aCSF). The aCSF consisted of 126 mM NaCl, 2.5 mM KCl, 1.2 mM NaH_2PO_4, 2.4 mM $CaCl_2$, 1.2 mM $MgCl_2$, 25 mM $NaHCO_3$, and 20 mM HEPES, adjusted to a pH of 7.4. Solutions used for generating the calibration curves were prepared by serial dilution of the stock solution. Stock solution of 4HPAA was refrigerated in glass vials in the dark when not in use. Stock solution of *p*HP-Glu was prepared daily. All chemicals for high performance liquid chromatography (HPLC) were obtained from Sigma-Aldrich (St Louis, MO). Ultrapure water (~18.2 MOhm-cm) was used to prepare all aqueous solutions.

Animals.

Adult *Danio rerio* (zebrafish, AB wild-type strain) were purchased from Zebrafish International Resource Center (ZIRC, University of Oregon, Eugene, OR) and housed in the

Shankel Structural Biology Center at the University of Kansas. The animals were housed in three-liter tanks (15 – 20 fish per three-liter system rack tank) and connected to a recirculation filtration system. All tanks were maintained under constant chemical, biological and mechanical filtration, as well as UV sterilizing unit to ensure adequate conditions. Conductivity (~ 800 μS cm^{-1}) and pH (7.2) of the reverse osmosis purified system water (maintained at 28 °C) was controlled and adjusted by Multiparameter Monitoring and Control Instrument 5200A (YSI, Yellow Springs, OH). Fish were fed twice a day and kept in a light/dark cycle (16h/8h). All procedures involving zebrafish were approved by the Animal Care and Use Committee of the University of Kansas.

Uncaging apparatus.

The experimental uncaging apparatus was adapted from an approach used previously for electrophysiology.[31] The output from a mercury lamp, directed through a 280 nm cut-off high-pass filter and gated with a shutter, was delivered to the sample through a fiber optic cable (PolyMicro Technologies, Inc, Phoenix, AZ). A micromanipulator was used to position the fiber-optic cable near the carbon-fiber microelectrode.

Fast-scan cyclic voltammetry.

A ChemClamp potentiostat (Dagan, Minneapolis, MN, USA), modified to enhance the range of available gain settings, was used. Data were collected and analyzed using TarHeel CV software (R.M. Wightman and M.L.A.V. Heien, University of North Carolina, Chapel Hill, NC, USA). Carbon-fiber working electrodes were constructed using previously published methods[25] and were trimmed to an exposed length of 40 μm. Electrodes were used in a flow injection analysis apparatus, the microliter reaction vessel, and in whole zebrafish brains. Flow injection analysis was carried out by directing the solution flow with a six-port sample injector through a custom designed flow cell. For the detection of 4HPAA, a triangular waveform was used in which potential (versus Ag/AgCl electrode) was linearly scanned from −0.4 V to +1.3 V to −0.4 V. The potential between scans was held at −0.4 V. The scan rate was 600V/s and the update rate was 10Hz.[30]

Electrochemical measurement of *p*HP-glutamate photo-activation.

A microliter reaction vessel (Fig. 2) was fabricated with 1 mm plastic tubing (Cole Parmer, Vernon Hills, Illinois) that allowed a 3 μL volume of aqueous *p*HP-glutamate solution to be held in place by surface tension. A 1 mm diameter optical fiber (Polymicro Technologies, Phoenix, Arizona) was press fitted into the plastic tubing from the bottom of the tubing, while the *p*Hp-glutamate solution was injected from the top of the tubing. The carbon-fiber working electrode and an Ag/AgCl reference electrode were micromanipulated into the solution from the top of the reaction vessel. Once the photo-uncaging occurred and the photo-released 4HPAA was measured using FSCV, the electrodes were removed, and the sample was carefully transferred from the reaction vessel to a vial for a further HPLC analysis. In order to ensure sufficient amount of material for HPLC analysis, three uncaging samples (*i.e.* 3 × 3 μL) were consolidated into a vial for an HPLC analysis for each of the three electrodes. Measurements performed in order to quantify the photoelectric effect were carried out in solutions in which *p*HP-Glu was not present.

Electrochemical detection of *p*HP-glutamate photo-activation in a zebrafish brain.

Zebrafish were euthanized by hypothermic shock followed by decapitation. Whole brains were harvested as described previously.[32] Briefly, the decapitated zebrafish head was immobilized in a Petri dish filled with 2% agarose (BioReagent grade, Sigma-Aldrich, St. Louis, MO, USA) and oxygenated (95% O_2 and 5% CO_2) aCSF. After removal from the skull, the fish brain was carefully lifted and transferred to a perfusion chamber. The brain was kept viable by continuous flow of oxygenated aCSF heated at a physiological temperature of 28 °C. Prior to any measurement, the fish brain was first kept in the perfusion chamber for 40 min in order to equilibrate. The carbon-fiber working electrode was positioned into the ventral telencephalon of the zebrafish with a micropositioner. The 50 μm optic fiber (Polymicro Technologies, Phoenix, Arizona) was further micro-manipulated into a close proximity of the tip of the carbon-fiber microelectrode. The photoelectric effect was examined in zebrafish brain perfused by only aCSF (no *p*HP-glutamate presented). Finally, the *p*Hp-glutamate (c = 1000 μM) in aCSF was perfused through the brain for 30 minutes and the electrochemical detection of *p*HP-glutamate (4HPAA, respectively) was carried out. Both the photoelectric effect and the uncaging of *p*HP-glutamate in zebrafish brain were performed using 1000 ms duration of light exposure.

HPLC analysis.

The HPLC system (Shimadzu Scientific Corp) consisted of a CBA-20A system controller, a DGV-20A3 degassing unit, a LC-20AD high pressure pump, a SIL-20AC autosampler, and SDP-20 AV UV-VIS detector. An Ascentis® C18 (15 cm × 4.6 mm × 5 μm) column (Millipore-Sigma, Inc., Burlington, MA) was used. The sample volume injected was 5 μL. The mobile phase consisted of (A) 99 % H_2O, 1 % MeOH and 0.06 % formic acid (B) 99 % MeOH, 1 % H_2O and 0.06 % formic acid. Analytes were eluted isocratically at A:B = 70:30 (v/v %) at a flow rate of 1 mL min^{-1}. The spectrophotometric detector was set at 220 nm. The quantification of 4HPAA was performed by generation of external calibration curve. The calibration curve was constructed from the height of the peak, as a function of 4HPAA concentration, with a linear dynamic range from 1 to 1000 μM (R^2= 0.9996, N = 3).

Statistics.

Statistical analysis and graphical presentation was carried out using OriginPro software, version 2020b (OriginLab Corp., Northampton, MA). A p-value of 0.05 or less was considered significant.

RESULTS AND DISCUSSION

Measuring 4HPAA with FSCV.

We have previously shown that 4HPAA can readily be measured by FSCV.[30] Thus, we sought here to demonstrate that the liberation of 4HPAA from *p*-hydroxyphenacyl-based caged compounds, such as *p*-hydroxyphenacyl glutamate, could be used to quantity the formation of the resulting bioactive molecule. Our approach quantifies glutamate photo-release by measuring differences between currents produced by the liberation of 4HPAA after light application and currents present prior to light application. Therefore, it is essential

that the current associated with 4HPAA increase linearly within a useful concentration range. Fig. 3A shows a CV of 4HPAA (0.1 mM) obtained by flow injection analysis and FSCV. As described by Shin et al.,[30] we observed two well-resolved peaks, suggesting that two distinct electrochemical processes occur. The first peak occurred at +1.23 V as the potential swept toward the most positive value, while the second peak occurred at +1.12 V as the potential swept toward the most negative value. Fig. 3B shows that the electrochemical response to 4HPAA, evaluated from peaks at +1.23 V (forward sweep) and +1.12 V (backward sweep), was linear from 10 μM up to at least 1000 μM (higher concentrations were not investigated). This result indicates that it is possible to quantify the amount of 4HPAA photo-released even at high concentrations.

Another concern was that the electroactivity of the caged form of the compound would complicate the interpretation of the electrochemical data because the CV is similar to that of 4HPAA. Despite the similarities, however, it is still possible to distinguish between the two voltammograms. For example, shown in Fig. 4 are CVs of 4HPAA and *p*HP-Glu, obtained by flow injection analysis. The red trace is the result of subtracting the CV of pHP-Glu from that of 4HPAA. These CVs are unfolded at the switching potential of +1.3 V so that the direction of the potential sweep, which occurs from left to right in the figure, is easier to visualize. The oxidation peak for *p*HP-Glu appears at a similar position compared to the first oxidation peak of 4HPAA (about +1.23 V on the forward scan) and a small second *p*HP-Glu oxidation peak appears at +1.05 V on the backward scan. As the subtraction of the CVs reveals, a measurable signal proportional to the amount of 4HPAA formed by photo-uncaging can be derived by subtracting the two CVs. Even though in an actual uncaging experiment the concentrations of 4HPAA and *p*HP-Glu may not be equal due to the formation of species other than 4HPAA, the measurements in Fig. 4 demonstrate that the CVs for the two species are qualitatively different and result in a characteristic CV upon subtraction.

Removing the artifactual light signal from the 4HPAA signal.

Currents produced by photons striking the surface of the carbon-fiber microelectrode complicate the measurement of the current produced by 4HPAA because the CVs are similar. Therefore, we explored the effects of subtracting this signal from the overall electrochemical signal produced by photo-activation of *p*HP-Glu. Samples of aCSF with different concentrations of *p*HP-Glu, ranging from 0 to 1000 μM, were placed in the reaction vessel described in Fig. 2. The solutions were exposed to light, gated by a shutter, of selected durations ranging from 200 to 1000 ms. Even in the absence of *p*HP-Glu, the application of light produced a large photo-induced current that gradually decayed (Fig. 5). The current response appeared to increase in linear fashion with increasing exposure time up to about 600 ms (Fig. 6A). Beyond this time, the current deviated from linearity. Measurements obtained in the presence of successively increasing concentrations of *p*HP-Glu resulted in stepwise increases of measured current for all examined solutions (concentration of *p*HP-Glu from 400 to 1000 μM). The curvature similar to that found in the absence of *p*HP-Glu was evident in measurements obtained with successively increasing concentrations of *p*HP-Glu present in the solution; however, increasing the concentration tended to remove the curvature, particularly above concentrations of 600 μM.

The generation of currents upon exposure of electrode surfaces to visible and ultraviolet light has been documented.[33,34] Although these currents reach peak values over extended continuous exposure times, their measurement at carbon-fiber microelectrodes with FSCV has not been published in the literature, to our knowledge. We found that, in our particular case, this photo-induced current could be subtracted from the currents produced in the presence of *p*HP-Glu to yield current time points that fall into a linear relationship with increasing time of light exposure (Fig. 6B; linear regression analysis: $R^2 = 0.9998$ (1000 μM), 0.9987 (800 μM), 0.9942 (600 μM), and 0.9690 (400 μM), N=3 electrodes). The linear character of these curves suggests that the light artifact can be removed from the overall electrochemical signal and the remaining currents can be used to monitor the formation of 4HPAA.

Generation of a calibration curve.

Our ability to isolate currents produced by photolysis indicates that quantitation of 4HPAA in the solution is feasible. However, a critical aspect of this quantitation is the correction for other electrochemically active species present. Therefore, we designed a microliter reaction vessel (Fig. 2) that allows direct comparison between oxidation currents that occur during photoreaction, obtained by FSCV, and the actual concentration of 4HPAA photo-released, determined by high performance liquid chromatography (HPLC). The reaction vessel was fabricated with a ~3 cm long segment of plastic tubing that allowed small volumes (~3 μL) of *p*HP-glutamate solution to be immobilized due to the surface tension of the water. A 1 mm fiber-optic cable was positioned in the tube, but below the solution, so that the entire solution could be irradiated. After adding the solution, the carbon-fiber and Ag/AgCl electrodes were inserted, thereby allowing the measurement of photo-uncaging events with electrochemistry.

We measured how 4HPAA concentration changes at different UV exposure times by combining FSCV and HPLC analyses. The process of generating a light intensity independent calibration curve is illustrated in Figs. 7A through 7C. The typical recording of a photo-uncaging measurement involved the background subtraction of an averaged group of reference CVs, collected prior to light application, from the entire set of CVs obtained in the file. This operation removes current contributions from un-photolyzed *p*HP-Glu and generates a CV similar to that shown in Fig. 4. The photo-uncaging of *p*HP-Glu, present in the vessel at an initial concentration of 1000 μM, was measured with FSCV as a function of exposure time. After removing the electrodes, the sample solution was analyzed by HPLC. Currents generated at each time point were also obtained in the absence of *p*HP-Glu, and were subtracted from the measurements in which *p*HP-Glu was present. This operation removes the artifactual current generated by light application, similar to the subtraction process in Fig. 6.

From this analysis we constructed two linear graphs that plotted current (Fig. 7A, $R^2 = 0.9985$) and 4HPAA concentration (Fig 7B, $R^2 = 9986$) against exposure time. Combining these graphs provided a third linear plot that directly related current to 4HPAA concentration (Fig. 7C, $R^2 = 0.9980$). By direct quantification of 4HPAA and knowing that 0.95 molecules of 4HPAA are released for every molecule of glutamate in aqueous solutions at

physiological pH,[35,36] we are able to quantify glutamate generated by photoactivation of *p*HP-Glu. Therefore, this method represents a means for quantifying the released, biologically active glutamate that is more direct than actinometry. Furthermore, knowing the relative yield and the quantum efficiency for 4HPAA from the photo-release of any *p*HP leaving group (whether electroactive or not), one can temporally track the concentration of the leaving group on a real-time basis in a microliter sized vessel.

Electrochemical detection of *p*HP-glutamate photo-activation in a zebrafish brain.

We next sought to validate our newly developed method for *in situ* electrochemical detection of photo released 4HPAA in living, whole zebrafish brain, which is opaque. After brain dissection, the carbon-fiber microelectrode and optic fiber were positioned in telencephalon, in close proximity to each other (Fig. 8), and the brain was perfused by oxygenated aCSF for 40 minutes. Upon stabilization of the background signal, 1000 ms light pulses were applied in order to quantify the photoelectric effect in brain tissue responsible for the above discussed light artifact. A current of 0.52 ± 0.04 nA (N = 3) was recorded.

The uncaging of *p*HP-Glu was photochemically evoked after 30 min of brain perfusion with 1000 μM *p*Hp-glutamate in aCSF. The light was applied with a duration of 1000 ms. Representative data documenting the successful uncaging process in whole brain and subsequent detection of 4HPAA are shown in Fig. 8. A cyclic voltammogram sampled from the color plot at the time of light exposure (5 s) exhibits characteristics reflecting the oxidation of 4HPAA, including a prominent peak in current on the reverse scan at +1.24 V. The examination of the photo-released current vs. time plot (Fig. 8, above color plot) shows a large increase in current at the time of light exposure. The measured current is significantly higher compared to the one recorded during light artifact measurement (Fig. 9, One-way ANOVA with Tukey test, $p < 0.0001$), and, therefore, can be assigned primarily as a voltammetric response to the appearance of photo-released 4HPAA.

We observed a prolonged current in the *I-t* profile. It is possible that this current arises from adsorption of 4HPAA or another uncaging product to the electrode surface, resulting in either a faradaic current or alteration of the electrode double layer capacitance. Another contribution to this current might be slower diffusion of 4HPAA in the brain tissue. More work is needed to characterize each of these contributions. After subtraction of the photo-induced current, the resulting current was 1.23 ± 0.06 nA (N = 3 different electrodes and locations), which corresponds to formation of 21.1 ± 0.9 μM of 4HPAA (calculated from the concentration *vs.* current plot, Figure 7C) and 22.2 ± 1.0 μM glutamate. Significantly lower signal was obtained for the experiments carried out in whole brain in comparison with the one performed in the reaction vessel (for the same exposure time of 1000 ms), suggesting lower uncaging power of the system in an opaque brain tissue. Despite this fact, we have successfully provided proof-of-concept for our newly developed method for the *in situ* monitoring of caged compound photochemistry. Importantly, the uncaging capacity is powerful enough to photo-release an amount of glutamate in excess of its estimated extracellular concentration range (0.02 to 20 μM).[37] Additionally, the amount of the photo-released glutamate can be tailored based on individual needs, as the released concentration can be altered by the length of the uncaging time and light intensity.

Finally, to ensure that the recorded signal arises from the oxidation of 4HPAA, we conducted an experiment in which we applied a pulse of light to the zebrafish brain in the region where the electrode was located and measured the current response with FSCV. Prior to adding *p*HP-Glu, a small artifactual current signal occurred that aligned with the light application. Upon application of *p*HP-Glu for 30 min, the magnitude of this light-induced signal increased several fold. After washing out the *p*HP-Glu (and the products of the uncaging process) for at least 30 min, the signal returned to a level similar to that noted prior adding *p*HP-Glu (Fig. 9, one-way ANOVA with Tukey test, $p = 0.3462$, $N = 3$ different locations). These data indicate that the observed current arises from 4HPAA formation and possibly other electrochemically active species formed from the uncaging process, and not simply the light artifact.

CONCLUSION

Our newly-developed method can be used to quantify the degree of caged compound photolysis in situ with FSCV, a well-characterized electrochemical method. This approach is largely independent of the characteristics of the light source because light artifacts are subtracted out and the electrochemical signal is related directly to the concentration. Thus, our method depends only upon the electroactivity of the photo-released cage, in this case 4HPAA. Importantly, we have shown that 4HPAA, the product of photo released *p*HP-glutamate, can be easily detected and quantified in the telencephalon of zebrafish whole brain. Thus, our work demonstrates the feasibility of photo delivering biologically active compounds in living tissues. In future studies, it will be important to validate this method in higher species such as mice and rats. This point is especially important since the brains in these species may have a more complex chemical makeup and opacity, resulting in problems such as increased electrode fouling or impairment of light access. Nevertheless, we expect this approach to have broad applicability, but it will be particularly well suited for cases that make quantitation of photons reaching the sample difficult, such as tissues or opaque liquids. Moreover, this method should also work when using caged compounds other than those based on *p*HP that release electroactive photocages, such as coumarins. Ultimately, adapting this method for *in vivo* application with a combined electrode, light-guide, and caged compound delivery method will maximize its utility.

ACKNOWLEDGMENTS

Support for this research was provided by grants from the National Institute of Neurological Disorders and Stroke of the National Institutes of Health under Award Numbers R21NS109659 (MAJ) and R21NS077485 (MAJ). Additionally, MAJ received support from the Center for Molecular Analysis of Disease Pathways and the Synthetic Chemical Biology Core, an NIH Center of Biomedical Research Excellence (COBRE), supported by an Institutional Development Award (IDeA) from the National Institute of General Medical Sciences of the National Institutes of Health under Award Number P20GM103638. RJ received financial support from Charles University in Prague under Award Number SVV260560.

REFERENCES

(1). McCray JA; Trentham DR Properties and Uses of Photoreactive Caged Compounds. Annu. Rev. Biophys. Biophys. Chem 1989, 18, 239–270. [PubMed: 2660825]

(2). Adams SR; Tsien RY Controlling Cell Chemistry with Caged Compounds. Annu. Rev. Physiol 1993, 55 (1), 755–784. [PubMed: 8466191]

(3). Ellis-Davies GCR Caged Compounds: Photorelease Technology for Control of Cellular Chemistry and Physiology. Nat. Methods 2007, 4 (8), 619–628. [PubMed: 17664946]

(4). Ellis-Davies GCR Chemist and Biologist Talk to Each Other about Caged Neurotransmitters. Beilstein J. Org. Chem 2013, 9, 64–73. [PubMed: 23399979]

(5). Furuta T Designing Caged Compounds for Spatiotemporal Control of Cellular Chemistry. Yuki Gosei Kagaku Kyokaishi/Journal Synth. Org. Chem 2012, 70 (11), 1164–1169.

(6). Corrie JET; Furuta T; Givens RS; Yousef AL; Goeldner M Photoremovable Protecting Groups Used for the Caging of Biomolecules. Dyn. Stud. Biol. Phototriggers, Photoswitches Caged Biomol 2005, 1–94.

(7). Klán P; Šolomek T; Bochet CG; Blanc A; Givens R; Rubina M; Popik V; Kostikov A; Wirz J Photoremovable Protecting Groups in Chemistry and Biology: Reaction Mechanisms and Efficacy. Chem. Rev 2013, 113 (1), 119–191. [PubMed: 23256727]

(8). Callaway EM; Katz LC Photostimulation Using Caged Glutamate Reveals Functional Circuitry in Living Brain Slices. Proc. Natl. Acad. Sci. U. S. A 1993, 90 (16), 7661–7665. [PubMed: 7689225]

(9). Augustine GJ Combining Patch-Clamp and Optical Methods in Brain Slices. J. Neurosci. Methods 1994, 54 (2), 163–169. [PubMed: 7869749]

(10). Wang SSH; Augustine GJ Confocal Imaging and Local Photolysis of Caged Compounds: Dual Probes of Synaptic Function. Neuron 1995, 15 (4), 755–760. [PubMed: 7576625]

(11). Lipp P; Lüscher C; Niggli E Photolysis of Caged Compounds Characterized by Ratiometric Confocal Microscopy: A New Approach to Homogeneously Control and Measure the Calcium Concentration in Cardiac Myocytes. Cell Calcium 1996, 19 (3), 255–266. [PubMed: 8732265]

(12). Hagen V; Frings S; Wiesner B; Helm S; Kaupp UB; Bendig J [7-(Dialkylamino)Coumarin-4-Yl]Methyl-Caged Compounds as Ultrafast and Effective Long-Wavelength Phototriggers of 8-Bromo-Substituted Cyclic Nucleotides. ChemBioChem 2003, 4 (5), 434–442. [PubMed: 12740815]

(13). Bardhan A; Deiters A Development of Photolabile Protecting Groups and Their Application to the Optochemical Control of Cell Signaling. Curr. Opin. Struct. Biol 2019, 57, 164–175. [PubMed: 31132552]

(14). Gienger M; Hübner H; Löber S; König B; Gmeiner P Structure-Based Development of Caged Dopamine D2/D3 Receptor Antagonists. Sci. Rep 2020, 10 (1).

(15). Asad N; Mclain DE; Condon AF; Gore S; Hampton SE; Vijay S; Williams JT; Dore TM Photoactivatable Dopamine and Sulpiride to Explore the Function of Dopaminergic Neurons and Circuits. ACS Chem. Neurosci 2020, 11 (6), 939–951. [PubMed: 32077679]

(16). Hatchard CG; Parker CA A New Sensitive Chemical Actinometer - II. Potassium Ferrioxalate as a Standard Chemical Actinometer. Proc. R. Soc. London. Ser. A. Math. Phys. Sci 1956, 235 (1203), 518–536.

(17). Heien MLAV; Johnson MA; Wightman RM Resolving Neurotransmitters Detected by Fast-Scan Cyclic Voltammetry. Anal. Chem 2004, 76 (19), 5697–5704. [PubMed: 15456288]

(18). Troyer KP; Wightman RM Dopamine Transport into a Single Cell in a Picoliter Vial. Anal. Chem 2002, 74 (20), 5370–5375. [PubMed: 12403595]

(19). Ortiz AN; Kurth BJ; Osterhaus GL; Johnson MA Dysregulation of Intracellular Dopamine Stores Revealed in the R6/2 Mouse Striatum. J. Neurochem 2010, 112 (3), 755–761. [PubMed: 19929911]

(20). Ortiz AN; Oien DB; Moskovitz J; Johnson MA Quantification of Reserve Pool Dopamine in Methionine Sulfoxide Reductase A Null Mice. Neuroscience 2011, 177, 223–229. [PubMed: 21219974]

(21). Maina FK; Khalid M; Apawu AK; Mathews TA Presynaptic Dopamine Dynamics in Striatal Brain Slices with Fast-Scan Cyclic Voltammetry. J. Vis. Exp 2012, No. 59, 1–6.

(22). Kaplan SV; Limbocker RA; Gehringer RC; Divis JL; Osterhaus GL; Newby MD; Sofis MJ; Jarmolowicz DP; Newman BD; Mathews TA; et al. Impaired Brain Dopamine and Serotonin Release and Uptake in Wistar Rats Following Treatment with Carboplatin. ACS Chem. Neurosci 2016, 7 (6), 689–699. [PubMed: 27145395]

(23). Johnson MA; Rajan V; Miller CE; Wightman RM Dopamine Release Is Severely Compromised in the R6/2 Mouse Model of Huntington's Disease. J. Neurochem 2006, 97 (3), 737–746. [PubMed: 16573654]

(24). Johnson MA; Villanueva M; Haynes CL; Seipel AT; Buhler LA; Wightman RM Catecholamine Exocytosis Is Diminished in R6/2 Huntington's Disease Model Mice. J. Neurochem 2007, 103 (5), 2102–2110. [PubMed: 17868298]

(25). Kraft JC; Osterhaus GL; Ortiz AN; Garris PA; Johnson MA In Vivo Dopamine Release and Uptake Impairments in Rats Treated with 3-Nitropropionic Acid. Neuroscience 2009, 161 (3), 940–949. [PubMed: 19362126]

(26). Mohanaraj S; Wonnenberg P; Cohen B; Zhao H; Hartings MR; Zou S; Fox DM; Zestos AG Gold Nanoparticle Modified Carbon Fiber Microelectrodes for Enhanced Neurochemical Detection. J. Vis. Exp 2019, 2019 (147).

(27). Smith AR; Garris PA; Casto JM Real-Time Monitoring of Electrically Evoked Catecholamine Signals in the Songbird Striatum Using in Vivo Fast-Scan Cyclic Voltammetry. J. Chem. Neuroanat 2015, 66–67, 28–39.

(28). Weisz CJC; Rubio ME; Givens RS; Kandler K Excitation by Axon Terminal GABA Spillover in a Sound Localization Circuit. J. Neurosci 2016, 36 (3), 911–925. [PubMed: 26791220]

(29). Goeldner M; Givens RS Dynamic Studies in Biology: Phototriggers, Photoswitches and Caged Biomolecules. Dyn. Stud. Biol. Phototriggers, Photoswitches Caged Biomol 2005, 1–557.

(30). Shin M; Kaplan SV; Raider KD; Johnson MA Simultaneous Measurement and Quantitation of 4-Hydroxyphenylacetic Acid and Dopamine with Fast-Scan Cyclic Voltammetry. Analyst 2015, 140 (9), 3039–3047. [PubMed: 25785694]

(31). Kandler K; Nguyen T; Noh J; Givens RS An Optical Fiber-Based Uncaging System. Cold Spring Harb. Protoc 2013, 8 (2), 118–121.

(32). Shin M; Field TM; Stucky CS; Furgurson MN; Johnson MA Ex Vivo Measurement of Electrically Evoked Dopamine Release in Zebrafish Whole Brain. ACS Chem. Neurosci 2017, 8 (9), 1880–1888. [PubMed: 28617576]

(33). Barker GC; Gardner AW; Sammon DC Photocurrents Produced by Ultraviolet Irradiation of Mercury Electrodes. J. Electrochem. Soc 1966, 113 (11), 1182.

(34). Barazzouk S; Hotchandani S; Vinodgopal K; Kamat PV Single-Wall Carbon Nanotube Films for Photocurrent Generation. A Prompt Response to Visible-Light Irradiation. J. Phys. Chem. B 2004, 108 (44), 17015–17018.

(35). Givens RS; Weber JFW; Conrad PG; Orosz G; Donahue SL; Thayer SA New Phototriggers 9: P-Hydroxyphenacyl as a C-Terminal Photoremovable Protecting Group for Oligopeptides. J. Am. Chem. Soc 2000, 122 (12), 2687–2697.

(36). Givens RS; Stensrud K; Conrad PG; Yousef AL; Perera C; Senadheera SN; Heger D; Wirz J P-Hydroxyphenacyl Photoremovable Protecting Groups Robust Photochemistry despite Substituent Diversity. Can. J. Chem 2011, 89 (3), 364–384. [PubMed: 24436496]

(37). Moussawi K; Riegel A; Nair S; Kalivas PW Extracellular Glutamate: Functional Compartments Operate in Different Concentration Ranges. Front. Syst. NeSSurosci 2011, 5 (11).

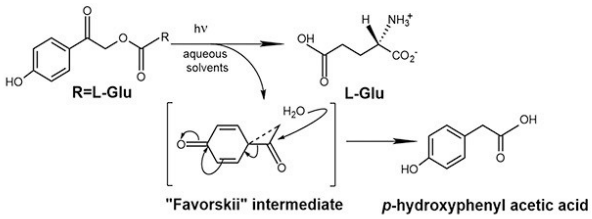

Figure 1.
Reaction mechanism of uncaging *p*-hydroxyphenacyl-based compounds.

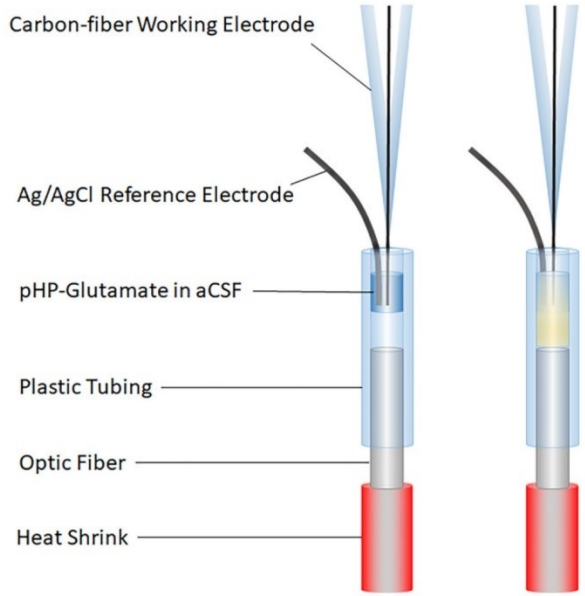

Figure 2.
Microliter-scale reaction vessel used to determine degree of photo-uncaging with FSCV. Left, without light application and right, with light application through the optical fiber.

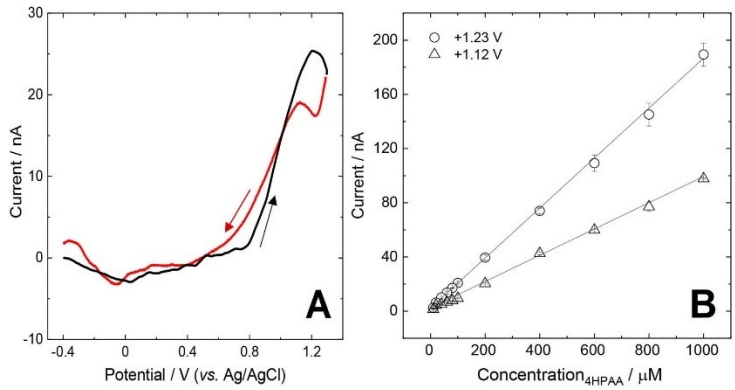

Figure 3.

(A) Fast-scan cyclic voltammetric *i-E* curve for 100 μM 4HPAA in aCSF measured at carbon fiber microelectrode in flow injection arrangement. Two oxidation peaks occur at 1.23 V and 1.12 V on the forward and backward sweep, respectively. Direction of the forward (black) and the reverse (red) potential sweep is indicated by arrows. (B) Response curve for 4HPAA in aCSF for injected concentrations from 1000 to 10 μM. Evaluated from the peak at +1.23 V, obtained on the forward sweep (○) and +1.12 on the backward sweep (△).N ≥ 3, data are presented as mean ± std. dev.

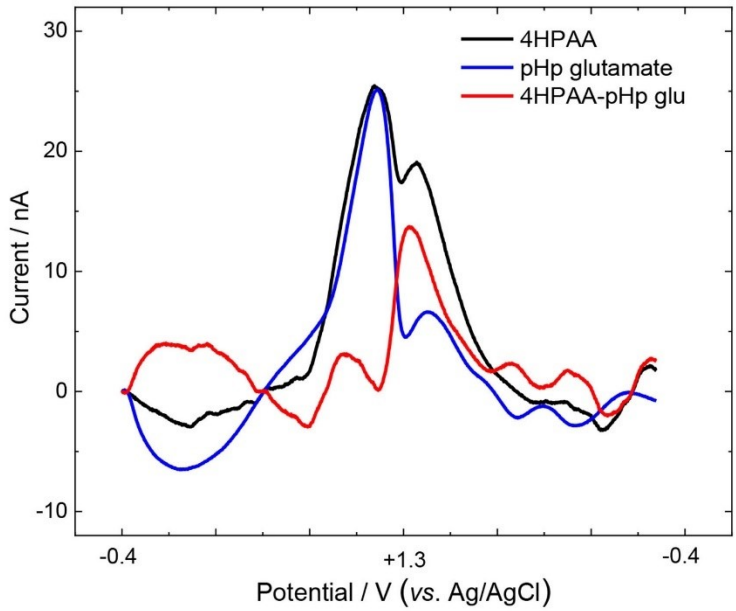

Figure 4.

Flow injection analysis of *p*HP-Glu and 4HPAA. Solutions of 100 μM *p*HP-Glu and 100 μM 4HPAA in aCSF were injected separately. Parameters: scan rate, 600 V/s, update rate, 10 CVs/s, holding potential, −0.4 V.

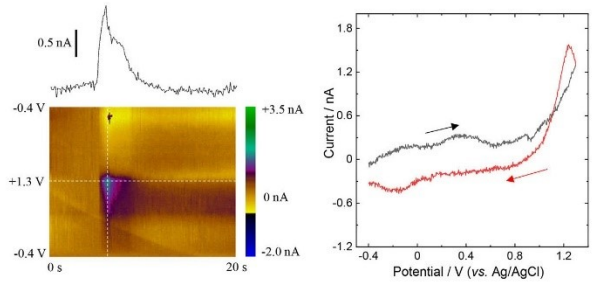

Figure 5.

Current response measured in a solution containing 0 μM of *p*HP-Glu and, therefore, attributed to a light artifact. A representative current vs. time plot (top), color plot (bottom), and FSCV (right) are shown. Direction of the potential sweep is indicated by arrows. Duration of light exposure: 1000 ms.

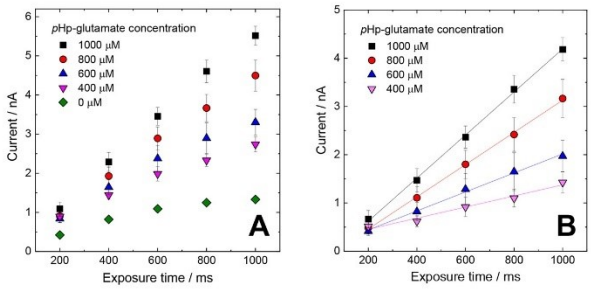

Figure 6.

Light artifact removal. (A) Plot of the oxidation current versus the duration of light exposure. (B) Current response after the subtraction of the light artifact. Data are presented for three measurement at three different carbon-fiber microelectrodes as mean ± std. dev.

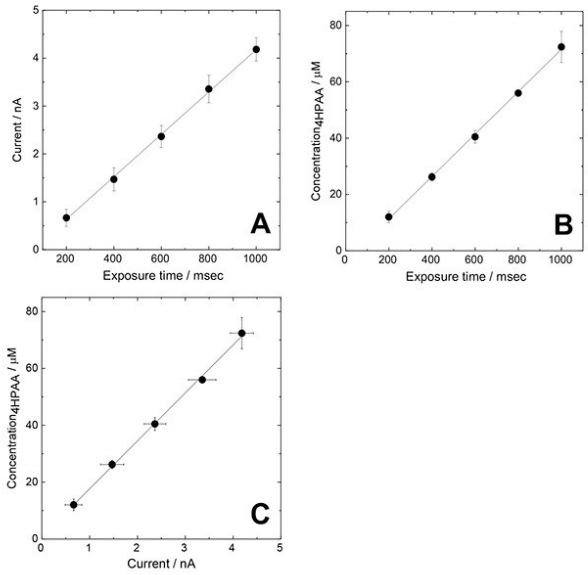

Figure 7.

Generation of a calibration curve independent of the light source characteristics for an electrode. (A) Light artifact-subtracted current response (for 1000 μM *p*HP-glutamate) *vs.* duration of light exposure (B) Concentration of photo-released 4HPAA determined via HPLC vs duration of light exposure. (C) Calibration curve obtained by combining A and B. Data are reported as mean ± std. dev for N = 3 separate electrodes.

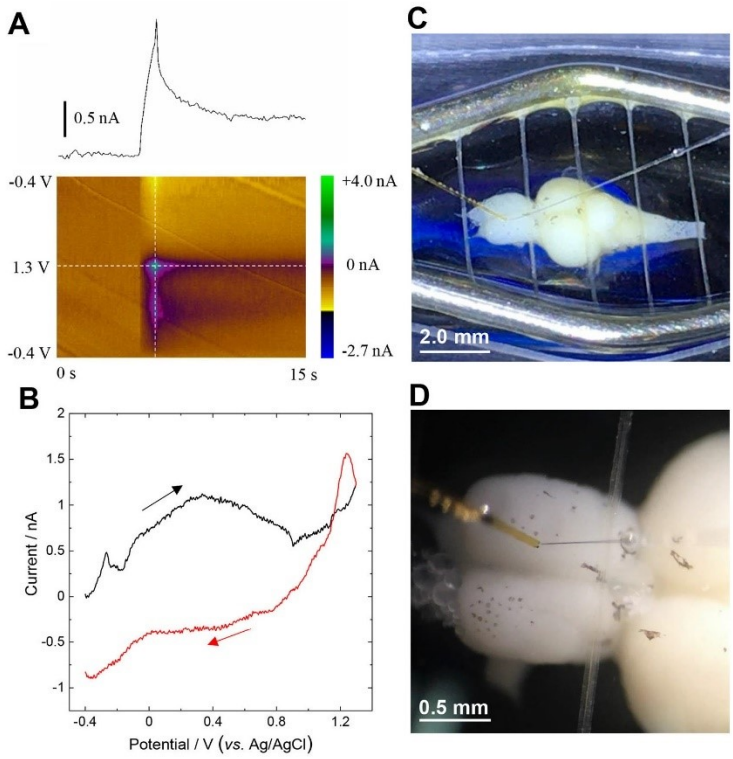

Figure 8.

Representative data of 4HPAA detection in zebrafish whole brain after *p*Hp glutamate photo uncaging. Current vs. time plot with corresponding color plot (A), and CV (B) are shown. 1000 μM of *p*HP-Glu in aCSF was perfused through the brain for 30 minutes. Direction of the potential sweep is indicated by arrows. Duration of light exposure: 1000 ms. The placement of the carbon-fiber working electrode and optic fiber in the telencephalon of zebrafish brain (C and D).

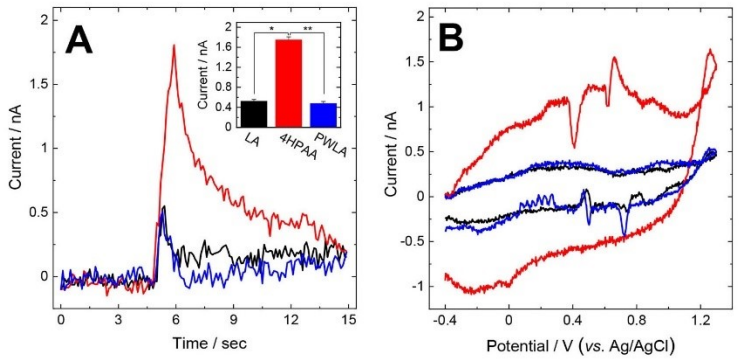

Figure 9.

Representative current *vs.* time (A) and CV (B) data for light artifact (LA) before the *p*Hp glutamate administration (black), photoactivation of *p*HP Glu (red), and the light artifact recorded after 30 minutes post washout (post washout light artifact, PWLA) with *p*Hp-Glu free aCSF (blue). Inset: Photoinduced 4HPAA release measured after 30 minutes of *p*Hp Glu perfusion through the brain was significantly increased in comparison with light artifact (*$p < 0.0001$, one way ANOVA, Tukey post hoc test, N = 3). The light artifact recorded after caged compound washout was significantly different from the 4HPAA measurement (**$p < 0.0001$), but not significantly different from the signal recorded before the caged compound administration ($p = 0.3462$). Duration of light exposure: 1000 ms.

APPENDIX VI

Impaired Dopamine Release and Latent Learning in Alzheimer's Disease Model Zebrafish

Romana Jarošová, Sayuri S. Niyangoda Sayuri, Piyanka Hettiarachchi, and Michael A. Johnson

ACS CHEMICAL NEUROSCIENCE

13 (2022) 2924-2931

ACS Chemical Neuroscience

pubs.acs.org/chemneuro Research Article

Impaired Dopamine Release and Latent Learning in Alzheimer's Disease Model Zebrafish

Romana Jarosova,* Sayuri S. Niyangoda, Piyanka Hettiarachchi, and Michael A. Johnson*

Cite This: https://doi.org/10.1021/acschemneuro.2c00484 Read Online

ACCESS | Metrics & More | Article Recommendations

ABSTRACT: Alzheimer's disease (AD) is a progressive, fatal, neurodegenerative disorder for which only treatments of limited efficacy are available. Despite early mentions of dementia in the ancient literature and the first patient diagnosed in 1906, the underlying causes of AD are not well understood. This study examined the possible role of dopamine, a neurotransmitter that is involved in cognitive and motor function, in AD. We treated adult zebrafish (*Danio rerio*) with okadaic acid (OKA) to model AD and assessed the resulting behavioral and neurochemical changes. We then employed a latent learning paradigm to assess cognitive and motor function followed by neurochemical analysis with fast-scan cyclic voltammetry (FSCV) at carbon fiber microelectrodes to measure the electrically stimulated dopamine release. The behavioral assay showed that OKA treatment caused fish to have lower motivation to reach the goal chamber, resulting in impeded learning and decreased locomotor activity compared to controls. Our voltammetric measurements revealed that the peak dopamine overflow in OKA-treated fish was about one-third of that measured in controls. These findings highlight the profound neurochemical changes that may occur in AD. Furthermore, they demonstrate that applying the latent learning paradigm and FSCV to zebrafish is a promising tool for future neurochemical studies and may be useful for screening drugs for the treatment of AD.

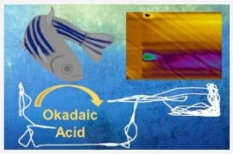

KEYWORDS: *zebrafish, Alzheimer's disease, okadaic acid, dopamine, fast-scan cyclic voltammetry, behavior*

INTRODUCTION

Alzheimer's disease (AD) is an irreversible and progressive neurodegenerative disease that accounts for 60−80% of all dementia cases. A patient with AD may undergo severe cognitive, mental, and social impairment, including memory loss that challenges daily life, confusion with place or time, and poor judgment.[1−3] More than 5.5 million Americans and 44 million people worldwide suffer from AD symptoms, and it is estimated that, by the year 2050, these numbers will triple. Moreover, the cost of treatment in the United States could rise as high as $1.1 trillion.[4−6] Unfortunately, there is still no cure or highly effective drug treatments for AD.[7] Therefore, the development of model organisms that can accurately model AD while providing a way to evaluate potential therapies with enhanced throughput is critical.

AD pathophysiology can be related to two main hallmarks: extracellular formation of amyloid plaques and intracellular aggregation of neurofibrillary tangles (NFTs). Studies of familial AD show sufficient relationship between the disease and mutations in amyloid precursor protein (APP), which is the precursor of Aβ peptides and pencillin1 (PSEN1) and pencillin2 (PSEN2). Both peptides are catalytic subunits in γ secretase responsible for APP cleavage. These mutations result in the formation of more hydrophobic and longer Aβ peptides, which further aggregate into amyloid plaques. Additionally, NFTs are likely also formed due to extensive deposition of tau aggregates. Tau proteins, which are responsible for stabilizing microtubules in the brain, undergo hyperphosphorylation, resulting in destabilization and disintegration into tau aggregates.[8,9] These aberrant molecular changes may cause atrophy, resulting in large-scale alterations in brain size and structure.

Over the past 2 decades, rodents that model AD through different genetic modifications and chemical treatments have contributed immensely toward understanding the cellular mechanisms of AD.[10,11] However, the development of simpler vertebrate model organisms that recapitulate the cellular pathology seen in AD model rodents, while also providing enhanced throughput and cost savings, would benefit AD research.[12] Zebrafish (*Danio rerio*), having a complex central nervous system, is rapidly emerging as a useful model for the study of multiple neurodegenerative diseases[13−15] and represents a potentially useful AD model organism that could provide information complementary to that found using rodents. Zebrafish have a fully sequenced genome, with 70% of the genes showing homology to that of humans, and possess neuronal pathways that are analogous in many cases to

Received: August 14, 2022
Accepted: September 7, 2022

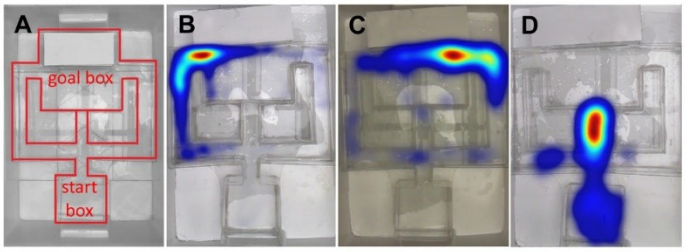

Figure 1. Heatmaps of zebrafish activity in the maze on the probe trial. (A) Testing maze, (B) chemically naive, (C) vehicle-treated, and (D) OKA-treated fish. All fish were trained to the left tunnel. Heatmap of the location of the fish over 10 min trial. The colors represent the duration of time the fish spent in each pixel with low wavelength. Red indicates the longest time, while blue represents the shortest time spent in each pixel.

those found in the mammals.[12,16] Additionally, depending on the experimental design, the use of zebrafish may provide enhanced throughput compared to rodents, as they offer the opportunity to group experiments (drug administration, behavioral analysis, etc.). Recent work has illustrated that a robust zebrafish AD model can be developed by treating the zebrafish with okadaic acid (OKA).[12]

OKA is a polyether fatty acid extracted from marine sponges, and it has been widely used to study the propagation of neurotoxicity of different animal models.[17−19] OKA selectively inhibits protein phosphatases PP1 and PP2A. Inhibition of PP2A, in particular, combined with triggered activation of several major phosphorylating pathways, including MAPK and ERK, induce the hyperphosphorylation of the tau protein, thereby giving rise to the tau aggregates. Additionally, even though the exact mechanism is not well known, OKA gives rise to neurodegeneration by oxidative stress and Aβ deposition.[20−24] The newly developed OKA-induced AD zebrafish model recapitulates most of the pathophysiological conditions prevalent in AD and captures changes in both Aβ-fragments and p-tau protein.[25] Therefore, the OKA acid treated zebrafish are a robust model to study the molecular mechanisms underlying the pathophysiology of AD, or drug discovery for AD, while cutting down the cost and time constraints.

Dopamine, an abundant catecholamine neurotransmitter, plays critical roles in cognitive and motor function in humans and rodents.[26−28] Alterations in dopamine synthesis, storage, release, and uptake likely influence motor and cognitive function in multiple neurological disorders, including Parkinson's disease,[29−33] Huntington's disease,[34−36] and schizophrenia.[37] Similarly, in AD, dopaminergic neurons in the nigrostriatal pathway have shown characteristic pathological changes such as the presence of Aβ plaques and NFTs.[38] However, the precise role of dopamine dysregulation in the expression of cognitive and motor symptoms in AD has not been fully investigated.[38]

Techniques for analyzing zebrafish neurochemistry and behavior have rapidly evolved over the past several years. Fast-scan cyclic voltammetry (FSCV) at carbon fiber microelectrodes is an electrochemical technique that allows measurement of dopamine release and uptake with nM limits of detection and sub-second temporal resolution.[39−43] Recently, our group and others measured sub-second dopamine release and uptake in zebrafish brains ex vivo with FSCV.[42−44]

Behavioral assays that assess cognitive function have also matured. Recently, a behavioral paradigm that targets latent learning was developed and applied to zebrafish.[45] This well-established test shows that zebrafish are capable of latent learning, that is, can acquire memory of their environment after being allowed to explore it.[45,46] Latent learning is a learning exercise based on spatial exploration that uses the natural tendency of the fish to explore novelty.[47,48] In this behavioral assay, zebrafish are exposed to a maze with a particular tunnel opened and allowed to explore the space without any external intervention or reinforcement (i.e., food motivation and punishment). During the free exploration (training) period, no monitoring of the behavioral activity is necessary. The training session is then followed by a short probe session wherein the swim tunnel choice (spacial bias) of the fish is recorded and quantified.[45] Importantly, during the probe period, stimulus fish are placed into a goal box of the maze to enhance their natural need for socialization[49−51] and promote the motivation to reach the goal box.

Critical advantages of this approach are that such training requires no controlled delivery of reinforcers, requires minimal experimenter intervention, and allows more fish to be trained simultaneously. Taken with data obtained by FSCV, this approach can provide an informative picture of how neurochemical changes compare with behavioral changes in disease model and control zebrafish.

Currently, the relation between dopamine release and uptake and cognitive performance in AD model zebrafish is not well characterized. To fill this knowledge gap, we administered OKA to zebrafish to recapitulate the main pathophysiological hallmarks and behavioral conditions observed in AD. We then analyzed the cognitive and locomotor activity of these fish with the latent learning behavioral paradigm[45,46] and measured dopamine release in whole brains ex vivo with FSCV. We found significant deficiencies in latent learning and locomotor activity in OKA-treated fish when compared to controls. These deficiencies were accompanied by impairments in dopamine release. To our knowledge, this study is the first to examine neurotransmitter release and uptake in AD model zebrafish and compare it to behavioral deficiencies.

■ RESULTS AND DISCUSSION

OKA-Treated Fish Showed Cognitive and Motor Impairment. Many AD symptoms are cognition and behavior related, with the majority of patients displaying memory loss, behavior deterioration, thought slowness, and performance impairment.[1,2,52] In this study, the latent learning paradigm was used to investigate the effect of OKA on zebrafish memory

https://doi.org/10.1021/acschemneuro.2c00484
ACS Chem. Neurosci. XXXX, XXX, XXX−XXX

and learning deficits.[45,46] During the probe trial, fish did not show any obvious signs of fear, such as jumping, erratic movement, or freezing since they were exposed to the maze for 9 days during the training period. The testing maze used is shown in Figure 1A. Representative heat maps show a single zebrafish movement (for each treatment) recorded for 10 min during the probe trial (Figure 1). All maps document probe trials for zebrafish trained to enter the left tunnel. Analysis of the heat maps revealed that while chemically naive and vehicle-treated zebrafish tend to spend majority of time in the goal box close to the stimuli fish (Figure 1B,C), OKA-treated fish remained mostly in the blind-ended tunnel and start box (Figure 1D). Such a behavior may be affected by several factors, including motor and locomotion impairment, lower interest to explore the maze, and/or decreased tendency to shoal. The activity level, that is, the swimming velocity and the distance swam, is shown in Figure 2A,B, respectively. Repeated

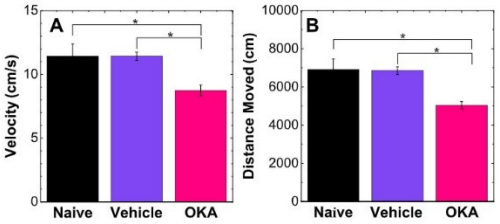

Figure 2. (A) The velocity and (B) moved distance are affected by the treatment condition. Fish treated with OKA showed a significant slower movement and higher freezing time as compared with the chemically naïve and vehicle-treated zebrafish (one-way ANOVA with Tukey's *post hoc* analysis, $p < 0.05$, $n = 14$). *$p < 0.05$. Mean ± SEM are depicted in the chart. Sample size (n) = 14 for each treatment condition.

analysis of multiple zebrafish revealed that OKA-treated zebrafish swam significantly slower and a smaller distance (one-way ANOVA with Tukey's *post hoc* analysis, $p < 0.05$, $n = 14$). These findings, therefore, suggest that OKA treatment causes cognitive and motor dysfunction in zebrafish. Even though motor impairments often occur prior to presentation of cognitive deficits in AD patients,[53] motor dysfunction in OKA-treated rodents is not well documented in the peer-reviewed literature. One study found no effect on motor function in OKA-treated rats;[54] however, other AD model rodents display motor deficits.[55−57] In contrast, we found significant changes in motor function in the OKA zebrafish model. Thus, OKA treatment seems to recreate motor dysfunction more faithfully in zebrafish than in rats. To our knowledge, this is the first study to incorporate latent learning paradigm to assess locomotor activity in AD model zebrafish.

OKA Treatment Affects the Learning and Memory of Zebrafish. Here, we analyzed the choice of the tunnel when they first come out of the start box. Previous studies have proven that repeated exposure of fish to a particular open tunnel significantly affects their choice of tunnel to reach the reward chamber as compared to the untrained groups.[58] Because the maze has two tunnels, a fish that randomly selects a tunnel has a 50% chance of being correct. Therefore, animals are only considered to demonstrate functional learning if they are at least 70% correct at the end of the testing period.[25] During the probe trial (when both tunnels leading to the reward box were opened), 86% of chemically naive and 92% of vehicle-treated fish chose correctly (Figure 3) and first entered

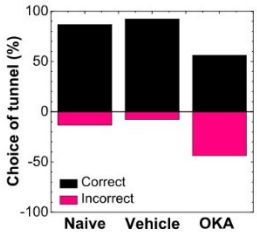

Figure 3. Percentage of individual fish choosing the correct and incorrect tunnel the first time they encounter this choice point when they come out of the start box during the probe trial. The fish treated with OKA tend to choose the incorrect tunnel compared to the naïve and vehicle-treated fish. Sample size $n = 14$ fish for each treatment condition.

the tunnel that was open during their training session. On the contrary, our results demonstrated that the fish treated with OKA have a high tendency to choose the incorrect tunnel (56%). Binominal test confirmed our observation and found that significantly more chemically naive and vehicle-treated fish chose the correct tunnel ($p > 0.05$, binomial distribution probability 0.9963 and 0.9983, respectively) as compared to random chance (50%). The OKA-treated fish did not deviate from the random chance ($p > 0.05$).

These results support our prediction that OKA induces learning and memory impairment of the zebrafish. A large body of literature has reported that OKA treatment in rodents causes memory deficits.[59−61] Inhibition of protein phosphatase 2A has been identified as the ultimate mechanism for the cognitive decline in AD pathology.[20] Given that OKA is a potent and selective inhibitor of PP1 and PP2A activity,[62] these results agree with earlier findings of OKA-induced memory impairments in rodents.

OKA-Treated Fish Have a Prolonged Latency to Leave the Start Box. Figure 4A depicts the results for the latency of fish to leave the start box. This demonstrates the level of motivation of the fish to actively explore the maze. Almost every fish regardless of the treatment condition left the start chamber and explored the maze. However, while the

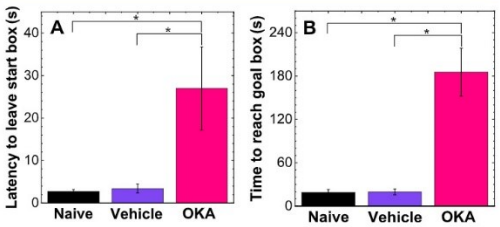

Figure 4. The latency to (A) leave the start box and (B) reach the goal box is affected by the treatment condition. Fish treated with OKA showed a significant latency to leaving the start box (reach the goal box) as compared with the chemically naive and vehicle-treated zebrafish (one-way ANOVA with Tukey's *post hoc* analysis, $p < 0.05$, $n = 14$). *$p < 0.05$. Mean ± SEM are depicted in the chart. Sample size $n = 14$ for each treatment condition.

https://doi.org/10.1021/acschemneuro.2c00484
ACS Chem. Neurosci. XXXX, XXX, XXX−XXX

chemically naive and vehicle-treated fish left the start box almost immediately after removal of the divider (2.7 ± 0.4 and 3.4 ± 1.4 s, respectively), the OKA-treated fish displayed significantly higher latency (one-way ANOVA with Tukey's *post hoc* analysis, $p < 0.05$) to leave the start box (27 ± 10 s). The lower tendency to leave the start box could be attributed to the decreased motivation of the fish to access the stimulus fish in the reward box.[63] The latency to leave the start box of chemically naive and vehicle-treated groups was not significantly different from each other.

OKA-Treated Fish Required a Greater Amount of Time to Reach the Goal Box. The period of time between leaving the start box and entering the reward chamber was greater when testing OKA-treated fish compared to controls. This time reflects the motivation and ability to reach the goal box and stay with the group of fish that served as the stimulus. As shown in Figure 4B, the fish treated with OKA showed a significantly higher latency to enter the reward box (185 ± 33 s) as compared to the chemically naive and vehicle-treated fish (18 ± 4 and 20 ± 4 s, respectively) (one-way ANOVA with Tukey's *post hoc* analysis, $p < 0.05$). No statistical difference was found between chemically naive and vehicle-treated fish. This increased latency to enter the reward chamber of the OKA-treated fish may indicate impaired latent learning and spatial memory. Our findings are consistent with previous studies that show deficits in spatial learning and memory in OKA-infused rats.[54]

OKA-Treated Fish Showed Significant Immobility. In addition to completing the behavioral study, we have also quantified freezing (immobility), a zebrafish innate response to aversive or painful events.[64] A growing body of evidence has reported on a link between immobility and fear-like behavior in zebrafish.[46,65,66] Figure 5 shows the fish freezing response

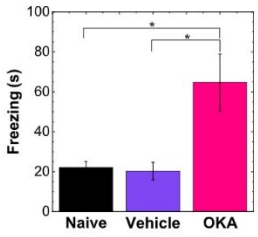

Figure 5. Duration of time freezing during the probe trial is affected by the treatment condition. Fish treated with OKA showed a significant immobility as compared with the chemically naive and vehicle-treated zebrafish (one-way ANOVA with Tukey's *post hoc* test, $p < 0.05$, $n = 14$). *$p < 0.05$. Mean ± SEM are depicted in the chart. Sample size $n = 14$ for each treatment condition.

within each group throughout the probe trial. Tukey's post hoc test ($p < 0.05$) confirmed that fish exposed to OKA exhibited significantly higher values of immobility as compared to chemically naive and vehicle-treated fish. We speculate that the observed increased freezing may be related to a fear or fear-induced anxiety. It is possible that dopaminergic impairment contributes to this behavior. Though often neglected, it has been suggested that dopamine has a greater significance to the induction of anxious states than generally appreciated and is one of the neurotransmitters most potently modulating the mechanism underlying states of fear and anxiety.[67−69] However, the significance of dopamine in fear-like behavior requires further investigation.

Taken collectively, our results indicate that OKA treatment impairs memory acquisition and consolidation in the zebrafish. The shorter latencies leaving the start box and entering the reward chamber observed in naive and vehicle fish have indicated that these control fish have learned the spatial layout of the maze better than the OKA-treated fish. For the first time, our results demonstrate that a latent learning paradigm can detect the cognitive and behavioral impairments in OKA-induced Alzheimer's model zebrafish.

Neurochemical Response to OKA Administration. Extensive evidence implicates dopamine in learning and memory. To determine if alterations in dopamine release correlate with behavioral deficits, we used FSCV to measure electrically stimulated dopamine release in live brains harvested from OKA-treated, vehicle-treated, and chemically naive fish. Representative raw data are shown in Figure 6. The color plots (Figure 6A) fail to reveal additional release chemical species. There is a tendency for the current signal to linger on the back side of the i versus t curves (Figure 6B). We have studied this phenomenon previously and concluded that it may result from adsorbed dopamine.[43]

Statistical comparison revealed that zebrafish exposed to OKA had significantly less dopamine release (one-way ANOVA with Tukey's *post hoc* analysis, $p < 0.05$, $n = 14$) than naive and vehicle-treated fish (Figure 7A). There was no significant difference between naive and vehicle-treated fish. When results were broken down by sex, analysis by two-way ANOVA revealed no main effect of sex on dopamine release ($p < 0.05$, $n = 7$) or interaction between treatment condition and sex ($p < 0.05$, $n = 7$) (Figure 7B). Dopamine release in the dorsal striatum[36,70] and nucleus accumbens in rodents[71] play important roles in motor control and learning. Therefore, it is possible that diminished dopamine release plays a role in locomotor and cognitive impairment in this AD model organism; however, more studies are needed to demonstrate cause and effect.

Several previous studies of dopamine release have been published.[42−44] However, to our knowledge, the only other published study to examine dopamine release in chemically treated fish was carried out by our group and involved the treatment of zebrafish with carboplatin, a cancer chemotherapy agent.[42] A previous study identified synaptic vesicle alterations in neurons from frogs.[72] However, this is the first study, to our knowledge, that examines dopamine release in a zebrafish model of neurodegeneration. We were easily able to resolve differences in dopamine release between treated and control fish. This work not only raises the possibility that dopamine release impairments play a role in cognitive and motor dysfunction in AD model zebrafish but also provides an assay to screen for potential therapies.

■ CONCLUSIONS

In this study, OKA was administered to zebrafish to induce an AD-like pathophysiology. By incorporating fish in a previously published latent learning paradigm, we found that treatment with OKA induced serious impairments in learning and locomotion. Also, OKA treatment resulted in diminished dopamine release. Considering the practical advantages of zebrafish, such as increased throughput in behavioral experiments compared to rodents, lower cost, and the ease of neurochemical measurements, we believe that our study

https://doi.org/10.1021/acschemneuro.2c00484
ACS Chem. Neurosci. XXXX, XXX, XXX−XXX

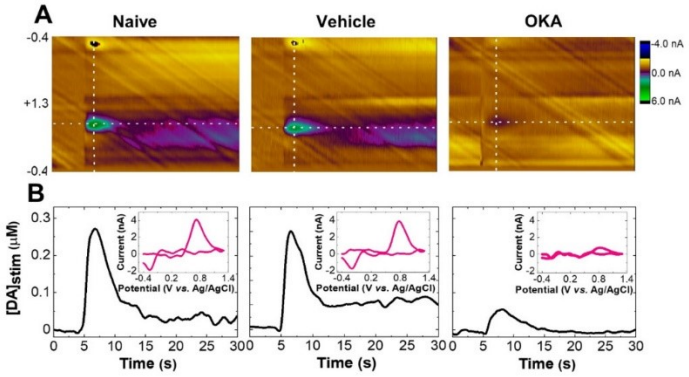

Figure 6. (A) Representative FSCV color plots of the stimulated dopamine release in chemically naïve, vehicle-, and OKA-treated zebrafish whole brain. (B) $i-t$ curve extracted from the horizontal dashed line. Inset: cyclic voltammograms extracted from the vertical dashed line.

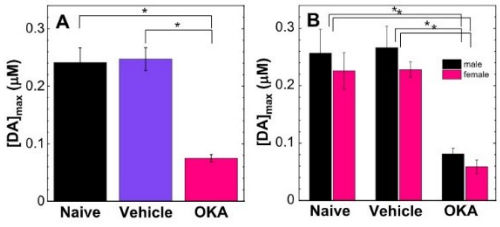

Figure 7. Effect of OKA treatment on evoked dopamine release. (A) OKA treatment has a significant effect on evoked dopamine release in zebrafish whole brains (one-way ANOVA with Tukey's *post hoc* analysis, $p < 0.05$, $n = 14$). (B) There was no significant difference in the DA release in male vs female zebrafish in each treatment group ($p < 0.05$, two-way ANOVA, $n = 7$). $p < 0.05$. Mean ± SEM are depicted in the chart. Sample size $n = 14$ for each treatment condition.

provides a promising step toward the sensitive detection of neurochemical and behavioral changes in models of AD and other neurological diseases. Moving forward, our approach will also be useful for the behavioral and neurochemical evaluation of therapeutic compounds with enhanced throughput.

■ EXPERIMENTAL SECTION

Chemicals. OKA Na salt was purchased from LC Laboratories (Woburn, MA) and dissolved in 95% ethanol. The dissolved OKA was diluted with system water to a final concentration of 100 nM. All chemicals for preparation of artificial cerebrospinal fluid (aCSF; 126 mM NaCl, 2.5 mM KCl, 1.2 mM NaH_2PO_4, 2.4 mM $CaCl_2$, 1.2 mM $MgCl_2$, 25 mM $NaHCO_3$, and 20 mM HEPES, adjusted to pH 7.4 with 1 M NaOH) were purchased form Sigma-Aldrich (St. Louis, MO) and used as received. Dopamine for electrode pre- and post-calibration was purchased from Sigma-Aldrich (St. Louis, MO). Dopamine stock solution was prepared in 0.2 M perchloric acid and diluted prior to the calibrations with aCSF (with no glucose). Ultrapure water (~18.2 MΩ cm) was used for the preparation of aCSF.

Animals and Housing. A total of 53 (4 months old, male: female = 1:1) adult wild-type zebrafish (*D. rerio*) were used in this study. The experimental fish were divided into six groups with each group containing eight fish. In addition, five stimulus fish were used. All fish were housed in the Shankel Structural Biology Center at the University of Kansas. Protocols and procedures involving zebrafish were approved by the Animal Care and Use Committee of the University of Kansas.

OKA Treatment. The 9 day-long treatment protocol was previously described by Nada et al.[25] The OKA-treated fish were exposed to a 100 nM OKA in system water. A stock solution of OKA was prepared by dissolving OKA in 95% ethanol (EtOH) and further diluted to a final concentration of 100 nM in fish system water. For a vehicle group, an equivalent volume of 95% EtOH was added to the system water, resulting in a final concentration of 0.01% of EtOH. Last, chemically naive fish were housed in system water with no treatment. The water, with OKA (EtOH, respectively) treatment in respective tanks, was refreshed every other day. The behavioral and neurochemical studies were performed on the 10th day.

Maze Apparatus and Learning Procedure. The maze apparatus used in this study was similar to the one designed by Gómez-Laplaza and Gerlai.[45] The homemade maze was constructed using transparent plexiglass that allowed a clear vision over the entire maze for all studied fish. The start box served as an acclimatization area and branched into three tunnels: a left and right tunnel that led to the goal box and a dead-ended straight tunnel. The maze was filled with system fish water to achieve approximately 10 cm water depth. The water was kept at the same temperature as water in the housing tanks and was exchanged daily.

To assess the learning protocol, fish were grouped based on their treatment protocol (chemically naive, vehicle, and OKA treatment) and further split based on the designated training tunnel (i.e., group trained to choose right or left tunnel). The learning procedure was adapted from a study described elsewhere.[46] Briefly, during the learning period, all fish from a specific group were placed into a start box and allowed to acclimatize for 30 s. After the acclimatization period, a divider between the start box and the rest of the maze was removed, and all fish were allowed to explore the maze without any intervention for 20 min. Half of the fish of each treatment protocol were allowed to explore the maze with the right tunnel closed, while the second half with the left tunnel closed. This tunnel arrangement remained the same during the entire training protocol. The goal box was kept empty during the learning session to ensure no stimulation and/or reinforcement for the fish. Such a training trial was carried out daily for 9 consecutive days and occurred at randomly selected times during the day. No video record was taken during the training period.

The learning period and the OKA treatment protocol were synchronized and concluded by a probe trial (day 10) to evaluate the zebrafish memory and learning. During the probe trial, only a single experimental fish was placed into the start box. After the acclimatization time, the experimental fish was released into the maze. Importantly, both left and right tunnels were open during the probe trial. In addition, five stimulus fish were placed into a newly created compartment in the reward box. We hypothesized that the

https://doi.org/10.1021/acschemneuro.2c00484
ACS Chem. Neurosci. XXXX, XXX, XXX−XXX

natural need for socialization[49−51] will drive the motivation of zebrafish to reach the goal box. The individual zebrafish behavior in the maze was monitored for 10 min using a Nikon D3500 DX camcorder. Video files were analyzed using a EthoVision XT video tracking software (Noldus, InfoTech., Wageningen, The Netherlands).

Electrochemical Measurements. The electrochemical measurement was carried out the same day as the behavioral probe trial. The procedure to harvest the zebrafish brain was described elsewhere.[43,73,74] Briefly, the examined fish was euthanized by a rapid cooling method, followed by decapitation. Immediately following euthanasia, the whole brain was harvested using previously described methods and transferred to a perfusion chamber. The brain was kept viable by a continuous flow of oxygenated and pH corrected aCSF. The system was kept at a stable temperature of 28 °C prior to any measurement, and the brain was allowed to equilibrate in the chamber for 40 min.

Carbon fiber working electrodes were constructed following the previously published procedure.[75] Briefly, a 7 μm diameter carbon fiber (Goodfellow Cambridge LTD, Huntingdon, UK) was aspirated into a glass capillary tube (1.2 mm outer diameter, 0.68 mm inner diameter, A-M system Inc., Carlsberg, WA, USA) and fixed in the position by sealing the glass capillary around the fiber using a heated coil puller (PE-22, Narishige Int. USA, East Meadow, NY). Next, the exposed carbon fiber was trimmed to approximately 40 μm from the end of the pulled glass capillary, and an epoxy seal was created (EPON resin 815C, EPIKURE 3234 curing agent, Miller-Stephenson, Danbury, CT, USA). The microelectrode was further cured at 100 °C for 1 h and cleaned by soaking in ultrapure isopropanol for 30 min. To ensure electrical connection between the carbon fiber and electrode holder, all electrodes were backfilled with 0.5 M potassium acetate, and a silver wire was inserted.

A Chem Clamp potentiostat (Dagan, Minneapolis, MN) modified to enhance the range of available gain settings was used. TarHeel CV software (M.L.A.V. Heien and R.M. Wightman, University of North Carolina, Chapel Hill, NC) with data acquisition PCI 6711 multifunction I/O board (National Instruments, Austin, TX) was used to collect and analyze all data. The traditional dopamine waveform (from −0.4 to 1.3 and back to −0.4 V at 400 V/s) was applied every 100 ms (i.e., 10 Hz application frequency). Dopamine release was evoked by multiple stimulus pulses (25 pulses, 2 ms, 350 μA) applied by stimulus electrode (two tungsten electrodes positioned 200 μm apart). The stimulus pulses were applied to the dorsal nucleus of the ventral telencephalon with a 10 min recovery time between each stimulation.

AUTHOR INFORMATION

Corresponding Authors

Romana Jarosova − *Department of Chemistry and R.N. Adams Institute for Bioanalytical Chemistry, University of Kansas, Lawrence, Kansas 66045, United States; Department of Analytical Chemistry, UNESCO Laboratory of Environmental Electrochemistry, Charles University, Prague 2 12843, Czech Republic;* orcid.org/0000-0002-0529-8294; Phone: 517-763-1417; Email: jarosova@msu.edu

Michael A. Johnson − *Department of Chemistry and R.N. Adams Institute for Bioanalytical Chemistry, University of Kansas, Lawrence, Kansas 66045, United States;* orcid.org/0000-0001-5078-9896; Phone: 785-864-4269; Email: johnsonm@ku.edu

Authors

Sayuri S. Niyangoda − *Department of Chemistry and R.N. Adams Institute for Bioanalytical Chemistry, University of Kansas, Lawrence, Kansas 66045, United States*

Piyanka Hettiarachchi − *Department of Chemistry and R.N. Adams Institute for Bioanalytical Chemistry, University of Kansas, Lawrence, Kansas 66045, United States*

Complete contact information is available at: https://pubs.acs.org/10.1021/acschemneuro.2c00484

Author Contributions

R.J., S.S.N., and P.H. contributed equally. R.J. and M.A.J. oversaw the conduct of the described work. R.J., S.S.N., P.H., and M.A.J. conducted the experiments, data analysis, and contributed to the writing. R.J. carried out the methodology regarding behavioral experimentation. R.J., S.S.N., P.H., and M.A.J. contributed to the design of the experiments, review of the experimental results, and review of the manuscript. All authors approved this submission.

Notes

The authors declare no competing financial interest.

All data are presented as mean ± standard error of the mean (SEM) unless mentioned otherwise. All statistical analysis and graphical depictions were carried out using OriginPro Software, version 2021 (OriginLab Corp., Northampton, MA).

ACKNOWLEDGMENTS

This work was funded by grants from the National Institute of Neurological Disorders and Stroke of the National Institutes of Health under Award Number R21 NS109659 (MAJ), the National Institute of General Medical Sciences of the National Institutes of Health under Award Numbers P20GM103638 and P30GM145499, and Charles University in Prague under award number SVV260560 (R.J.).

REFERENCES

(1) Atri, A. The Alzheimer's Disease Clinical Spectrum. *Med. Clin. North Am.* **2019**, *103*, 263−293.

(2) Arvanitakis, Z.; Shah, R. C.; Bennett, D. A. Diagnosis and Management of Dementia: Review. *JAMA, J. Am. Med. Assoc.* **2019**, *322*, 1589−1599.

(3) Livingston, G.; Sommerlad, A.; Orgeta, V.; Costafreda, S. G.; Huntley, J.; Ames, D.; Ballard, C.; Banerjee, S.; Burns, A.; Cohen-Mansfield, J.; Cooper, C.; Fox, N.; Gitlin, L. N.; Howard, R.; Kales, H. C.; Larson, E. B.; Ritchie, K.; Rockwood, K.; Sampson, E. L.; Samus, Q.; Schneider, L. S.; Selbæk, G.; Teri, L.; Mukadam, N. Dementia Prevention, Intervention, and Care. *Lancet* **2017**, *390*, 2673−2734.

(4) Hebert, L. E.; Weuve, J.; Scherr, P. A.; Evans, D. A. Alzheimer Disease in the United States (2010-2050) Estimated Using the 2010 Census. *Neurology* **2013**, *80*, 1778−1783.

(5) Weuve, J.; Hebert, L. E.; Scherr, P. A.; Evans, D. A. Deaths in the United States among Persons with Alzheimer's Disease (2010-2050). *Alzheimers. Dement.* **2014**, *10*, No. e40.

(6) No author. Fact sheet; Alzheimer's association. https://act.alz.org/site/DocServer/2012_Costs_Fact_Sheet_version_2.pdf;jsessionid=00000000.app20004a?docID=7161&NONCE_TOKEN=F667F4CA3909631883502F4EE4F316E2 (accessed Jan 07, 2022).

(7) Briggs, R.; Kennelly, S. P.; O'Neill, D. Drug Treatments in Alzheimer's Disease. *Clin. Med.* **2016**, *16*, 247−253.

(8) Eratne, D.; Loi, S. M.; Farrand, S.; Kelso, W.; Velakoulis, D.; Looi, J. C. L. Alzheimer's Disease: Clinical Update on Epidemiology, Pathophysiology and Diagnosis. *Australas. Psychiatr.* **2018**, *26*, 347−357.

(9) Scheltens, P.; Blennow, K.; Breteler, M. M. B.; de Strooper, B.; Frisoni, G. B.; Salloway, S.; Van der Flier, W. M. Alzheimer's Disease. *Lancet* **2016**, *388*, 505−517.

(10) Esquerda-Canals, G.; Montoliu-Gaya, L.; Güell-Bosch, J.; Villegas, S. Mouse Models of Alzheimer's Disease. *J. Alzheimer's Dis.* **2017**, *57*, 1171−1183.

(11) Nazem, A.; Sankowski, R.; Bacher, M.; Al-Abed, Y. Rodent Models of Neuroinflammation for Alzheimer's Disease. *J. Neuroinflammation* **2015**, *12*, 74.

(12) Koehler, D.; Williams, F. E. Utilizing Zebrafish and Okadaic Acid to Study Alzheimer's Disease. *Neural Regener. Res.* **2018**, *13*, 1538−1541.
(13) Kodera, K.; Matsui, H. Zebrafish, Medaka and Turquoise Killifish for Understanding Human Neurodegenerative/Neurodevelopmental Disorders. *Int. J. Mol. Sci.* **2022**, *23*, 1399.
(14) Xi, Y.; Noble, S.; Ekker, M. Modeling Neurodegeneration in Zebrafish. *Curr. Neurol. Neurosci. Rep.* **2011**, *11*, 274−282.
(15) Wang, J.; Cao, H. Zebrafish and Medaka: Important Animal Models for Human Neurodegenerative Diseases. *Int. J. Mol. Sci.* **2021**, *22*, 10766.
(16) Kalueff, A. V.; Stewart, A. M.; Gerlai, R. Zebrafish as an Emerging Model for Studying Complex Brain Disorders. *Trends Pharmacol. Sci.* **2014**, *35*, 63−75.
(17) Vieira, A. C.; Rubiolo, J. A.; López-Alonso, H.; Cifuentes, J. M.; Alfonso, A.; Bermúdez, R.; Otero, P.; Vieytes, M. R.; Vega, F. V.; Botana, L. M. Oral Toxicity of Okadaic Acid in Mice: Study of Lethality, Organ Damage, Distribution and Effects on Detoxifying Gene Expression. *Toxins* **2013**, *5*, 2093.
(18) Emery, H.; Traves, W.; Rowley, A. F.; Coates, C. J. The Diarrhetic Shellfish-Poisoning Toxin, Okadaic Acid, Provokes Gastropathy, Dysbiosis and Susceptibility to Bacterial Infection in a Non-Rodent Bioassay, Galleria Mellonella. *Arch. Toxicol.* **2021**, *95*, 3361−3376.
(19) Tubaro, A.; Sosa, S.; Altinier, G.; Soranzo, M. R.; Satake, M.; Della Loggia, R.; Yasumoto, T. Short-Term Oral Toxicity of Homoyessotoxins, Yessotoxin and Okadaic Acid in Mice. *Toxicon* **2004**, *43*, 439−445.
(20) Kamat, P. K.; Rai, S.; Swarnkar, S.; Shukla, R.; Nath, C. Molecular and Cellular Mechanism of Okadaic Acid (OKA)-Induced Neurotoxicity: A Novel Tool for Alzheimer's Disease Therapeutic Application. *Mol. Neurobiol.* **2014**, *50*, 852−865.
(21) Cohen, P.; Holmes, C. F. B.; Tsukitani, Y. Okadaic Acid: A New Probe for the Study of Cellular Regulation. *Trends Biochem. Sci.* **1990**, *15*, 98−102.
(22) Choi, J. Y.; Ryoo, H. M.; Lee, B. H.; Kim, H. J.; Sohn, K. Y.; Jo, J. S. Okadaic Acid Inhibits Alkaline Phosphatase Activity in MC3T3-E1 Cells. *Biochem. Mol. Biol. Int.* **1995**, *37*, 943−947.
(23) Meštrović, V.; Pavela-Vrančič, M. Inhibition of Alkaline Phosphatase Activity by Okadaic Acid, a Protein Phosphatase Inhibitor. *Biochimie* **2003**, *85*, 647−650.
(24) Murata, T.; Shirakawa, S.; Takehara, T.; Kobayashi, S.; Haneji, T. Protein Phosphatase Inhibitors, Okadaic Acid and Calyculin A, Induce Alkaline Phosphatase Activity in Osteoblastic Cells Derived from Newborn Mouse Calvaria. *Biochem. Mol. Biol. Int.* **1995**, *36*, 365−372.
(25) Nada, S. E.; Williams, F. E.; Shah, Z. A. Development of a Novel and Robust Pharmacological Model of Okadaic Acid-Induced Alzheimer's Disease in Zebrafish. *CNS Neurol. Disord.: Drug Targets* **2016**, *15*, 86−94.
(26) Schallert, T.; Fleming, S. M. Dopamine and Motor Function in Rat and Mouse Models of Parkinson's Disease. In *Dopamine Handbook*, Iversen, L., et al., Eds.; Oxford Academic, 2010, pp 279−285.
(27) Cools, R.; D'Esposito, M. 5.4 Dopaminergic Modulation of Flexible Cognitive Control in Humans. *Dopamine Handb.* **2009**, *14*, 249−260.
(28) Lelos, M. J.; Dunnett, S. B. Aberrant Dopamine Transmission and Cognitive Dysfunction in Animal Models of Parkinson's Disease. *J. Parkinson's Dis.* **2011**, *1*, 151−165.
(29) Masoud, S. T.; Vecchio, L. M.; Bergeron, Y.; Hossain, M. M.; Nguyen, L. T.; Bermejo, M. K.; Kile, B.; Sotnikova, T. D.; Siesser, W. B.; Gainetdinov, R. R.; Wightman, R. M.; Caron, M. G.; Richardson, J. R.; Miller, G. W.; Ramsey, A. J.; Cyr, M.; Salahpour, A. Increased Expression of the Dopamine Transporter Leads to Loss of Dopamine Neurons, Oxidative Stress and l-DOPA Reversible Motor Deficits. *Neurobiol. Dis.* **2015**, *74*, 66−75.
(30) Masato, A.; Plotegher, N.; Boassa, D.; Bubacco, L. Impaired Dopamine Metabolism in Parkinson's Disease Pathogenesis. *Mol. Neurodegener.* **2019**, *14*, 35.
(31) Latif, S.; Jahangeer, M.; Maknoon Razia, D.; Ashiq, M.; Ghaffar, A.; Akram, M.; El Allam, A.; Bouyahya, A.; Garipova, L.; Ali Shariati, M.; Thiruvengadam, M.; Azam Ansari, M. Dopamine in Parkinson's Disease. *Clin. Chim. Acta* **2021**, *522*, 114−126.
(32) Segura-Aguilar, J.; Paris, I.; Muñoz, P.; Ferrari, E.; Zecca, L.; Zucca, F. A. Protective and Toxic Roles of Dopamine in Parkinson's Disease. *J. Neurochem.* **2014**, *129*, 898−915.
(33) Warren, N.; O'Gorman, C.; Lehn, A.; Siskind, D. Dopamine Dysregulation Syndrome in Parkinson's Disease: A Systematic Review of Published Cases. *J. Neurol., Neurosurg. Psychiatry* **2017**, *88*, 1060−1064.
(34) Ortiz, A. N.; Kurth, B. J.; Osterhaus, G. L.; Johnson, M. A. Dysregulation of Intracellular Dopamine Stores Revealed in the R6/2 Mouse Striatum. *J. Neurochem.* **2010**, *112*, 755−761.
(35) Ortiz, A. N.; Osterhaus, G. L.; Lauderdale, K.; Mahoney, L.; Fowler, S. C.; von Hörsten, S.; Riess, O.; Johnson, M. A. Motor Function and Dopamine Release Measurements in Transgenic Huntington's Disease Model Rats. *Brain Res.* **2012**, *1450*, 148−156.
(36) Ortiz, A. N.; Kurth, B. J.; Osterhaus, G. L.; Johnson, M. A. Impaired Dopamine Release and Uptake in R6/1 Huntington's Disease Model Mice. *Neurosci. Lett.* **2011**, *492*, 11−14.
(37) Howes, O. D.; Williams, M.; Ibrahim, K.; Leung, G.; Egerton, A.; McGuire, P. K.; Turkheimer, F. Midbrain Dopamine Function in Schizophrenia and Depression: A Post-Mortem and Positron Emission Tomographic Imaging Study. *Brain* **2013**, *136*, 3242−3251.
(38) Martorana, A.; Koch, G. Is Dopamine Involved in Alzheimer's Disease? *Front. Aging Neurosci.* **2014**, *6*, 252.
(39) Venton, B. J.; Wightman, R. M. Psychoanalytical Electrochemistry: Dopamine and Behavior. *Anal. Chem.* **2003**, *75*, 414A.
(40) Hermans, A.; Keithley, R. B.; Kita, J. M.; Sombers, L. A.; Wightman, R. M. Dopamine Detection with Fast-Scan Cyclic Voltammetry Used with Analog Background Subtraction. *Anal. Chem.* **2008**, *80*, 4040−4048.
(41) Wightman, R. M. Probing Cellular Chemistry in Biological Systems with Microelectrodes. *Science* **2006**, *311*, 1570−1574.
(42) Field, T. M.; Shin, M.; Stucky, C. S.; Loomis, J.; Johnson, M. A. Electrochemical Measurement of Dopamine Release and Uptake in Zebrafish Following Treatment with Carboplatin. *ChemPhysChem* **2018**, *19*, 1192−1196.
(43) Shin, M.; Field, T. M.; Stucky, C. S.; Furgurson, M. N.; Johnson, M. A. Ex Vivo Measurement of Electrically Evoked Dopamine Release in Zebrafish Whole Brain. *ACS Chem. Neurosci.* **2017**, *8*, 1880−1888.
(44) Jones, M. O.; McCutcheon, M.; Young, M.; Norton, A. M. J.; Norton, W. H. J.; Jones, L. J.; Mccutcheon, J. E. Neurochemical Measurements in the Zebrafish Brain. *Front. Behav. Neurosci.* **2015**, *9*, 246. www.frontiersin.org
(45) Gómez-Laplaza, L. M.; Gerlai, R. Latent Learning in Zebrafish (Danio Rerio). *Behav. Brain Res.* **2010**, *208*, 509−515.
(46) Luchiari, A. C.; Salajan, D. C.; Gerlai, R. Acute and Chronic Alcohol Administration: Effects on Performance of Zebrafish in a Latent Learning Task. *Behav. Brain Res.* **2015**, *282*, 76−83.
(47) Wong, K.; Elegante, M.; Bartels, B.; Elkhayat, S.; Tien, D.; Roy, S.; Goodspeed, J.; Suciu, C.; Tan, J.; Grimes, C.; Chung, A.; Rosenberg, M.; Gaikwad, S.; Denmark, A.; Jackson, A.; Kadri, F.; Chung, K. M.; Stewart, A.; Gilder, T.; Beeson, E.; Zapolsky, I.; Wu, N.; Cachat, J.; Kalueff, A. V. Analyzing Habituation Responses to Novelty in Zebrafish (Danio Rerio). *Behav. Brain Res.* **2010**, *208*, 450−457.
(48) Stewart, A.; Cachat, J.; Wong, K.; Gaikwad, S.; Gilder, T.; DiLeo, J.; Chang, K.; Utterback, E.; Kalueff, A. V. Homebase Behavior of Zebrafish in Novelty-Based Paradigms. *Behav. Processes* **2010**, *85*, 198−203.
(49) Ogi, A.; Licitra, R.; Naef, V.; Marchese, M.; Fronte, B.; Gazzano, A.; Santorelli, F. M. Social Preference Tests in Zebrafish: A Systematic Review. *Front. Vet. Sci.* **2021**, *7*, 590057.

https://doi.org/10.1021/acschemneuro.2c00484
ACS Chem. Neurosci. XXXX, XXX, XXX−XXX

(50) Saverino, C.; Gerlai, R. The Social Zebrafish: Behavioral Responses to Conspecific, Heterospecific, and Computer Animated Fish. *Behav. Brain Res.* **2008**, *191*, 77−87.
(51) Geng, Y.; Peterson, R. T. The Zebrafish Subcortical Social Brain as a Model for Studying Social Behavior Disorders. *Dis. Models Mech.* **2019**, *12*, dmm039446.
(52) Wolinsky, D.; Drake, K.; Bostwick, J. Diagnosis and Management of Neuropsychiatric Symptoms in Alzheimer's Disease. *Curr. Psychiatr. Rep.* **2018**, *20*, 117.
(53) Buchman, A. S.; Bennett, D. A. Loss of Motor Function in Preclinical Alzheimer's Disease. *Expert Rev. Neurother.* **2011**, *11*, 665−676.
(54) Zhang, Z.; Simpkins, J. W. An Okadaic Acid-Induced Model of Tauopathy and Cognitive Deficiency. *Brain Res.* **2010**, *1359*, 233−246.
(55) Chen, T.; Shou, L.; Guo, X.; Wei, M.; Zheng, H.; Tao, T. Magnolol Attenuates the Locomotor Impairment, Cognitive Deficit, and Neuroinflammation in Alzheimer's Disease Mice with Brain Insulin Resistance via up-Regulating MiR-200c. *Bioengineered* **2022**, *13*, 531−543.
(56) Das, T. K.; Jana, P.; Chakrabarti, S. K.; Abdul Hamid, M. R. W. A. Curcumin Downregulates GSK3 and Cdk5 in Scopolamine-Induced Alzheimer's Disease Rats Abrogating A 40/42 and Tau Hyperphosphorylation. *J. Alzheimer's Dis. Rep.* **2019**, *3*, 257−267.
(57) Gloria, Y.; Ceyzériat, K.; Tsartsalis, S.; Millet, P.; Tournier, B. B. Dopaminergic Dysfunction in the 3xTg-AD Mice Model of Alzheimer's Disease. *Sci. Rep.* **2021**, *11*, 19412.
(58) Naderi, M.; Jamwal, A.; Ferrari, M. C. O.; Niyogi, S.; Chivers, D. P. Dopamine Receptors Participate in Acquisition and Consolidation of Latent Learning of Spatial Information in Zebrafish (Danio Rerio). *Prog. Neuro-Psychopharmacol. Biol. Psychiatry* **2016**, *67*, 21−30.
(59) Hamidi, N.; Nozad, A.; Sheikhkanloui Milan, H.; Amani, M. Okadaic Acid Attenuates Short-Term and Long-Term Synaptic Plasticity of Hippocampal Dentate Gyrus Neurons in Rats. *Neurobiol. Learn. Mem.* **2019**, *158*, 24−31.
(60) Kamat, P. K.; Tota, S.; Saxena, G.; Shukla, R.; Nath, C. Okadaic Acid (ICV) Induced Memory Impairment in Rats: A Suitable Experimental Model to Test Anti-Dementia Activity. *Brain Res.* **2010**, *1309*, 66−74.
(61) Kaushal, A.; Wani, W. Y.; Bal, A.; Gill, K. D.; Kaur, J. Okadaic Acid and Hypoxia Induced Dementia Model of Alzheimer's Type in Rats. *Neurotoxic. Res.* **2019**, *35*, 621−634.
(62) Garcia, L.; Garcia, F.; Llorens, F.; Unzeta, M.; Itarte, E.; Gómez, N. PP1/PP2A Phosphatases Inhibitors Okadaic Acid and Calyculin A Block ERK5 Activation by Growth Factors and Oxidative Stress. *FEBS Lett.* **2002**, *523*, 90−94.
(63) Facciol, A.; Gerlai, R. Zebrafish Shoaling, Its Behavioral and Neurobiological Mechanisms, and Its Alteration by Embryonic Alcohol Exposure: A Review. *Front. Behav. Neurosci.* **2020**, *14*, 572175.
(64) Gerlai, R.; Ahmad, F.; Prajapati, S. Differences in Acute Alcohol-Induced Behavioral Responses Among Zebrafish Populations. *Alcohol.: Clin. Exp. Res.* **2008**, *32*, 1763.
(65) Faustino, A. I.; Tacão-Monteiro, A.; Oliveira, R. F. Mechanisms of Social Buffering of Fear in Zebrafish OPEN. *Sci. Rep.* **2017**, *7*, 44329.
(66) Agetsuma, M.; Aoki, T.; Aoki, R.; Okamoto, H. *Cued Fear Conditioning in Zebra Fi Sh (Danio Rerio)*, 2012 66.
(67) Oei, T. P. S.; King, M. G. Catecholamines and Aversive Learning: A Review. *Neurosci. Biobehav. Rev.* **1980**, *4*, 161−173.
(68) Millan, M. J. The Neurobiology and Control of Anxious States. *Prog. Neurobiol.* **2003**, *70*, 83−244.
(69) Pezze, M. A.; Feldon, J. Mesolimbic Dopaminergic Pathways in Fear Conditioning. *Prog. Neurobiol.* **2004**, *74*, 301−320.
(70) Johnson, M. A.; Rajan, V.; Miller, C. E.; Wightman, R. M. Dopamine Release Is Severely Compromised in the R6/2 Mouse Model of Huntington's Disease. *J. Neurochem.* **2006**, *97*, 737−746.
(71) Phillips, P. E. M.; Stuber, G. D.; Heien, M. L. A. V.; Wightman, R. M.; Carelli, R. M. Subsecond Dopamine Release Promotes Cocaine Seeking. *Nature* **2003**, *422*, 614−618.
(72) Betz, W. J.; Henkel, A. W. Okadaic Acid Disrupts Clusters of Synaptic Vesicles in Frog Motor Nerve Terminals. *J. Cell Biol.* **1994**, *124*, 843−854.
(73) Jarosova, R.; Kaplan, S. V.; Field, T. M.; Givens, R. S.; Senadheera, S. N.; Johnson, M. A. In Situ Electrochemical Monitoring of Caged Compound Photochemistry: An Internal Actinometer for Substrate Release. *Anal. Chem.* **2021**, *93*, 2776−2784.
(74) Jarosova, R.; Douglass, A. D.; Johnson, M. A. Optimized Sawhorse Waveform for the Measurement of Oxytocin Release in Zebrafish. *Anal. Chem.* **2022**, *94*, 2942−2949.
(75) Kraft, J. C.; Osterhaus, G. L.; Ortiz, A. N.; Garris, P. A.; Johnson, M. A. In vivo dopamine release and uptake impairments in rats treated with 3-nitropropionic acid. *Neuroscience* **2009**, *161*, 940−949.

https://doi.org/10.1021/acschemneuro.2c00484
ACS Chem. Neurosci. XXXX, XXX, XXX−XXX

APPENDIX VII - CONFIRMATION OF PARTICIPATION

1. **Jarošová, R.**; Rutherford, J.; Swain, G. M. Evaluation of a Nitrogen-Incorporated Tetrahedral Amorphous Carbon Thin Film for the Detection of Tryptophan and Tyrosine Using Flow Injection Analysis with Amperometric Detection. *Analyst* **2016**, *141* (21), 6031–6041.
   - 5-year Impact Factor: **4.16**; Percentage of participation of Mgr. Romana Jarošová ~ **75 %**

2. **Jarošová, R**.; Sanchez, S.; Haubold, L.; Swain, G. M. Isatin Analysis Using Flow Injection Analysis with Amperometric Detection – Comparison of Tetrahedral Amorphous Carbon and Diamond Electrode Performance. *Electroanalysis* **2017**, *29* (9), 2147–2154.
   - 5-year Impact Factor: **2.81**; Percentage of participation of Mgr. Romana Jarošová ~ **75 %**

3. **Jarosova, R.**;***** Irikura, K.; Rocha-Filho, R.; Swain, G. Detection of Pyocyanin with a Boron-Doped Diamond Electrode Using Flow Injection Analysis with Amperometric Detection and Square Wave Voltammetry. *Electroanalysis* **2021**, *34*, 1–12. ******Co-corresponding author.*
   - 5-year Impact Factor: **2.81**; Percentage of participation of Mgr. Romana Jarošová ~ **75 %**

4. **Jarosova, R**.; Douglass, D. A. ; Johnson, M. A. Optimized Sawhorse Waveform for the Measurement of Oxytocin Release in Zebrafish. *Anal. Chem.* **2022**, *94* (6), 2942-2949.
   - 5-year Impact Factor: **6.74**; Percentage of participation of Mgr. Romana Jarošová ~ **85 %**

5. **Jarosova, R**.; Kaplan, S. V.; Field, T. M.; Givens, R. S.; Senadheera, S. N.; Johnson, M. A. In Situ Electrochemical Monitoring of Caged Compound Photochemistry: An Internal Actinometer for Substrate Release. *Anal. Chem.* **2021**, *93* (5), 2776-2784.
   - 5-year Impact Factor: **6.74**; Percentage of participation of Mgr. Romana Jarošová ~ **75 %**

6. **Jarosova, R.**;***** Niyangoda, S. S.; Hettiarachchi, P.; Johnson, M. A. Impaired Dopamine Release and Latent Learning in Alzheimer's Disease Model Zebrafish. *ACS Chem. Neurosci.* **2022**, *13* (19), 2924–2931. ***** *Co-corresponding author.*
   - 5-year Impact Factor: **3.83**; Percentage of participation of Mgr. Romana Jarošová ~ **75 %**

I declare that the percentage of participation of Mgr. Romana Jarošová, Ph.D. at the above given papers corresponds to the above given numbers.

Prague, 2023 ……

Prof. RNDr. Jiří Zima, CSc.

APPENDIX VIII - LIST OF PUBLICATIONS, PRESENTATIONS, ACHIEVEMENTS, AND GRANTS

PUBLICATIONS

1. **Jarosova R,** Ostertag BJ., Ross AE. Graphere Oxide Fiber Microelectrodes with Controlled Sheet Alignments for Sensitive Neurotransmitter Detection. A revised version submitted, 2023.
2. **Jarosova, R.,** Woolfolk, S. K., Martinez-Rivera, N., Jaeschke, M. W., Rosa-Molinar, E., Tamerler, C., Johnson, M. A. Spatiotemporal Imaging of Zinc Ions in Zebrafish Live Brain Tissue Enabled by Fluorescent Bionanoprobes. *Molecules,* 2023, 28, 2260.
3. Hettiarachchi R., Niyangoda P., **Jarosova R.,** Johnson MA. Dopamine Release Impairments Accompany Locomotor and Cognitive Deficiencies in Rotenone-Treated Parkinson's Disease Model Zebrafish. *ACS Chemical Research in Toxicology,* 2022, 35, 1974-1982.
4. **Jarosova R*.**, Niyangoda P., Hettiarachchi R., Johnson MA*. Impaired Dopamine Release and Latent Learning in Alzheimer's Disease Model Zebrafish. *ACS Chemical Neuroscience*, 2022, 13, 2924-2931. **Corresponding author.*
5. **Jarosova R.**, Douglass AD, Johnson MA. Optimized Sawhorse Waveform for the Measurement of Oxytocin Release in Zebrafish. *Analytical Chemistry,* 2022, 94, 2942-2949.
6. **Jarosova R*.**, Irikura K., Rocha-Filho R., Swain GM. Detection of Pyocyanin with a Boron-Doped Diamond Electrode Using Flow Injection Analysis with Amperometric Detection and Square Wave Voltammetry. *Electroanalysis,* 2022, 34, 1-12. **Corresponding author.*
7. **Jarošová R**., Kaplan S., Field T., Givens R., Seaheera S., Johnson MA. *In situ* Electrochemical Monitoring of Caged Compound Photochemistry: An Internal Actinometer for Substrate Release. *Analytical Chemistry*, 2021, 93, 2776-2784.
8. Wang Y., Parvis F., Iqbal Hossain MD., Ma K., **Jarošová R.**, Swain GM., and Blanchard GJ. Local and Long-Range Organization in Room Temperature Ionic Liquids. *Langmuir*, 2021, 37, 605-615.
9. **Jarošová R.**, Bhardwaj K., Swain GM. Temperature Dependence of the Heterogeneous Electron-Transfer Rate Constant for Ferrocene Carboxylic Acid in Room Temperature Ionic Liquids at Microstructurally Distinct Carbon Electrodes. *Journal of Electroanalytical Chemistry*, 2020, 875.
10. Wang J., **Jarošová R.**, Swain GM., Blanchard GJ. Characterizing the Magnitude and Structure-Dependence of Free Charge Density Gradients in Room-Temperature Ionic Liquids. *Langmuir*, 2020, 36, 3038-3045.
11. **Jarošová R.**, McClure ES., Gajda M., Jović M., Girault HH., Lesch A., Maiden M., Waters Ch., Swain GM. Inkjet-Printed Carbon Nanotube Electrodes for Measuring Pyocyanin and Uric Acid in a Wound Fluid Simulant and Culture Media. *Analytical Chemistry*, 2019, 91, 8835-8844.
12. Ma K., **Jarošová R**., Wang Y., Swain GM., Blanchard GJ. Ionic Liquids. a Unique and Useful Class of Materials. *the Chemical Educator*, 2018, 23, 265 – 272.

13. Espinoza E., Qui J., Castiaux A., **Jarošová R**., Swain GM. HPLC-EC Analysis of Estrogenic Compounds Using Tetrahedral Amorphous Carbon Thin-Film Electrodes. *Electroanalysis*, 2018, 30, 1575-1582 (Special Issue).
14. Ma K., **Jarošová R.**, Swain GM., Blanchard GJ. Modulation of an Induced Charge Density Gradient in the Room Temperature Ionic Liquid $BMIM^{+}BF_4^{-}$. the *Journal of Physical Chemistry C*, 2018, 122, 7361-7367.
15. Koudelkova B., **Jarošová R.**, Koukol O. Are Endophytic Fungi from Rhododendron Tomentosum Preadapted for its Essential Oil? *Biochemical Systematics and Ecology,* 2017, 75, 21-26.
16. **Jarošová R.**, Sanchez S., Haubold L., Swain GM. Isatin Analysis Using Flow Injection Analysis with Amperometric Detection: Comparison of Tetrahedral Amorphous Carbon and Diamond Electrode Performance. *Electroanalysis*, 2017, 29, 2147-2154.
17. Ma K., **Jarošová R.**, Swain GM., Blanchard GJ. Charge-Induced Long-Range Order in a Room Temperature Ionic Liquid. *Langmuir*, 2016, 32, 9507-9512.
18. **Jarošová R.**, Rutherford J., Swain GM. Evaluation of Nitrogen-Incorporated Tetrahedral Amorphous Carbon Thin-Film for the Detection of Tryptophan and Tyrosine Using Flow Injection Analysis with Amperometric Detection. *Analyst*, 2016, 141, 6031-6041.
19. **Jarošová R.**, De Sousa Bezerra PM., Munson C., Swain GM. Assessment of Heterogeneous Electron-Transfer Rate Constants for Soluble Redox Analytes at Tetrahedral Amorphous Carbon, Boron-Doped Diamond, and Glassy Carbon Electrodes. *Physica Status Solidi A: Applications and Material Science*, 2016, 213, 2087-2098.
20. Wachter N., Munson C., **Jarošová R.**, Berkun I., Hogan T., Rocha-Filho R., Swain GM. Structure, Electronic Properties, and Electrochemical Behavior of a Boron-Doped Diamond/Quartz Optically Transparent Electrode. *ACS Applied Materials and Interfaces,* 2016, *8, 28325-28337.*
21. **Jarošová R.**, Swain GM. Rapid Preparation of Room Temperature Ionic Liquids with Low Water Content as Characterized with a t*a*-C:N Electrode. *Journal of the Electrochemical Society,* 2015, 162, H507-H511.
22. **Jarošová R.,** Barek J., Zima J., Dejmková H. Voltammetric, Amperometric, and Chronopotentiometric Determination of Submicromolar Concentrations of Carboxin. *Electroanalysis*, 2015, 28, 445-451.

CONFERENCE CONTRIBUTIONS

Oral Presentations

1. **Jarošová R.**, Kaplan S., Field T., Givens R., Senadheera SN., Johnson MA. *In situ Electrochemical Monitoring of Caged Compound Photochemistry: An Internal Actinometer for Substrate Release*. University of Kansas Analytical Seminar. Lawrence, KS, 2020.
2. **Jarošová R.**, Kaplan S., Field T., Givens R., Senadheera SN., Johnson MA. *In situ Electrochemical Monitoring of Caged Compound Photochemistry.* Pittcon, Chicago, IL, 2020.
3. **Jarošová R.**, Swain GM. *Electroanalytical Performance of Nitrogen-Incorporated Tetrahedral Amorphous Carbon Thin-Films in Room Temperature Ionic Liquids*. ACS Fall Meeting, Boston, MA, 2018.

4. **Jarošová R.**, Espinosa EKA., Swain GM. *Nitrogen-Incorporated Tetrahedral Amorphous Carbon Thin-Films – a New Electrode for the HPLC-EC of Biological and Environmental Analytes.* HPLC Symposium, Prague, Czech Republic, 2017.
5. **Jarošová R.**, Gajda M., Lesch A., Swain GM. the *Electrochemical Characterization of Ink-Jet Printed Carbon Nanotubes Electrodes.* Pittcon, Chicago, IL, 2017.
6. **Jarošová R.**, Espinosa EKA., Swain GM. *Electroanalytical Performance of Nitrogen-Containing Tetrahedral Amorphous Carbon Thin-Film Electrodes*. Association of Analytical Chemists Symposium, Livonia, MI, 2017.
7. **Jarošová R.**, Munson C., Swain GM. the *Electrochemical Properties of Diamond and Tetrahedral Amorphous Carbon Electrodes in Room temperature Ionic Liquid.* 227th Electrochemical Society Meeting, Chicago, Illinois, 2015.
8. **Jarošová R.**, Zima J., Barek J., Dejmkova H. *Chronopotentiometric Determination of Organic Pollutants Using Reticulated Vitreous Carbon Electrode.* XXIV. Modern Electrochemical Methods, Jetrichovice, Czech Republic, 2014.
9. **Jarošová R.**, Barek J., Zima J., H. Dejmkova. *Voltammetric and Amperometric Determination of Carboxin Using Carbon Paste Electrode*. 14th Student Scientific Conference Bratislava, Slovakia 2012. This presentation won second place in the Electrochemistry category.
10. Němcová L., Fahnrichová B., **Jarošová R.**, Zima J., Barek J. *Determination of Natural Antioxidants at a Carbon Paste Electrode.* XXX. Modern Electrochemical Methods, Jetrichovice, Czech Republic, 2010.

Posters

1. **Jarošová R.**, Swain GM. the *Electrochemical Behavior of Boron-Doped Diamond and Nitrogen-Incorporated tetrahedral Amorphous Carbon Thin-Film Electrodes in Ionic Liquid.* ACS Central Regional Meeting, Covington, Kentucky, 2016.
2. **Jarošová R.**, Swain GM. *Heterogeneous Electron-Transfer Rate Constants for Inorganic Redox Systems at Carbon Electrodes in Aqueous Solutions and Room-Temperature Ionic Liquids*. ElectroChemOhio, Columbus, Ohio, 2014.
3. **Jarošová R.**, Zima J., Barek J., Dejmkova H. *Chronopotentiometric Determination of Nitrophenols Using Reticulated Vitreous Carbon Electrode*. 15th International Conference of Electroanalysis, Malmö, Sweeden, 2014.
4. **Jarošová R.**, Barek J., Zima J., Dejmkova H. *Electrochemical Determination of Carboxin.* 56. Zjazd Polskiego Towarzystwa Chemicznego I Stowarzyszenia Inzynierow I Technikow Przemyslu Chemicznego, Siedlce, Poland, 16th-20th September 2013. Poster S04P60. ISBN 978-83-60988-15-2.